Modelling and experimental validation of the hygrothermal performances of earth as a building material

Lucile, Caroline, Laurence Soudani

n°ordre NNT: 2016LYSET011

Thèse de doctorat

opérée au sein de
Ecole Nationale des Travaux Publics de l'Etat
LGCB-LTDS UMR 5513

Ecole doctorale n°162
MEGA (Mécanique, Energétique, Génie Civil, Acoustique)
Spécialité : Génie Civil

Soutenue publiquement le 09/12/2016, par

Lucile, Caroline, Laurence SOUDANI

Modelling and experimental validation of the hygrothermal performances of earth as a building material

devant le jury composé de

Stéphane Lassue	Professeur	Université d'Artois	*Président*
Stéphane Lassue	Professeur	Université d'Artois	*Rapporteur*
Nathan Mendes	Professeur	PUCPR Curitiba, Brésil	*Rapporteur*
Thibaut Colinart	Maître de conférence	Université Bretagne Sud	*Examinateur*
Jean-Claude Morel	Professeur	Coventry University	*Examinateur*
Anne-Cécile Grillet	Maître de conférence	Université Savoie Mont-Blanc	*Examinatrice*
Antonin Fabbri	Chargé de recherche	ENTPE	*Directeur*
Monika Woloszyn	Professeur	Université Savoie Mont-Blanc	*Directrice*

Avant-propos

Ce travail de thèse a été financé par l'Agence Nationale de la Recherche (ANR) à travers l'appel à projet « Villes et Bâtiments Durables », et le projet Primaterre (n° ANR-12-VBDU-0001).

Je tiens tout d'abord à exprimer ma reconnaissance aux membres du jury pour le temps consacré à mon travail et leurs suggestions, plus précisément aux rapporteurs Mr Stéphane Lassue et Nathan Mendes. Un remerciement particulier également à Thibaut Colinart pour avoir accepté d'examiner ma thèse ainsi que pour son implication dans la revue de mon premier article.

Cette thèse s'est déroulée alternativement au laboratoire LGCB-LTDS à l'ENTPE (Vaulx-en-Velin), ainsi qu'au laboratoire LOCIE de l'Université de Savoie Mont Blanc (Chambéry).

Je souhaite adresser un immense merci à mes encadrants, qui m'ont donner ma chance en me confiant ce travail et qui ont su me faire profiter de leur expérience et de leur bienveillance. Merci à Antonin, qui a accepté de me prendre tout d'abord en stage de Master (sur les recommandations de Stéphane Hans, que je remercie également), puis en thèse dont il a assuré l'encadrement au quotidien. Merci d'avoir répondu présent à chaque moment de ce travail, même pour les moins drôles, et pour nos discussions, pas uniquement professionnelles, mais qui ont toujours été agréables. Je remercie également Jean-Claude qui, même depuis l'Angleterre, s'est toujours inquiété de me savoir sereine et motivée. Du côte de Chambéry, un grand merci à Monika pour le temps que tu m'as accordé et pour tes conseils avisés. J'ai beaucoup aimé les moments que nous avons passé à travailler ensemble . Enfin, un petit mot pour Anne-Cécile, pour avoir su m'apporter ton soutien, jusque dans l'autre hémisphère !

Au terme de ces trois années, je suis très heureuse d'avoir bénéficié de ce co-encadrement qui, au-delà de multiplier la charge de travail pour chaque relecture, m'a surtout apporté des visions différentes sur le plan scientifique, ainsi que d'un grand soutien, et c'est ce qui a permis d'aboutir à une telle diversité dans ce travail.

Je tiens aussi à remercier les membres du projet Primaterre que j'ai eu l'opportunité de rencontrer à plusieurs reprises, et avec lesquels j'ai eu plaisir à collaborer.

Mes remerciements vont également à l'ensemble des membres des deux laboratoires dans lesquels j'ai été amenée à travailler, chercheurs, techniciens et doctorants, qui ont contribué à égayer la vie du laboratoire pendant ces trois années.

Enfin, je remercie profondément mes amis proches, ma famille et ma belle famille, dont le soutien permanent m'a permis d'arriver jusqu'au bout de cette thèse et plus largement au bout de toutes ces années d'études. Un dernier mot tout particulier pour mon Flo qui a surgit de manière inattendue, pour donner à ces trois ans, et aux années à venir, leur raison d'être.

Je suis également consciente de la chance que j'ai eu de pouvoir étudier librement et dans de bonnes conditions en étant une femme, et j'écris ces mots pour ne pas oublier, comme c'est trop souvent le cas, toutes celles qui luttent pour avoir le droit d'apprendre.

Je vais conclure cet avant-propos en utilisant un extrait du récit de voyage de Charles Darwin, qui représente en quelque sorte la manière dont j'ai vécu cette thèse, comme une aventure:

> "*Il me semble que rien ne peut être plus profitable pour un jeune naturalise qu'un voyage dans les pays lointains. Il aiguise, tout en la satisfaisant en partie, cette ardeur, ce besoin de savoir qui entraine tous les hommes.*
> *Ce voyage m'a causé des joies si profondes, que je n'hésite pas à recommander à tous les naturalistes, bien qu'ils ne puissent espérer trouver des compagnons aussi aimables que les miens, de courir toutes les chances et d'entreprendre des voyages. Ces voyages enseignent la patience, et on découvre en même temps combien il y a des gens à l'excellent cœur*"
>
> **"Voyage d'un naturiste autour du monde: fait à bord du navire le "Beagle" de 1831 à 1836", Charles Darwin, traduction de 1875**

Contents

Abstract / Résumé

The Ph.D. is part of a national research project (ANR Primaterre) aiming at promoting real performances (mechanical and thermal) of primary construction materials with low embodied energy such as raw earth.

This work focuses on the thermal and hygrothermal behaviour of rammed earth, i.e. coupled transfers of heat and moisture (liquid water and water vapour) within the material. On the one hand, an evaluation of the thermal and hygric performances of a monitored house with rammed earth walls is provided. This study is completed with laboratory measurements of the thermal and hydric properties of the material. A numerical coupled model, suitable for the specific characteristics of the material, provides a better understanding of the link between the characterization parameters measured and its (hygro)thermal performances. Because of their ability to store and release heat from the sun, their capacity to store moisture and the complexity of the transfers occurring in their pores, earthen walls display many distinctive features that are essential to count for in order to provide an accurate prediction of their impact on the global performances of a building.

La thèse s'inscrit dans un projet de recherche national (ANR Primaterre) qui a pour but d'étudier les performances (mécaniques et thermiques) réelles des matériaux de construction premiers à faible énergie grise que sont la terre crue et la limousinerie.

Le travail de thèse se concentre sur les aspects thermiques et hygrothermiques de la terre crue, c'est-à-dire le couplage entre les transferts de masse d'eau (liquide et vapeur) et de chaleur au sein du matériau. Dans une première partie, une analyse des performances thermiques et hydriques d'une habitation comportant des murs en pisé (terre crue compactée) instrumentés a été réalisée. Cette étude a été complétée par la mesure, en laboratoire, des propriétés thermiques et hydriques du matériau. Le lien entre les paramètres matériaux mesurés et les performances (hygro)-thermiques a été appréhendé à la lumière d'un modèle numérique couplé, adapté aux caractéristiques particulières du matériau. Cette étude a mis en évidence que, de par leur aptitude à stocker puis restituer l'énergie solaire, leur capacité de stockage hydrique et la complexité des transports et changements de phases de l'eau se produisant en leur sein, les murs en terre crue présentent de nombreuses particularités qu'il convient de prendre en compte pour une bonne prédiction de leur impact sur les performances d'une habitation.

Synthèse

Un rapport évaluerait à environ un tiers la part de la population mondiale vivant dans une maison en terre aujourd'hui. En France, comme en Europe ou d'autres régions du monde, le patrimoine de construction en terre crue est très vaste. Par exemple, environ 40% des constructions anciennes en Rhône-Alpes sont en pisé, technique locale de construction en terre crue qui consiste à compacter des couches de terre les unes après les autres, au sein d'un coffrage. Ailleurs en France, d'autres techniques comme la bauge ou le torchis sont également employées. L'avènement de l'ère industrielle a apporté de nouveaux matériaux de construction qui ont peu à peu remplacé les matériaux premiers, et ainsi provoqué leur disparition. Les maisons centenaires encore en état aujourd'hui constituent pourtant les vestiges d'un temps et d'un savoir-faire qu'il est important de préserver.

La recherche actuelle sur la construction en terre crue comporte deux enjeux majeurs.

D'une part, étant donné le nombre de constructions anciennes en pisé, il est important d'être capable d'évaluer correctement les différents aspects du comportement du matériau, de manière à ce que, in fine, les travaux de réhabilitation soient discutés et réalisés uniquement en cas de besoin. D'autre part, le contexte environnemental mondial actuel force à réduire les impacts écologiques du secteur du bâtiment, et la promotion de leur potentiel pourrait apporter une réponse aux problématiques tant énergétique qu'environnementales.

Ceci peut être réalisé grâce à l'existence d'outils scientifiques performants et à des règlementations adaptées. Leur existence n'est plus à faire, mais l'un comme l'autre requièrent une adaptation au matériau terre. De plus, la conception de ce type de construction doit se faire en tenant compte des besoins de conforts de notre époque.

En réponse à ces questions, mes travaux de thèse s'organisent autour de deux grandes parties.

La première composante de mon travail a pour objectif de mettre en évidence les bonnes performances du matériau, à travers la caractérisation de son comportement thermique, hygrique et hygrothermique.

Les performances thermiques de murs en pisé sont étudiées à partir de mesures sur site d'une maison habitée. Les données analysées révèlent une grande atténuation des variations de température, ainsi que de grands déphasages, ce à travers les saisons et

pour différentes expositions. Les apports solaires jouent également un rôle important dans les performances énergétiques de la maison.

Les pores du matériau sont capables de retenir de grandes quantités d'eau, qui peuvent être présentes sous différentes formes (liquide, gazeuse, solide). Ceci rend le comportement hygrique légèrement plus difficile à évaluer, du fait de devoir tenir compte des différents domaines de saturation. Le domaine hygroscopique est le plus commun et est évalué à travers des mesures de sorption/désorption et des mesures de résistance à la vapeur. Le domaine capillaire est quant à lui caractérisé par des tests de remontées capillaires ainsi que des mesures de succion. En parallèle, l'influence de différents paramètres ou conditions d'essai est également examinée.

Le comportement hygrothermique couplé est étudié sous différents aspects : les paramètres caractéristiques du stockage et des transferts thermiques, resp. hygriques, varient avec l'humidité, resp. la température. D'autre part, des mesures thermographiques sont réalisées sur des échantillons pendant des essais de remontée capillaire.

Une fois le comportement clarifié expérimentalement, la seconde tâche principale de ma thèse est la modélisation numérique de ce comportement. Le modèle couplé proposé repose sur les équilibres de chaleur et de masse dans les pores et considère séparément la cinétique de chaque phase (eau liquide, vapeur d'eau, air sec et matrice solide). Les hypothèses simplificatrices communément faites dans la modélisation hygrothermique des matériaux de construction sont évaluées au regard des spécificités du matériau terre et leur adéquation, dans ce contexte, est questionnée. Le modèle est ensuite comparé avec des benchmarks et les paramètres d'entrée sont calibrés par confrontation avec les données expérimentales collectées dans la première partie.

Etude expérimentale

Mesure des performances de la maison

La maison étudiée dans cette thèse est localisée à Saint-Antoine-L'abbaye dans l'Isère. Elle possède une superficie de 150 m^2, sur deux niveaux, ainsi que des combles perdues. Son enveloppe est composée de quatre murs porteurs en pisé non isolé (exposés au sud, est et ouest), de 50 cm d'épaisseur et d'environ 3m de hauteur, ainsi que d'une structure en ossature bois remplie de terre-paille (principalement en exposition nord et dans la partie supérieure du bâtiment), comme illustré dans la Figure 1. La terre utilisée pour la construction des murs a été prélevée à environ 10km du site.

La maison est occupée par cinq personnes (deux adultes et trois enfants de 11 à 19 ans en 2016). Pour l'hiver, le système de chauffage est un poêle à bois situé dans le séjour, qui consomme environ 2 stères par an, soit environ 3000 kWh d'après [4], c'est-à-dire 20 $kWh.m^{-2}.an^{-1}$ (la surface étant la superficie de la maison). Pendant l'été, aucun système de climatisation n'est utilisé.

Concernant l'instrumentation, 7 capteurs (température, humidité relative) ont été placés à différents endroits dans la maison, et 12 autres (température, humidité relative, teneur en eau) à l'intérieur des murs et agencés comme illustré dans la Figure 2.

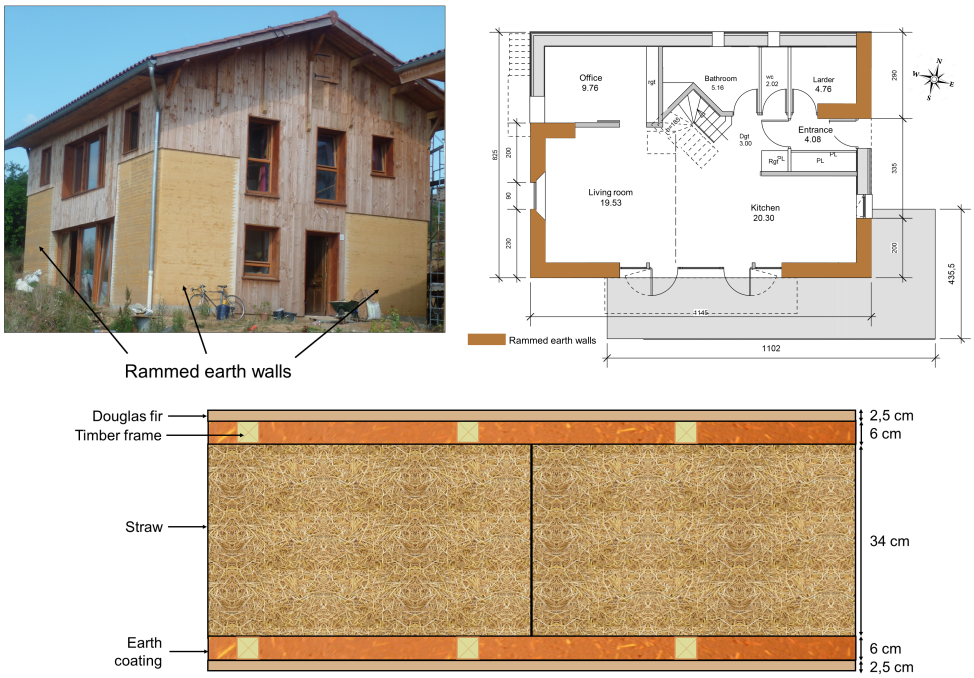

Figure 1: Maison à Saint-Antoine-l'Abbaye (2014) : photo de 2004; plans du RDC ; composition des murs hors pisé.

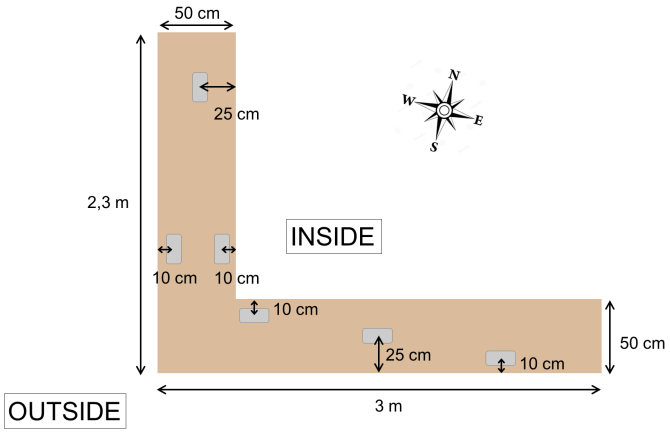

Figure 2: Localisation des capteurs sans le mur instrumenté.

Cette partie traite ensuite des performances thermiques de la maison. Tout d'abord, les flux de chaleur entrants sont étudiés à l'échelle de l'année, puis de la saison et enfin de la journée. Ensuite, les capacités de transmission et de stockage du mur sont analysées et interprétées. Le rôle important des apports solaires étant soupçonné, une étude ayant pour objectif de les quantifier suit et clôt cette partie.

La Figure 3 présente les températures moyennes mensuelles ainsi que le flux solaire pour la période d'étude complète allant d'Avril 2013 à Juin 2015. Nous pouvons remarquer que le flux solaire est maximum en été et minimum en hiver. La régulation en température opérée par les murs est également perceptible : en été, la température intérieure est maintenue à un niveau raisonnable sans climatisation, alors qu'en hiver où très peu de chauffage a été utilisé, les différences de température intérieure/extérieure vont jusqu'à 10°C.

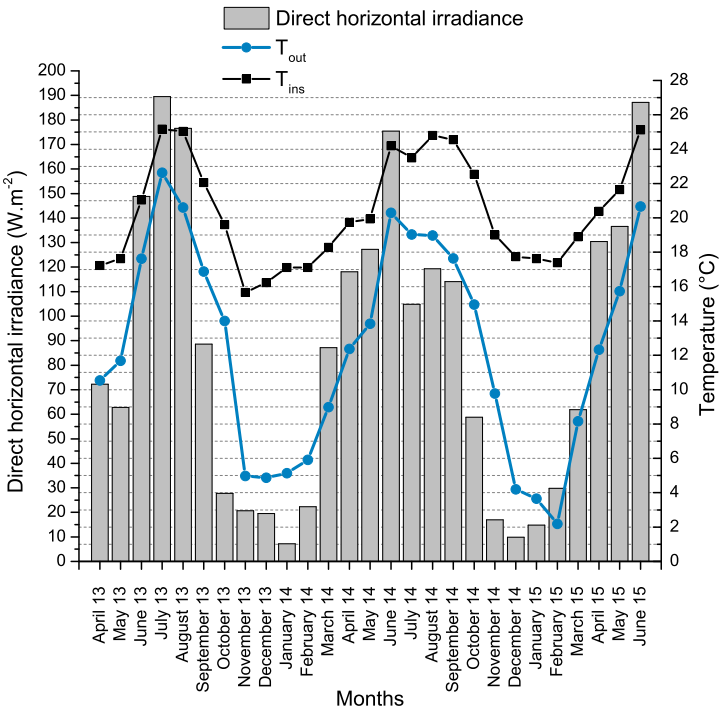

Figure 3: Moyennes mensuelles des températures intérieures et extérieures, et flux solaires pendant la période d'étude.

Afin de pouvoir présenter une analyse plus poussée, l'étude est réalisée en se focalisant sur l'été d'une part et l'hiver d'autre part. Pour illustration, regardons ce qu'il en est du cas d'étude de l'hiver.

La Figure 4 présente les gains et les pertes de chaleur pour deux hivers et les deux orientations de mur. Nous pouvons constater une majorité de pertes pour les deux orientations, ce qui était attendu étant donné l'utilisation du chauffage. En

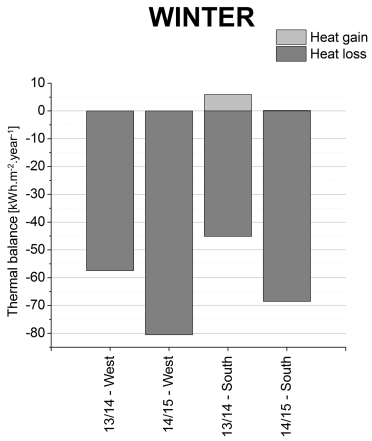

Figure 4: Bilan thermique des murs ouest et sud pour les hivers 13/14 et 14/15.

revanche, nous pouvons aussi remarqué que les pertes sont moins importantes pour l'orientation sud qu'à l'ouest: les radiations solaires chauffent le mur sud pendant une période plus grande, ce qui limite le gradient de température et donc les pertes de chaleur.

Nous pouvons également remarquer la présence de gains sur la face sud pendant l'hiver 13-14, qui atteint même environ 13% des pertes sur cette période. Ces mesures révèlent le relâchement de chaleur du mur vers l'intérieur de la maison. Pour étudier le phénomène de plus près, la Figure 5a présente la superposition du flux solaire et du flux entrant pendant une période de trois jours. Il est alors constaté que, autour de 3h du matin, le flux devient positif. D'autre part, il semble d'autant plus grand que le pic de flux solaire a été important dans la journée précédente.

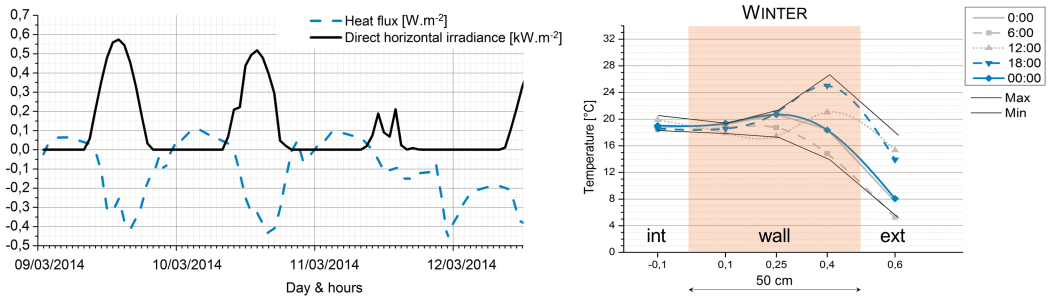

Figure 5: Mars 2014 - Flux entrant dans le mur sud et flux solaire et Profil de température du mur sud au 1er Janvier 2014.

Afin de s'assurer qu'il ne s'agit pas de chaleur accumulée par le chauffage, mais bel et bien de chaleur solaire, les profils de température dans le mur sont représentés dans la Figure 5b. Nous y constatons que la température au centre du mur atteint une valeur supérieure aux températures intérieure et extérieure, et nous pouvons

également remarquer la propagation du "ventre" de chaleur depuis l'extérieur vers l'intérieur. Ceci apporte donc la preuve que la source de chaleur provient de l'extérieur et non du chauffage à l'intérieur de la maison.

Enfin, une dernière étape consiste à quantifier la part des apports solaires dans le flux thermique entrant dans le mur depuis l'extérieur. Celui-ci est calculé grâce à la formulation suivante:

$$\phi_{X_e} = \phi_{wall,X} + \phi_{sun,X} = \frac{T_{out} - T_{Xext_{wall}}}{\frac{e}{\lambda} + \frac{1}{h_e}} + \frac{\alpha I_X}{1 + \frac{eh_e}{\lambda}} \quad (1)$$

Le coefficient d'absorption solaire d'une surface, appelé α, est un nombre situé entre 0 et 1 et qui exprime le pourcentage d'énergie solaire absorbée. Ce coefficient a été mesuré expérimentalement pour la terre utilisée (voir détails dans [28]) et sa valeur est de 0.55. Une valeur presque similaire (0.6) a d'autre part été obtenue en comparant les mesures sur site avec une modélisation thermique sur plusieurs périodes choisies par leurs conditions climatiques (orientation, rayonnement solaire, présence ou non de vent).

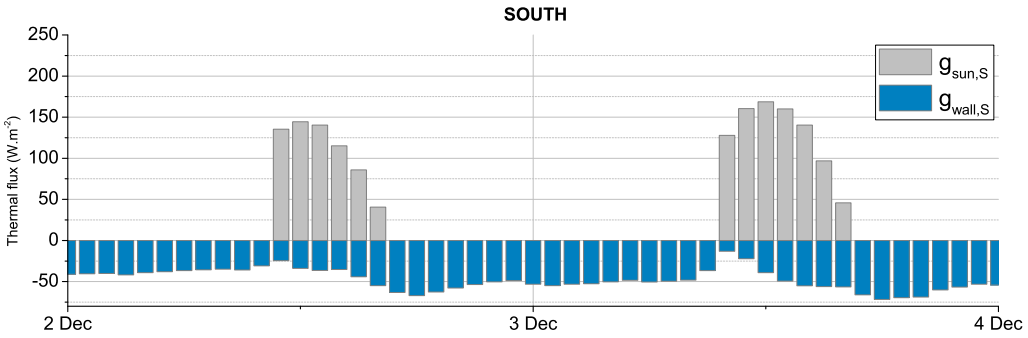

Figure 6: Proportions des flux thermiques dus à l'environnement et aux apports solaires pour une période d'hiver, et pour le mur sud.

En considérant cette valeur de α, la Figure 6 représente la proportion de chaque partie du flux thermique de l'équation (1) : celle due à l'air environnant et celle due aux apports solaires, et ce pour une période d'hiver et l'orientation sud. Nous pouvons constater que lorsque le soleil est levé, la part des apports solaires est bien supérieure à celle de l'air environnant, jusqu'à un facteur trois. Pendant la majorité du temps, les flux sont de signe opposé (le mur étant plus souvent plus chaud, il relâche de la chaleur vers l'extérieur), mais il arrive également que, lorsque les pertes de chaleur diminuent jusqu'à devenir des gains, le mur est doublement chauffé.

Cette première partie met en évidence le relâchement de chaleur depuis le mur vers l'intérieur de l'habitation pendant la nuit, conduisant ainsi à enquêter sur la quantification des apports solaires effectivement absorbés par le mur. Ceux-ci étant

non-négligeables, ils révèlent donc l'importance d'une bonne exposition des murs en pisé, afin de profiter au maximum de ces propriétés.

Mesures en laboratoire

L'étude de l'humidité dans l'habitation a permis de mettre en évidence la régulation de l'humidité à l'échelle de la saison, mais non de façon journalière avec l'absorption et le relâchement d'humidité par les murs. En effet, ce phénomène se produit sur les premiers centimètres à la surface du mur et l'emplacement des capteurs à 10cm ne l'a pas permis. De ce fait, une investigation en laboratoire a été nécessaire.

Pour ce faire, le matériau a été soumis aux tests de caractérisation usuels des matériaux de construction: mesures de sorption/désorption, de perméabilité à la vapeur, de tampon hygrique et d'absorption capillaire. Pour mettre en évidence le couplage hygrothermique, les variations avec la température ont également été étudiées.

Une étude plus particulière a eu pour objectif d'étudier les variations d'absorption liquide en fonction de la densité, étant donné qu'elle n'est pas homogène au sein d'un même mur. D'autre part, trois conditions limites ont également été testées afin de mettre en évidence les différentes vitesses de remontées d'eau. Les variations de température en surface liées à l'évaporation ont également pu être mesurées grâce à une caméra thermique.

La variation du coefficient d'absorption liquide, noté A, en fonction de la densité est représenté dans la Figure 7, ainsi que les valeurs prises pour les différentes conditions limites.

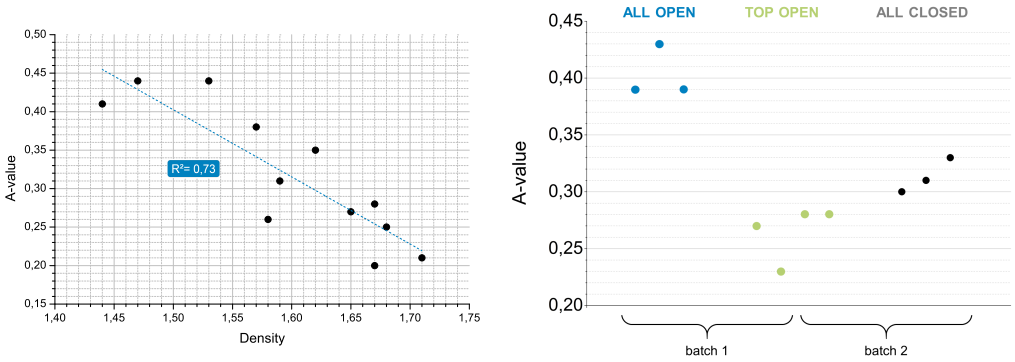

Figure 7: Coefficient A en fonction de la densité (gauche) et des conditions limites (droite).

Nous remarquons que, globalement, l'absorption liquide diminue avec l'augmentation de la densité. Il y a même presque un facteur 2 entre le coefficient le plus haut et le plus bas, pour une gamme de densité effectivement représentée dans un mur.

Cette partie expérimentale a permis de mettre en évidence les comportements thermique et hygrique du matériau, à la fois à l'échelle de l'habitation, et à l'échelle de l'échantillon. Les performances thermiques du matériau semblent prometteuses, à condition qu'il y ait une exposition suffisante au soleil, tandis que les caractérisations en laboratoire laissent transparaitre une bonne régulation en humidité en comparaison avec les matériaux de construction plus communs. Enfin, dans le cas de pathologies comme les remontées capillaires, les hétérogénéités de densité semblent jouer dans la propagation plus ou moins rapide de l'eau liquide.

Modélisation numérique

Au-delà des mesures expérimentales, qu'elles soient sur site ou en laboratoire, le développement d'outils numériques, validés et calibrés, constitue une partie essentielle de l'étude du matériau. La partie suivante se concentre sur ces objectifs.

Développement du modèle

Le matériau est modélisé comme la superposition d'un squelette solide (S) et un réseau poreux partiellement saturé par de l'eau liquide (L), supposée pure. L'espace poreux restant est rempli par une phase gazeuse continue (G), considérée comme un mélange parfait de gaz parfaits composés d'air sec (A) et de vapeur d'eau (V). La porosité (ϕ) est définie comme le volume actuel de milieu poreux par unité de volume initial de matériau, alors que le taux de saturation (S_r) est défini par le volume actuel d'eau liquide par unité de volume poreux. Ce dernier est relié à la teneur en eau massique ($w_L = m_L/m_S$, où m_L et m_S sont respectivement les masses de liquide et de squelette par unité de volume de matériau) à travers :

$$S_r = w_L \frac{\rho_d}{\phi \rho_L} \tag{2}$$

Les proportions d'air sec et de vapeur d'eau dans la phase gazeuse est quantifiée par leur densité apparente où I=A,V définis tels que :

$$\rho_I = \frac{m_I}{(1 - S_r)\phi} \quad ; \quad \rho_G = \sum_{I=A,V} \rho_I \tag{3}$$

- Équilibre liquide-vapeur

L'équilibre local entre l'eau liquide (L) et la vapeur (V) implique l'égalité de leur enthalpie spécifique. En supposant que la pression totale de gaz est constante, égale à la pression atmosphérique, la pression de liquide est reliée à l'humidité relative de l'air ambiant à travers la loi de Kelvin:

$$p_G - p_L = -\frac{\rho_L R T}{M_{H_2O}} \ln \varphi \tag{4}$$

Sous l'hypothèse des petites perturbations, cette dernière peut être estimée par [41]:

$$p_V^{sat}(T) = p_V^{sat}(T_{ref}) \exp\left\{ \frac{M_{H_2O}}{RT} \left[\frac{L_0}{T_{ref}} \Delta T + (C_{p,V} - C_{p,L}) \cdot (T - \ln\left(\frac{T}{T_{ref}}\right) - \Delta T) \right] \right\} \tag{5}$$

avec $\Delta T = T - T_{ref}$ et où $L_0 = 2,26.10^6$ J.kg^{-1} est la chaleur latente de vaporisation de l'eau à $T_{ref} = 373K$ et $p_G = p_L = 1$bar.

D'autre part, la différentiation de la loi de Kelvin conduit aux équations suivantes:

$$dp_L = \frac{\rho_L RT}{M_{H_2O}} d\ln\varphi + \frac{\rho_L R \ln\varphi}{M_{H_2O}} dT \quad ; \quad dp_V = p_V^{sat}(T) d\varphi + \varphi \frac{dp_V^{sat}}{dT} dT \tag{6}$$

- Équation de conservation de l'eau

En ignorant le flux d'air dans le réseau poreux, la conservation de la masse de vapeur conduit à:

$$\frac{\partial m_V}{\partial t} = -\underline{\nabla} \cdot \left(\rho_V \phi_G (\underline{V_V} - \underline{V_G}) \right) + \dot{m}_{\to V} \tag{7}$$

où $\dot{m}_{\to V}$ est la masse de vapeur produite par les processus d'évaporation/ condensation. Le terme $\rho_V \phi_G (\underline{V_V} - \underline{V_G})$ représente le transport diffusif de vapeur d'eau au sein de la phase gazeuse. Ce dernier peut être évalué à travers la loi de Fick qui est exprimée en termes de pression partielle de vapeur plutôt qu'en concentration massique [78]. À noter que dans le cas de gaz parfaits, les deux formulations sont équivalentes. On obtient :

$$\frac{\partial m_V}{\partial t} = \underline{\nabla} \cdot \left(\frac{M_{H_2O}}{RT} D_e^V \underline{\nabla} p_V \right) + \dot{m}_{\to V} \tag{8}$$

Sachant que la vitesse relative du liquide dans le milieu poreux suit la loi de Darcy généralisée, en négligeant le terme de gravité, la conservation de la masse d'eau liquide m_L peut être écrite comme:

$$\frac{\partial m_L}{\partial t} = \rho_L \underline{\nabla} \cdot \left(\frac{\kappa \kappa_r^L}{\eta_L} \underline{\nabla} p_L \right) - \dot{m}_{\to V} \tag{9}$$

L'eau dans le matériau est présente sous forme de liquide et de vapeur. En utilisant les équations précédentes et en négligeant la variation de teneur en eau avec la température à humidité relative constante, le bilan massique total d'eau ($m_{H_2O} = m_L + m_V = \phi S_r \rho_L + \phi(1 - S_r)\rho_V$) est:

$$\frac{1}{\rho_L} \left(\rho_d \frac{\partial w_L}{\partial \varphi} + \phi_G \frac{M_{H_2O}}{RT} p_V^{sat}(T) \right) \frac{\partial \varphi}{\partial t} + \phi_G \frac{\rho_V^\alpha}{\rho_L} \frac{\partial T}{\partial t} = \underline{\nabla} \cdot (K^\varphi \underline{\nabla} \varphi + K^T \underline{\nabla} T) \tag{10}$$

avec :

$$\rho_V^{\alpha} = \varphi p_V^{sat}(T) \frac{M_{H_2O}}{RT} \left(\frac{1}{p_v^{sat}(T)} \frac{dp_v^{sat}(T)}{dT} - \frac{1}{T} \right) \tag{11}$$

$$K^T = \frac{\kappa \kappa_r^L}{\eta_L} \frac{\rho_L R}{M_{H_2O}} \ln \varphi + D_e^V \frac{\varphi M_{H_2O}}{\rho_L RT} \frac{dp_v^{sat}(T)}{dT} \tag{12}$$

$$K^{\varphi} = \frac{\kappa \kappa_r^L}{\eta_L} \frac{\rho_L RT}{M_{H_2O} \varphi} + D_e^V \frac{M_{H_2O}}{\rho_L RT} p_v^{sat}(T) \tag{13}$$

- Équation de la chaleur

Le bilan enthalpique du mur conduit à une équation de la chaleur sous sa forme classique pour les milieux poreux avec changements de phases (e.g. [54]):

$$\rho_d C_P \frac{\partial T}{\partial t} = \underline{\nabla} \cdot (\lambda \underline{\nabla} T) - \dot{m}_{\to V} \tag{14}$$

où $\rho_d C_p$ est la capacité calorifique moyenne à pression constante donnée par:

$$\rho_d C_p = (1-\phi)\rho_d C_{p,d} + \phi S_r \rho_L C_{p,L} + \phi(1-S_r)(\rho_A C_{p,A} + \rho_V C_{p,V}) \tag{15}$$

L est la chaleur latente associée au changement de phase liquide/vapeur ayant lieu à un état différent de l'état de référence. En utilisant eq.(4), elle peut être exprimée en fonction de la température et de l'humidité relative d'équilibre :

$$L(T,\varphi) = L_r ef + (C_{p,V} - C_{p,L})(T - T_{ref}) - \frac{RT}{M_{H_2O}} \ln \varphi \tag{16}$$

Pour résoudre le système d'équation (10-14), il est nécessaire d'avoir une évaluation du taux massique de changement de phase pouvant provenir des équations (8) ou (9). En optant pour l'équation (9) et en l'injectant dans (14), on obtient :

$$\rho C_p \frac{\partial T}{\partial t} - \left(L(T,\varphi) \rho_d \frac{\partial w_L}{\partial \varphi} \right) \frac{\partial \varphi}{\partial t} = \underline{\nabla} \cdot (\lambda \underline{\nabla} T) + L(T,\varphi) \underline{\nabla} \cdot (L^T \underline{\nabla} T + L^{\varphi} \underline{\nabla} \varphi) \tag{17}$$

avec:

$$L_a^T = -\rho_L^2 \frac{\kappa \kappa_r^L}{\eta_L} \frac{R}{M_{H_2O}} \ln \varphi \tag{18}$$

$$L_a^{\varphi} = -\rho_L^2 \frac{\kappa \kappa_r^L}{\eta_L} \frac{RT}{M_{H_2O} \varphi} \tag{19}$$

Validation et calibration du modèle

Le modèle a tout d'abord été validé à l'aide de benchmarks numériques, à température constante puis de manière couplée. La correspondance entre les solutions

analytiques et la réponse du modèle est très satisfaisante et permet de valider théoriquement le modèle (voir Figure 8). De même, une confrontation avec des données mesurées dans une maquette de mur est également réalisée (voir Figure 9). Cependant, dans toutes ces configurations, les sollicitations restent assez simples. Pour cette raison, des situations plus complexes sont ensuite étudiées.

Deux autres simulations permettent de calibrer des paramètres d'entrée qu'il est difficile de mesurer directement sur le matériau terre : le coefficient de diffusion de la vapeur et la perméabilité liquide. Pour cela, elle utilisent les mesures, respectivement du coefficient de perméabilité à la vapeur (voir Figure 10) et au coefficient d'absorption liquide (voir Figure 11). D'autre part, la variation de ces coefficients avec la teneur en eau est prise en compte, et la formulation adoptée comparée avec les expressions de la littérature. Celles-ci prennent la forme suivante:

$$D_e^V = D_V^0 \cdot \frac{w_{sat} - w_L}{w_{sat}} \quad ; \quad \kappa\kappa_r^L = \frac{\kappa}{w_{sat}} w_L = \kappa^* \cdot w_L \tag{20}$$

Etude numérique de l'impact des hypothèses

Enfin, le dernier chapitre consiste en une étude numérique de l'impact, sur un certain type de sollicitations, des hypothèses simplificatrices faites dans le développement des équations des modèles couplés de logiciels commerciaux couramment utilisés pour les autres matériaux de construction. Le modèle développé dans ce travail considère un minimum d'hypothèses.

Plus précisément, l'étude se concentre sur deux hypothèses :

- le flux de liquide est exclusivement conduit par un gradient d'humidité (hyp 1)
- la variation dans le temps de la masse de vapeur est négligeable (hyp 2)

La figure 12 compare, selon deux chemins de chargement (LP1 et LP2) et pour les deux hypothèses faites séparément, le poids des termes négligés vis-à-vis de ceux qui ne le sont pas. Plus précisément, faire l'hypothèse 1 revient à négliger le terme K_1^T devant le terme K_2^T; tandis que l'hypothèse 2 néglige le terme MV par rapport à DD. Les résultats obtenus révèlent que, dans les gammes du coefficient de diffusion et de la perméabilité liquide correspondantes au matériau terre, ces hypothèses ne sont pas valables.

Pour conclure, ce travail de thèse regroupe deux axes majeurs : une mise en évidence expérimentale du comportement du matériau, à plusieurs échelles, ainsi qu'une modélisation numérique adaptée au matériau, qui est validée et calibrée.

L'étude du comportement thermique sur site a permis de mettre en évidence les bonnes performances énergétiques du matériau et de la maison dans son ensemble, en soulignant l'importance des apports solaires, et donc d'une architecture adaptée. La régulation de l'humidité à l'échelle de la maison n'a pu que partiellement être étudiée,

mais les caractérisations en laboratoire confirment une bonne gestion de l'humidité par le matériau. Enfin, l'étude du matériau saturé a permis d'en connaitre plus sur cet état afin de pouvoir mieux appréhender les cas pathologiques de remontées capillaires.

La modélisation numérique a permis de souligner les manques des outils de simulations hygrothermiques couplées en ce qui concerne le matériau terre, et de proposer une formulation qui a ensuite été validée dans des cas de figure divers et variés. Une bonne calibration des paramètres d'entrée demeure cependant une étape cruciale afin de reproduire fidèlement le comportement ce de matériau.

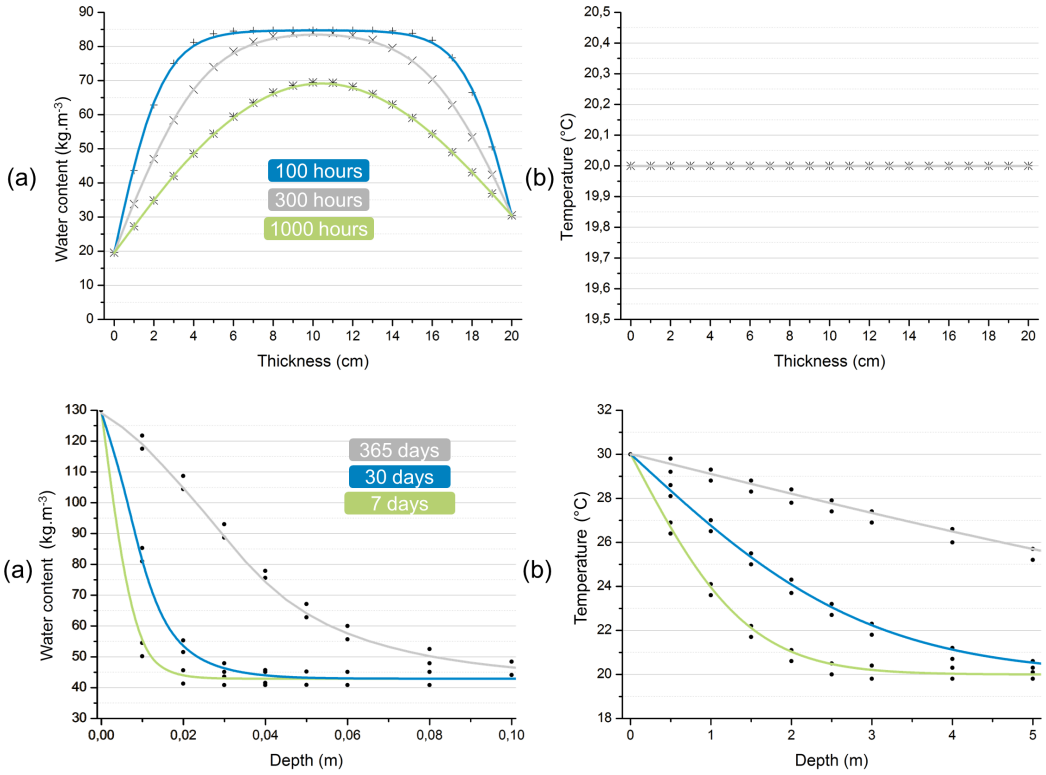

Figure 8: Résultat de la comparaison de la modélisation numérique avec deux benchmarks : HAMSTAD 2 "Homogeneous wall" et EN 15026.

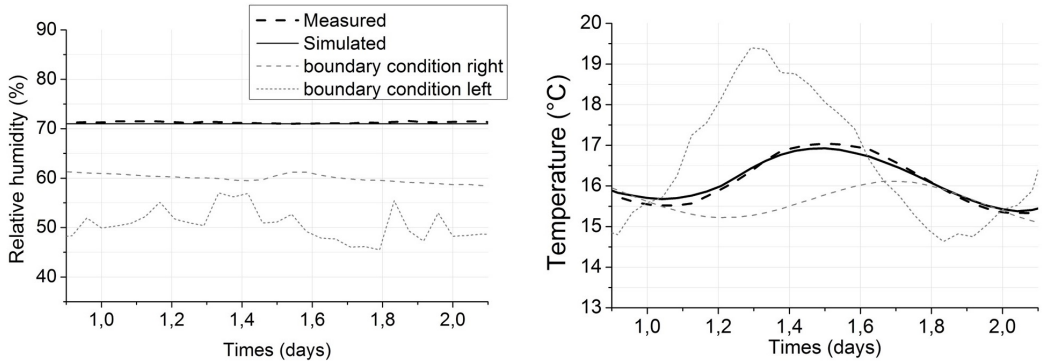

Figure 9: Résultat de la comparaison de la modélisation numérique avec les mesures sur la maquette en pisé.

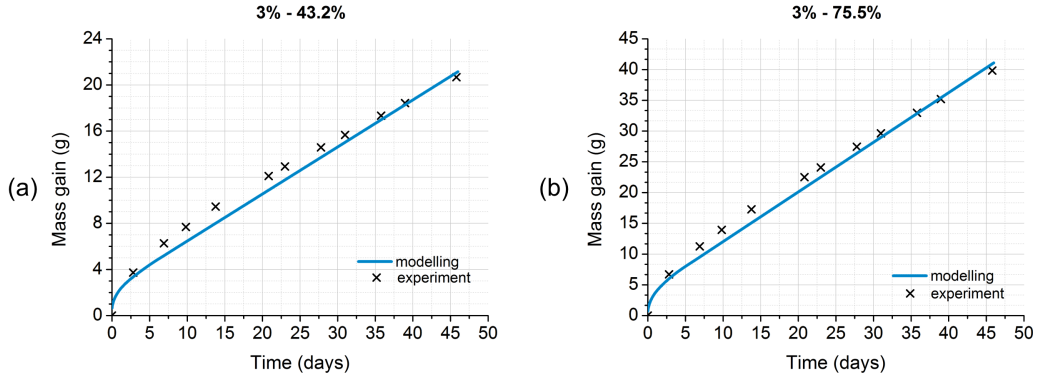

Figure 10: Résultat de la comparaison de la modélisation numérique avec l'expérimental sur la mesure du facteur de résistance à la diffusion de la vapeur.

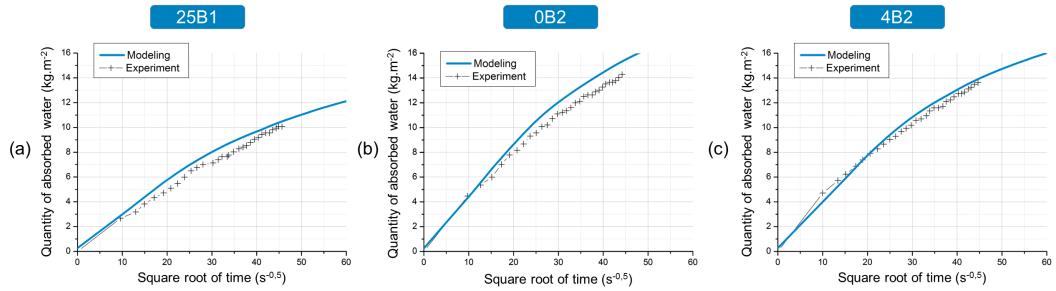

Figure 11: Résultat de la comparaison de la modélisation numérique avec l'expérimental sur la mesure du coefficient d'absorption liquide.

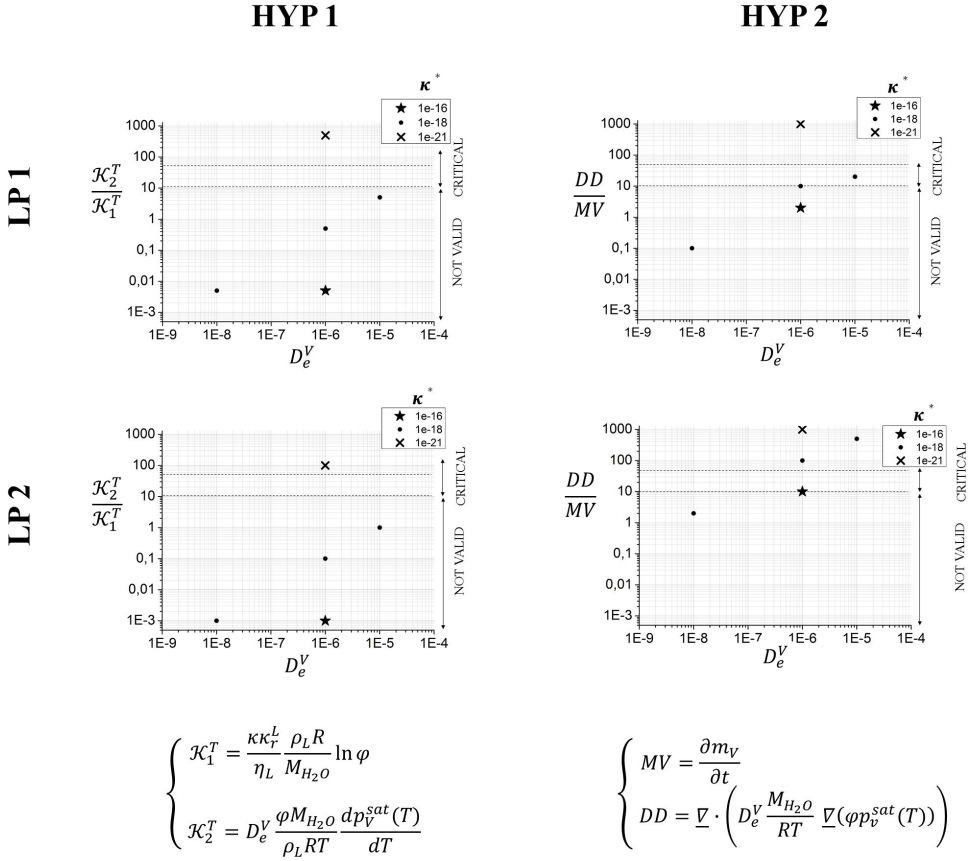

$$\begin{cases} \mathcal{K}_1^T = \dfrac{\kappa \kappa_r^L}{\eta_L} \dfrac{\rho_L R}{M_{H_2O}} \ln \varphi \\ \mathcal{K}_2^T = D_e^V \dfrac{\varphi M_{H_2O}}{\rho_L RT} \dfrac{dp_V^{sat}(T)}{dT} \end{cases} \qquad \begin{cases} MV = \dfrac{\partial m_V}{\partial t} \\ DD = \underline{\nabla} \cdot \left(D_e^V \dfrac{M_{H_2O}}{RT} \underline{\nabla}(\varphi p_v^{sat}(T)) \right) \end{cases}$$

Figure 12: Variation du rapport entre le coefficient gardé et celui négligé pour différentes valeurs de permébilités liquides et coefficients de diffusion, pour les deux chemins de chargement et les deux hypothèses.

Nomenclature

Symbols

∇	-	nabla symbol
$\underline{X}$	-	vector X

Latin notations

A	$kg.m^{-2}.s^{-1/2}$	liquid absorption coefficient
az_{sun}	$^\circ$	azimuth of the sun
az_{wall}	$^\circ$	azimuth of the wall (with respect to the south)
$C_{p,X}$	$J.kg^{-1}.K^{-1}$	specific heat capacity at constant pressure
D	$m^2.s^{-1}$	diffusivity
D_e^V	$m^2.s^{-1}$	effective diffusion coefficient
D_V^0	$m^2.s^{-1}$	effective diffusion coefficient at saturation
DF	-	decrement factor
e	m	thickness of the material or the layer
E	$J.kg^{-1}.m^{-2}.s^{-1/2}$	effusivity
g_{th}	$W.m^{-2}.K^{-1}$	thermal flux
g_{gain}	$W.m^{-2}.K^{-1}$	thermal flux from the wall to the indoor environment
$g_{wall,X}$	$W.m^{-2}.K^{-1}$	part of the thermal flux at the surface due to convection
$g_{sun,X}$	$W.m^{-2}.K^{-1}$	part of the thermal flux at the surface due to solar radiation
g_φ	$kg.m^{-2}.s^{-1}$	moisture flux
h_X	$W.m^{-2}.K^{-1}$	heat convection coefficient
ht_{sun}	$^\circ$	height of the sun
I_{sun}	$W.m^{-2}$	direct horizontal irradiance
I_X	$W.m^{-2}$	instantaneous solar radiation incident to the external surface of the wall
i	$^\circ$	incidence angle
L	$J.kg^{-1}$	latent heat of evaporation per unit of mass
m_X	kg	mass of X per unit of representative elementary volume
$\dot{m}_{\rightarrow V}$	$kg.m^{-3}.s^{-1}$	rate of vapour mass production due to evaporation/condensation
M_{H_2O}	$kg.mol^{-1}$	molar mass of water molecules

p_0	Pa	atmospheric pressure
p_G	Pa	gas pressure
p_L	Pa	liquid pressure
p_v	Pa	water vapour partial pressure
p_v^{sat}	Pa	saturated vapour pressure
q_{th}	J	heat quantity
R-value	$m^2.K.W^{-1}$	thermal resistance
R	$J.mol^{-1}.K^{-1}$	perfect gas constant
S	Pa	suction
S_r	-	saturation ratio
T	K	temperature
T_{ins}	K	temperature inside the house, near the wall
TL	h	time lag
U	$W.m^{-2}.K^{-1}$	thermal conductance
V_X	m.s	relative velocity of X in the porous media
w_L	$kg.kg^{-1}$	liquid mass water content
	$kg.m^{-3}$	
w_{sat}	$kg.m^{-3}$	saturated water content

Greek notations

α	-	solar absorption coefficient
α_{th}	$W/m^{-2}.K^{-1}$	heat transfer coefficient
β_X	$kg.m^{-2}.s^{-1}.Pa^{-1}$	water vapour transfer coefficient
δ_p	$kg.m^{-1}.s^{-1}.Pa^{-1}$	water vapour permeability
η_L	$Pa.s^{-1}$	dynamic viscosity of water
ϕ_X	-	porosity filled by X
ε	-	emissivity of the material
γ_{GL}	$N.m^{-1}$	interfacial tension between the liquid water and the air
κ	m^2	intrinsic permeability of the porous medium
κ_r^L	-	relative liquid permeability
λ	$W.m^{-1}.K^{-1}$	thermal conductivity
μ	-	water vapour resistance coefficient
φ	-	relative humidity
ρ_d	$kg.m^{-3}$	dry density
ρ_G	$kg.m^{-3}$	density of the gaseous mixture
ρ_L	$kg.m^{-3}$	liquid water density
σ	$W.m^{-2}$	energy radiated per unit surface area
σ_0	$W.m^{-2}$	Stefan-Boltzmann constant
θ	°	wall inclination

Dissemination

Publications in scientific journals

submitted	*Material and Structures* Soudani, L., Fabbri, A., Woloszyn, M., Grillet, A.-C., Morel, J.-C. Water uptake experiments on rammed earth samples to fit the liquid permeability – variation with density and lime content.
2016	*Solar energy* Soudani, L., Woloszyn, M., Fabbri, A., Morel, J.-C., Grillet, A.-C. Energy evaluation of rammed earth walls using long term in-situ measurements.
2016	*Energy and Buildings* Soudani, L., Fabbri, A., Morel, J.-C., Woloszyn, M., Chabriac, P.-A., Grillet, A.-C Assessment of the validity of some common assumptions in hygrothermal modeling of earth based materials.

Proceeding of international conferences with acts and peer review

2016	*12th REHVA World Congress CLIMA 2016, Aalborg, Denmark* Soudani, L., Fabbri, A., Woloszyn, M., Grillet, A.-C., Morel, J.-C. Energy evaluation of rammed earth wall with long term in situ measurements.
2015	*ICREC 2015. Perth, Australia.* Soudani, L., Fabbri, A., Woloszyn, M., Chabriac, P.-A., Morel, J.-C., Grillet, A.-C. On the relevance of neglecting the mass vapor variation for modeling the hygrothermal behavior of rammed earth.
2015	*ICREC 2015. Perth, Australia.* Woloszyn, M., Soudani, L., Grillet, A.-C., Morel, J.-C., Fabbri, A. Potential of existing whole-building simulation tools to assess hygrothermal performance of rammed earth construction.

Proceeding of national conferences with acts and peer review

2014 *IBPSA France 2014, Arras, France*
Soudani, L., Fabbri, A., Woloszyn, M., Chabriac, P., Grillet, A., Morel, J-C.
Étude de la pertinence des hypothèses dans la modélisation hygrothermique du pisé.
Prix de la meilleure présentation dans la catégorie "articles".

Participation in international workshops

2015 *International PhD school "Energy and Moisture in Buildings: from the microstructure of porous materials to the building energy efficiency, PUCPR, Curitiba, Brésil.*
Hygrothermal behaviour of rammed earth constructions.

2014 *Forum franco-suisse de l'innovation pour la transition énergétique dans le bâtiment, Lyon, France*
Champiré, F., Soudani, L., Fabbri, A., Morel, J.-C., Woloszyn, M., Wong, H.
Poster : « Le pisé, un atout pour la transition énergétique dans le bâtiment »
Prix du jury pour le meilleur poster.

Participation in national workshops

Mars 2016 *Constructions en terre crue : avancées scientifiques, Chambéry, France*
Evaluation énergétique de murs en pisé à partir de mesures sur site.

March 2015 *Rencontres interdisciplinaires doctorales de l'architecture et de l'aménagement durable, Lyon, France.*
Caractérisation expérimentale des capacités d'absorption du pisé et mise en évidence des paramètres influents.

List of Figures

List of Tables

Part I

General introduction

Chapter 1

Rammed earth as a building material

Contents

1 Earth building materials

Across the world and throughout history, directly available materials have always been used to build homes and shelters. In hot-arid and temperate climates, the most prevalent building material was the earth. Even nowadays, one third of the world population lives in earthen houses and this number reaches more than one half in developing countries [42][107].

Examples of outstanding historical earthen architectures can be found in every continent and for multiple building types (see Figure 1.1). Earth techniques have been known for over 9000 years and the material can come in countless different compositions and methods. The citadel of Bam in Iran counts parts of more than 2500 years old, even if some constructions were destroyed by an earthquake; the great Mosque of Djenne in Mali is the larger edifice in earth; the 4000-year old Great Wall of China was originally built in rammed earth despite a later covering of stones; the Sun Pyramid in Teotihuacan, Mexico, is made out of adobe; the town of Shibam in Yemen, covering about 20 000 m^2, dates from the 15th century.

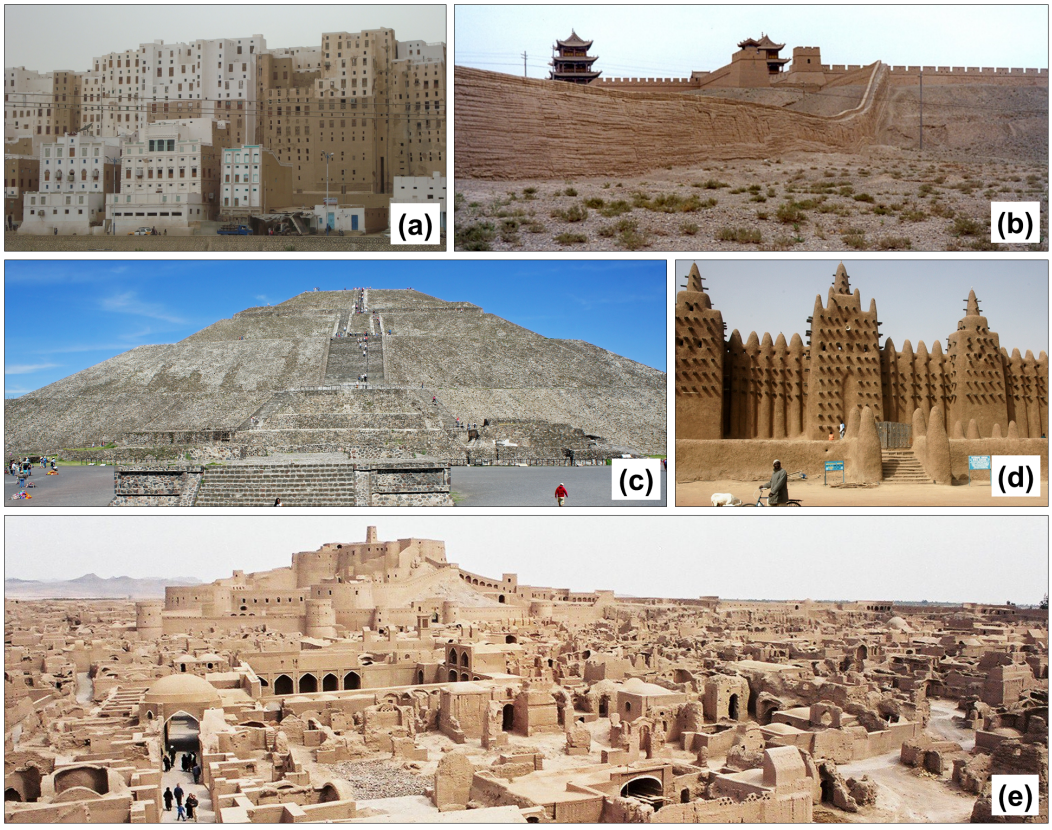

Figure 1.1: Earthen constructions around the world; (a) Town of Shibam, Yemen; (b) Great Wall of China, China; (c) Sun Pyramid in Teotihuacan, Mexico; (d) Great Mosque of Djenne, Mali; (e) Citadel of Bam, Iran.

Earth building constructions are diversified : the Earth has been providing various soil compositions at different places and the construction techniques have been evolving for hundreds of years. Each technique differs from the composition of the soil used, the compaction method, the initial moisture in the material and the drying process. The methods principally used are reported on the map of Europe in Figure 1.2 and detailed in the following parts.

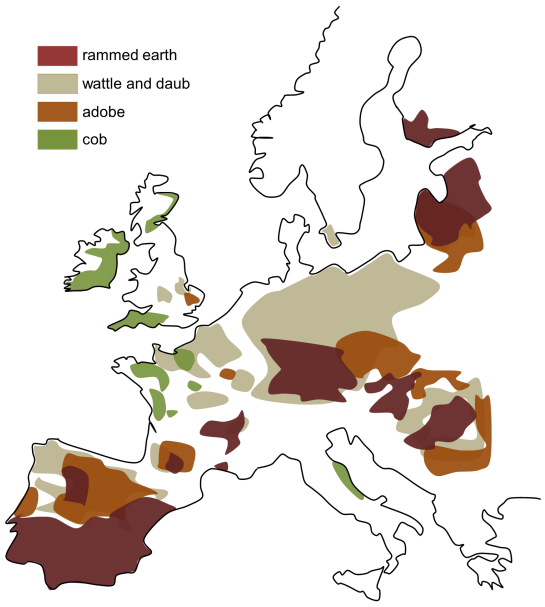

Figure 1.2: Earthen construction types in Europe.

1.1 Adobe and earth blocs

Adobe is the most common name used to denote sun dried bricks, moulded from a moist clayey soil. The soil can also be mixed with organic fibres. The bricks were originally hand-made, and then compacted manually in prismatic wooden or metallic frameworks. Devices enabled compaction with a pestle or a heavy lid. Nowadays, industrial machines are designed to produce Compressed Earth Blocks (CEB).

Buildings in the town of Shibam illustrated in Figure 1.1 are made in adobe, covered by an earth rendering, which is a common practice for this type of constructions. Another example is illustrated in Figure 1.3 : a modern house built with CEB in Rhône-Alpes, France.

Globally, the mean width of adobe walls is about 50 cm without any variation with the height. Common buildings count between one and two storeys, i.e. a height between 2.5 and 5 m.

Figure 1.3: House built with CEB (the tower being in rammed earth) in Rhone-Alpes, France [23].

1.2 Cob

The cob technique is built up in free-standing lifts without the use of mortar or formwork. For this type of construction, the earth is moderately wetted and is often mixed with organic fibres. The mixed material is either pile up by hand in clods or vigorously thrown directly onto the wall. The rough surface is later rendered so that the wall looks soft. The technique can be used to create artistic and sculptural forms.

Given the necessary amount of water in the material during construction, the technique is shrinkage prone, thus requiring a careful selection of materials and construction detailing. The low compaction energy leads to low densities, even if the shrinkage tends to increase the density.

Figure 1.4: Cob wall under construction in France [101].

The Great Mosque of Djenne illustrated in Figure 1.1 is made with a local technique based on the same process as the cob. A wall under construction is also illustrated in Figure 1.4.

1.3 Daub

Daub or "wattle and daub" technique uses a timber structure in-filled with earth or more often with a mix of earth and straw. The material in plastic state is then forced to fill the gaps. The surface can be left as it stands or rendered for a smoother finish. Daub walls are not load-bearing and the thickness, ranging from 15cm to 20cm, is suitable to create light walls for dividing interior spaces. As the earth is not load-bearing, a wide range of soil can be used.

Figure 1.5a shows a daub wall during the construction while Figure 1.5b is a daub construction in Angers, France.

Figure 1.5: (a) Daub technique illustrated [22]; (b) Daub building in Angers, France.

1.4 Rammed earth

Rammed earth technique, as its name indicates, consists in ramming layers of raw earth in a formwork. It results in a superposition of layers, between a footing and a large roof.

Given that this work focuses more precisally on this technique, information about this technique will be provided more in detail in the following part of the chapter.

2 Rammed earth : history and technique

2.1 An historical construction technique in Rhône-Alpes

Using earth as a building material is an 11 000 years old tradition. Yet, the rammed earth technique appears to be quite recent in comparison with other common techniques already described, as the first appearance seems to be in Carthage, Tunisia around 814 BC. This technique has then spread in the Mediterranean basin and reached Europe through Spain starting from the 8th century [8]. In France, Rhône-Alpes is the region where rammed earth is the most present as around 40% of rural architectural heritage is in rammed earth [36].

The city of Lyon is classified as a "World Heritage Site" for, among other reasons, its heritage in earthen architecture [146]. The conurbation of Lyon is one of the few in Europe to concentrate such a wide proportion of "urban" earthen constructions. They are buildings, some of them high, built in the center or in the outskirts, following an ancient traditional technique until the 20th century.

First earthen constructions in Lyon appeared during the Gallo-Roman era in the form of adobe and daub [48] but the apex of rammed earth is related to the rural exodus of the 19th century. Indeed, the growing city attracted more and more farming populations, which settled at the edge of the city. Needing cheap and quickly built houses, their knowledge in earth construction lead to a large amount of rammed earth houses. However, a great rise in the water level in 1856 destroyed almost all the earthen constructions, which made this type of housing judged non-reliable and be banned by the prefect Vaïsse. The advent of the industrial age brought new construction materials, which have progressively replaced rammed earth and caused its disappearance. Nowadays, the remaining rammed earth houses, coming from before 1900, are still fairly numerous. They constitute witnesses of a time and a lost savoir-faire which is important to preserve.

2.2 How to build in rammed earth ?

Rammed earth is a construction technique consisting in a superposition of compacted layers of raw earth using a formwork and rammed with a rammer. The first layer rests on a footing usually in stones, pebbles, or concrete (Figure 1.6) from 50 cm to around 2 m high, in order to protect the earthen material from sprayed water, rising damps and even animals. In the modern constructions, the stone masonry is usually replaced by concrete. The upper part of the wall is also protected from the rain by an overhanging roof.

Even if the principle is the same, there have been and there are different techniques to build a rammed earth wall. The traditional technique uses lime mortar joints between the layers and between the panels (whether horizontally or slanting; see Figure 1.7a) to strengthen the structure and limit cracking. Nowadays, no joint is used between the layers but they still can be found in the corner (Figure 1.7b).

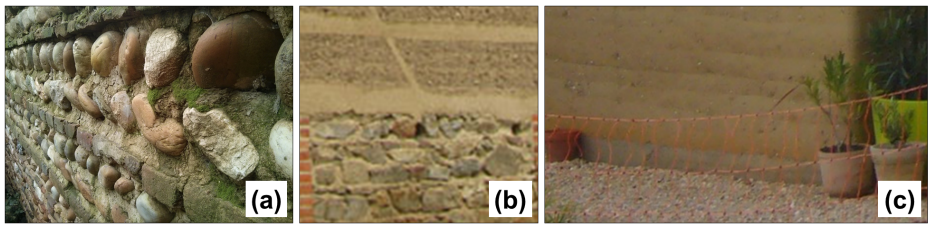

Figure 1.6: Different types of footings: (a) pebbles; (b) stones; (c) concrete.

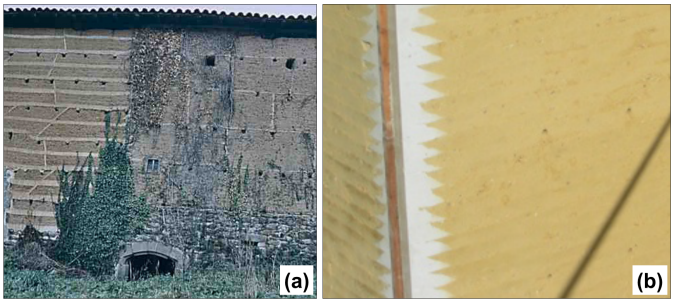

Figure 1.7: Different types of lime joints: (a) traditional vertical and slanting from [23]; (b) in the corner of a modern construction in St-Antoine-L'Abbaye.

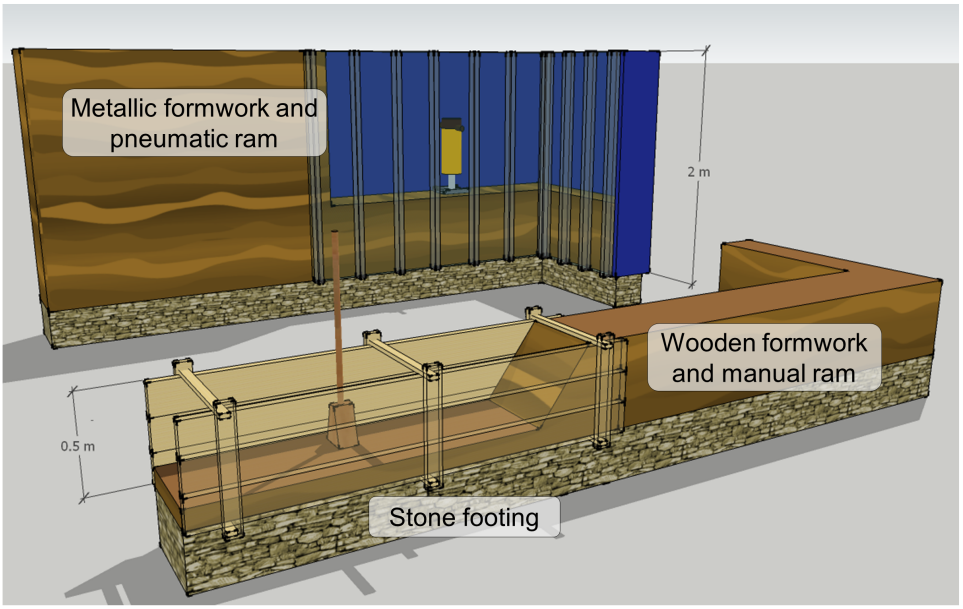

Figure 1.8: Comparison between traditional and modern tools for rammed earth construction [31].

2.2.1 Tools and processing

Formwork :

The traditional wooden formwork is nowadays replaced by a metallic one, which allows a higher compaction energy ((Figure 1.8 and Figure 1.9). In fact, the only requirement is to be solid enough to bear jolts due to compaction. It has to be reinforced in order to avoid any distortion during the process which may lead to shapeless and irregular walls. Tightenings, between formwork elements themselves and with the ground, must be strong enough to prevent any opening of the formwork during the building.

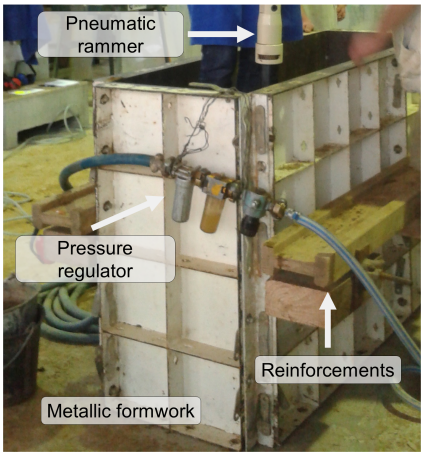

Figure 1.9: Metallic formwork and its equipment, from N. Meunier.

Traditionally, the formwork was about 80 cm high, so that the mason can step over it. Nowadays, it depends on the mason whether (s)he prefers high formworks to reach the wanted height for the wall more quickly, or low formworks to enable him to see around and be seen by other workers. They can reach 2 m high. Starting the construction, the formwork needs to be clean and dry so that the surface of the wall stays smooth after its removal.

Rammer :

Traditionally, the rammer was manual and in wood, composed of a handle and a rectangular sabot to fit closely to the formwork. The sabot was in wood in order to prevent any damage on the formwork and to improve auditive comfort. The manual rammer illustrated in Figure 1.10a weights 7.5kg.

Nowadays, rammer is pneumatic: it requires to be connected to a supercharger and a pressure regulator so that it can be easily controlled by the mason and greatly improve the handling ability and its comfort. For the same reasons, a wooden sabot is usually used. The pneumatic rammer illustrated in Figure 1.10b weights around 20kg.

Figure 1.10: (a) Manual rammer in wood; (b) Pneumatic rammer with a wooden sabot.

2.2.2 Earth type and preparation

Not every soil is suitable for rammed earth constructions. Historically, the best soil for rammed earth constructions is found in the same regions as the centenarian rammed earth houses that are still standing.

The material is taken off between 20 and 40 cm deep from the soil surface, under the arable layer. Indeed, this later, composed of organic matter, won't provide a material strong enough and increases the risk of colonization by plants.

The soil must be prepared to the right water content in order to be wet enough to ensure a good consistency but not too much to prevent cracks formation when drying or weaken compaction ability. It is thus important to keep the earth dry enough until the construction so that only water should be added and not any drying device used. A mixing device is required to homogenize the soil with the added water while the dry balls need to be taken off as they may prevent the right compaction of the soil.

The amount of water to be added is judged according to the experienced mason. In practice, the technique consists in analysing a little sample of earth shaped like a stretched out spheroid, fell down of about one meter:

- If the sample is crushed, the soil is too dry
- If the sample stays in one piece and is a bit doughy, the soil is too wet
- If the sample splits into two or three pieces, the water content is correct

The density, the height of the layer and the water content are all related and a test wall is necessarily built for every construction site to determine the good amount of water in the soil and amount of soil for each layer.

2.2.3 Wall construction

Layers :

The mason needs to stand in the form work and pour the right quantity of the prepared soil before levelling the layer manually. The ramming is divided into two steps as described in Figure 1.11, in order to ensure a good planarity and homogeneity of the layer.

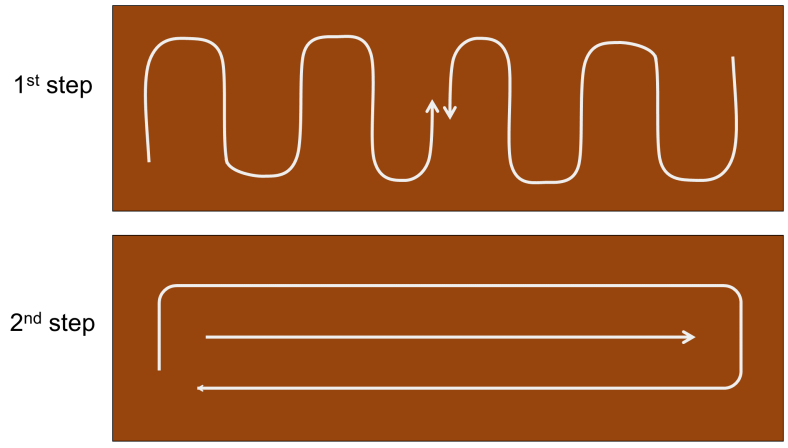

Figure 1.11: The two steps to compact an earth layer.

Formwork removal :

The removal of the formwork can be done right after the ramming of the last layer, thus enabling the immediate reuse of the formwork for another part of the construction. It is even important not to let the wall dry with the formwork on as it can lead to wrenching and alter the surface of the wall. The formwork needs to be loosen gradually for fear of tearing angles of the wall as illustrated in Figure 1.12.

Figure 1.12: Tear of a corner while removing the formwork.

2.2.4 Questioning modern practices

Stabilization :

Many of the newly built rammed earth buildings are stabilized with lime or cement.

Adding lime in the earth before compaction limits the water sensibility of the soil: the lime chemically reacts with the clay minerals and enables it to bear a higher water content. The amount of lime usually added ranges between 6% and 12% by dry weight [99].

Cement stabilization is more spread, especially in Anglo-Saxon countries such as Australia, USA or India, where the proportions ranges from 6% to 15% [99]. The use of such stabilizers increases the compressive strength due to the formation of a cement gel matrix binding together the soil particles and the bonding of the clay particles within the soil [99]. Moreover, high levels of cement stabilization improve the surface coating (reducing erosion) as well as the resistance of the soils. [152]. However, using cement leads to the reduction of the permeability of soils and thus the natural ability of earth to allow moisture to pass. Environmental impacts of cement production is also added to the reduction of possible recycling of the material, to the notable disadvantages of such method.

This technique is disputed as, despite of improving mechanical resistance of the material or enabling a better control of high moisture contents, it avoids any recycling of the soil, which is a non-negligible advantage of using earthen materials, and penalize the embodied energy. The process of earth preparation requires also a larger amount of time due to mixing and setting time. In any case, requirements are changing from a region of the world to another, for climatic or aesthetic reasons, as well as the consequences. However, in many situations, the use of cement or lime can be avoided by a good design and construction appropriate to earth building.

Prefabrication :

Another modern practice consists in the prefabrication of rammed earth walls. Built up in workshops and then brought to the construction site to be put together. This enables to work under cover during the wet periods. However, care should be taken as the workshop must not be established far away from the construction site in order to preserve the low embodied energy of the construction technique.

For example, a recent factory Ricola in Switzerland built in modern rammed earth is illustrated in Figure 1.13. During the works, a workshop was established near the construction site to provide prefabricated rammed earth walls.

Figure 1.13: Prefabricated rammed earth wall used to build Ricola's factory in Switzerland; credits: Ricola.

3 A sustainable construction material

3.1 The strong environmental impact of the construction industry

Facing the serious consequences of global climate change during the last decades and the forecast of natural resources depletion in a near future, sustainable development is at the heart of the current concern in all human industries. More acute problems are related to energy and wastes and all sectors are working to reduce the environmental impact of their activities.

According to [49], the building sector plays a key role as it accounts for about 40% of the generation of greenhouse gases ; 44% of the wastes collected in France come from the building industry which represented around 345 millions of tons in 2012 [3].

The energy consumption during a building life can be divided into three major categories:

- Construction : raw materials extraction, usually transportation, the manufacturing of construction material (cement, reinforcements, carpentry,...), transportation, construction on site
- Life time: heating, ventilation, cooling, lightening,... and even restoration

- Demolition and wastes treatment

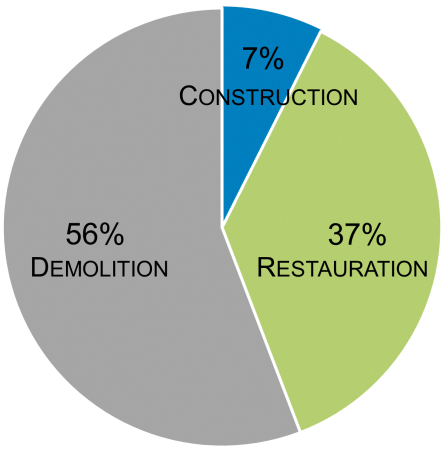

Figure 1.14: Wastes contribution of different stages of a building for a total of 31 million of tons for the year 1999 according to ADEME in [23].

The diagram in Figure 1.14 represents the repartition of wastes for the different steps of a building's life. The large portion held by the demolition can be easily noticed. However, it is commonly thought that a building with a good energy efficiency is a building with low energy consumption during the housing phase, as several studies reveals that the construction phase only represents around 15% of the energy consumption over 50 years [1]. It can however be interesting to point out that these methods don't take into account the wastes treatment after demolition. On the other hand, Thormak in [141] relates the thermal performance of a building (usually connected to insulating materials) to the additional construction costs required. The study even reveals that for low consumption buildings (below 45 kWh.m^{-2}.year^{-1}), the energy used during the construction phase reaches 40% of the total energy. What's more, the study also established the percentage of wastes treatment to reach 15% of the total energy.

3.2 The low embodied energy of rammed earth construction

The embodied energy is a concept used to evaluate the energy required to produce any good or service for their entire life-cycle. It is the sum of all energies, whether human, animal, electrical, thermal, etc.

The low embodied energy of rammed earth constructions is synthesized in Figure 1.15.

First of all, as already mentioned, the raw material is a soil taken from the ground and easily prepared to be used for construction. It is extracted only a few kilometres away from the construction site to minimize transport costs. According to [108] whose data is reported in Table 1.1, the comparison for three construction types, in terms

of transport in t.km, reveals that concrete construction is 644% more important than rammed earth. What's more, the material, being composed of natural soil, doesn't release any noxious substances.

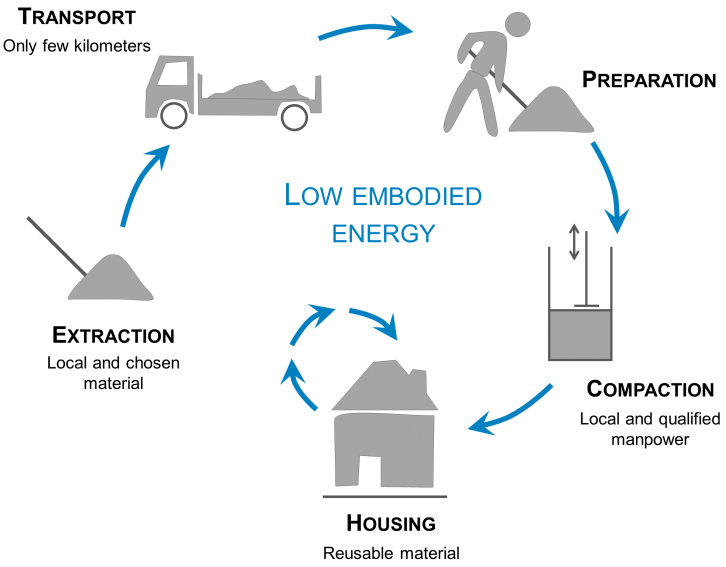

Figure 1.15: Low embodied energy of rammed earth construction, from [31].

	Stone masonry with soil mortar	Rammed earth	Concrete
Total Energy (GJ)	97	70	239
Transport (t.km)	1390	1041	6707

Table 1.1: Energy consumption for different construction types, from [108].

The process of building in rammed earth requires a numerous and qualified manpower. From the soil extraction and preparation, the formwork set-up to the ramming process, one meter square of a 50 cm width rammed earth wall requires about 8h whereas this time is divided by four for other classical construction methods such as reinforced concrete (Vincent Rigassi Architecte in [39]). The work of a rammed earth craftsman requires a savoir-faire to guarantee the good achievement and durability of the earthen construction. This heritage is transmitted through apprentices, which puts the approach far away from the other construction methods where automation, industrialization and mechanization rule. On the other hand, rammed earth constructions need an important human work but very few energy and raw materials. It follows that, on the contrary, other construction methods cost much more in terms of materials, transport and less in wage costs. Indeed, according to [39], manpower represents around 20% of the energy to build $1m^2$ of rammed earth wall, whereas it represent 0.3% for an industrial masonry. This data is confirmed in Table 4.3, where

the total energy necessary for concrete is 341% higher than for rammed earth.

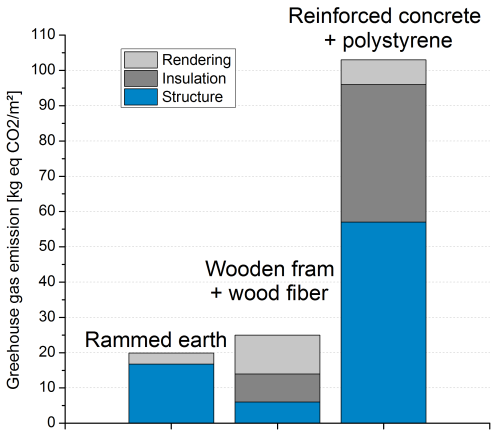

Figure 1.16: Greenhouse gas emission for different construction methods, according to [39].

The comparison in terms of greenhouse emission is made by [39] and summarized in Figure 1.16.

Finally, the non-stabilized rammed earth buildings are reusable. This process is quite easy to perform thanks to its water sensibility: the re-wetting of the material is sufficient. The soil can be reused for another construction project in the neighbourhood or given back to the nature without treatment, i.e. limiting the environmental impact.

To conclude, the development of earth based buildings appears to be a sustainable alternative to conventional constructions as the major interest of earth lies in the fact that it is a local material than can be produced and used immediately on the construction site or nearby and does not require any industrial processing. It is not a renewable but a reusable material: it requires no treatment to be used and has therefore a very low environmental impact.

3.3 The good energy performance of rammed earth houses

Another aspect of the energy consumption in the building sector corresponds to the living period. Actually, the energy performance of a house doesn't only depend on the building material but is also related to the architectural design, the outdoor climate and the occupants' habits. However, the following summary gives access to the potential of rammed earth houses.

Rammed earth construction is brought up to date in industrialized countries for its thermal performance, especially in summer. From the 80s, earthen constructions have appeared to provide a good thermal comfort in rather hot climates and, as a consequence, more new houses have come out in developed countries such as the United States or Australia [60][109]. Earth houses are known to improve the comfort

through temperature and relative humidity buffering and time lags (see Figure 1.17). Moreover, the buffering capacities of the material enable pollutant absorption and thus may improve air quality [107]. However, too few scientific studies are conducted in order to precisely assess this behaviour.

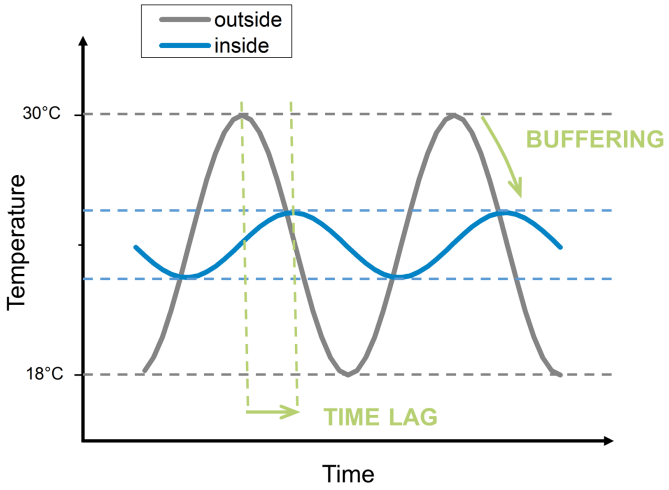

Figure 1.17: Temperature buffering and time lag.

The material is able to hold a large amount of water, from its manufacturing, from the ground or from the surrounding air. This water is likely to evaporate and condensate, catching and releasing heat: the material seems to act like a natural phase change material, i.e. a cooling and heating device (see Figure 1.18). These phase changes contribute to the ability of the material for passive control of the indoor temperature (together with the thermal mass), but also water vapour transfers enable a moisture control and limit the chance of mould growth. However, well documented scientific studies are still lacking in the literature, but they are thought to be necessary for correct assessment of energy performances of rammed earth houses.

This Ph.D. will provide more experimental evidences of the behaviour of such material in order to better assess the contribution of the previous phenomena in the good living conditions reported by rammed earth houses' occupants.

4 ...endangered by wrong practices

4.1 Current evaluation of the thermal performance of a wall

The first function of a wall is to shelter the internal environment from the outside climate, from days and nights temperature fluctuations. The lower the temperatures are, the more efficient the wall will be. As a consequence, the evaluation is focusing on its behaviour as an insulating material.

Along with the thermal conductivity, the thermal resistance is an indicator of the performance of an insulating material. The thermal resistance is often written

R or R-value, and formulated in $m^2.K.W^{-1}$. The higher it is, the more efficient the insulation material will be. The thermal resistance can be calculated from the thermal conductivity and the thickness of the material, according to eq.1.1:

$$R - value = \frac{e}{\lambda} \tag{1.1}$$

Note that the thermal conductance U is also commonly used, and is defined as the inverse of the thermal resistance, i.e $U = 1/R = \lambda/e$.

The definition of the thermal resistance appears to be convenient, as materials shouldn't be compared directly from their thermal conductivity but proportionally to their thickness.

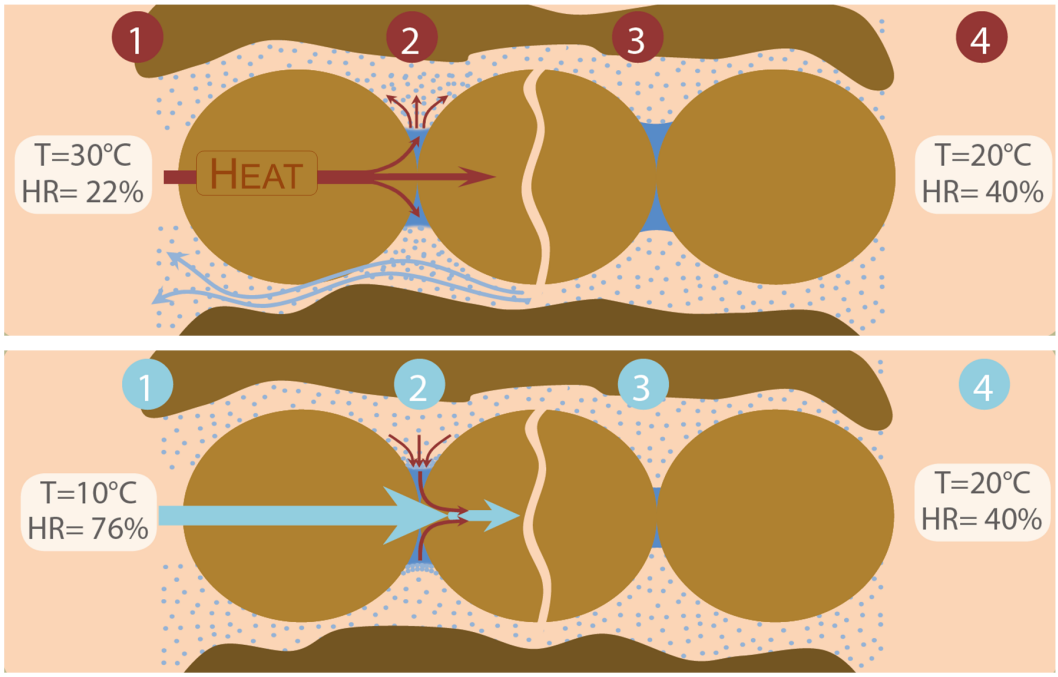

❶ Increase of the external temperature.
❷ Partial consumption of the heat released due to evaporation.
❸ Constant temperature and start of a moisture gradient.
❹ The inside is kept cool and moisture is drained out.

❶ Decrease of the external temperature.
❷ Condensation and heat release.
❸ Constant temperature.
❹ The inside is kept warm.

Figure 1.18: Scheme of the natural heating (winter) and cooling (summer) processes, from [31].

4.2 Earthen materials as bad insulating material

Following this approach, a study has been carried out in 2000 by the Australian national research organisation (CSIRO for Commonwealth Scientific and Industrial Research Organisation) [43], which intended to provide scientific proof of the thermal

behaviour of rammed earth houses. It appeared that the majority of rammed earth houses in Australia has a R-value under 0.4, where the local standard demands at least 1.3. Other studies such as [28][71] measured the same order of magnitude, and confirm the bad performances of earthen walls in stopping heat flows.

However, these measures went against the global opinion on the comfort experienced with this material. It appeared that the R-value wasn't representative enough, and that other aspects of the material behaviour had to be taken into account. Where in cold area, the insulation is primordial, in temperate climate, the thermal mass of the wall can have a greater impact on its behaviour [154]. It has even be shown to reduce the cooling and heating consumption [15]. Indeed, the high thermal mass enables the wall to hold a large quantity of heat during the day, and thus stopping heat flows in and out the house depending on the seasons. Some authors [87] affirm that the high thermal mass of earthen materials can counterbalance a low R-value. Some suggest that it should have the same status as the thermal resistance in regulations. Nevertheless, the impact of the thermal mass is different depending on the climate (the optimal case being a warm days and cold nights).

5 Conclusion

In the light of the previous elements, rammed earth study has to take into account all the phenomena to which a construction can be submitted to. Figure 1.19 displays the majority of them. Globally, they can be gathered into two categories : hygrothermal and hydro-mechanical behaviours. The main challenge is to precisely characterize the material and its interaction with the environment so that it can be dealt with as reliably as the other common construction materials, from the standard point of view as well as the good practices.

The latest French thermal standard RT2012 compels newly built buildings to improve their overall energy efficiency, and urges to act on larger aspects (natural lightning, solar exposition, air tightness, thermal bridges,...). It is thus important to evaluate the ability of the material regarding these aspects, which could be profitable to a better evaluation of the material, and, as a consequence, to a beneficial promotion.

Solutions have already been proposed to make earthen material meet the expectation in terms of insulation [65][106][115]. It is important to note that, in all these cases, the insulating material is vapour permeable. It is actually a necessary (not sufficient though) condition when dealing with materials strongly impacted by the presence of water. Indeed, if the insulating material is vapour proof, the water may rise up in the wall, the earth tends to liquefy, and the risk of collapse greatly increases. Such an accident has been reported in France in 2015.

To conclude, a better understanding of the material's behaviour and the development of appropriate scientific tools will promote their potential to answer the actual challenges regarding both energy and environment. Indeed, the actual and growing pressure put on fossil fuel compels to pre-empt the use of this kind of material for

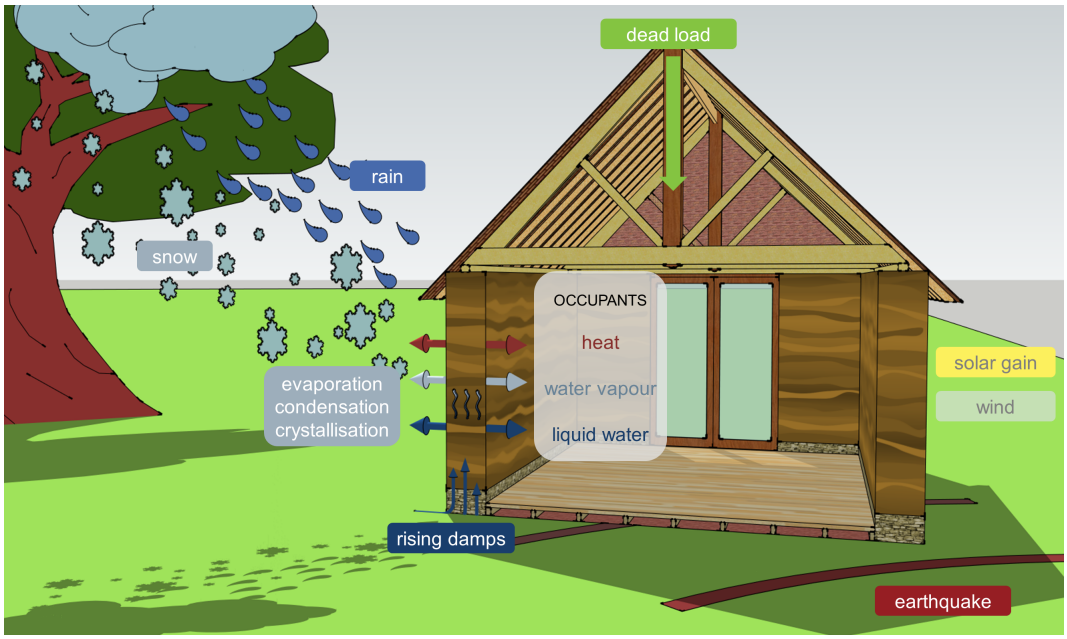

Figure 1.19: Multiple fields of study around a rammed earth construction.

modern constructions, which goes together with a demand for greater comfort.

The PhD has been founded by the French National Agency for Research (ANR) through the project "Primaterre", whose objectives are to provide means for measuring and guaranteeing hygrothermal performances, mechanical and seismic resistances and to ensure the corresponding dissemination. To achieve these objectives, a global, multi-scale and multi-disciplinary (materials, energy and sociology of innovation, laboratory and in situ, experiment and modelling) research is proposed.

The aim is to identify the key parameters needed to describe the thermo-hygro-hydro-mechanical behaviour of clayey materials, of walls and structures, thanks to physico-mechanical modellings and experimentations at different scales. Those parameters will have to be measurable on site and integrable in suitable calculation codes. Regarding the material, earth as rammed earth, mortar and render are studied. The addition of particles (resp. fibres) plant is also studied for their hygrothermal (resp. mechanical) performances.

In the end, the project wish to develop design guidances, recommendations and teaching modules. It should give insights on both scientific and practical levels, which also means to be realistic in terms of economic and political conditions in the construction sector in France and Europe.

In this context, the work presented in my PhD is focusing on the study of the coupled hygrothermal behaviour of rammed earth constructions and more generally earthen materials.

Chapter 2

Introduction to heat and moisture modelling in rammed earth as a porous media

Contents

This chapter intends to sum up the different and well-known heat and moisture phenomena occurring in or around the walls of a building, and to introduce the classical hygrothermal coupled models and common building simulation tools. Secondly, the research concern for rammed earth and the objectives of the thesis are introduced.

1 Thermal behaviour of building materials

1.1 Heat in building materials

When two elements at a different temperature are in the same environment, a heat transfer occurs until the two temperatures become equal. Heat always goes from the hottest source to the coolest, since cold is nothing but the absence of heat energy. This phenomenon is impossible to prevent, and the aim of insulating materials is to restrain it as much as possible. In building physics, heat exchanges can occur through three processes:

- conduction
- convection
- radiation

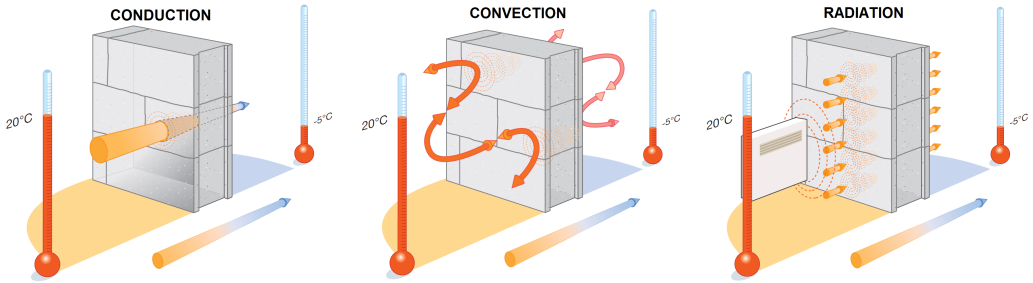

Figure 2.1: Schematic representations of possible heat exchanges, from [126].

1.1.1 Conduction

Heat conduction or thermal conduction is the movement of heat from one solid to another, which has a different temperature, through a physical contact. The transfer occurs at the molecular level when heat energy is absorbed by a surface and causes the molecules of that surface to move to their neighbours and transfer them energy. The process of heat conduction depends on different factors, among them the temperature gradient and the properties of the materials.

The thermal flux g_{th} (equal to $\underline{g_{th}} \cdot \underline{n}$, where $\underline{n}$ is the unit vector perpendicular to the exchange surface) is the energy or heat quantity crossing a $1m^2$-wall for a second,

when there is a temperature difference between its two faces.The thermal flux can be expressed through the Fourier Law as:

$$\underline{g_{th}} = -\lambda \underline{\nabla} T \tag{2.1}$$

with :
λ [W.m^{-1}.K^{-1}] : thermal conductivity of the material
T [K] : temperature

The thermal conductivity is the energy quantity crossing a 1m-thick wall with a surface of 1 m^2, for a temperature difference of 1°C. It represents the ability of the material to let the heat pass through. The lower the thermal conductivity is, the more insulating is the material. It is measured in laboratories and lists of thermal conductivities of common materials can be found in thermal standards.

1.1.2 Convection

When a heat transfer is associated to molecules movement, it is called heat convection. This type of transfer occurs in fluids or when a fluid is moving in contact with a solid. In contact with a hot element, the fluid in motion shifts toward the cool element, to which heat is transferred.

The heat quantity exchanged by convection depends on various parameters, including temperature difference, velocity of the fluid, heat capacity, exchange surface, etc.

Two types of convection can take place :

- **Natural convection**: it occurs due to temperature differences which affect the density of the fluid. A common example is the rise of fog from a pot of boiling water.
- **Forced convection**: the fluid movement results from external forces, such as a fan or a pump.

Along this work, the convective exchanges are not deeply studied but are considered in boundary conditions, for which well-known formulations exist.

The Newton Law provides the expression of heat quantity exchanged between a solid of temperature T_s and a fluid of temperature T_f. During a time interval dt, the transmitted power by convection through a surface dS is:

$$\frac{\delta q_{th}}{dt} = h \cdot (T_s - T_f) dS \tag{2.2}$$

with :
q_{th} [J] : heat quantity
h [W.m^{-2}.K^{-1}] : heat convection coefficient

1.1.3 Radiation

The radiation is a heat transfer from an element to another through electromagnetic waves without direct contact. This type of transfer doesn't need any material medium to transport heat.

Every material radiates energy in every direction, following the perpetual movement of its surface molecules. Whereas the solar radiation is composed essentially by short wave radiations at high temperatures, the on-Earth thermal radiation is mainly composed by long wave radiations produced at much lower temperatures.

The thermal radiation intensity of a material depends on the temperature, but also on its emissivity. It follows the Stefan-Boltzmann equation:

$$\sigma = \sigma_0 \varepsilon T^4 \tag{2.3}$$

with:
σ [W.m^{-2}] : energy radiated per unit surface area and per time unit
σ_0 [W.m^{-2}.K^{-4}] : Stefan-Boltzmann constant, equal to 5,67.10^{-8}
ε [-] : emissivity of the material

The emissivity is the ability of a surface to absorbed and retransmit heat by radiation. The lower the emissivity is, the lower are the heat losses by radiation. For the glazings, the low emissivity is an essential characteristic to improve their thermal performance.

1.2 Research concern for rammed earth

Earthen materials are known to have a low thermal resistance (R-value) when compared with insulated materials, which makes them likely to provide poor thermal performance, as underlined in [43][45]. Indeed, high thermal resistance prevents heat loss from indoor spaces, and consequently, less heating energy is needed to maintain constant indoor temperature, even for high outdoor temperature variations over days and seasons. During the summer, the aim is to prevent outdoor heat from entering as well as to expulse indoor heat to refresh the house during the night. On the other hand, to minimize energy consumption in winter, or more generally when the weather is cold, it is important not only to keep indoor heat but also to capture the maximum amount of outdoor heat during the day so that it can be used during the night when the temperature drops.

The passive use of solar energy for the heating of buildings is therefore becoming increasingly important and has been the subject of many studies since the work of Trombe [128][143][162]. Solar radiation is a time-dependent energy source which requires an energy storage being able to collect and store heat during the day and release it to indoor air when the temperature falls at night, and as a consequence, decreasing indoor temperature swings and improving the thermal comfort level [135]. The thermal energy may be stored in the form of sensible heat in a massive material, to be introduced between direct solar radiation and the living place [160]. Another

type of thermal storage system is based on the concept of latent heat storage, which has been originally experienced in building consuctions by the use of Phase Change Materials (PCM). These materials are able to store more heat and whose melting temperature ranges from 20°C to 32°C [63][144]. Indeed, they use chemical bonds to store and release heat when the material changes from solid to liquid and the other way round [144]. More generally, many authors work on improving, by means of additional devices, the energy performance of buildings [62][80][127][158].

In this context, earthen materials, and rammed earth particularly, appear to be able to store both sensible heat as a massive material and latent heat due to liquid to vapour phase changes occurring within the pores. Indeed, several works support that the high thermal mass of the material avoids low temperatures in winter and hot temperatures in summer [13][57][139]. When exposed to a heat source (internally with heater or externally with solar radiation), the wall absorbs and stores the heat to release it when the surrounding temperature drops. This effect may be enhanced by the so-called hygrothermal couplings between heat and mass transfers which occur within the earthen walls [129].

The chapter 4 aims at illustrating the thermal behaviour of rammed earth walls, and is mostly leaning on the in-situ measurements on the house presented in the chapter 3.

2 Hygric behaviour of building materials

2.1 Moisture in building materials

2.1.1 Moist air

Moist air can be defined as a mixture of dry air and water vapour. The psychrometric chart describes the physical characteristics of moist air at different temperatures between -10 and 55°C, as illustrated in Figure 2.2.

In this mixture of gases, the partial pressure of water vapour p_v is defined as the pressure of the water vapour if it was alone to occupy the same volume.

The saturated vapour pressure $p_v^{sat}(T)$ is the maximal value of partial vapour pressure at a given temperature. Above this value, the water vapour condensates.

The relative humidity is defined as the ratio between the vapour partial pressure and the corresponding saturating vapour pressure at the same temperature. The formulation is:

$$\varphi = \frac{p_v}{p_v^{sat}(T)} \tag{2.4}$$

with:
φ [-] : relative humidity
p_v [Pa] : water vapour partial pressure
$p_v^{sat}(T)$ [Pa] : saturated vapour pressure at a given temperature

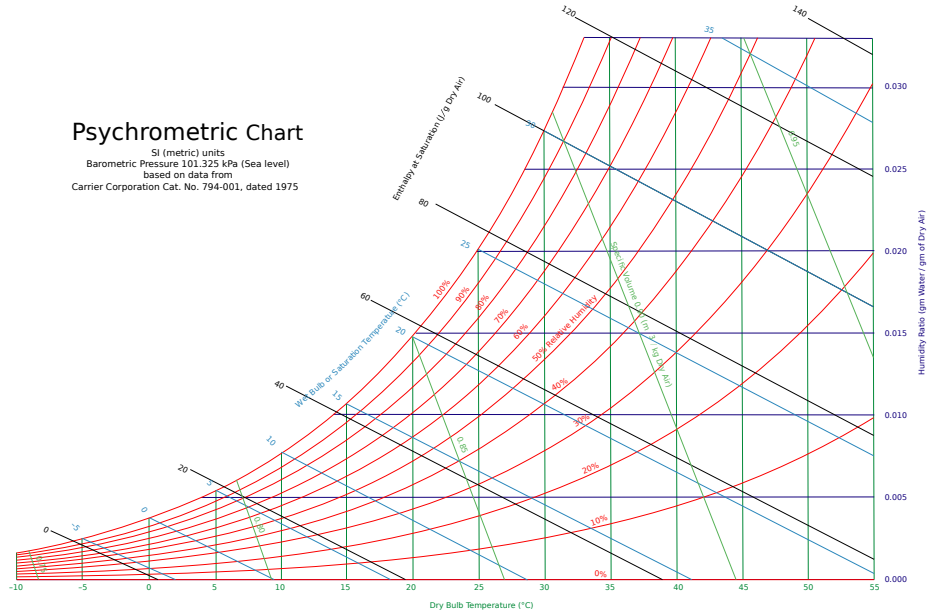

Figure 2.2: Psychrometric chart, from Willis Carrier, 1975.

2.1.2 Moisture in materials

A material is called "hygroscopic" if a measurable quantity of moisture from the surrounding air can be fixed at its surface and in its pores. It is usually measured thanks to the sorption isotherm, which displays the amount of water absorbed by the material for a given relative humidity of the environment, at a constant temperature.

Moisture can be fixed in a porous material along two processes : surface adsorption and capillary condensation. For a given hygroscopic state, both phases exist simultaneously. Figure 2.3 displays the different steps of these phenomena.

Adsorption :

The weight of a sample of porous material changes when the relative humidity of its surrounding environment is modified, and this proportionally with the relative humidity. This phenomenon is due to attraction forces between the surface of the pore and the molecules of water vapour. The maximum water content that can be achieved with this phenomenon is usually far lower than the one at saturation.

Water molecules are adsorbed by the total surface provided by the pores in the material, gathering in layers, one after the other, as represented in Figure 2.3.

Capillary condensation :

Within a pore, the different layers of molecules, added to one another, are able to join if the pore radius is small enough and if the relative humidity is high enough. A meniscus, a liquid bridge, is thus built and the liquid phase of water cohabits with its vapour phase in equilibrium.

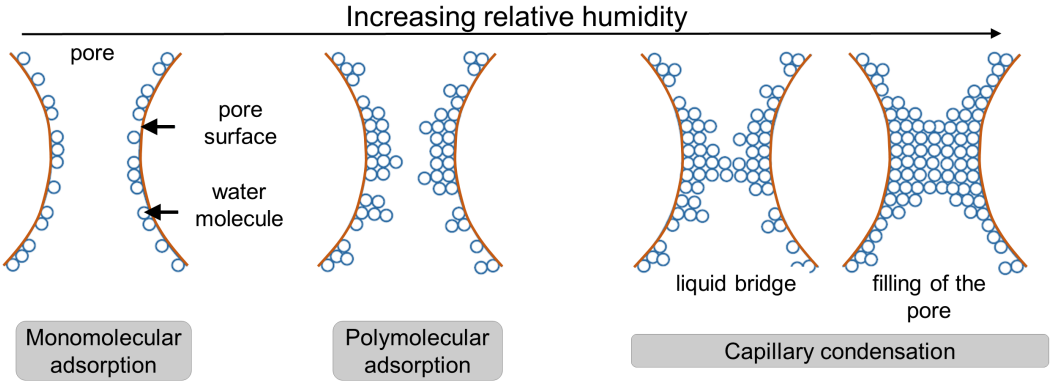

Figure 2.3: Adsorption phenomenon, from one layer to the total filling of the pore [37].

Moisture transport in porous media results from different phenomena leading to the transfer of both liquid and vapour phases. The proportion of each depends on the material properties and the surrounding environment.

Water vapour transfer :

In large pores, the collision probability of molecules against the pore walls is lower than against other molecules. In this case, the mean free path (mfp) of water vapour molecule, which represents the average distance travelled by a moving particle between successive impacts, is small compared to the pore size. Depending on the pore size, the vapour transfer occurs whether by molecular diffusion (pore size $>$ mfp) or by Knudsen diffusion (pore size $<$ mfp).

The molecular diffusion is the movement occurring in moist air, in the presence of water vapour concentration or vapour partial pressure gradients when the total pressure remains constant. The Fick law describes this phenomenon, and several formulations can be found in the literature (see Part III for more details).

The water vapour transfer in materials is often characterized by its capacity to be penetrated by a gaseous phase when submitted to different pressures. The water vapour resistance factor is the reference coefficient and is well documented (see Part II for more details).

Liquid water transfer :

The liquid water flow is due to a liquid pressure difference in the water and the corresponding flux density is described by the Darcy Law. The latter can be expressed thanks to several driving potentials such as capillary pressure, suction, water content, ... (see Part III for more details).

The liquid transport in porous materials is characterized by its liquid permeability or capillary transport coefficient. They can be measured thanks to water permeameter or to the liquid absorption test (see Part II for more details).

2.2 Research concern for rammed earth

Indoor air quality, and even air pollution, are related to the relative humidity levels in the building. Relative humidity in enclosed spaces can have a significant impact on the health of the inhabitants. The micro-organisms are seeking high relative humidity levels to proliferate, and the emission of volatile organic compounds from materials increases in those conditions [55]. On the opposite, dry relative humidity over a long period of time may affect the mucous and increases the chances to be subjected to viral infections [18]. There is now a consensus that relative humidity between 40% and 60% is the optimal interval for a better indoor air quality. Figure 2.4 displays the multiple risks of each RH zones [10].

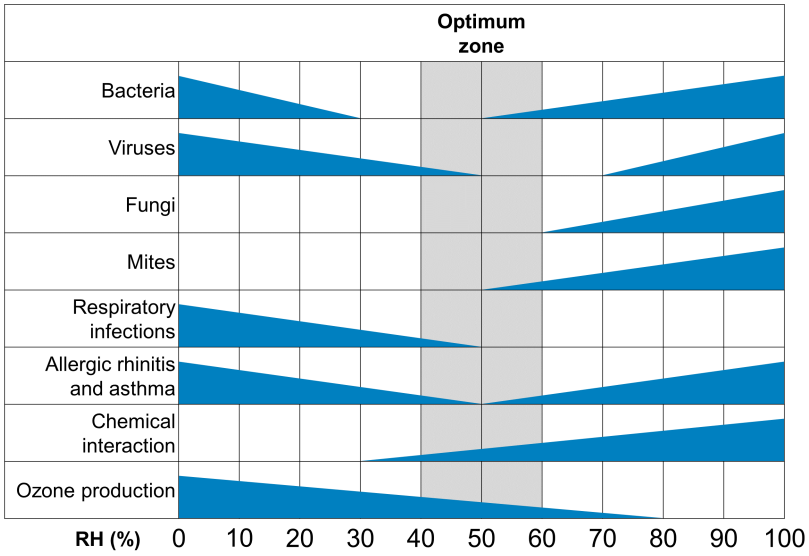

Figure 2.4: Optimum relative humidity ranges for minimizing adverse health effects, from [10].

As a consequence, the awareness raised of the importance of a good indoor air quality, and not only the thermal comfort, led to multiple mechanical devices in charge of renewing the air. In their study, [98] "question whether "total environmental control" is possible, effective and desirable" and draw a picture where a "dreamed" indoor environment is created regardless of the human adaptability.

On the other hand, some building materials have proven to be able to passively control the indoor environment thanks to phenomena such as moisture buffering or thermal mass. A passive control offers not only a sustainable but a more efficient solution, as it is not likely to break down, and worsen the situation, as mechanical devices are. However, such materials have to be integrated from the construction, and a good design is often essential.

In chapter 5, the passive moisture control of the house will be first investigated,

and quantified. In order to provide a better and more specific understanding of the material, experimental measurements in the laboratory are then described, from the common characterization to more specific investigations related to the particular feature of earthen materials.

During its lifetime, an earthen wall is submitted to very different saturation states, including the highest ones. Knowing the behaviour of the material close to saturation is a matter of concern in two main cases. First, the manufacture requires a large amount of water to be added; the material is thus saturated when it has to bear all the dead loads [29]. Second, pathologies such as rising damps can drastically increase the water content which reaches values close to saturation. The stability of the whole structure can be at stake, hence the importance of a good understanding and modelling for a better predictability of collapses.

Concerning earth-based material, the use of the absorption coefficient, commonly called the A-Value, is the most widespread method to assess the behaviour of the material in highly saturated states. However, laboratory tests are commonly made on homogeneous samples, which have been dried and cured under controlled external conditions, and are tested under specific boundary conditions. The similarity between the tested material and the one manufactured on site is thus questionable. For that reason, the chapter 5 studies the value of the liquid absorption coefficient for the studied material, with its variability with the density, and the boundary conditions of the samples during the measurement.

3 Heat and moisture coupled models for building materials

3.1 Hygrothermal modelling

In the previous section, the different phenomena occurring in porous material, regarding heat and moisture, have been introduced. The following section aims at describing the main existing models for coupled heat and moisture transfers that can be found in the literature.

3.1.1 Glaser method

The Glaser method analyses the condensation phenomena in building materials, and is mainly recognized for its convenient graphical analysis. Indeed, it was developed in 1959, i.e. before the advent of computing.

The method aims at predicting the condensation risk in a wall. To do so, it compares the water vapour partial pressure and the saturating vapour pressure at a given temperature. If the saturating vapour pressure is reached, condensation is expected. However, this method considers the steady state of the wall and thus doesn't take into account variations in the boundary conditions (temperatures, relative humidity, solar radiation, wind driven rain, ...). It also only foresees the condensation risks due

to vapour diffusion and not to the air leakage, rising damps, rain water infiltration, etc.

This method should thus be used as an evaluation tool but isn't reliable enough for precise predictions: real risks are usually well predicted but non-existent ones also are.

3.1.2 Hygrothermal dynamic modelling

The development of theoretical formulations for coupled heat and mass transfers in porous media in the mid-20th century [97][118] enabled the rather fast emergence of numerical software as soon as it has become possible in computing science. These models consider more precise phenomena such as the distinction between water vapour and liquid water, the initial moisture state of the material, their storage capacity and the variations of heat parameters with the moisture content.

Among many others, two well-known software, WUFI[59] and Delphin[16], are able to predict precisely the hygrothermal behaviour of complex walls. They also provide a large amount of basic parameters for common building materials, thus being very convenient for anyone to use.

More recently, the HAMSTAD project [69], initiated by the European Union, aimed at developing a frame for the assessment of HAM modelling for building materials. It is divided into two stages : the first one is focusing on proper material characterization and the second one provides a standard methodology for HAM modelling, in order to provide an alternative to the Glaser method for calculation, prediction and evaluation of the moisture performances of the building envelope.

This section is only an introduction to the coupled phenomena and detailed equations are discussed later in the present work.

3.2 Whole-building simulation tools and case study for rammed earth constructions

There is now a growing interest in the investigations of possible contributions of rammed earth building envelopes to the reduction of energy used to ensure good thermal comfort in buildings for heating, cooling and managing humidity level. In order to analyse precisely this contribution, it is anticipated that dynamic hygrothermal phenomena at whole building scale should be investigated, both using experimental measurements and numerical simulations. In this section, after an overview of whole-building simulation tools, existing works on hygrothermal performance of rammed earth buildings are reported. Finally, an overview of potential further studies are proposed.

3.2.1 Whole-building simulation tools

Numerous energy performance simulation tools for whole buildings have been developed in the last decades. Most enable at least computing of instant indoor temperature and/or heating/cooling demand, under the combined dynamic effect of oc-

cupancy (internal loads), weather conditions, together with transfers through building's envelope, as well as some representation of HVAC (heating, ventilating and air conditioning) systems.

In September 2014, 417 building software tools for evaluating energy efficiency, renewable energy, and sustainability in buildings were described in [149]. However, only few of these tools are able to predict combined heat, air and moisture (HAM) transfers in buildings. The development of these tools has been encouraged by the collaborative project Annex 41 – MOIST-ENG (Whole building heat, air and moisture response of the International Energy Agency project, ECBCS) and was reported in [157]. Some of the tools have been further developed and successfully used since then. Those that have been most frequently used recently for whole building hygrothermal simulations are reported below. All of them include heat, air and moisture balance in the indoor air.

- **EnergyPlus**[148]: is an energy performance simulation engine with the possibility of association of graphical interfaces. This is a very powerful tool, more and more used throughout the world.
- **ESP-r**[147]: is one of the oldest tools, able to deal with hygrothermal phenomena. It has been successfully used for modelling moisture transfer and mould growth [33][34].
- **IDA ICE**: Indoor Climate and Energy is fundamentally a tool for simulation of building energy consumption. Most hygrothermal simulations done with IDA were devoted to wooden construction in Scandinavian climate [74][90].
- **PowerDomus**[119]: simultaneously solves heat and moisture transfer in walls, according to a method developed by [105]. It has been used for hygrothermal simulations of buildings, but also for the ground and building foundations [50][104].
- **Wufi Plus**: is a recent whole-building extension of a well known Wufi® software, originally limited to envelope calculations. Its users' friendly interface, together with the popularity of Wufi 2D tool, makes Wufi®Plus popular in consulting offices.
- **TRNSYS**: TRNSYS program (TRaNsient SYstems Simulation) is one of the oldest and most popular WB tools. Some examples of specific types, dedicated to HAM transfers in envelopes (e.g. [134]), have been published in the literature. However none of them is available in the standard libraries, nor was used for rammed earth walls.

Many validation and case studies are described in the literature using theses simulation tools. In general, correct performance regarding temperature and energy calculations is reported, as well as correct estimations of indoor air relative humidity [156]. However, only a very limited number of studies compare hygrothermal

values both at room and wall level (see for example [91]). Moreover, for highly hygroscopic materials and dynamic boundary conditions, more discrepancy is reported for humidity calculations.

3.2.2 Case studies of energy evaluation

Energy used for ensuring good hygrothermal comfort is of interest in the present section. The first result is the limited number of papers devoted to rammed earth constructions, in the flourishing field of building energy performance papers. The most important are described below.

Taylor in [138] investigated an office building in Australia, with stabilized rammed earth walls. The authors used experimental investigations in an occupied building, and TRNSYS modelling to deepen the analysis. In this work, investigations focused mainly on HVAC system, and very little attention was devoted to rammed earth envelope.

An extensive study using numerical simulation was conducted by[115], using whole building heat simulation tool, TAS (Thermal Analysis System). This software assumes only one-dimensional heat transfer through the wall elements. An attempt to model the effects of the variation of moisture content throughout the wall was done by dividing the wall model into three layers with different thermal conductivities. The indoor environmental performance and the energy consumption of an adobe building was assessed for three different latitudes in Mexico. The results showed the importance of modelling of massive internal walls on the attenuation of the indoor temperature fluctuations. Moreover, during the cold part of the year, the external wall thermal conductivity was the most significant variable.

Allinson in [9] analysed the hygrothermal behaviour of a small building in the UK, built with stabilized rammed earth (SRE). It is probably the first paper where a whole building HAM simulation tool (WUFI®Plus) is used to investigate the behaviour of a rammed earth construction. The validity of the simulation was checked using experimental measurements of temperature and relative humidity of the indoor air. The parametric study showed high moisture buffering potential of SRE walls. Some complementary works are now needed, in order to extend the validation of the model to the transfers within the walls.

3.3 Research concern for rammed earth

This brief overview of existing works shows, on one hand, the numerous simulation tools able to deal with hygrothermal transfers in building envelopes, and, on the other hand, the need of precise assessment of energy performance of rammed earth constructions. This large variety of codes are based on various assumptions, not necessarily suitable of all existing construction materials, and on the other hand, taking into account every phenomena would lead to complex codes with an increasing number of in-come parameter to measure, thus bringing difficulties in their numerical implementation and calibration.

In this context, the aim here is to develop the simplest model which allows to properly simulate the behaviour of earthen constructions, and the first step, to identify the key elements that have to be considered:

Modelling of massive wall :

As the high thermal mass is an advantage of rammed earth constructions [38][100], this point must be considered by the tool. This can be assessed by dynamic simulation, which makes all the above mentioned tools able to take this effect into account. However, in some cases of very massive walls, the use of transfer function should be done with care [95].

Coupled heat and mass transfers :

The assessment of moisture impact on thermal properties and moisture buffering capacity of the wall can be modelled by hygrothermal tools. However, this modelling is not always straightforward. First, detailed material properties are needed (vapour permeability, liquid conductivity, sorption isotherms...), that can be costly and difficult to measure. Second, existing models still need additional experimental validations in the case of rammed earth walls. There is still no consensus on some of the modelling hypotheses [130][129] such as the use of latent heat of evaporation instead of the latent heat of sorption, modelling of hysteresis in sorption isotherm, etc.

Rising damps :

As well as built-in moisture, it requires the modelling of liquid transport, and of at least two-dimensional transfers: the vertical movement of raising damp, and horizontal movement of heat and mass due to weather and indoor loads. None of the above mentioned tools can perform such complex simulations at whole building level. An interesting way of analysing it is to perform a co-simulation, using two simulation tools: the first one at whole building level, with 1D HAM transfers through the envelope, and second for 2D HAM transfers in the envelope, such as proposed by [137] to study flooded constructions.

Precise simulation tools are essential in order to assess the performance of rammed earth constructions in terms of energy and hygrothermal comfort. Such tools are necessary to validate the compliance with energy standards as well as benefits and drawbacks in comparison with different types of building's envelope. From the analysis of the literature, it clearly appears that additional researches are needed to analyse and quantify precisely the hygrothermal behaviour of rammed earth walls, and their impact on indoor conditions. Additional validation studies are necessary, combining measurements at both wall and room levels. At the same time, many advanced simulation tools are available, and their use should be encouraged.

4 Scope of my PhD

The first objective of my work aims at exhibiting and quantifying the energy performance of the material through in-situ measurements.

The thermal performance of rammed earth walls is studied from in-situ measurements where an occupied house is instrumented. The data analysis enables the assessment of decrement factors and thermal lags through the seasons and for different orientations. The role of solar gains is also quantified.

The hygric performance is also studied on the same house, and more precisely how the moisture is regulated in the building and in the wall. Unfortunately, to highlight hygrothermal couplings on site has revealed to be hard due to the multitude of phenomena occurring at the same time.

This leads to the second aspect on the experimental investigation : the laboratory characterization of the material regarding its thermal, hygric and hygrothermal behaviour.

In order to fulfil the above mentionned objectives, once the different aspects are clarified experimentally, the second main task of my Ph.D. is the numerical modelling of this behaviour. The coupled model proposed is based on heat and mass balances inside the pores and considers separately the kinematics of each phase (liquid water, water vapour, dry air and solid matrix). As the software WUFI® is reported to be widely use by consulting offices, the simplifying assumptions made in [89] are evaluated regarding the specificity of earthen materials and their suitability, in this context, is questioned. The model is successfully compared with benchmarks and the input parameters are calibrated thanks to experimental data at the different scales and saturations.

Part II

Experimental evidence of earthen material's behaviour

Chapter 3

Description of the monitored house

Contents

The house on which a large part of the experimental part is focused is located in Saint-Antoine-l'Abbaye, in Isère, South-Eastern France. In 2000 was born the association "Ecosite Sud Grésivaudan" gathering ecological committed citizens willing to create an ecological hamlet, named "La Chabeaudière". The site counts 8 dwellings made out of diverse materials with low environmental impact, such as hemp, straw, and of course, rammed earth.

The house is occupied by a family of 5 people, two adults and their three children from 11 to 19 years old (in 2016).

1 Main characteristics

The house has a living area of 150 m^2, over two floors, and a cold attic. Its envelope is composed of four non insulated load bearing walls in rammed earth (exposed to the South, East and West) 50 cm thick and 3 m high and a timber-frame wall filled with straw (mainly North orientation and upper parts of the construction), as it can be seen in Figures 3.1, 3.2, and 3.3. The timber-frame wall is filled with 34 cm of straw and coated with 6cm of earth plaster and 2.5cm of Douglas fir. The thermal transmittance of this highly insulated assembly is estimated at 0.13 $W.m^{-2}.K^{-1}$.

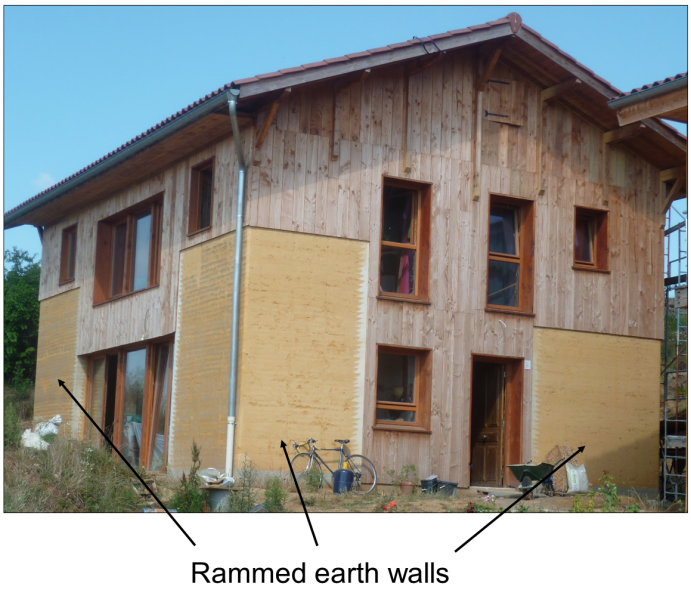

Figure 3.1: House in Saint-Antoine-l'Abbaye (2014).

The slab is made out of a mix of cement, lime, straw, sawdust and cellulose wadding, and covered with fired earth tiles.

Openings, counting windows and doors, are described below (information gathered by[151]):

- Double glazing Argon for South, East and West facades (U=1.70 W.m^{-2}.K^{-1})
- Triple glazing Argon for North facade (U=1.09 W.m^{-2}.K^{-1})
- Double glazing for wooden bay window (U=2.95 W.m^{-2}.K^{-1})
- Wooden door (U=5.00 W.m^{-2}.K^{-1})

The heating system is a wood stove made with bricks, operated by the occupants and located in the living room. Yearly energy used for heating is evaluated at two cubic meters of wood with the stove turned on two hours a day in winter, early spring and late autumn, which corresponds approximately to 3000 kWh according to [4], i.e. 20 kWh.m^{-2}.year^{-1} (the surface being the living area). The low wood consumption can be put in perspective of the internal mean temperature in cold seasons and to the low ventilation rate. The house is also equipped with solar panels, but the heating is dedicated to the domestic hot water.

No cooling system is installed, only natural ventilation is used in summer to avoid over heating. Regarding the neighbouring environment, a mound of earth is located near the western rammed earth wall, providing some shade from the incident solar radiation.

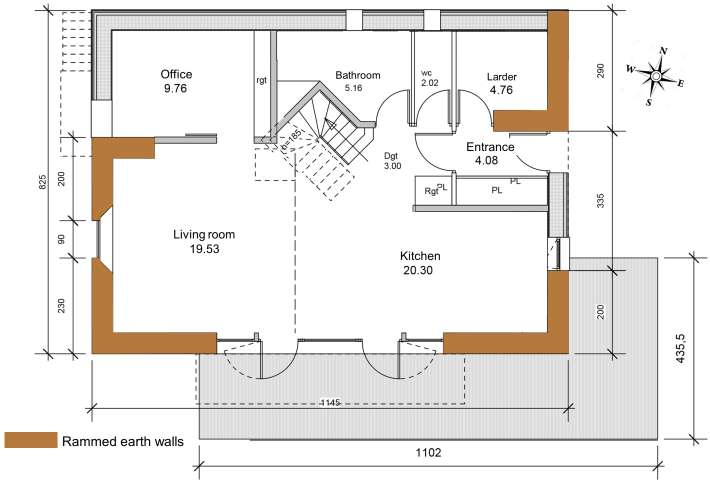

Figure 3.2: Home plan for the ground floor, with the four rammed earth walls.

2 Instrumentation

The house has been monitored from construction in summer 2011 until now, and the monitoring was part of the PhD of Chabriac [28]. The monitoring was designed at

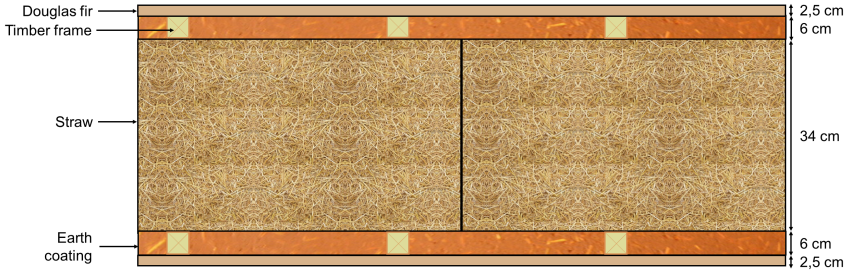

Figure 3.3: Composition of non-rammed earth walls and thicknesses.

different levels : in the wall, in the surrounding internal and external environments, and at various locations in the house.

2.1 Monitoring the wall

12 sensors were placed inside the South/West wall during the construction, at 6 different positions (in the middle and at 10 cm from both surfaces, for both south and west parts, and at the height of about 2 m), as illustrated in Figure 3.4 ; their names are gathered in 3.1. At each location, two sensors were placed: a temperature/relative humidity sensor (CS215, Campbell Scientific, Inc., Logan, UT) and a TDR sensor (CS616, Campbell Scientific, Inc., Logan, UT) to evaluate the water content.

Two additional temperature/relative humidity sensors (CS215) were placed at the internal, respectively external, surfaces, in the corner of the South/West wall.

The measure is recorded every 15 min and the mean value over an hour is saved. All these sensors were connected to a CR1000 Campbell measurement and control system.

According to the constructor, the accuracy of the measurements of the CS215 is +/-1.5°C for the temperature and 2% for the relative humidity. The TDR sensors, for Time Domain Reflectometry, measure the dielectric permitivity (with an accuracy of +/-2.5%) and were calibrated following the protocol in [29].

2.2 Monitoring the indoor air

Regarding the indoor environment, 7 sensors for temperature and relative humidity (EL-USB-2, Lascar electronics, Salisbury, UK) were placed inside the house at different locations: in the living room (near the south-west rammed earth wall), in the kitchen (near the south-east rammed earth house), in the WC and in the middle of the ground floor. Upstairs, one sensor was placed in the central room and two in each bedroom located in the western part of the house, as illustrated in Figure 3.5.

The measures are taken every 15 min and mean value is saved every hour.

The weather station installed near the house records only outdoor temperature and relative humidity. The complementary weather data (solar irradiance) was taken from the most complete station in the region located in Vaulx-en-Velin, France [53].

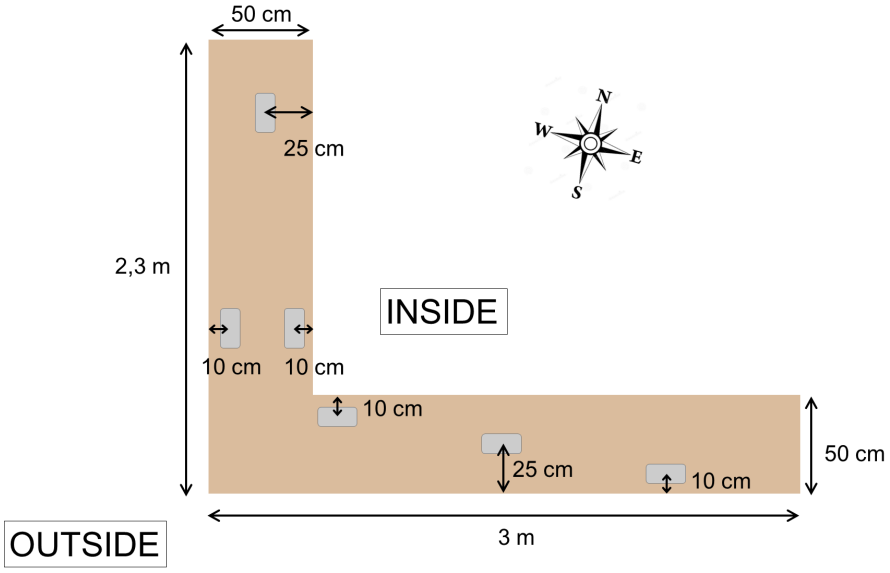

Figure 3.4: Sensors location in the studied wall.

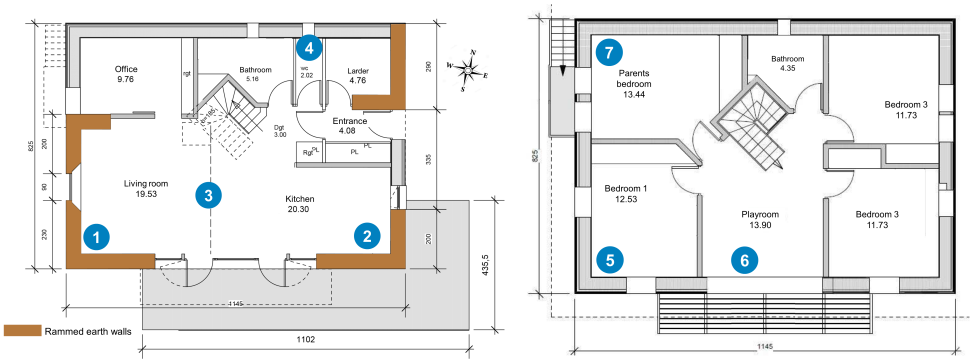

Figure 3.5: Sensors location in the house for the ground and first floors.

It provides, every minute and since 1992, a large amount of measurements related to the temperature, relative humidity, sun (light and energy) and wind. The distance of the station to the house location (about 110 km) should be noticed. Therefore, the Vaulx-en-Velin weather station measurements were compared with those from a non-professional station located in Saint-Marcellin at 8 km from the house (recording temperature, relative humidity, mean solar irradiance and wind speed per hour) and didn't show much difference on the studied periods.

Name	Location
Wext_{wall}	in the western wall, at 10 cm from the external surface
Wmid_{wall}	in the western wall, in the middle the wall
Wint_{wall}	in the western wall, at 10 cm from the internal surface
Sext_{wall}	in the southern wall, at 10 cm from the external surface
Smid_{wall}	in the southern wall, in the middle the wall
Sint_{wall}	in the southern wall, at 10 cm from the internal surface
Ins	Inside the house, near the wall
Out	Outside the house, near the wall

Table 3.1: Corresponding names of the sensors.

3 Basic characterization of the material

The soil for the construction was extracted from a village located at less than 6km from the work-site in Saint-Antoine-L'Abbaye. At material scale, various measurements were made, among which the particle size distribution, given in Figure 3.6. It can be noticed that the soil includes around 10% of granulate with a diameter above 40 mm, typical of the houses of the area. The points below 2μm give the clay quantity, which reaches 16% for this material.

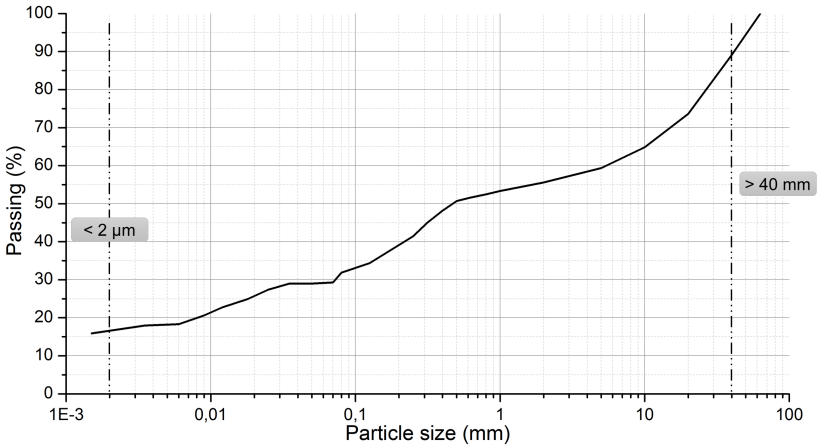

Figure 3.6: Particle size distribution of the studied soil, from [28].

Rammed earth constructions can be stabilized adding lime to the soil before compaction. The lime works on the clay minerals and can improve its resistance against water [58][81][150]. It can also provide a better control of liquid water in the soil during construction. Note that its use remains controversial as it may also deteriorate its hygrothermal behaviour. However, for the earth used as a reference in this study, the mason mixed the natural soil with 2.5% of NHL5 lime, which remains

a low amount. In those conditions, the manufacturing moisture content was about 0.183 kg.kg^{-1}.

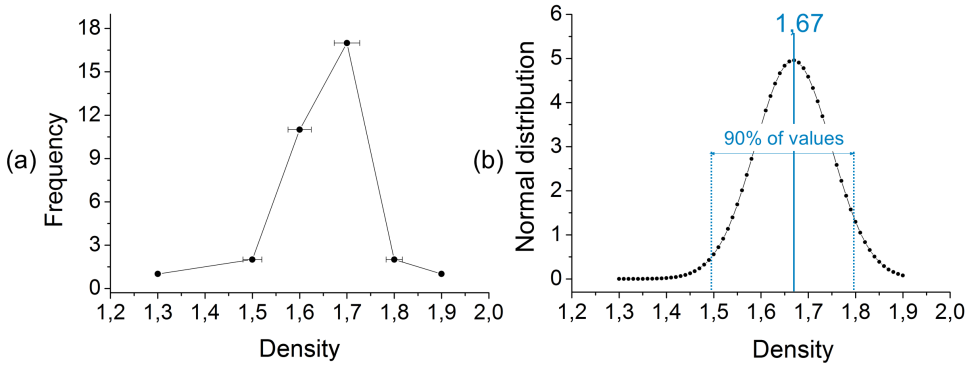

Figure 3.7: (a) Frequency of appearance of a density in a wallet sample, with the corresponding standard deviation; (b) Normal distribution of the density in a wallet following a Normal law.

The dry density on site of the studied soil was measured on samples taken from a "test wall" realized before building the house, and was equal to 1,7. This density can be considered as low, in comparison to other modern rammed earth constructions (broad range of 1.7-2 [2]). An explanation can be the high built-in moisture content that prevents, up to a certain point, the compacting - the water being incompressible. However, after the destruction of one of the experimental wallet, occurring about one and a half year after its construction, the density was measured at 34 different spots. No regular distribution was found. Nevertheless, it appears to follow a normal law, as represented in Figure 3.7. About 90% of the 34 studied samples had a density ranging from about 1.5 to 1.8.

Chapter 4

Thermal behaviour of rammed earth

Contents

This chapter aims at illustrating the thermal behaviour of rammed earth walls, and is mostly leaning on the in-situ measurements on the house presented in the previous chapter.

1 Global energy performance

The following study uses experimental data from a monitored house to investigate its energy performance over the seasons. In particular, the importance of the solar exposure of the rammed earth walls is questioned for both winter and summer thermal performances. In order to explain these performances, the thermal behaviour of the wall, at material scale, is then investigated. The aim is to identify parameters needed to evaluate accurately the thermal performance of the material.

1.1 Heat balance at building scale

1.1.1 General observations

Estimation of the heat fluxes using measured data :

Energy performance can be difficult to quantify as it depends not only on building's intrinsic parameters but also on the occupants and their habits. However, a first sight can be given by the study of heating demand, calculated from the outgoing flux (illustrated as "heat loss" in Figure 4.1).

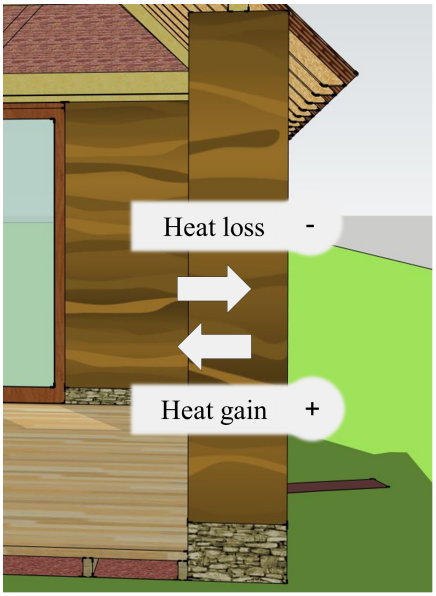

Figure 4.1: Sign convention for heat gain and loss in this study.

The heat flux g_{th} (W.m^{-2}) through the wall can be calculated using the already mentioned Fourier's law.

In steady conditions, the heat flow is constant throughout the wall. In unsteady real conditions, it varies because of the heat storage within the materials. Consequently, at a given time, heat flow value can be different in the middle of the wall as well as at the external and internal surfaces. In the present work, we are interested in the value of heat flux exchanged between indoor air and the wall as it impacts directly the heating demand. This heat flux is estimated using temperatures measured in the air near the wall, and in the wall at 10 cm from the indoor surface:

$$g_{gain} = \left(\frac{e}{\lambda} + \frac{1}{h_i}\right)^{-1} \cdot (T_{Xint_{wall}} - T_{ins}) \tag{4.1}$$

with:

T_{ins} [°C]: temperature inside the house

$T_{Xint_{wall}}$ [°C]: temperature inside the wall, at 10 cm from the internal surface

X : S for the southern wall and W for the western wall

e [m] : thickness of the layer between the sensor and the surface, i.e. 10 cm

λ [W.m^{-1}.K^{-1}] : thermal conductivity of the layer between the sensor and the surface, (here taken equal to 1 W.m^{-1}.K^{-1} according to [129])

h_i [W.m^{-2}.K^{-1}]: surface heat transfer coefficient for indoor surface, taken equal to 8 according to [89].

Negative value of heat flux (when indoor air temperature is higher than wall temperature) means that the heat exchanged between the air and the wall is a loss for the room.

Note that the use of flux-meters could have provided interesting data but they couldn't have been used on south surfaces because of the sun, and would have created a too important local perturbation of the thermal flux. As a consequence, the internal sensors were preferable, even if they still disrupt natural transfers and that they don't provided information between the surface and the first 10 cm of the wall.

What's more the applicability of the stationary law in eq.(4.1) can be questioned. The characteristic time of thermal conduction through the wall is:

$$\tau = \frac{\rho_d C_p}{\lambda} L^2 \tag{4.2}$$

and in our case, $\rho_d C_p \approx 1500$ kJ.m^{-3}.K^{-1}, $\lambda \approx 1$ W.m^{-1}.K^{-1}, and L=0.1 m. This leads to approximately 4 hours. Looking at Figure 4.8, at this time scale the indoor temperature is almost constant. On the other hand, the temperature measured by the external sensor ($S_{ext,wall}$) rather shows a variation periodicity in the range of 24 hours. As a consequence, even if some uncertainties can be induced by the "stationary state", this assumption leads to valuable results.

Indoor and outdoor climates overview :

The heat fluxes through the wall depend mainly on indoor and outdoor temperatures as well as on solar irradiance.

In Figure 4.2 are reported interior (next to the surface) and exterior temperatures for the entire period from April 2013 to June 2015. These temperatures are, for each month, the mean value of measurements collected every hour. Is also reported the direct horizontal irradiance of the sun. For each month, it corresponds to the mean value of data collected every minute.

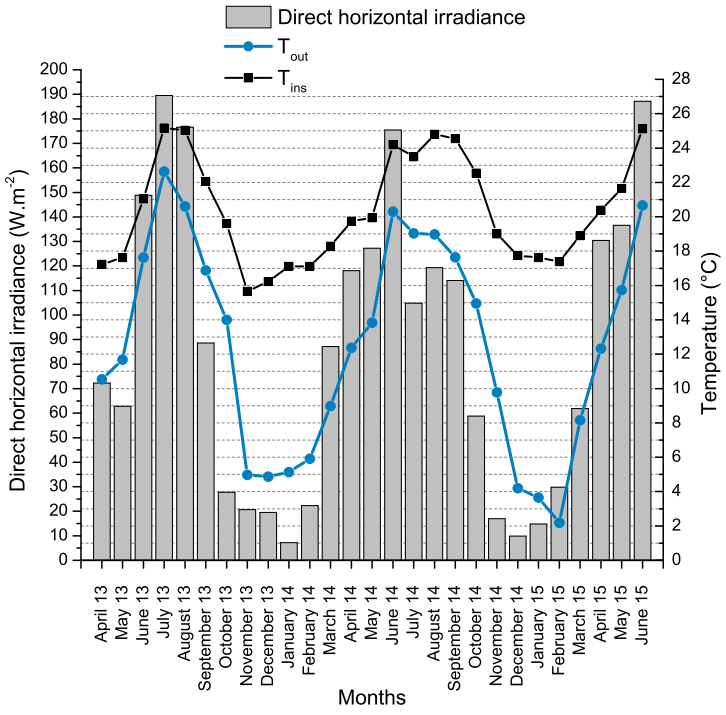

Figure 4.2: Outside and inside temperatures and direct horizontal irradiance of the studied period.

As expected, it can be noticed that the maximal solar radiation reaches the house in summer and the minimal in winter. However, even for the same season, solar radiation can be different (e.g. July in 2013 and 2014) and this, even if the mean temperature is the same (e.g. October 2013 and May 2014). Solar radiation thus provides an additional information to temperatures. These observations lead to consider, for the different seasons, periods with "sunny weather" (understood as high direct horizontal irradiance) and "cloudy weather" (understood as low direct horizontal irradiance).

Information provided in Figure 4.2 gives an interesting overview, however it is not sufficient to study several specific phenomena such as daily variations. For example,

as mean values are considered, the inside temperature of summer months is always higher than the outside temperature, the latter not going above 25°C, as well as the winter outside temperature not going below 2°C. To carry out a deeper analysis, the following parts focus on the winter and summer thermal balances, dealing more in details with data just introduced.

To be clearer on the periods considered, in the following analyses, seasons dividing a year in the northern hemisphere as recalled in Table 4.1.

Spring	March 20th to June 20th
Summer	June 21st to September 22nd
Autumn	September 23rd to December 20th
Winter	December 21st to March 19th

Table 4.1: Seasons in the northern hemisphere.

1.1.2 Thermal balance in winter

First of all, the study of the whole season provides the main tendency. In Figure 4.3, the thermal balances of both western and southern walls are illustrated, for two winters 13/14 and 14/15. The "heat gain", respectively "heat loss", corresponds to the integral in the season of the mean hourly value of negative, respectively positive, flux. The integral is then multiplied by the number of hours in a year, thus enabling a better comparison of the involvement of each season in the annual thermal balance, despite the different number of days considered for each period. The flux can thus be expressed in kWh.m^{-2}.year^{-1} (reference surface being the vertical surface of the walls).

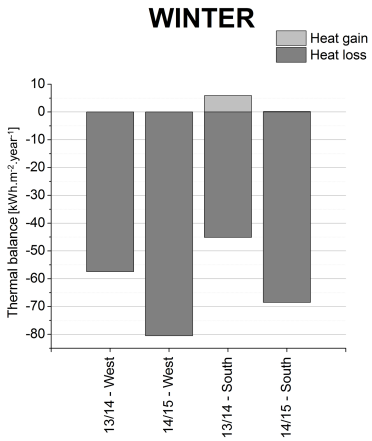

Figure 4.3: Thermal balance of western and southern walls for winters 13/14 and 14/15.

The first observation is the majority of heat losses in both orientations, and for

each year. Indeed, the temperature is higher inside the house than outside, partly because of the heating system, thus driving out the heat through the wall. But the losses are lower for the southern wall than for the western: the solar radiations heat the wall, which lowers the gap between wall surface and inside temperatures, consequently lowering the heat flux. As the southern wall is exposed to the solar radiation earlier in the morning and longer in the daytime, this observation remains intuitive. A difference is also noticeable between the two winters: the losses are globally more important in 14/15 than in 13/14. This can be explained by the mean weather of each winter, the first being milder than the second. Indeed, although the internal mean temperature is quite similar (17.5°C for winter 13/14 and 17.9°C for winter 14/15), the outside temperature is lower for winter 14/15 (4.7°C) than for winter 13/14 (6.7°C). What's more, looking at Figure 4.2, the mean monthly irradiance value of winter 13/14 (/per month) is equal to 38.9 $W.m^{-2}$ whereas it is 35.5 $W.m^{-2}$ for winter 14/15.

At last, the presence of heat gains through the southern wall for winter 13/14 can be noticed, whereas they are almost equal to zero in winter 14/15. The heat gains reach around 13% of the amount of heat losses over the winter 13/14 for the southern wall. It means, that despite lower outside temperatures, heat can go from the wall to the inside of the house.

To carry out a deeper investigation, let us focus on three days, among others, when the reversed heat flux occurred, e.g. from March the 9th to March the 12th of 2014. In Figure 4.4a are represented the hourly total heat flux (positive being heat gain and negative being heat loss) in the southern wall, as well as the direct horizontal irradiance over the same period of time.

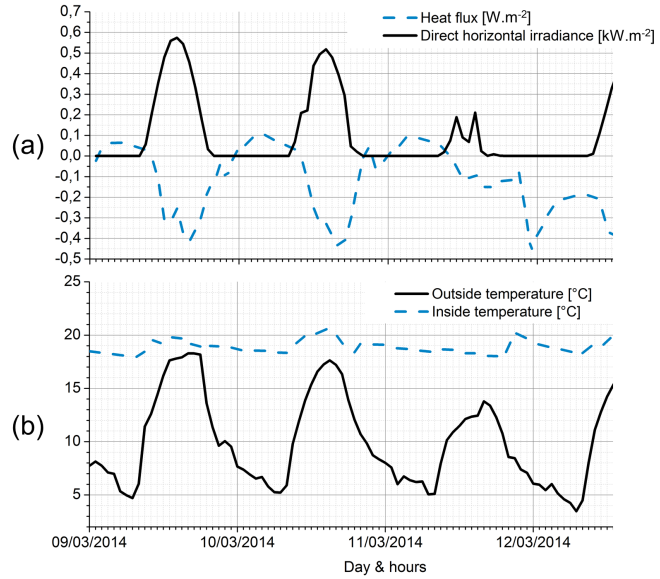

Figure 4.4: March 2014 - Heat flux coming in the south wall and solar radiation.

It can be noticed that the peak of the maximal flux (i.e. the maximal heat gain) always occurs around 4 a.m., whereas the maximum solar irradiance occurs around noon. As soon as the sun goes down (i.e. when the solar irradiance is equal to 0), the heat flux becomes positive. More precisely, the heat gain seems to be proportional to the intensity of the solar irradiance of the daytime before (e.g. on the 9th and 10th, the irradiance is high, so is the heat gain, whereas on the 11th, the irradiance is low and there is no heat gain the night after). This means that the drop of temperature due to the sunset leads to a positive flux within the house: the heat is stored during the day and released during the night.

In Figure 4.4b, outside and inside temperatures over the same period are represented. It is easily remarkable how the outside temperature is related to the direct horizontal irradiance. On the other hand, the inside temperature remains stable, with the exception of slight increase at approximately 6 pm, which might correspond to owners coming back home and starting the heater and is not related to the solar irradiance peak.

These analysis reveal the energy performance of the house during the cold season which generated rather comfortable inside temperatures with low heating consumption, a good thermal mass allowing interesting phase shifts of solar gains and an overall good insulation of the house despite the non-insulated rammed-earth walls.

1.1.3 Thermal balance in summer

The other aspect to be kept in mind regarding energy performance of building envelope is the summer comfort, understood here as moderated indoor temperatures when outside temperatures are high.

First of all, an overview of heat fluxes in summer is presented in Figure 4.5.

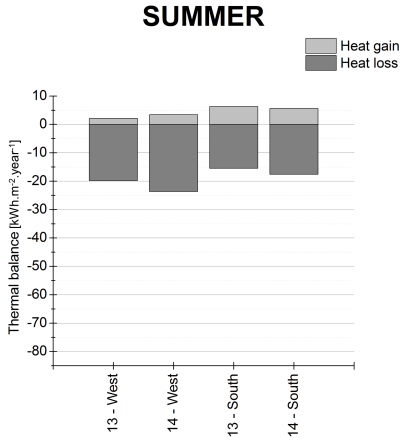

Figure 4.5: Thermal balance of west and south walls in summer 2013 and 2014.

As the same scale is kept for both Figure 4.3 and Figure 4.5, it can easily be

noticed that the heat losses are far lower in summer than in winter. Losses are lower and gains higher, for the southern wall than the western wall, for the same reasons as previously detailed. A slight difference in both losses and gains between the two summers can be explained by a more sunny summer 2013. Indeed, looking back at Figure 4.2, the mean solar irradiance is 152 W.m^{-2} in 2013 against 113 W.m^{-2} in 2014.

The heat gains are notably low, there is thus no need for any cooling system. More precisely, the heat losses are to be considered as saved energy to cool the room. In order to study more in detail heat fluxes at daily scale, two periods were selected during summer 2013, one qualified as "sunny weather" and the other as "cloudy weather". They are reported in Table 4.2.

	Periods	**Mean daily direct solar irradiance**
Sunny weather	July 20th to 27th 2013	5.4 kWh.m^{-2}
Cloudy weather	June 24th to 30th 2013	2.8 kWh.m^{-2}

Table 4.2: Selected weeks in summer 2013.

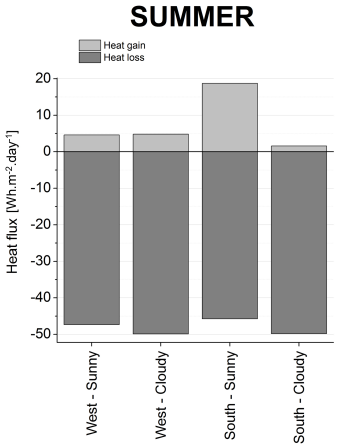

Figure 4.6: Daily thermal balance for sunny and cloudy weathers of west and south walls in summer 2013; Mean values are calculated over the corresponding periods.

The Figure 4.6 focuses on the thermal balance of western and southern walls during these two periods. For both orientations, the losses are higher than the heat gains, consequently due to higher indoor than outdoor temperatures. On the other hand, the western wall seems to be less impacted by the decrease of solar irradiance. Indeed, the heat gains are almost the same for both cloudy and sunny weathers. This can be due to the presence of a mound of earth near the western part of the house, and thus preventing it from receiving a part of direct solar irradiance. This raises the importance of the rammed earth walls location to ensure their optimal behaviour.

The Figure 4.7 provides the inside and outside temperatures for the two periods mentioned above. First of all, for both periods, the inside remains at a comfortable

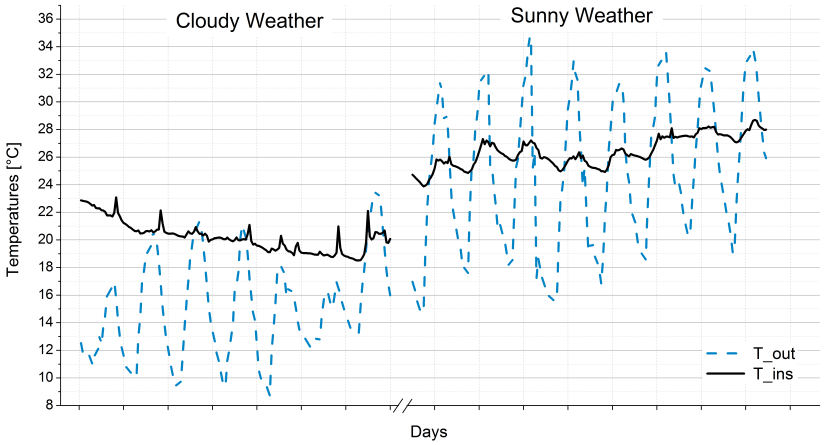

Figure 4.7: Inside and outside temperatures for the two weeks referenced as "cloudy" and "sunny" weathers during summer 2013.

level, regarding the outside temperature. Indeed, whereas the outside temperature reaches 35°C, the inside temperature doesn't increase above 28°C. During the "cloudy weather" week, the inside temperature decreases slightly from 23°C to 19°C in seven days whereas the outside temperature falls beyond 10°C. This highlights the very good thermal mass of rammed earth and the rather good insulation of the house.

The results clearly show excellent stability of indoor temperatures: daily variations are lower than 2°C. Such stable indoor climate in an occupied dwelling is clearly an advantage of the house and demonstrates its high thermal mass.

The first section focused on the relation between outdoor and indoor environments. The following is looking more into the thermal properties of the wall which can explain such global behaviour.

1.2 Thermal behaviour of the wall

Temperature profiles in the wall are functions of the inside and outside temperature, as well as of the thermophysical properties of the materials. The heat wave on the outer surface of the wall travels through the wall and its deformation depends on the material properties. It reaches the inner surface, with a smaller amplitude and after a certain time. The taken time is named "time lag" (see eq.4.3) and the ratio of the two amplitudes is known as "decrement factor" (see eq.4.4). Associated with the thickness, time lags and decrement factors are very useful characteristics to quantify the heat storage capacities of a wall.

The thermal mass of a material is related to its abilities to store and release the heat with its surroundings, and thus depends on how fast the heat is absorbed and distributed. Parameters usually used are the diffusivity and, at some point, the effusivity. They enable to quantify heat exchanges for different materials.

In the following paragraphs, the results of experimental measurements are given, then a more detailed analysis is conducted on time lag, decrement factor as well as on thermal diffusivity and effusivity.

1.2.1 Time lag and decrement factor

As already mentioned above, measurements through seasons reveal different phenomena occurring within the rammed earth wall: the outside temperature and its variations are not only lowered when passing through the wall, but also delayed, thus inducing a time lag in temperature transmission. Those phenomena depend on the material properties, and can be related to its thermal mass.

In order to provide an overview of the thermal behaviour of rammed earth walls, the following study focuses on the whole year 2014, divided in four seasons.

Figure 4.8 is composed of 4 graphs, each one representing temperature variations for a typical week in each season. On each graph, there are 4 temperature distributions corresponding to the internal and external temperatures in the wall, and the outside and inside temperatures of the air near the wall. Only the southern wall is represented here, as the tendencies are similar for the western wall.

For each season and each orientation, the two phenomena of time lag and temperature buffering can be observed. The following analysis will focus on their quantification depending on the orientation of the wall and the season.

The decrement factor (DF) is defined as:

$$DF = \frac{T_{ins}^{max} - T_{ins}^{min}}{T_{out}^{max} - T_{out}^{min}} \tag{4.3}$$

while the time lag (TL) is:

$$TL = t_{T_{ins}^{max}} - t_{T_{out}^{max}} \quad with \quad t_{T_{ins}^{max}} > t_{T_{out}^{max}} \tag{4.4}$$

where $t_{T_{out}^{max}}$ is the time of the external temperature peak and $t_{T_{ins}^{max}}$ is the time of the following internal temperature peak.

We assume here that TL cannot be equal to zero. In consequence, if the peaks of internal and external temperature occur at the same time, TL is taken equal to the period of the temperatures oscillations.

In order to facilitate the comparison, the numerical values of the decrement factor from the external to the internal value of temperature in the wall, as well as the time lag between the two peaks are reported in Figure 4.9. The graphs (a) and (b) deal with the time lag and decrement factor of western and southern walls.

A non-season nor orientation dependent time lag :

As it can be noticed in Figure 4.9a, for all seasons and orientations, the time lag between external and internal temperatures is important: it varies from 6 to 9 hours, with a mean value of about 8 hours. However, care should be taken when considering

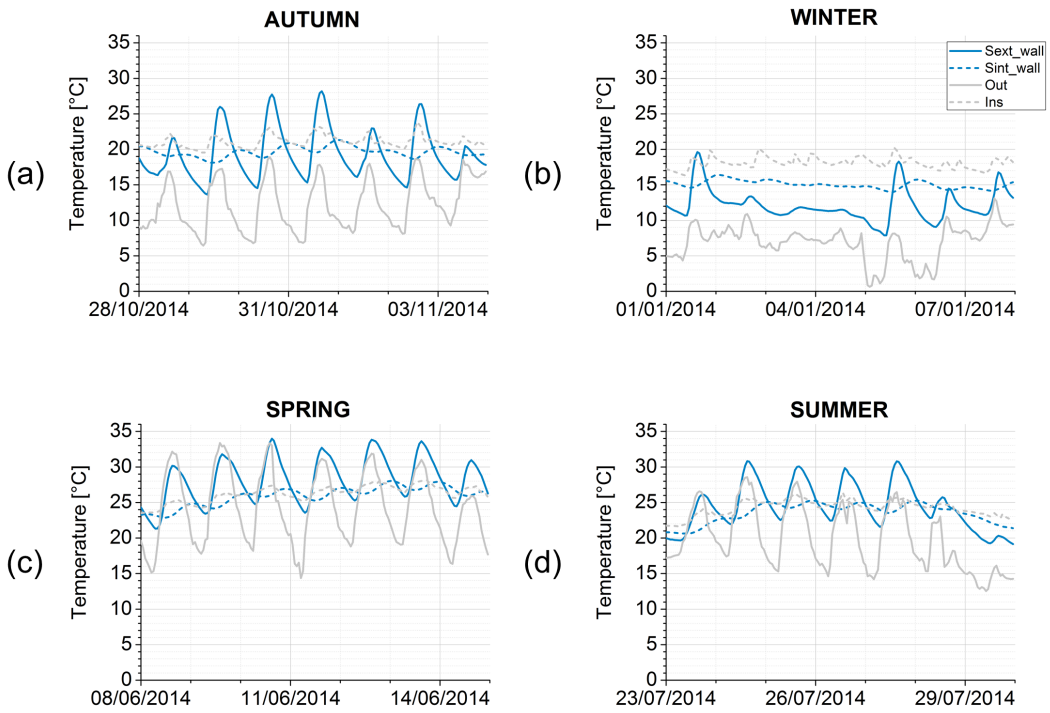

Figure 4.8: Wall and air temperatures in and near the southern wall throughout the year 2014.

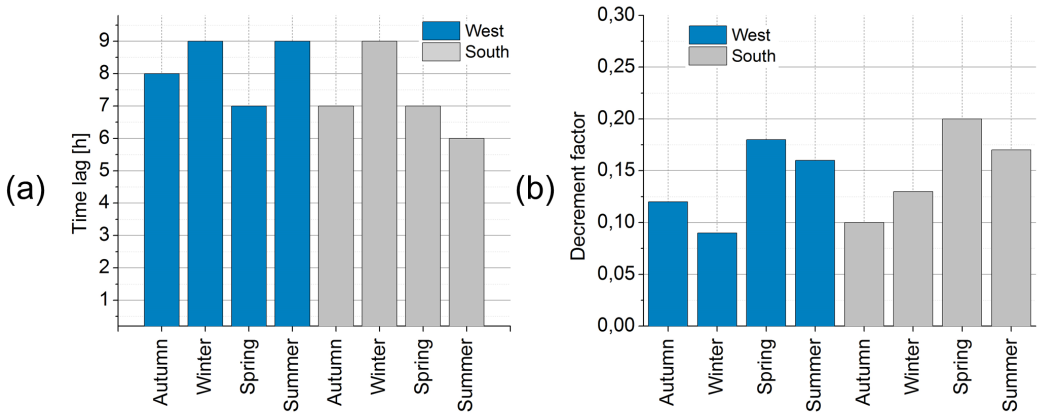

Figure 4.9: (a) Time lag; (b) Decrement factor.

the precision of the given values as the data is collected every hour, being the mean value of 4 measurements.

For all seasons, the daily temperature variations can be observed in Figure 4.8. A

time lag can be noticed between temperatures near the exterior and interior surfaces: the inside temperature reaches it maximum on average 8 hours after the outside temperature. Given the precision of the values, this time lag doesn't seem to depend on the seasons nor the orientation of the wall: it may be related to the material properties. This observation follows theoretical results, as developed in the literature, for example in [136] or [140].

However, another time lag can be measured between the temperature variation of the western wall and southern wall (around 3 hours on average), when comparing the western and southern data (especially in summer, see Figure 4.9). This difference might be due to the variation of the sun position (taking the Earth as a reference) during the day: the southern wall is exposed earlier in the morning all day long whereas the western wall is in the shade in the early morning; even more considering the mound of earth located near the western wall and masking the sun earlier in the afternoon.

Temperature buffering and decrement factor :

In Figure 4.8, for all seasons, a decrement factor is observable in terms of temperature: the effect of the external temperature is lowered and buffered by the wall. During the selected periods, the maximum temperature difference between the internal and external position of the wall reaches 7°C. In the same graph, the comparison of extremum temperatures is interesting. Indeed, whereas the external temperature reaches 35°C, the maximal internal temperature is 26°C. On the contrary, when the external temperature of winter reaches 6°C, the minimal internal temperature is 14°C.

In Figure 4.9b, the decrement factor varies from 0.09 to 0.20, which can be considered as low in comparison with other wall's compositions studied experimentally in [145] (from 0.24 to 0.41). What's more, the decrement factor seems to depend on the amplitude variation of the external temperature, as the internal temperature tends to reach the more stable variation. Indeed, even if high or low temperatures are measured in the external position, the temperature measured in the internal position is stable (low variation during the day), as it is drawn in Figure 4.8. However, data from cold season should be analysed with care as the heating device, even low as it was, have an impact on the decrement factor.

In the literature, many authors studied the variation of decrement factor depending on the material parameters and wall thickness [11], [92]. It appears that the amplitude of the heat wave on the outer surface of the wall influences the decrement factor.

1.2.2 Thermal mass

Previous observations highlight the strong potential of rammed earth wall to buffer temperature variations and to establish a time lag in temperature transmission into the house. According to the theory, the experimental data as well as the literature, these phenomena seem to depend on the material properties themselves.

Effusivity and diffusivity :

When a material is at equilibrium with its environment, its temperature is constant and heat exchanges are equilibrated. Thermal mass is the ability of the material to keep its initial temperature when subjected to a perturbation. If the perturbation tends to bring the material to a new equilibrium temperature, thermal mass represents how long it will take to reach this new equilibrium. The higher the thermal mass is, the slower the transition will occur. Correspondingly, temperature buffering and time lag increase with the thermal mass.

Two parameters are often used to quantify thermal mass of a construction material: diffusivity D ($m^2.s^{-1}$) and effusivity E ($J.kg^{-1}.m^{-2}.s^{-1/2}$).

The thermal diffusivity is defined as the ratio between the thermal conductivity and the product of the density with the thermal capacity. It thus reflects the ability of the material to transmit temperature variations; it characterizes the speed of calories displacement. The lower the diffusivity is, the higher are the buffering effects of the material.

$$D = \frac{\lambda}{\rho_d C_p} \tag{4.5}$$

with:
λ [$W.m^{-1}.K^{-1}$] : thermal conductivity of the material
ρ_d [$kg.m^{-3}$] : dry density
C_p [$J.kg^{-1}.K^{-1}$]: thermal capacity at constant pressure

The thermal effusivity is defined as the square root of the product of the thermal conductivity, density and thermal capacity. It is a measure of the ability of the material to exchange energy with its surroundings and to absorb heat. The higher the effusivity is, the less the surface temperature is impacted by an incoming flux.

$$E = \sqrt{\lambda \rho_d C_p} \tag{4.6}$$

It is interesting to compare these coefficients for different building materials and to study the place of earthen materials. Note here that the parameters can vary for each material and that the values used, being common ones, endeavour to be as realistic as possible. As their sensitivity to water is well known, two earthen materials will be considered in the following: dry and wet earth, with a mass water content of 10%.

One way of improving thermal performance of a building material, is to find a good compromise between a low diffusivity and a high effusivity.

Looking more in details at Figure 4.10 and Table 4.3, it can be noticed that materials such as wood or gypsum have a very low diffusivity but a high effusivity: they will be able to buffer temperature variations but not to store heat efficiently. On the contrary, materials such as solid concrete or stone, have a high effusivity but a low diffusivity: they will be able to absorb heat without an important temperature rise in surface, but will transmit heat quickly and the outside temperature variations

Materials	Conductivity $W.m^1.K^{-1}$	Density $kg.m^{-3}$	Specific Heat $J.kg^{-1}.\mathrm{K}^{-1}$	Diffusivity $m^2.s^{-1}$	Effusivity $J.kg^{-1}.m^{-2}.s^{-1/2}$
Wood fibre	0.04	160	2100	1.2e-7	116
Wood (fir)	0.15	500	1600	1.9e-7	346
Gypsum	0.25	825	1000	3.0e-7	454
Dry earth	0.6	1730	648	5.4e-7	820
Solid brick	0.74	1800	1000	4.1e-7	1154
Wet earth	1.1	1730	648	6.4e-7	1158
Stone	1.7	2000	1000	8.5e-7	1844
Concrete	1.8	2300	1000	7.8e-7	2035

Table 4.3: Building material parameters used to calculate diffusivity and effusivity according to [116] and [28].

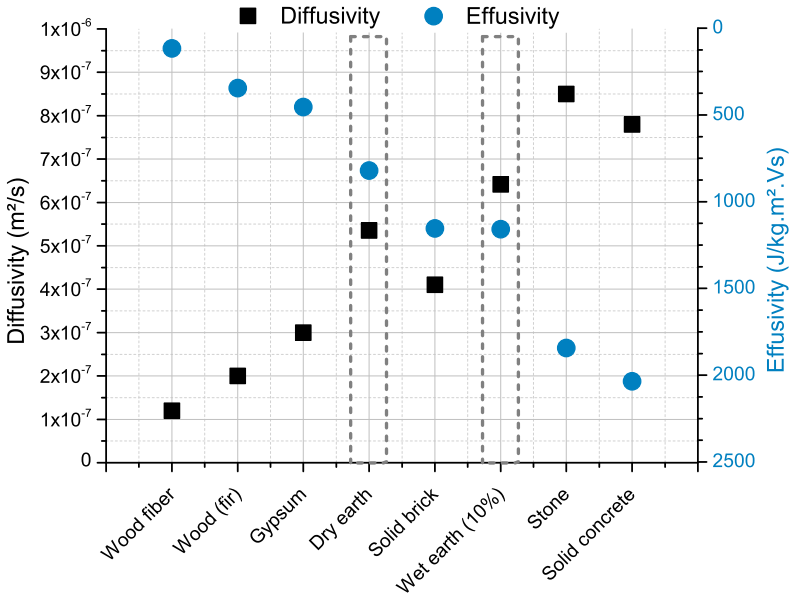

Figure 4.10: Diffusivity and effusivity for different building materials, according to [116] and [28].

won't be lowered by the material. Finally, earthen materials, dry, wet or fired (solid brick), seem to offer both moderate diffusivity and effusivity (located in the central part of the graph).

Link with time lag and temperature buffering :

A material which induces high time lags and low decrement factors provides almost constant inside temperatures which results in a good comfort level. This has been stated by many authors [11][92][136]. These characteristics have to be imputed

to material parameters such as thermal conductivity and thermal capacity, which are thus indirectly related to the diffusivity and effusivity previously presented. Several studies investigate the relationship between these parameters and the induced time lags and decrement factors.

In [11], a numerical study over twenty-six building materials explores the influence of the thermal diffusivity, the heat capacity and the thickness of the walls. It reveals that "materials with high thermal diffusivity give considerable lower time lags than materials with small diffusivity", as well as "materials with high heat capacity and high thermal conductivity [$\cdots$] give considerable lower time lags". Regarding the decrement factor, it seems to get lowered by greater thicknesses, greater heat capacities and low diffusivity.

In [79], time lags and decrement factors are used to evaluate the thermal performance of a wall. Here again, increasing the thermal conductivity leads to a decrease of time lag and the increase of the decrement factor. The increase of thermal capacity leads to the increase in time lag and decrease in decrement factor. The increase of thickness leads to the increase in time lag and the decrease in decrement factor.

These observations are in accordance with the previously made study regarding effusivity. A good thermal performance requires a high effusivity which grows with the increasing of thermal capacity and thermal conductivity.

Heat storage capacity of the rammed earth walls :

This section focuses on the temperature profile variations through the day. It is observed for two seasons: winter and spring. The data from the three sensors in the wall as well as the outside and inside temperatures are represented in Figure 4.11 , at different times during a whole day.

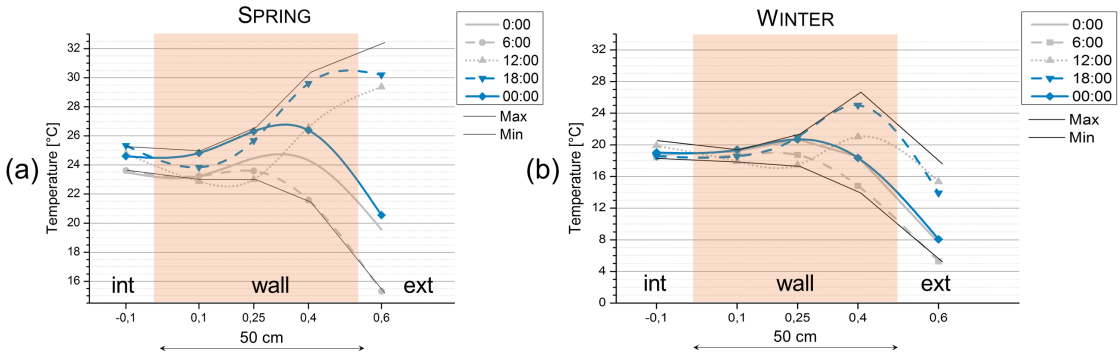

Figure 4.11: (a) Wall section of the southern wall for the winter (January 1st 2014); (b) Wall section of the southern wall for the spring (June 8th 2014).

In Figure 4.11a, during the spring, the temperature buffering can easily be noticed with the extremum temperature profiles. The heat propagation from the external surface to the interior of the wall is observable when comparing profiles at 12:00 and

18:00: the outside temperature rise leads to an increase of the temperature in the external part of the wall, with a delay related to the thermal mass.

In Figure 4.11b, during the winter, the outside temperature is always lower than the inside temperature and the temperature buffering previously mentioned can also easily be observed. However, a part of the wall reaches a higher level of temperature than both maximum inside and outside temperatures. The accumulation of heat is discernible when comparing profiles at 12:00 and 18:00. On the other hand, the comparison of the profiles at 18:00 and the following 00:00 reveals the time lag with which the heat wave is transmitted through the wall.

These two profiles give evidence of the capacity of the rammed earth wall to store a large amount of heat, taking advantage of the surrounding heat sources, including the sun. This feature is linked to the ratio of diffusivity and effusivity previously mentioned. However, the thermal modelling of the wall could be improved by taking into account the radiation at the boundaries. Moreover, the influence of the coupling between thermal and hygric behaviours should be carefully considered, as suggested by [91].

1.3 Conclusion

Experimental results from rammed earth walls in a real occupied house were presented and analysed. The first part of this study focuses on the energy evaluation of the house through the seasons and compares wall orientations. The house provides a good comfort in summer, judging with regards to stability and level of temperatures. Moreover, it offers a good energy performance in winter as the temperature remains comfortable given a very low heating load. Findings confirm good thermal mass of the studied walls and an overall good insulation of the house. The impact of the orientation is also discussed, thus highlighting the importance of a good architecture for rammed earth houses.

The second part focuses more precisely on the thermal behaviour of the walls, revealing important time lags and low decrement factors, which constitutes an explanation of the thermal performance illustrated in the first part. These phenomena are related to the thermal properties of the materials, and can be more precisely correlated with common coefficients such as thermal diffusivity and effusivity.

The thermal parameters of usual building materials are rather constant, thus making their behaviour easier to predict. However, in the case of rammed earth, the thermal parameters are function of the amount of water located in the porous media. A difference is even already remarkable in Figure 4.9 when dry earth and wet earth lead to different values of diffusivity and effusivity. A study of the influence of the water content on the thermal behaviour of the rammed earth walls is to be conducted. The hygrothermal couplings can be an additional element to analyse the thermal behaviour, and more generally the energy performance, of the house.

2 Evaluation of the solar energy storage capacity

The previous section highlighted the importance of the sun for the heat storage in the walls. This section is aiming at quantifying those solar gains, using in-situ measurements.

When the rays of the sun reach an opaque wall, a part of the energy is absorbed whereas the other part is reflected. Solar absorption is a natural phenomenon that enables materials to catch photons from the sunlight and transform them into heat. The absorption coefficient of a surface, named α, evolves between 0 and 1, and expresses the percentage of solar energy absorbed by this surface. The darker a surface is, the more heat will be absorbed, and the higher α will be. In our case, the higher α is, the better it is for the global performance of the house. However, when dealing with insulating materials or plasters, care should be taken not to have an α too high that will induce temperature differences between the layers, and thus create stresses due to thermal dilatation, this added to the risk of condensation at the interfaces.

This coefficient was measured on the studied earth material from St Antoine, and details can be found in [28]. It was measured on earth blocs (CEB) and rough samples, both at a dry state. Since, for some materials, the solar absorption coefficient depends on the angle of radiation, two angles were investigated : 45°and 90°. The mean value of the α was 0.55, and no clear difference was noted between the orientation or the type of samples. However, it could have been interesting to measure the evolution of this coefficient with the water content, the material becoming darker with the increase of moisture. Consequently, this value has to be considered as a minimum.

On the surfaces of the wall, from one part to the other, the mathematical formulation of the boundary conditions are the following :

$$g_{X_i} = h_i(T_{ins} - T) \tag{4.7}$$

$$g_{X_e} = h_e(T_{out} - T) + \alpha I_X = g_{wall,X} + g_{sun,X} \tag{4.8}$$

with:
g_{X_i} [W.m^{-2}] : thermal flux at the internal surface of the wall
g_{X_e} [W.m^{-2}] : thermal flux at the external surface of the wall
X : S for the southern wall ; W for the western wall
h_i [W.m^{-2}.K^{-1}] : surface heat transfer coefficient for internal surface
h_e [W.m^{-2}.K^{-1}] : surface heat transfer coefficient for external surface
α [-] : solar absorption coefficient of the external surface
I_X [W.m^{-2}] : instantaneous solar radiation incident on the external surface of the wall
$g_{wall,X}$ [W.m^{-2}] : part of the thermal flux at the surface due to convection
$g_{sun,X}$ [W.m^{-2}] : part of the thermal flux at the surface due to solar radiation

The objective of this part is to quantify $g_{sun,X}$, the last term of the right part of eq.(2), in order to assess the proportion of heat flux due to solar radiation. However, it requires to know both internal and external heat transfer coefficients, the incident solar radiation for each orientation, and the solar absorption coefficient. This is defining the steps of the following investigation.

2.1 External and internal heat exchange coefficients

2.1.1 Literature review on the coefficient variability

At both external and internal surfaces of a building, heat transfer occurs through convection and radiation. The "heat transfer coefficient" usually accounts for the sum of the convective and radiative heat transfer coefficients. The following focuses on the convective part of the coefficient. The convective heat coefficients strongly depend on the local air flow, the temperature, the geometry of the wall, etc, which makes its derivation very complex and hard to generalize.

To simplify calculation, it is often assumed to be constant [12][76][89]. Nevertheless, many researches have been conducted on the convection heat transfer inside buildings, provided a diversity of theoretical expressions as well as correlation of experimental data, both on vertical and horizontal surfaces. A wide literature review on the coefficient correlation can be found in [82][83]. The standard form of the correlation is function of the temperature difference between air and wall surface, as stated in [82] or [17]. Other correlations include a dependence on the height of the vertical surface [7]. Table 4.4 gathers some of them. Yet, discrepancies are found to be around a factor 2 (vertical surfaces) or even 4 (horizontal surfaces)[82].

On the contrary, fewer researches have been conducted on the heat transfer coefficient at external wall as the variability of wind characteristics around buildings makes it even more difficult to evaluate. Indeed, the convective part is function of multiple variables such as wind speed and direction, flow regimes, roughness, orientation, etc. It has even been stated that the lack of accuracy is responsible from 20 to 40% errors in energy demand calculations [17][52]. Nevertheless, for design purpose, standard values have been adopted [12][32][89] whereas many works have produced experimental and numerical data on the variation of the convective heat transfer coefficient with the wind speed and surface roughness [19][52][96][114]. Table 4.5 gathers some of them.

Finally, the coefficient for natural (i.e. internal) convection is mainly influenced by the surface to air temperature difference, while, for forced (i.e. external) convection, air velocity is the main parameter.

2.1.2 Adjusting the coefficients

In the case of our study, to be as accurate as possible, external and internal heat coefficients are determined from the comparison of on-site measurements and a 1D basic thermal modelling. Indeed, the idea is to use the two ambient air temperatures

Authors	Formulations	Observations
KHALIFA[83]	$h_c = C(\Delta T)^n$	*Laminar* : n=1/4 and C [0.516;0.726] *Turbulent* : n=1/3 and C [0.056;0.130]
ALAMDARI[7]	$h_c = \left\{1.5^6 \cdot \left(\frac{\Delta T}{H}\right)^{1.5} + 1.23^6 \cdot \Delta T^2\right\}^{1/6}$	
KUNZEL[89]	$h_c = 8$	
EN STANDARD[76]	$h_c = 7.7$	
ASHRAE[12]	$h_c = 8.29$	for an emissivity of 0.9
with: ΔT [°C] : air-surface temperature difference H [m] : height of the vertical surface		

Table 4.4: Convective heat transfer coefficients for internal surfaces, in $W.m^{-2}.K^{-1}$.

(inside and outside) and three temperatures inside the wall to obtain a temperature profile to be compared with a numerical simulation. A numerical analysis then provides the required coefficients to match both results.

Selection of the wiser data to be used :

In order to fit with the above assumptions, the periods were chosen following a couple of expectations.

- For the external coefficient:

As mentioned before, only the convective part of the heat transfer is dealt with. The solar irradiance is as limited as possible (the second term of the eq. (1) can be ignored) and only the western part of the wall is regarded. To analyse the question of the wind properly, periods with and without wind are considered.

- For the internal coefficient:

Given that earthen materials have a low effusivity [132], it is assumed that the air-surface temperature difference is low, which leads us to consider a constant convective heat transfer coefficient.

What's more, so that the discrepancies are lowered on the determination of the coefficients, a high temperature gradient between inside and outside temperatures,

Authors	Formulations	Observations
ASHRAE[12]	$h_c = 18.63 V_{loc}^{0.605}$	*Leeward* : $V_{loc} = 0.05 V_{10} + 0.3$ *Windward* : $V_{loc} = 0.25 V_{10}$ for $V_{10} < 2$ $V_{loc} = 0.5$ for $V_{10} \geq 2$
LOVEDAY[96]	$h_c = 16.21 V_{loc}^{0.452}$	*Leeward* : $V_{loc} = 0.157 V_{10} - 0.027$ *Windward* : $V_{loc} = 0.68 V_{10} - 0.5$
NUSSELT[111]	$h_c = 5.678 \left\{ a + b \left[\left(\frac{294.26}{273.16+T_a} \right) \frac{V_{loc}}{0.3048} \right]^n \right\}$	
	$V_{loc} < 4.88$	$4.88 \leq V_{loc} < 30.48$
	Smooth surface	*Smooth surface*
	a=0.99 ; b=0.21 ; n=1	a=0 ; b=0.5 ; n=0.78
	Rough surface	*Rough surface*
	a=1.09 ; b=0.23 ; n=1	a=0 ; b=0.53 ; n=0.78
McADAMS[102]	$h_c = 5.7 + 3.8 V_{loc}$	for smooth surfaces
KUNZEL[89]	$h_c = 17$	
with: V_{loc} [m.s^{-1}] : local wind velocity V_{10} [m.s^{-1}] : wind free stream velocity at alt. 10m T_a [°C] : ambient temperature		

Table 4.5: Convective heat transfer coefficients for external surfaces, in W.m^{-2}.K^{-1}.

is sought as well as a limited solar irradiance. Only winter periods have thus been selected.

The six selected periods are gathered in Table 4.6 with their respective characteristics. Note that mean values are calculated per hour for the temperature and per minute for wind speed and solar irradiance. Note also that the period are named as follows: the "NW/W" stands respectively for "no wind"/"wind", and the last is the number of the period.

Thermal modelling with COMSOL Multiphysics :

The thermal model is used in its classical form, with no heat source and constant

No Wind			
Name	**NW-1**	**NW-2**	**NW-3**
Periods	9-11 Dec. 13	18-20 Dec. 14	19-21 Jan. 15
Mean outside T (°C)	2.6	9.7	1.0
Mean inside T (°C)	15.8	19.1	17.4
Mean initial T inside the wall (°C)	11.8	12.1	11.1
Mean wind speed ($m.s^{-1}$)	0.5	0.7	0.9
Mean solar irradiance ($W.m^{-2}$)	9.2	0.0	0.0
Wind			
Name	**W-1**	**W-2**	**W-3**
Periods	24-26 Dec. 13	11-13 Dec. 14	4-6 Feb. 15
Mean outside T (°C)	8.6	6.3	4.2
Mean inside T (°C)	16.9	17.3	18.1
Mean initial T inside the wall (°C)	13.8	10.0	13.5
Mean wind speed ($m.s^{-1}$)	4.9	3.2	3.2
Mean solar irradiance ($W.m^{-2}$)	2.7	0.6	0.2

Table 4.6: Selected periods to be used for the calibration of heat transfer coefficients.

thermal conductivity:

$$\rho_d C_p \frac{\partial T}{\partial t} = -\lambda \nabla^2 T \tag{4.9}$$

with :
ρ_d [$g.m^{-3}$] : dry density of the material
C_p [$J.kg^{-1}.K^{-1}$] : thermal capacity at constant pressure
λ [$W.m^{-1}.K^{-1}$] : thermal conductivity at a given moisture content

It is implemented in COMSOL Multiphysics , using a 1D geometry whose dimension corresponds to the thickness of the wall (i.e. 0.5 m). The boundary conditions on both sides are set according to measurements of temperature during the selected periods (Neumann flux). Given the assumption of a low solar irradiance and high temperature gradient, the boundary conditions are assumed to be reduced to :

$$g_{W_i} = h_i(T_{ins} - T) \tag{4.10}$$

$$g_{W_e} = h_e(T_{out} - T) \tag{4.11}$$

The initial temperature is considered as homogeneous and equal to the mean temperature of the three measurements in the wall during the first hour of the studied period. The material properties (density, thermal capacity, and thermal conductivity) were measured in the laboratory on the same earth as the one used for the house construction. There are gathered in Table 4.7.

Finally, the results for the different convective heat transfer coefficients are obtained using a double parametric sweep. The internal, resp. external, coefficients varies from 2 to 10 $W.m^{-1}.K^{-1}$, resp. from 2 to 20 $W.m^{-1}.K^{-1}$, with a step of $1W.m^{-1}.K^{-1}$, following the analysis of the literature previously presented.

Parameters	Values	Units	References
Density	1.67	-	[131]
Thermal capacity	647	$J.kg^{-1}.K^{-1}$	[28]
Thermal conductivity	1.0	$W.m^{-1}.K^{-1}$	[28]

Table 4.7: Material properties used for the simulations.

Results analysis :

The modelling can provide the temperature at the three different spots in the wall (at the middle and at 10 cm from each surface) for each hour of the selected periods, so that the calculation data can directly be compared with the measurements. The comparison is done for each pair of internal/external coefficients and each position in the wall, using the least squares method. The sum of squared residuals of each position is added up to obtain a single sum for each pair; the pairs are then classified from the smallest to the highest sum.

For each cases (with and without wind), the best ranked pair simultaneously for the three periods is kept. Results are given in Table 4.8.

	No Wind	Wind
h_i [$W.m^{-1}.K^{-1}$]	7	6
h_e [$W.m^{-1}.K^{-1}$]	14	18

Table 4.8: Convective heat transfer coefficients with and without wind.

It is interesting to notice that, as expected, the internal coefficient differs little from the windy or not situation. On the other hand, the external coefficient is increasing with the wind. The obtained values are thus in accordance with the literature review detailed before.

However, even if the chosen coefficients correspond to the "best" agreement between simulation and measurement, it is logical to question the absolute accuracy of the thermal modelling of the wall. Figure 4.12 displays the temperature evolution for three of the tested periods and for the three positions in the wall, and compares the experimental data with the modelling.

Note that the first six hours of each period hasn't been represented in Figure 4.12 in order to ignore the effects of the homogeneous temperature assumed in the wall.

Looking at the temperatures close to the internal surface (in black), a good agreement is found between the modelling and the experimental measurements. On the contrary, looking at the ones close to the external surface (in blue), there can be higher differences when the temperature variations are more important. It seems that a phenomenon isn't taken into account in the thermal modelling. At last, comparing the cases "with" and "without" wind, no clear conclusion can be drawn regarding the accuracy of the pure thermal modelling, but the tendency seems to be correct.

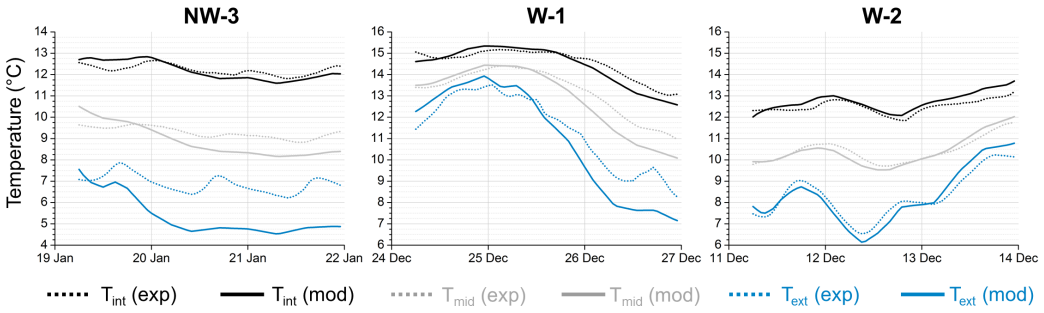

Figure 4.12: Temperature evolution in the wall at the three spots for three periods and from the experimental data and modelling.

2.2 Direct incident solar flux depending on the orientation

As illustrated in Figure 4.13, the solar irradiance can reach the surface of a wall along three ways :

- the direct radiation comes, as expected, directly from the sun to the surface
- the diffuse radiation is first passing through the atmosphere, clouds, etc
- and the radiation called "albedo" is reflected by the environment before getting to the surface

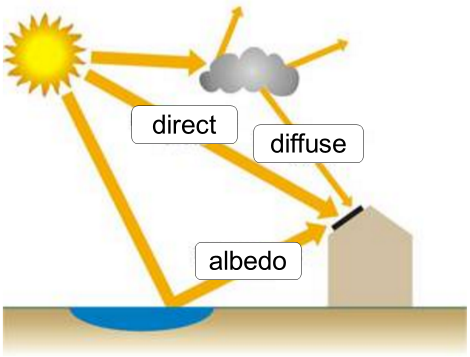

Figure 4.13: Three different types of solar radiations, from [148].

Here again, the direct solar irradiance is taken from the meteorological station located in Vaulx-en-Velin [53]. However, the data provided is the "direct horizontal irradiance", whereas the direct irradiance for each wall is necessary. For the location and orientation, the wanted fluxes can be deduced according to the following method.

As illustrated in Figure 4.14, the position of the sun varies throughout the day and the season. For example, the sun stays lower in the sky in December than in June, and goes from East to West throughout the day, along the red line.

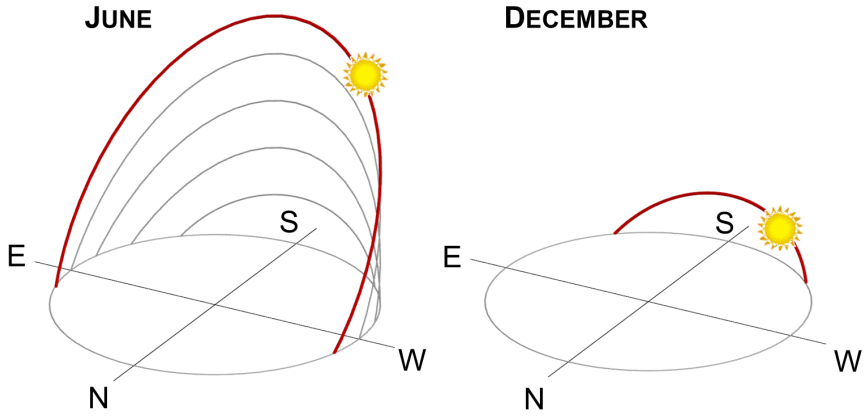

Figure 4.14: Sun positions throughout the day for June and December.

Two parameters are thus needed to know precisely its position:

- height of the sun ht_{sun} in °
- azimuth of the sun az_{sun} in °

The geometrical representation of these parameters is provided in Figure 4.15.

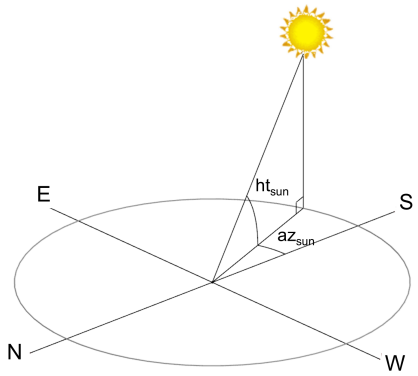

Figure 4.15: Schematic representation of sun height and azimuth.

The data from the meteorological station counts the height and azimuth of the sun and the direct solar irradiance every minutes. Note that, in order to study solar radiation, it is necessary to deal with data every minutes, and not every hour, as illustrated in [51]. In order to obtain the right solar flux perpendicular to each of the wall surface, several angles are needed.

First of all, the incidence angle is calculated thanks to [35]:

$$\cos(i)(t) = \cos(ht_{sun}(t)) \cdot \sin(\theta_{wall}) \cdot \cos(az_{wall} - az_{sun}(t)) + \sin(ht_{sun}(t)) \cdot \cos(\theta_{wall}) \tag{4.12}$$

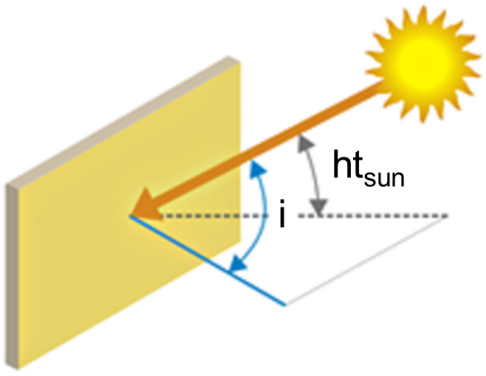

Figure 4.16: Schematic representation of the incidence angle, from [148].

with :
i [°] : incidence angle
az_{wall} [°] : azimuth of the wall (with respect to the south)
az_{sun} [°] : azimuth of the sun
ht_{sun} [°] : height of the sun
θ_{wall} [°]: wall inclination (here equal to 90°as the wall is vertical)

Once the incidence angle calculated, the direct flux received by the wall is :

$$I_X(t) = I_{sun} \cdot \frac{\cos(i)(t)}{\sin(ht_{sun}(t)} \tag{4.13}$$

with :
I_{sun} [W.m^{-2}] : direct horizontal irradiance, from the weather data

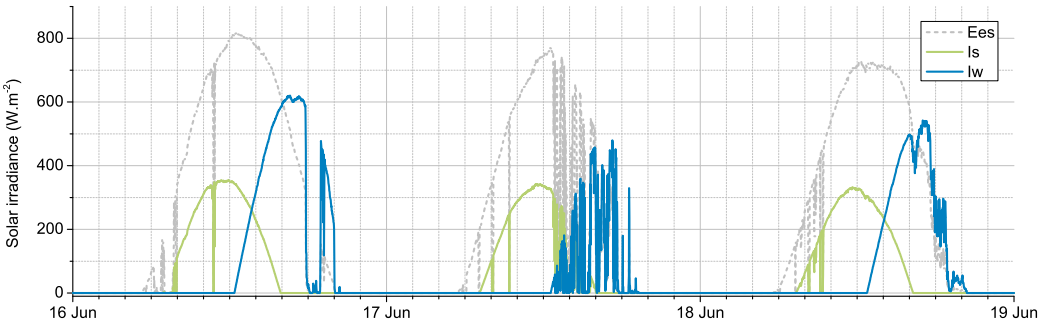

Figure 4.17: Solar fluxes for different orientations : direct horizontal (I_{sun}), perpendicular to the southern surface of the wall (Is) and perpendicular to the western surface of the wall (Iw).

For example, the comparison between direct horizontal flux, and direct fluxes on the western and southern walls are displayed in Figure 4.17. The difference of the two orientations is noticeable : there is a time lag of about 5 hours between the south and the west.

2.3 Solar absorptivity of rammed earth surfaces

The aim of this simulation is to evaluate the value of the solar absorption coefficient α needed to match the thermal measurements in the wall and the climatic data, more precisely the global solar irradiance. Even if the solar absorption coefficient is expected to be constant, the influence of the season and wind has been investigated.

2.3.1 Selection of the interesting periods

Following the same approach, 3-days periods in summer and in winter, with and without wind have been selected. All chosen day are sunny and the mean solar irradiance, together with their main characteristics, are provided in Tables 4.9 and 4.10. Note that the periods are named as follows: the "II" stands for the second batch of periods, the "NW/W" stands respectively for "no wind"/"wind", the second letter respectively "S"/"W" for "summer"/"winter", and the last one is the number of the period.

Summer			
Name	**NW-S-1**	**NW-S-2**	
Periods	29-31 Jul. 13	16-18 Aug. 14	
Mean outside T (°C)	20.8	18	
Mean inside T (°C)	24.5	23.5	
Mean initial T inside the wall (°C	26.3	21.8	
Mean wind speed ($m.s^{-1}$)	1.0	1.2	
Mean solar irradiance ($W.m^{-2}$)	178.8	217.9	
Winter			
Name	**NW-W-1**	**NW-W-2**	**NW-W-3**
Periods	2-4 Dec. 13	22-23 Feb. 14	10-12 Feb. 15
Mean outside T (°C)	2.4	7.4	3.2
Mean inside T (°C)	14.9	18.3	18.1
Mean initial T inside the wall (°C)	8.8	13.4	10.7
Mean wind speed ($m.s^{-1}$)	0.7	1.0	0.8
Mean solar irradiance ($W.m^{-2}$)	51.1	92.3	68

Table 4.9: Selected periods to be used for the determination of the solar absorption coefficient - Without wind.

2.3.2 Thermal modelling with COMSOL Multiphysics

The same model as previously presented is used in this part, with the exception of the heat transfer coefficient that are no more variable, but set as defined in the previous

Summer			
Name	**W-S-1**	**W-S-2**	**W-S-3**
Periods	16-18 Jun. 13	1-3 Aug. 13	10-12 Jun. 14
Mean outside T (°C)	24.1	25.4	24.7
Mean inside T (°C)	24.6	26.5	26.7
Mean initial T inside the wall (°C)	24.1	26.2	26.7
Mean wind speed ($m.s^{-1}$)	2.8	2.9	2.0
Mean solar irradiance ($W.m^{-2}$)	232.4	221.3	249.4
Winter			
Name	**W-W-1**	**W-W-2**	**W-W-3**
Periods	22-24 Dec. 13	29-31 Dec. 14	13-15 Jan. 15
Mean outside T (°C)	10.4	-2.1	7.6
Mean inside T (°C)	17.1	16.9	17.7
Mean initial T inside the wall (°C)	11.6	8.5	13.9
Mean wind speed ($m.s^{-1}$)	6.2	2.6	4.8
Mean solar irradiance ($W.m^{-2}$)	21.6	38.1	29.4

Table 4.10: Selected periods to be used for the determination of the solar absorption coefficient - With wind.

part, and the boundary conditions are now as defined in eq.(2) and eq.(4.8). The absorption coefficient α varies from 0 to 1, with a step of 0.05, using a parametric sweep.

The comparison between calculation and in-situ measurement is made in terms of temperature, and more precisely comparing the temperature inside the wall at 10 cm from the external surface.

2.3.3 Determination of the absorption coefficient

The least square method is also used in this section, to determine the value of α leading to the lowest sum of residuals, for each period. For each period, the α are ranked from the least sum of residuals to the greatest. The best ranked value simultaneously for the 4 cases (2 seasons and 2 wind cases) is kept.

This process chose $\alpha = 0.6$. There doesn't seem to have a difference between summer and winter despite the seasonal water content difference. This variation in saturation, even if it affects the colour, is too low that it doesn't affect the solar absorption.

Note that this value is in accordance with the one measured experimentally.

Again the accuracy of the modelling is checked in Figure 4.18, on which is displayed the temperature evolution in the wall, at 10 cm from the external surface, for the two orientations and for three periods among the one selected for the calibration. The first twelve hours is also not represented in Figure 4.18 in order to ignore the effects of the homogeneous temperature assumed in the wall.

It can be noticed the global good agreement between the experimental data and the modelling, for both western and southern orientations. However, again, discrep-

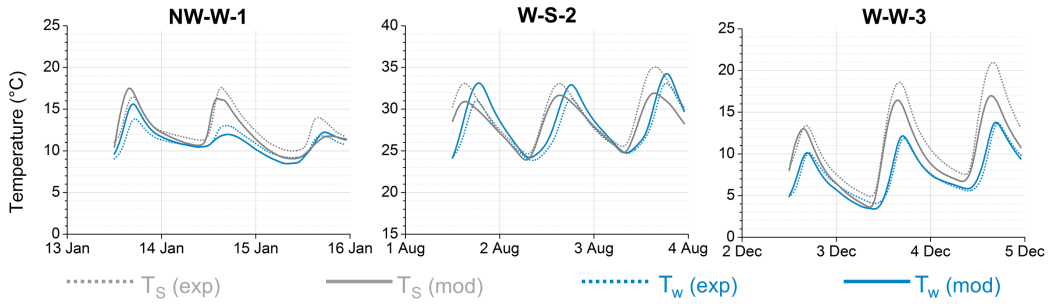

Figure 4.18: Temperature evolution in the wall, at 10 cm from the external surface, for the two orientations and for three of the selected periods.

ancies in the high temperatures can also be observed and are certainly due to pure thermal calculation, it doesn't cast doubts on the evaluation method of the coefficient.

2.4 Solar influence on incoming thermal fluxes

Both part of the expression of the thermal flux at the external surface of the wall can now be evaluated. The following studies the proportion between each part of this flux (the one due to the surrounding air and the other one to the solar gain), according to the following expression :

$$g_{X_e} = g_{wall,X} + g_{sun,X} = \frac{T_{out} - T_{Xext_{wall}}}{\frac{e}{\lambda} + \frac{1}{h_e}} + \frac{\alpha I_X}{1 + \frac{eh_e}{\lambda}} \tag{4.14}$$

Figure 4.19 and Figure 4.20 display the proportion of each part of the total incoming flux at the external surface of the wall for both orientation and for one period of, respectively, summer and winter.

For all cases, when the sun is risen, the solar gains appear to be much higher than the heat flux due to the surrounding air, until more than ten times higher. The sign of each flux are most of the time opposite : as the wall is often warmer than the surroundings, it releases heat in the air, whereas the solar gains heat the wall. However, during the daylight, the heat losses from the wall are decreasing and even become positive (mostly in summer, west wall): both the sun and surrounding air provide heat to the wall.

Note that a delay can be observed between the maximum/minimum $g_{wall,X}$ and the maximum $g_{sun,X}$. This differences may be related to the cross-referencing of the data from different sources (measurements in the house and at the meteorological station). However, it doesn't prevent the analysis of the results.

2.5 Conclusion

The first part of this chapter pointed out the heat releasing from the wall to the indoor environment during the night, and this lead drove to a deeper study of the

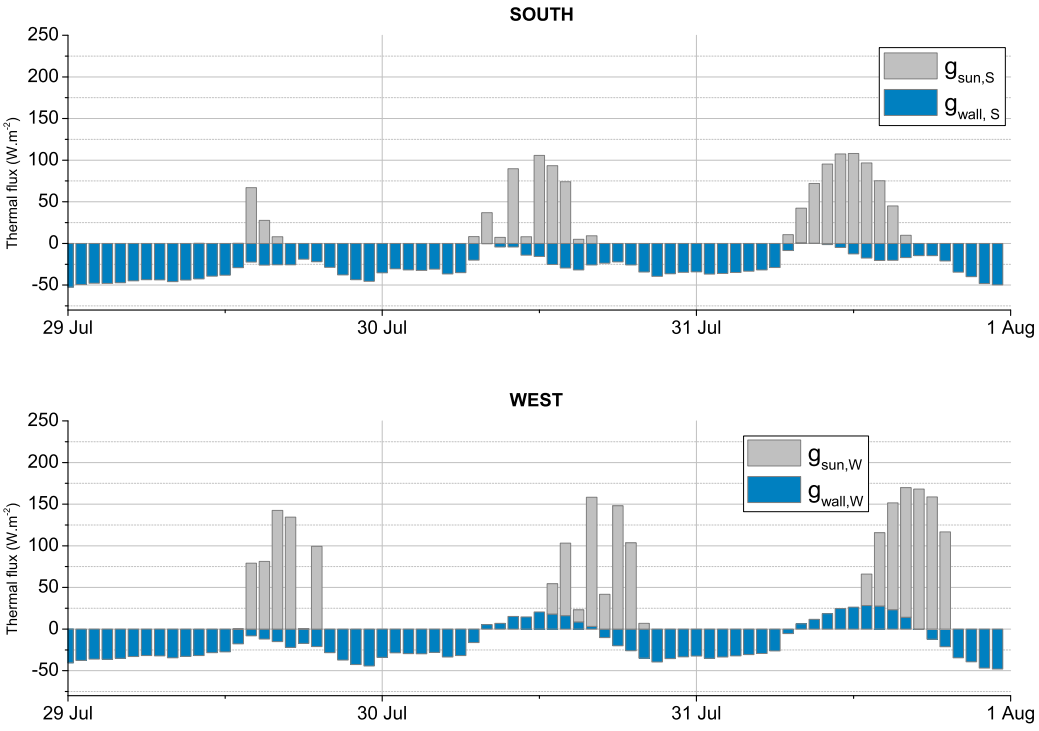

Figure 4.19: Proportion of each part of the total incoming flux at the external surface of the wall for summer, without wind (NW-S-1).

solar gains in the wall. The aim of the previous part was thus to quantify the amount of heat available at the surface of the wall, and the thermal fluxes occurring at the external surface.

This process required to know the thermal exchange coefficients at both internal and external surfaces, which were calculated statistically comparing a basic thermal calculation with the measured temperatures. The results was in good accordance with the recommendations found in the literature.

Secondly, the surface absorption coefficient of the rammed earth used for the house was needed. It was also determined thanks to a comparison between numerical and experimental data. The results were in accordance with measurements carried out in the laboratory.

Finally, the whole thermal flux at the external surface of the wall could be assessed, and the great part played by the sun in the heating of the wall, could be highlighted.

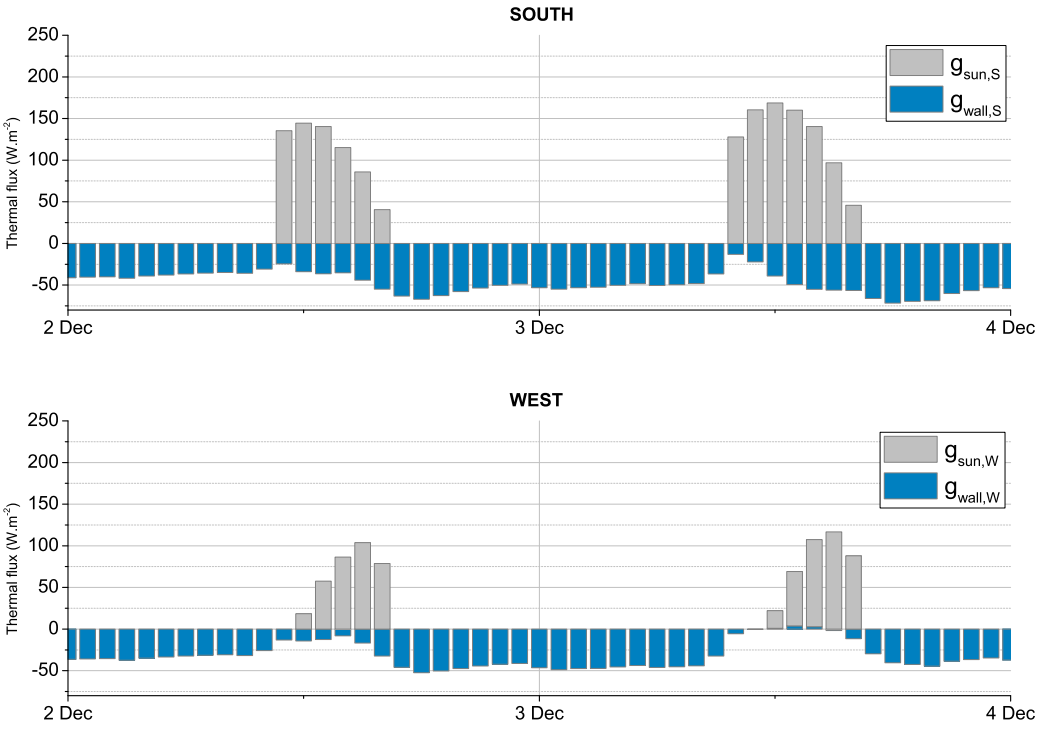

Figure 4.20: Proportion of each part of the total incoming flux at the external surface of the wall for winter, without wind (NW-W-1).

At the moment, the thermal behaviour of buildings is evaluated through the French national thermal standards RT 2012, which follows on the previous RT since 1974 with a clean break in terms of reducing the energy consumption in the building sector.

The RT2012 is applicable to every new constructions and new parts added during a renovation, since January the 1st of 2013. Before regarding one or another part, the standard regulates the energy efficiency of the whole building. It demands performance thresholds through three requirements :

- Bioclimatic design (thanks to the *Bbio* coefficient), which aims at taking advantage of a site and its environment for a naturally more comfortable dwelling for their occupants. It advices for example to maximize the solar gains in winter, to reinforce the thermal mass, to use the natural light,etc...
- Summer comfort (thanks to the *Tic* coefficient) is regulated through a maximal temperature not to be reached after five days of hot weather.
- Primary energy consumption (thanks to the *Cep* coefficient) must remains under 50 $\mathrm{kWh}_{PE}/\mathrm{m}^2$/year. It thus urges to insulated walls with a thicker or a

more efficient insulating material, but also to take care of thermal bridges and air tightness.

Avoiding any calculation, it can easily be noticed that the main points to be worked on in order to improve the energy consumption in the construction sector have been highlighted in the thermal behaviour of rammed earth walls studied in this chapter. Indeed, earthen constructions incite to take advantage of the environment (e.g. using the solar gains) in order to limit the primary energy consumption and offer a good comfort even in summer. Issues professionals have to face thus seems to be related to a misunderstanding or a misreading of the material's behaviour more than to intrinsic flaws of earth constructions.

Chapter 5

Hygric behaviour of rammed earth

Contents

In this part, the passive moisture control of the house will be first investigated, and quantified. In order to provide a better and more specific understanding of the material, experimental measurements in the laboratory are then described, from the common characterization to more specific investigations related to the particular feature of earthen materials.

1 In-situ measurements

The house being monitored since its construction, the hydric state of the wall will first be checked in order to appraise the ability of the house to reduce the variations of relative humidity.

1.1 In-situ water content variation

The monitored house was equipped with TDR sensors, in charge of measuring the water content at three different spots in both western and southern orientation, as explained in Part II, Chap. 1.

The evolution of the water content in the western wall is provided in Figure 5.1, since the construction. The three curves represent measurements in the external, middle, and internal parts of the wall.

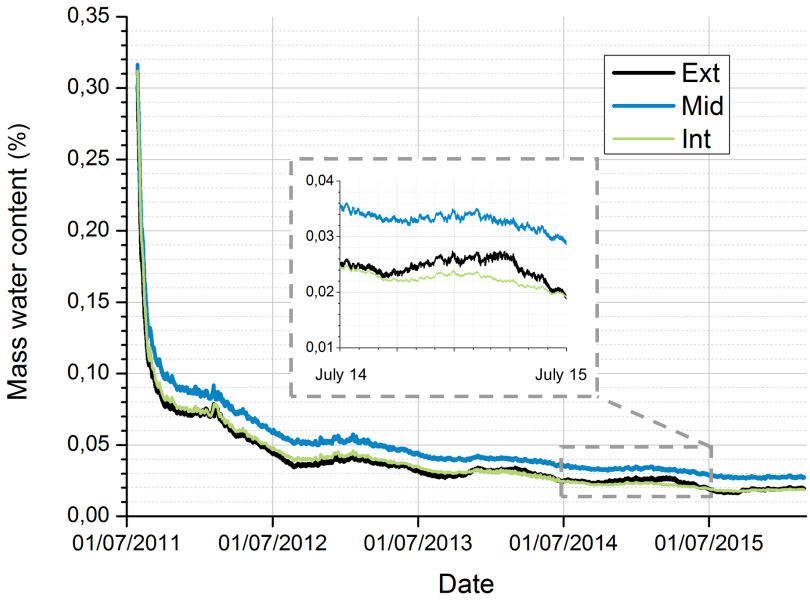

Figure 5.1: Evolution of the mass water content in the western part of the wall of the house in St-Antoine, at three different spots (external, middle, and internal) and a zoom between July 2014 and July 2015.

The first thing that can be noticed is the very high water content of the material just after manufacture : it reaches more than 30% in mass. As a comparison, for a wall of 1m x 2m x 0.5m, i.e. $1m^3$. It means that it is holding around 520 L of water ! Note that the manufacturing moisture content was measured in the soil and estimated at around 18%. However, the sensors were active about 3 weeks after the manufacture, and at that time, as can be observed in Figure 5.1, the water content reached nearly 30%. As the calibration of TDR sensors was deeply studied (see [28]), further investigation is needed on the gravimetric influence of the water content repartition when the material is highly saturated.

The drying is very slow, as it requires about one year to reach its usual hydric state (i.e. a water content around 3-5%), and as, after three months, the water content remains around 10%, which represents around 170 L. It requires around two weeks to divide the water content by 2, one month to divide it by 3 and one year to divided by 10.

After the first year, beside that evolving between 3 and 5 %, the water content seems to vary sinusoidally with the seasons : the water content is higher in winter and lower in summer.

Comparing the different curves, it can be noticed that the middle of the wall seems to dry slightly less quickly than the internal and external part of the wall. This can be imputed to the exchange of relative humidity occurring between the wall and its surrounding, and starting right after the formwork removal.

After its manufacturing, earthen walls can be subject to other events that can significantly increase their water content : moisture accumulation from the environment and rising damps. Indeed, if the wall footings are not high enough, or worse, if a non-permeable insulating material has been added, the moisture is kept inside the wall and the water content increases. As a pathological case, such phenomenon hadn't been recorded on the studied house but collapses of buildings suggest that the water content may have been close to saturation.

1.2 Moisture control in the house

As explained in introduction, the hydric state of the ambient air is a matter of concern for the inhabitants' health and comfort. The following section studies the moisture range of the indoor air and its exchanges with the wall. However, since the wall isn't totally dried, the phenomena described here may certainly be modified in a couple of years.

To avoid any confusion, note that the description of the house detailed in Part II, Chap.1 revealed the presence of a sensor very close to the monitored wall. This set of data is used when dealing with fluxes in/out the wall. However, when dealing with indoor climate, the data from the sensor located in the middle of the living room is used, in order to be more representative of the living conditions. This sensor is referred as "3" in the Figure 3.5.

1.2.1 Study of the indoor environment

The study will focus on the behaviour of the house during one year, from July 2014 to July 2015. The overall relative humidity variations over this period, with a monthly average value, are displayed in Figure 5.2.

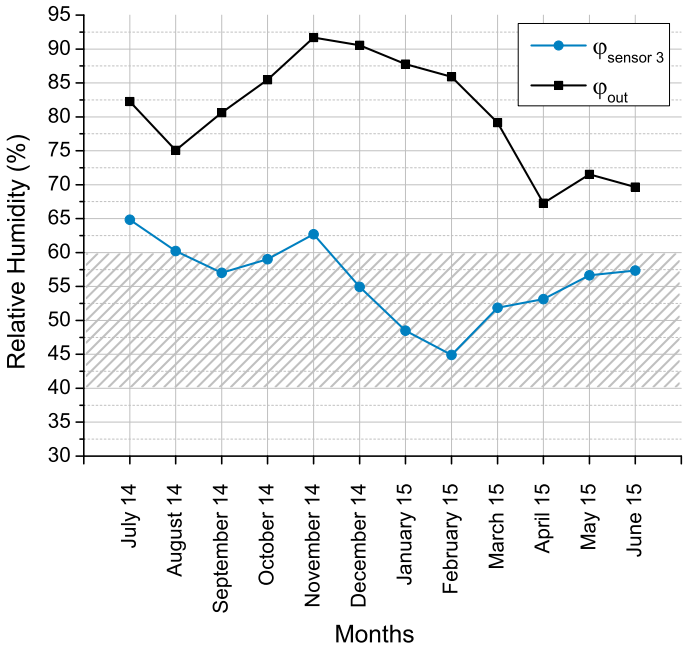

Figure 5.2: Monthly mean value of internal and external relative humidity variations, from July 2014 to June 2015.

The main observation is the large gap between the internal and external mean value of the relative humidity, observable through the year and in particular during cold and humid periods. Indeed, in terms of average values, the relative humidity is reduced up to nearly 40% RH. Note that the lower value of inside relative humidity in February may be due to heating periods.

Regarding the interval of comfort previously introduced, it can be noticed that the monthly mean values come close to the lower limit (the lowest value being around 45%) and go above the upper limit (up to 65%). They remain below 70%, which is acceptable. What's more, when the internal RH goes above 60%, the outside RH is far higher, usually around 90%. To be more precise on the conclusions, the number of hourly values below the lower limit is equal to about 1%. Nearly a third of the measurements seems to be above the 60% limit, but only 3% to the 70% limit, which confirm the previous observation.

Finally, the seasonal repeatability of the RH variations for the outside measurements is clearly visible but is less observable for the inside measurements.

In terms of vapour pressure, the Figure 5.3 displays the internal and external

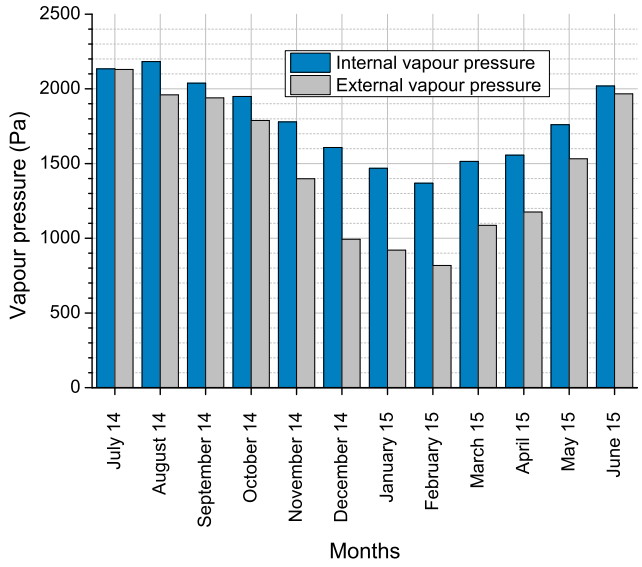

Figure 5.3: Monthly mean value of internal and external vapour pressure, from July 2014 to June 2015.

vapour pressures corresponding to the same period. The difference between internal and external vapour pressure is almost equal to zero in the summer months : the windows are usually open and the indoor and outdoor air are more or less in equilibrium. However, for the cooler periods, the internal vapour pressure is much higher than the external vapour pressure. Here again, the seasonal repeatability of the vapour pressure distribution is visible.

In addition, several standards and classifications concerning hygrometric classes can be found in the literature:

- The French standard NF DTU 20.1 from April 1994 defines four types of premises, based on their value of W/n where W is the produced quantity of water vapour inside a premise, per hour, in g/h; and n the hourly air change rate, in m^3/h. The different classes can be found in Table 5.1.
- The Belgian standard NIT 183 of the CSTC, uses the mean annual internal vapour pressure to classify the premises, which are detailed in Table 5.2.
- At last, the international standard ISO 13788 classifies the building depending on the vapour pressure differences between internal and external environments. The graphical representation can be found in Figure 5.4, and the corresponding classes in Table 5.3.

Regarding the previous classifications, the behaviour of the studied house is as follows :

Hygrometry	**Intervals**
Low hygrometry	$\frac{W}{n} < 2.5 g.m^{-3}$
Medium hygrometry	$2.5 < \frac{W}{n} < 5 g.m^{-3}$
High hygrometry	$5 < \frac{W}{n} < 7.5 g.m^{-3}$
Very high hygrometry	$\frac{W}{n} > 7.5 g.m^{-3}$

Table 5.1: Classification according to NF DTU 20.1.

Classes	**Definition of the premises**	p_v^{int} **(Pa)**
I	Building with a very low water vapour production	$1100 < p_v^{int} < 1165$
II	Well ventilated building with a limited water vapour production	$1165 < p_v^{int} < 1370$
III	Very used buildings	$1370 < p_v^{int} < 1500$
IV	Building with a high water vapour production	$1500 < p_v^{int} < 3000$

Table 5.2: Classification according to NIT 183 of the CSTC.

Hygrometry classes	**Building types**
1	Storage area
2	Offices, shops
3	Dwellings with a low occupation rate
4	Dwellings with a high occupation rate (gymnasium, canteen, ...)
5	Specials buildings (swimming pool, laundry,...)

Table 5.3: Classification according to ISO 13788.

- Considering the mean value of three different months of the cold season (November 14, December 14 and January 15), the respective values of W/n are 1.9, 4.2, and 3.6 (mean being 3.2). The house can thus be classified in "medium hygrometry".
- Requiring a mean value over a year, only one pressure is considered and, from July 14 to July 15, the annual internal vapour pressure is equal to 1784 Pa. The house thus fits to the category "Building with a high water vapour production".
- Finally, the repartition of the difference of vapour pressure between internal and external environments, against the external temperature is displayed in Figure 5.4. It can be noticed that, when the house wasn't closed (the walls were built but the windows and doors weren't in place), the building was classified as a "storage area", whereas afterwards it reaches other classifications, to end around the class 4.

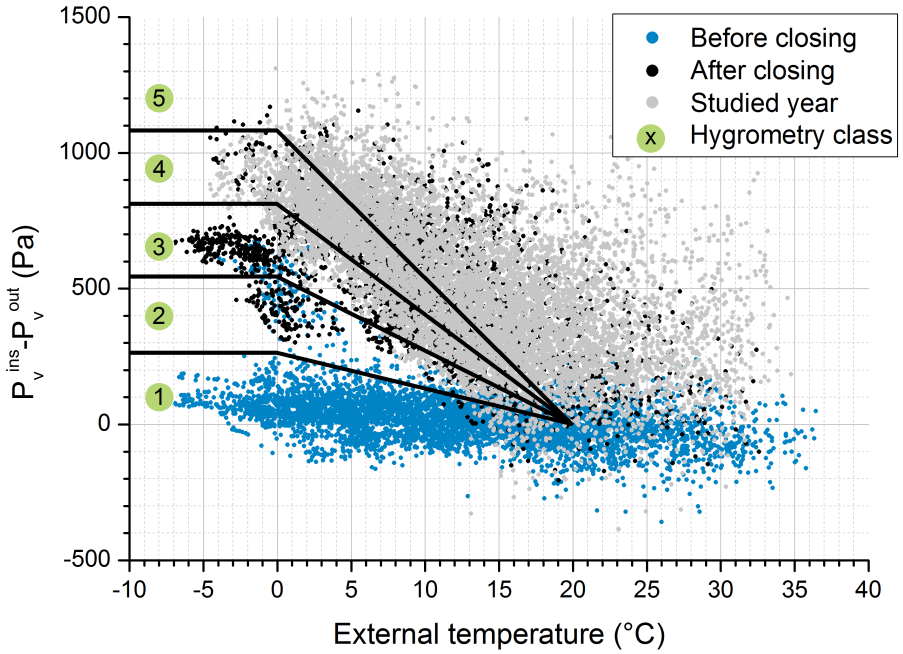

Figure 5.4: Internal moisture production variation against temperature; data from the house and normative hygrometry classes.

All these observations tend to classify the studied house as a rather humid building. The hygric initial state of the wall or low air change can be at stake for these observations. To be more precise on the exchanges between the wall and the indoor environment, the following section deals with the water vapour transfers from the wall.

1.2.2 Water vapour transfer and storage in the walls

The previous investigation focuses on the moisture variations at building level, whereas the following will focus on what's happening at material scale. This part will deal with the water vapour fluxes occurring from the wall to the inside environment.

To avoid any confusion, Figure 5.5 sets the sign convention for the water vapour fluxes : positive fluxes are gain for the indoor environment whereas negative fluxes are loss of water vapour.

At first approximation, considering a steady state and taking into account that the sensor is located at 10 cm from the surface, the water vapour flux is calculated

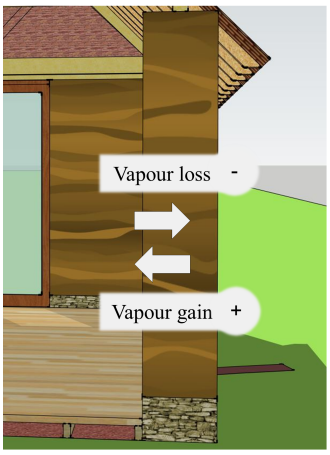

Figure 5.5: Sign convention for water vapour fluxes.

thanks to the following formula :

$$g_{\varphi,gain} = \left(\frac{e}{\delta_p} + \frac{1}{\beta_i}\right)^{-1} (p_v^{sat}(T_{X,int_{wall}})\varphi_{X,int_{wall}} - p_v^{sat}(T_{ins})\varphi_{ins}) \tag{5.1}$$

with:

φ_{ins} [-]: RH inside the house, near the wall

T_{ins} [°C]: temperature inside the house, near the wall

$\varphi_{Xint_{wall}}$ [-]: RH inside the wall, (here at 10 cm from the internal surface)

X : S for the southern wall and W for the western wall

β_i [kg.m^{-2}.s^{-1}.Pa^{-1}]: water vapour transfer coefficient for indoor surface, taken equal to 25.10^{-9} according to [89].

p_v^{sat} [Pa] : saturation vapour pressure, at a given temperature

δ_p [kg.m^{-1}.s^{-1}.Pa^{-1}] : water vapour permeability, equal to $2{,}10^{-11}$ according to [28].

Figure 5.6 displays the flux variation at the western internal surfaces of the wall, during the whole selected year, and a zoom for two weeks of winter and summer.

Several observations can be made on the first graph of Figure 5.6. First, it can also be noticed that the seasonal variation observed in Figures 5.2 and 5.3 is also present in the flux variation : the moisture flux is maximum in summer and minimum in winter, when the vapour pressure in the indoor environment becomes lower the for the outdoor environment. Even if 92% of hourly measurements lead to a positive flux, the flux becomes negative in winter. Indeed, the vapour pressure inside the wall decreases to become closer to the indoor vapour pressure, and even becomes lower, which creates a vapour flux from the indoor environment to the wall. Looking more precisely at Figure 5.6b, it can be noticed that the negative vapour flux mostly occurs in the afternoon and the phenomenon can also be observed in summer (see Figure 5.6c) with the alternation of maximum and minimum fluxes.

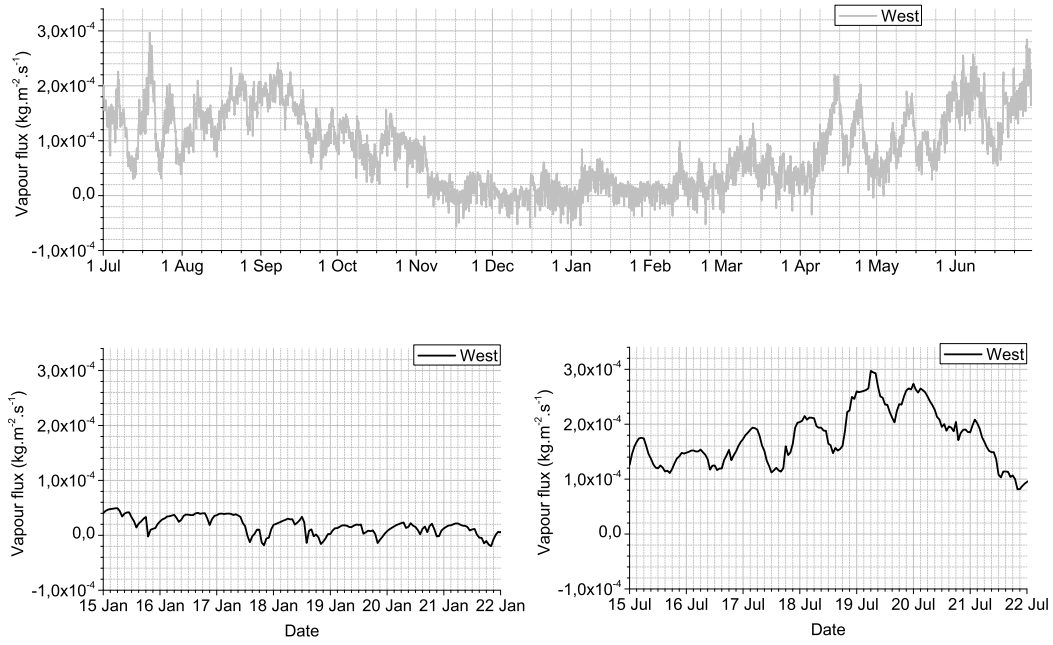

Figure 5.6: Flux variation for the western part of the wall, (a) from June 2013 to June 2014 ; (b) For two weeks resp. in winter and summer.

On the other hand, it can also be questioned whether the measurement of relative humidity at 10 cm from the wall surface is providing all the needed information regarding the vapour regulation of the wall. To carry out a deeper investigation, the data collected inside the wall and at its surface are compared in Figure 5.7 in terms of relative humidity and vapour pressure. First, the relative humidity variations are almost constant in the wall whereas daily fluctuations are observable in the indoor environment : the regulation seems to occur within the 10 first centimetres. Note that the same variations are measured in term of water content (with another sensor) which attests to the validity of the data. In terms of vapour pressure, on the contrary, the daily variations are almost as important inside the wall than for the indoor environment, and given the previous observation on relative humidity, they are likely to be due to the thermal variations. Indeed, the heat seems to travels quicker in the wall than the water vapour. Note that the previous explanation concerning the sign evolution of the vapour flux can be validated looking at the variation of the differences in vapour pressure between winter and summer.

The previous observations are instructive in terms of moisture control of the house, assessed both thanks to indoor climate and moisture fluxes in the wall. However, they remain incomplete regarding the evaluation of the moisture buffering capacity of the wall, as it seems to occur mainly in the first centimetres of the surface, i.e.

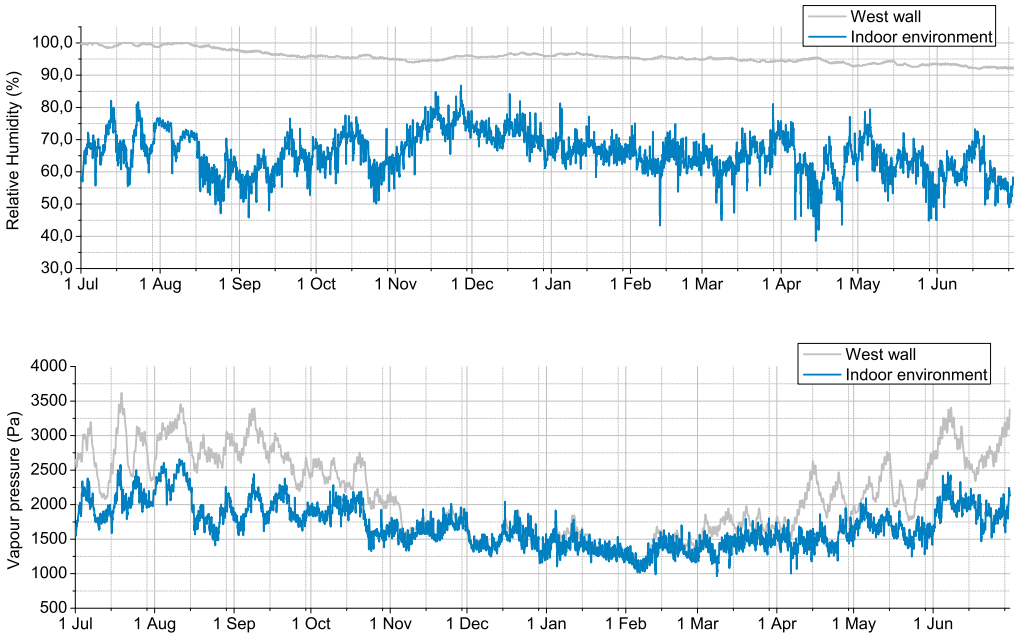

Figure 5.7: Vapour pressure and relative humidity variation for the western part of the wall from June 2013 to June 2014.

before the first sensor placed at 10 cm. What's more, the initial hydric state of the wall certainly has an influence of the rather important moisture flux from the wall to the indoor environment. To complete this investigation, the following section of the chapter focuses on the laboratory parameters, well-established in building physics, to measure the behaviour of the earthen material regarding moisture.

2 Laboratory measurements

As explained before, the moisture content of the material induces different types of moisture transport, from vapour transfer to liquid absorption. These different phenomena can be characterized by several parameters, enabling a comparison between building materials. The following part describes the most common among them and the value taken for earthen materials.

2.1 Laboratory characterisation of the water vapour storage and transfer in the material

In the hygroscopic domain, the porous media is partially saturated and the water vapour can be adsorbed and transferred in the material. The different coefficients detailed in this section aim at characterizing the different aspects of water vapour storage and transfer :

- the sorption/desorption isotherm describes how the water molecules are adsorbed by the solid skeleton of the porous material, when submitted to different atmosphere with various relative humidity.
- the water vapour permeability evaluates how a material allows itself to be crossed by a water vapour flux.

Also, the moisture buffering value is a dynamic test which quantifies how the material is able to breathe, i.e. how much moisture it is able to store, and at what speed it is able to release it when the surrounding atmosphere changes.

2.1.1 Sorption and desorption

A hygroscopic material has the ability to absorb and store moisture from the surrounding air. In order to face a relative humidity change and maintain the equilibrium, the material absorbs or desorbs moisture thanks to the vapour partial pressure difference. Among building materials, great variations in terms of hygroscopicity is recorded between the materials.

Sorption/desorption isotherms are usually used to characterise the hygroscopic behaviour of materials. It establishes the relationship between the moisture content in the material against the relative humidity of the environment in contact with it, at a given temperature.

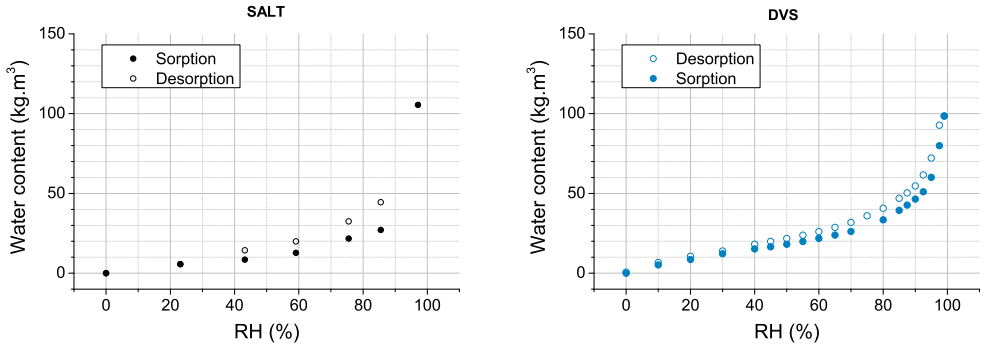

Figure 5.8: Sorption and desorption isotherms with saline solutions (measured by P-A. Chabriac) and a DVS (measured by F. McGregor), at 20°C, from [28].

The sorption/desorption isotherm, depending on the relative humidity, defines different domains :

- The hygroscopic domain ranges from the dry state to about 95%RH. This domain is the most common one for on-site building materials.
- The capillary domain ranges from about 95%RH to the free water saturation.
- The supersaturated region, where there is no more air in the pores nor equilibrium state, and which can not be reached by normal suction. Because, in

this domain, the gravity forces prevail over capillary forces, the domain is also called "gravimetric domain".

The sorption/desorption isotherm is compound of two curves, one for the sorption, and another one for the desorption. This reveals the existence of a hysteresis effect between sorption and desorption, which is more or less important depending on the materials. The importance of sorption-desorption hysteresis on sorption isotherms has been pointed out for many building materials, such as wood [25][117][159], hemp concrete [94][113], concrete [46], and even for papers and books [47].

Regarding experimental measurements on earthen materials found in the literature [28][30][72][103], as well as as can be seen in Figure 5.8, the hysteresis appears to be much lower than other building materials cited above. That is the reason why, it is often called the "sorption isotherm" and even the "sorption curve". Consequently, the impact of the hysteresis isn't taken into account in the model details further in the manuscript.

Figure 5.9 displays the variations with RH of ξ defined as the slope of the sorption/desorption isotherms, i.e. $\partial w_L/\partial\varphi$. It can here also be observed that the value of both slopes are very close to each other, what confirms the previous observations.

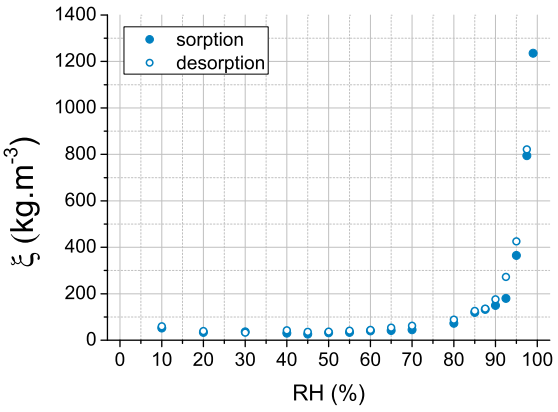

Figure 5.9: Variation with RH of the liquid capacity ξ equal to $\partial w_L/\partial\varphi$, for sorption and desorption isotherms.

The sorption/desorption isotherm of the studied earth material was measured by Chabriac in [28]. It was realized with a use of saline solutions until free water saturation. The sorption isotherm was also determined with a DVS by McGregor in [103]. A good agreement was found between the two methods. Both curves are gathered in Figure 5.8.

However, the measurement of sorption-desorption curves through salt solutions or gravimetric dynamic sorption analysers at relative humidity higher than 95% is usually inaccurate. In addition, these methods cannot reach the saturated state, and the point RH=100% must be obtained theoretically (calculated from the porosity).

Consequently, the use of the sole sorption-desorption curve leads to high uncertainties in the range between 95% and 100% of relative humidity.

Therefore, to complement information, further measurements were carried out using a different experimental technique. They are based on the suction (or capillary pressure), which is the difference between the atmospheric and the liquid pressure, and which is denoted by S. The relation between the capillary pressure and the water content can be measured through different methods, more or less accurate for different types of soils and pressure ranges. The document [44] provides a good overview of the common methods:

- The most spread technique, the *tensiometric measurement* consists in measuring the negative pressure of liquid water using a thin saturated porous stone. The range of practical application is for pressures between 0 and 80 kPa.

- In *psychrometric measurements*, the relative humidity is measured close to the interstitial water of the non-saturated soil, from which is deduced the suction thanks to the Kelvin law. The relative humidity is calculated through the dew point temperature of the considered atmosphere. It is a quite sophisticated method and remains unusual. The pressures thus determined don't exceed 7 MPa.

- *Filter paper* method is a simple and convenient method to measure suction as it only requires a 1/10 000e weighting scale. It consists in using a filter paper whose retention curve was determined before, putting it in a sample and waiting for equilibrium between the filter paper and the soil. After extraction, knowing the water content of the paper, and its retention curve, it leads to the suction of the soil. Depending on which type of filter paper is used, several calibration curves can be found in the literature[14] [20][21][110].

This last method was chosen and the practical protocol is described in the standard [14]. The link between the suction curves (water content in function of suction) and the sorption curves (water content in function of relative humidity) is eventually made through the Kelvin's law (chemical equilibrium between liquid water and its vapour):

$$S = p_0 - p_L = -\frac{\rho_l RT}{M_{H_2O}} ln\varphi \tag{5.2}$$

with:
p_0 [Pa] : atmospheric pressure
R [J.mol^{-1}.K^{-1}] : perfect gas constant
M_{H_2O} [kg.mol^{-1}] : molar mass of water molecules
φ [-] : relative humidity

The suction of the soil was determined for different moisture contents, and, thanks to the calibration curve of the filter paper, the retention curve of the soil could

be deduced (the detailed method and results can be found in Appendix B). Both measurements can be found in Figure 5.10.

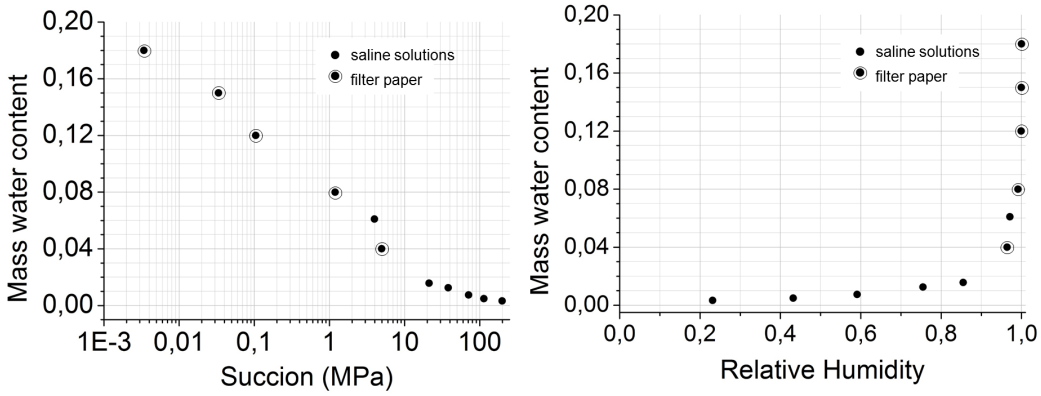

Figure 5.10: Final retention curve and sorption isotherm at 20°C.

A good correlation can be observed between the "saline solution" data and the one measured with the filter paper. It then appears that these two methods complement one another to describe the behaviour of the soil in both hygroscopic and capillary domains.

2.1.2 Water vapour permeability

The water vapour permeability is the measure of the amount of water vapour able to pass through a porous material. Its measurement is well documented and can be found in an international standard EN ISO 12572:2001.

The water vapour permeability δ_p is defined as the mass of vapour transferred through the specimen per second and per unit area. The measurement is made weighting a sample placed between environments with two different relative humidity until equilibrium. Depending on these relative humidity, the test is called "dry cup" or "wet cup".

The water vapour permeability gives access to the water vapour resistance factor μ, which is the ratio between the water vapour permeabilities of the material and the one of the air. This coefficient is the most spread, and Table 5.4 provides the values of this coefficient for different building materials.

The water vapour permeability and thus the water vapor resistance factor was measured on the studied earth by P-A; Chabriac, using the standard protocol and reported in [28]. The values are gathered in Table 5.5.

Earthen materials can thus be considered as rather permeable materials.

Note that the difference between the two relative humidity are slight as the reliability and repetability of this experimentale set-up have been pointed out by many authors [51][122][125][142].

μ-value	Dry cup	Wet cup
Cellular concrete	7.7	7.1
Lime silica brick	27	18
Solid brick	9.5	8
Gypsum board	8.3	7.3
Concrete	260	210
Lime plaster	7.3	6.4

Table 5.4: Water vapour resistance factor for different building materials, from [89].

μ-value	3.3-43.2%	3.3-75.5%
Water vapour resistance factor	10.6	9.4

Table 5.5: Water vapour resistance factor for the studied material, from [28].

2.1.3 Moisture Buffering value

The moisture buffering of envelopes has been measured and studied for decades. However, the need of scientific tools to characterise this absorption of moisture peaked in 2003 when the Nordtest project [121] was launched with the aim of determining a protocol for moisture buffering, and the definition of the coefficient "Moisture Buffering Value" (MBV). It indicates "the amount of moisture transported in or out of a material, per open surface area, during a certain period of time, when subjected to variations in the relative humidity of the surrounding air" [121]. The unit of MBV is kg.m^{-2}.%RH^{-1}, and calculated as follows :

$$MBV = \frac{\Delta m}{A \cdot \Delta \%RH} \tag{5.3}$$

with:
Δm [kg] : mass difference of the sample
A [m^2]: open surface area
ΔRH [%] : variation of moisture levels

Experimentally, it follows a cycle of 8h of high relative humidity and a cycle of 16h of low relative humidity. The MBV thus depends on the boundary conditions. The MBV values can be classified using five different categories, gathered in Table 5.6. The Nordtest report also provides MBV values for common construction materials and are reported in Table 5.7.

Regarding the studied material, the MBV was measured by F. McGregor between 50 and 85% at 23°C and in a climatic chamber where the air velocity was arounr 0.6 m.s^{-1}. The measurements on 3 samples are gathered in Figure 5.11. The mean value of the MBV for this soil is 1.6, which belongs to the category "Good". Note that various earthen materials were tested in [103] and the values varied between 1.5 and 2.5.

Classes	Minimum	Maximum
Negligible	0	0.2
Limited	0.2	0.5
Moderate	0.5	1.0
Good	1.0	2.0
Excellent	2.0	...

Table 5.6: Classification of materials using practical MBV.

Material	MBV 33-75%	Class
Spruce boards	1.16	Good
Concrete	0.38	Limited
Gypsum	0.64	Moderate
Laminated wood	0.46	Limited
Concrete aggregate with stucco	0.76	Moderate
Cellular concrete	1.04	Good
Brick	0.48	Limited

Table 5.7: Practical MBV between 33-75%RH for different building materials.

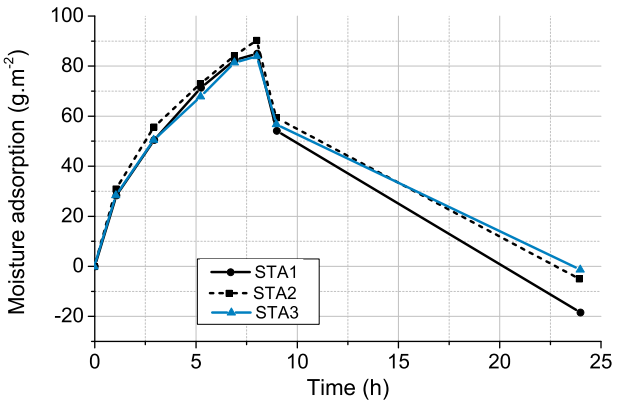

Figure 5.11: Moisture variations for three samples for the MBV measurement, from [103].

2.2 Liquid water absorption in rammed earth samples

In this section, the behaviour of liquid water in the material is focused on, and more precisely on the ability of the material to absorb liquid water, which constitutes a important aspect of moisture storage and transfer to obtain a complete characterization.

2.2.1 Literature review on the protocol

The protocol of measurement is provided by the European standard [6] [133]. Its calculation is illustrated Figure 5.12. The standard deals with masonry mortar but the same procedure can be applied to other porous materials. The A-value is measured on prismatic samples of 0.80 x 0.40 x 0.40 m^3, initially dry, and submerged in 5 to 10 mm of water for 90 minutes. Samples are weighted after 10 and 90 minutes and the absorption speed is deduced. The water level has to be constant during the measure and the sample shouldn't stand directly on the bottom of the tank but on wedges so that the whole lower surface can be in contact with water.

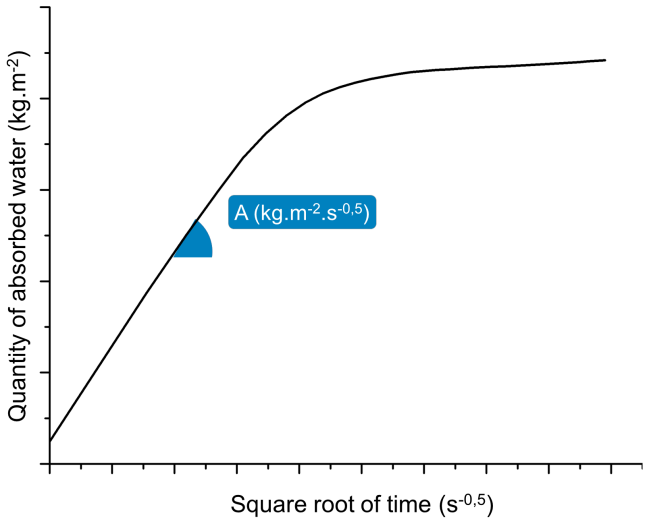

Figure 5.12: Calculation of the liquid absorption coefficient A.

The British standard BS 3921 deals with measuring the capillary suction of water in building materials, and explains the specifications of the Initial Rate of Suction (IRS) test. The test is to be done on dry samples and weightings every minute during 5 min. However, some instructions aren't suitable for earthen materials. Hall [73] suggested another method, based on the standard. The measurement is made on cube samples of 10 cm. The samples are weighted at 1, 2, 3, 4, 5, 10, 20, 30, 40 and 60 min.

The study described in [120] consists in measuring the A-value for 15 clay brick samples. The sample are cylindrical with a diameter of 20 cm and between 1,5 and 2 cm thick. Each sample laid on a 1 cm thick paper saturated with distilled water at 20°C, put in a closed vessels to reach saturation conditions. Samples were weighted after 10, 20, 30 minutes and 1, 4, 6, 24, 48 and 72 hours.

In [28], the A-value, was determined according to the method described by Krus & Holm [88] and Hall [73] with the adaptation of the BS-3921 standard to rammed earth. Indeed, some precautions need to be taken regarding the sensitivity of earth to water. In his PhD, Chabriac measured the A-value on compacted earth blocks of

0.295 x 0.14 x 0.10 m^3. The samples were weighted every 5 minutes for about one hour.

Finally, many publications deal with the free water uptake experiment on different materials, one even presents an inter-laboratory investigation in order to point out the reliability of the method [56][89], [124][123]. A recent publication [64] studies the impact of stabilizers (lime, concrete) on the water transport properties.

2.2.2 Material and methods

The main characteristics of the soil were detailed in Part II, Chap. 1. Given the range of density variation measured on the wallet, it has been decided to work on samples with different densities between 1.5 and 1.8.

Samples preparation :

The experimental investigation was carried out in two phases: the first one studied the variation of the A-value with the density, whereas the second one the influence of the boundary conditions.

- First campaign

The shape of the sample was chosen with a penetration surface wide enough in order to enable the rising damp phenomenon. The Proctor type samples were prepared, cylinders with a diameter of 10 cm and a height of approximately 6 cm. In these conditions, the penetration surface (bottom of the cylinder) was 7.85 cm^2. In order to obtain the sample as homogeneous as possible, the soil was compacted in one layer. The preparation of the samples is illustrated in Figure 5.13.

Samples with different densities, all in the studied range, are investigated. The characteristics of the 12 samples are reported in Table 5.8.

Name	S1	S2	S3	S4	S5	S6	S7	S8	S9	S10	S11	S12
Density	1.44	1.47	1.53	1.57	1.58	1.59	1.62	1.65	1.67	1.67	1.68	1.71
T [°C]	23.3	24.1	24.6	23.5	25.0	25.3	25.8	24.2	24.0	29.5	24.5	29.5
RH [%]	47	44	40	42	39	39	38	54	53	44	55	44

Table 5.8: Sample recap for the first campaign.

The aim of this task is to measure the rising of water by capillarity. To ensure a one dimensional transport of liquid water, the lateral surfaces of the samples were sealed with paraffin and foil, as can be seen in Figure 5.14. Note that the foil is going from the top of the sample to 3-5mm before the bottom, so that no water is absorbed between the paraffin and the foil.

- Second campaign

For the second campaign, the cylindrical samples were realized with a hydraulic press to ensure a better repeatability. Their dimensions were 6 cm high with a

Figure 5.13: Making the samples.

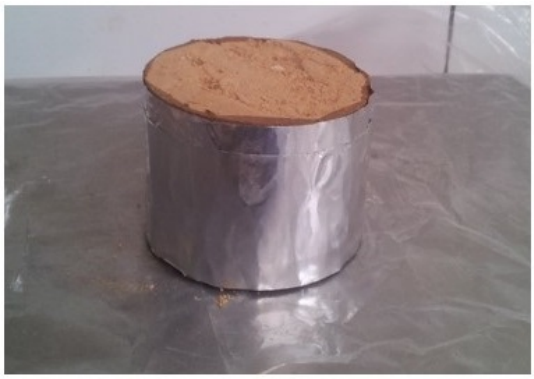

Figure 5.14: Sealing the lateral faces with paraffin and foil.

circular base of 10 cm for diameter. The manufacturing water content was 18% and the samples were dried at 50°C in an oven just after manufacture. Before testing, they were left an hour in a regulated room so that the equilibrium in temperature could be reached.

The expected density was 1.6. However, the 10 samples were manufactured on two different days and slight differences appeared in the samples: the dry masses were 0.761 kg and 0.777 kg, which resulted in two densities, respectively of 1.61 and 1.64. These two categories are from now named "batch 1" and "batch 2".

Three boundary conditions, named as cases a, b, and c, were chosen:

- Case a : the sample is left as it is, with a free boundary on the lateral surfaces and on the top
- Case b: the lateral surfaces of the sample are covered with foil, the top is a free boundary
- Case c : the lateral surfaces and the top are covered with foil

The chosen case for each sample is reported in Table 6.2.

Batch	**Batch 1**					**Batch 2**				
Name	a.1	a.2	a.3	b.4	b.5	b.6	b.10	c.7	c.8	c.9
Density	1.61					1.64				
Porosity	0.547	0.547	0.547	0.547	0.464	0.464	0.464	0.547	0.481	0.481
BC	a	a	a	b	b	b	b	c	c	c

Table 5.9: Samples recap for the second campaign.

Protocol of the absorption test :

The device used for the measurement of liquid absorption coefficient was composed by a tank filled with water and a grid on wedges. Tea filter papers were added between the sample and the grid so that the tiny particles of earth didn't go in the water as the sample was becoming wet, as described in [28]. The samples were put on the grid and the grid on the water. After a certain time (shorter periods of time in the beginning and increasing), the grid was taken off and weighted. Care was taken not to keep water on the grid that wasn't absorbed by the sample, and the grid was wiped out carefully when necessary. After the weighting (happening within 30 seconds), the grid was put back on the edges and the capillary absorption could go on.

Questions have been raised concerning the time to be considered. Several references ([5][68]) highlight the fact that the weighting operation has to be done as quick as possible. However, the time considered was strictly the time during which the sample was absorbing water, i.e. every weighting times were deleted from the whole time measurement.

For the first campaign, the tests were realized in a room where none the relative humidity nor the temperate were controlled, whereas for the second campaign, the room was regulated in temperature. To ensure a better understanding of the results, the temperature and relative humidity were measured with a USB sensor (EL-USB-2, Lascar electronics, Salisbury, UK).

2.2.3 Experimental results and discussion

As announced before, the experimental part of the study is divided into two tasks: liquid absorption measurements for samples with varying densities, and for three types of boundary conditions.

Variation with the density - First campaign

- Cinematic of the rising water

The experiment enabled to measure the total amount of water absorbed in the sample divided by the surface area, against the square root of time. The cinematic of the rising water was measured and is synthesized in Figure 5.15. In order to enable a better reading of the results, the 12 samples are separated into two groups, respectively for lower and higher densities.

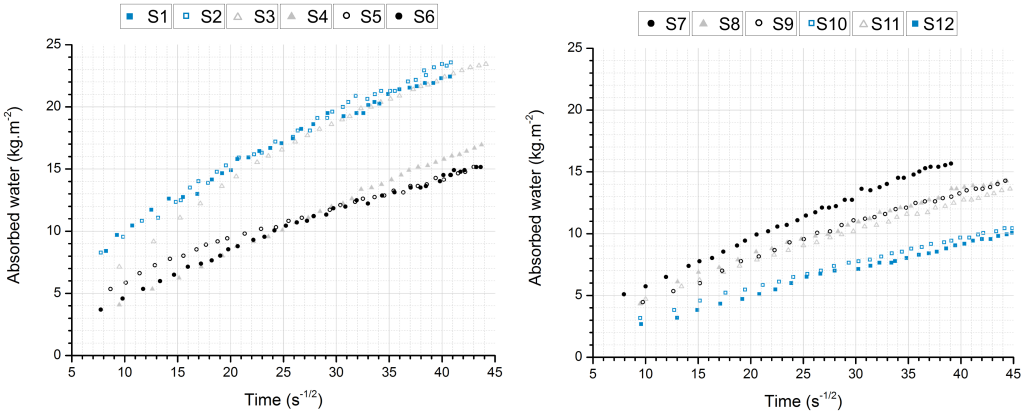

Figure 5.15: Comparaison of the samples with density <1.6 and >1.6.

The linear regression for each case provides the A-value (slope) and the R^2. The Table 5.10 provides the A-value for every samples.

Name	S1	S2	S3	S4	S5	S6	S7	S8	S9	S10	S11	S12
Density	1.44	1.47	1.53	1.57	1.58	1.59	1.62	1.65	1.67	1.67	1.68	1.71
A	0.41	0.44	0.44	0.38	0.26	0.31	0.35	0.27	0.28	0.20	0.25	0.21

Table 5.10: Sample recap of the first campaign.

For all cases, the linearity of the relation between the two parameters represented (absorbed water per surface unit and square root of time) can be noticed. Observing a straight line (R^2 always above 0.97), the liquid water absorption coefficient, which is the slope of this line, could be deduced without any trouble.

In the case of lower density (below 1.6), a good repeatability of the measurement can be observed. A first batch (S1, S2) and a second (S5,S6) can easily be distinguished and both repeatability and density influences can be observed. On the other hand, the sample S4 seems to behave like the batch (S5,S6), whereas the sample S3 absorbs water at a medium speed. When looking at the density, this repartition is logical.

In the case of higher densities (above 1.6), the same type of results can be observed: the batch (S10,S12) on one side, and batch (S8,S9,S11) on the other side.

Regarding the sample S7, it seems to be closer to the batch (S5,S6) from the first graph. Indeed, their densities are very close (1.62 against 1.58-1.59).

However, looking at the density, it could have been expected that samples S9 and S10 would absorbed the same amount of water with time, but they aren't : the differences in the relative humidity of the environment during the measure can be an explanation. In the second campaign, the influence of the boundary conditions is studied more in detail.

The influence of the boundary conditions developed in the second campaign is studying this more in detail.

In all cases, the slight heterogeneity of the samples may explain differences in the repeatability of the results.

- Link with density

At last, the relationship between the density and the A-value for the 12 samples is gathered in Figure 5.16.

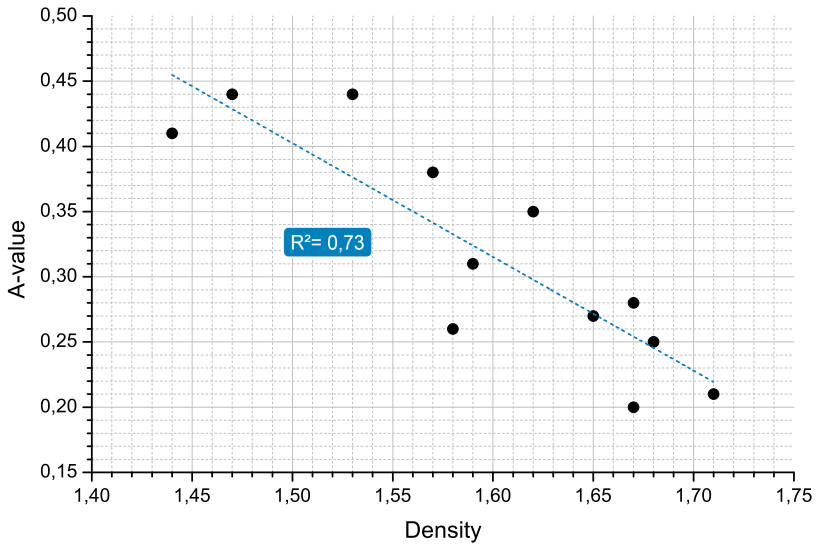

Figure 5.16: Comparison of A-value for different densities and for the 12 samples.

It seems that the A-value decreases as the density increases, which is quite intuitive, and reported in the literature (e.g.[73]). What's more, there seems to be a linear correlation between the density and the A-value, with a correlation coefficient equal to 0.73.

The important variation of the absorption capacity of the soil depending on the density, given that the density is usually heterogeneous in the walls, should be considered as it can have mechanical consequences.

Variation with boundary conditions - Second campaign

Regarding the second campaign, the whole cinematic can be found in Figure 5.17. The Table 5.11 provides the A value for every samples of the second campaign, depending on the boundary conditions. Finally, the Figure 5.18 gathers and compares the A-value between the three boundary condition cases.

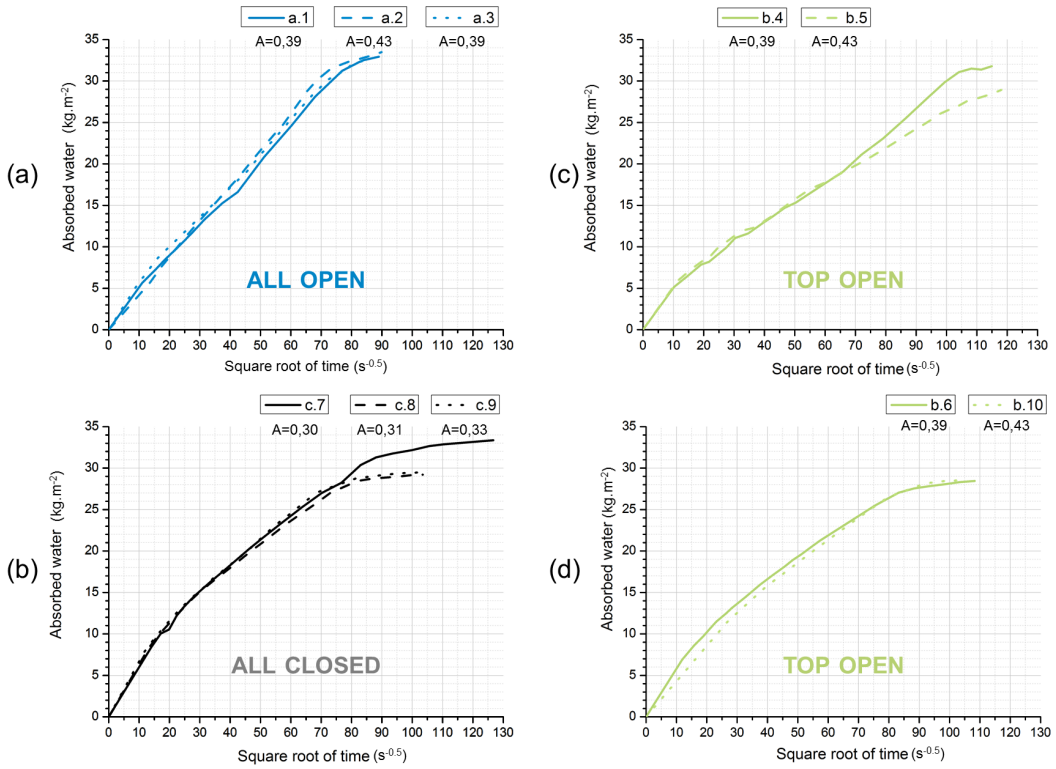

Figure 5.17: Comparison of samples with different boundary conditions (second campaign).

Batch	**Batch 1**					**Batch 2**				
Name	a.1	a.2	a.3	b.4	b.5	b.6	b.10	c.7	c.8	c.9
A-value	0.39	0.43	0.39	0.27	0.23	0.28	0.28	0.30	0.31	0.33
R^2	0.998	0.999	0.999	0.996	0.997	0.990	0.998	0.991	0.993	0.997
BC	a	a	a	b	b	b	b	c	c	c

Table 5.11: Samples recap for the second campaign.

The main observation that can be made is the very good repeatability of the results. Indeed, curves are almost overlaid and the standard deviation is always below 2 and even reaches zero.

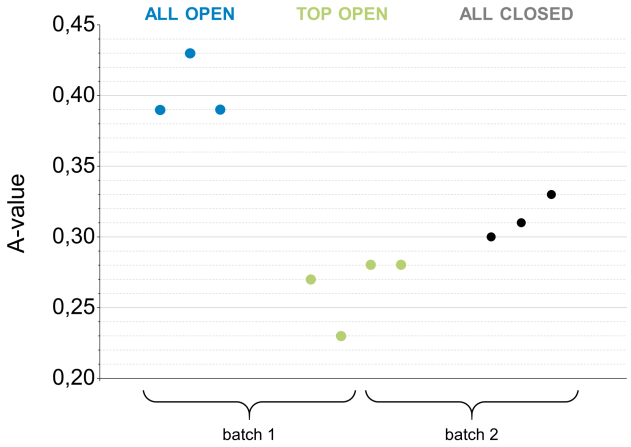

Figure 5.18: Comparison of samples with different boundary conditions (second campaign).

However, different saturation levels can be observed in the last moments of the measurements, and this even if the behaviour of the two samples was exactly the same during several hours. The main explanation can be the heterogeneity of the samples, despite all care that was taken. Indeed, an over-compaction on the top of the sample can result from a single side compaction. This also leads to a slight difference in porosity, as it has been reported in Table 6.2.

Differences between batch 1 and batch 2 can also be observed when comparing the absorption speed for the case b. This behaviour can be attributed to the measure uncertainty given the very slight difference in density.

Looking at Figure 5.18, it remains unclear why the "all open" case leads to higher speed for moisture ingress despite the surface evaporation that should be more important in this case. A plausible explanation can be a swelling of the sample that enables a larger amount of water to be absorbed, or a caption of water molecules in the ambient air (measured around 50%). Whatever, the experimental process is not to reconsidered, give the very good repeatability of the test.

The study of the available data on the house provided a good confidence on the regulation of relative humidity, even if the moisture buffering couldn't properly be highlighted. On the contrary, laboratories measurements provided precious information on how the material behave in contact with moisture, for different saturations and both for transfer and storage. The behaviour could also be evaluated on pathological cases such as rising damps.

Chapter 6

Hygrothermal behaviour of rammed earth

Contents

The two previous chapters precisely described the thermal and hygric behaviour of rammed earth at different scales, and thanks to several characterization parameters. The following section first studies the impact of the presence of moisture on the thermal parameters, as well as the impact of temperature on hygric parameters. Secondly, this hygrothermal coupling is measured experimentally, and more precisely the temperature evolution due to evaporation/condensation of the water vapour is measured during moisture ingress.

1 Temperature/moisture variations of key parameters

The walls are subjected to strong thermal and hydric gradients leading to migration of liquid water and water vapour at different temperatures. A synthetic representation of the coupling between thermal and hydrodynamic processes is reported in Figure 6.1, where φ stands for the relative humidity, T for the temperature, and p_v^{sat} for the equilibrium vapour pressure.

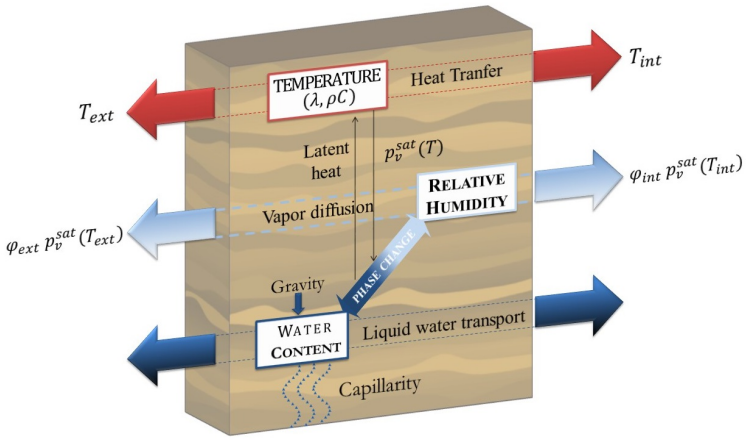

Figure 6.1: Schematic representation of the heat and moisture transfers within an earth wall.

1.1 Thermal parameters

1.1.1 Thermal conductivity

The thermal conductivity represents the heat quantity conducted under a temperature gradient of 1 K, per surface and time units. When the material is dry, the thermal conductivity is the ability to conduct heat of the solid skeleton. However, when the material is wet, at different moisture saturations, the total thermal conductivity takes into account the solid skeleton and the water in its different phases.

It thus appears natural to measure a thermal conductivity varying with the moisture content.

The measurements on the earth of St Antoine was made by Chabriac, and is detailed in [28]. The thermal conductivity was measured on compressed earth blocks (CEB) of 30 x 14 x 10 cm^3 just after manufacture (when its water content was equal to 19% in mass), and after a drying period of 48 h, which resulted in a water content equal to 17%. To ensure the homogeneity of water content within the samples, they were wrapped in a sealed plastic film at least 48 h at constant temperature before each measurements of the thermal conductivity. The values are gathered in Table 6.1.

Mass water content %	Thermal conductivity $W.m^{-1}.K^{-1}$	Method
19 %	2.4	CEB just after manufacturing
17%	2.1	after 48 h of drying
0%	0.6	totally dried

Table 6.1: Thermal conductivity on CEB for different moisture contents.

The evolution of the thermal conductivity with water content is linear, as it has been stated by many authors on other earth materials [28][71][72].

In [93], a formulation of the thermal conductivity's variation with the water content is developed:

$$\lambda_{moist} = \lambda_{dry} \cdot \left(1 + \frac{C w_L}{\lambda_{dry}}\right) \tag{6.1}$$

with:
C [-] : a constant dependant of the soil

It is also advised to consider a increasing of 20% of the dry value as a plausible estimation of the thermal conductivity for a current hygric state (excluding thus the saturated state after manufacture).

To be accurate, the influence of the moisture on the thermal conductivity has to be taken into account. Indeed, taking the studied soil as example, the thermal conductivity increases by 30% between a dried state and a water content of 2% and by 75% between a dried state and a water content of 5%.

1.1.2 Heat capacity

The heat capacity is the amount of heat needed to raise the temperature of a system by one degree, and usually expressed in $J.m^{-3}.K^{-1}$. A porous material is the superposition of a solid skeleton and a porous network partially saturated by liquid water, and a gaseous phase composed by an ideal mixture of dried air and water vapour. The average heat capacity of the material (more preciselly the product ρC_p) is the addition of the heat capacity of each component, proportionality to their mass concentration. Numerical formulation is developed in the third part of the thesis but

the experiemental evidence of this common relationship was provided in [93], and the variation is displayed in Figure 6.2.

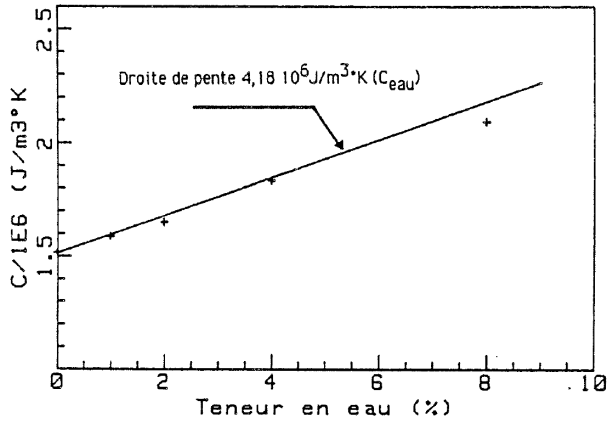

Figure 6.2: Evolution of the heat capacity ρC_p of earthern material at 20°C, from [93].

The influence of the saturation of the material on the capacity of the wall to store heat is not negligible. For example, for the studied material, the numerical formulation reveals that the heat capacity increases by about 40% between the dry state and a water content of 2% in mass.

Note that, in this section, the influence of temperature on the thermal parameters hasn't been investigated, as only a slight modification was pointed out by J-P. Laurent in [93].

1.2 Sorption isotherms

The influence of temperature on the sorption isotherm has been studied for many building materials and is most of the time non-negligible. However, the investigation has never been realized for earthen materials.

The Figure 6.3a displays the sorption isotherm for earthen material at two different temperatures 23°C and 0°C, and no significant variation can be observed. The similarity is even more remarkable in Figure 6.3b where the moisture capacity (i.e. the slope of the sorption isotherm) is displayed. As a consequence, the variation of temperature on the moisture content at a given relative humidity will be disregarding in the modelling part of this work.

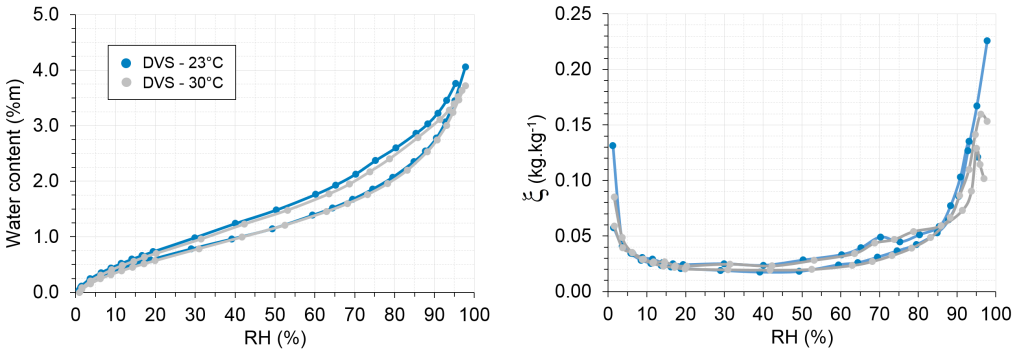

Figure 6.3: Sorption isotherms at 23°C and 40°C, and the corresponding moisture capacity.

2 Measuring the hygrothermal coupling on rammed earth samples

Experimental set-up has already been described in the previous chapter, concerning the liquid water ingress in rammed earth samples. This revealed differences in water uptake between different types of boundary conditions, and suggested the non-negligible impact of evaporation / condensation phenomena on the lateral surface. Surface temperature measurements, thanks to a thermographic camera, ensured and the set-up appeared to provide a good medium for laboratory measurements of hygrothermal couplings.

2.1 Material and methods

Material and samples used in this section are the ones described in the second campaign of the previous chapter. For the record, the liquid absorption coefficient was measured on 10 samples with three different boundary conditions (see Figure 6.4):

- Case a : the sample is left as it is, with a free boundary on the lateral surfaces and on the top
- Case b: the lateral surfaces of the sample are covered with foil, the top is a free boundary
- Case c : the lateral surfaces and the top are covered with foil

The recap of the samples' characteristics are provided in Table 6.2.

The thermographic measurements are realized thanks to a FLIR camera, and images treatment through the software Altair. The camera was placed at about 1 m from the sample and the time step of caption was 1 min. A point of reference was added in the top of the sample (with foil), aligned to the camera axis in order to make the image analysis easier. Indeed, the samples being cylinders, the surface

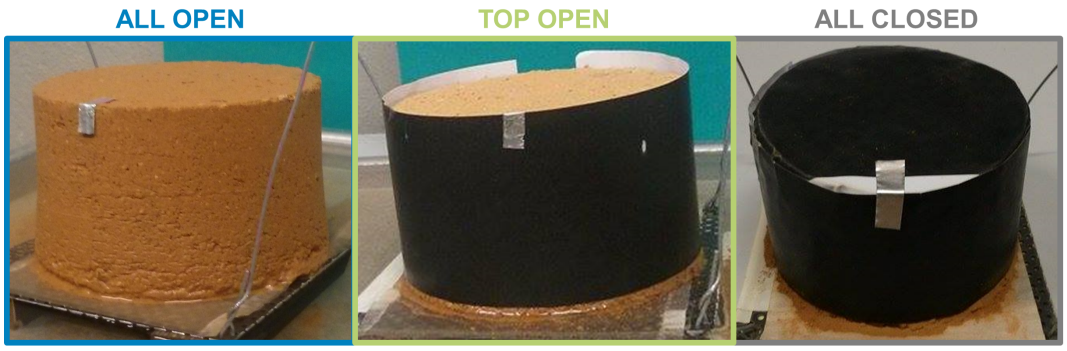

Figure 6.4: Photographies of the three boundary conditions.

Batch	**Batch 1**					**Batch 2**				
Name	a.1	a.2	a.3	b.4	b.5	b.6	b.10	c.7	c.8	c.9
Density	1.61					1.64				
Porosity	0.547	0.547	0.547	0.547	0.464	0.464	0.464	0.547	0.481	0.481
BC	a	a	a	b	b	b	b	c	c	c

Table 6.2: Samples recap for the second campaign.

wasn't plane and side effects could appear. The temperature extracted was the vertical repartition along the sample and aligned with this point.

The camera measures the radiated power by the surface's sample and requires the emissivity of the material to calculate the temperature. The calculation follows the Stefan-Boltzmann law as:

$$\sigma = \sigma_0 \varepsilon T^4 \tag{6.2}$$

with :
σ [W.m^{-2}] : energy radiated per unit surface area and per time unit
σ_0 [W.m^{-2}] : Stefan-Boltzmann constant, equal to 5.67.10^{-8}
ε [-] : emissivity of the surface
T [K] : surface temperature

The emissivity for brown material is usually around 0.9 [86], and equal to 1 for black surfaces. Given a certain uncertainty, the impact of this assumption is quantified later.

2.2 Results and discussions

Figure 6.5 illustrates the water intake in the sample a.1 at different times, as well as the corresponding images of the thermographic camera. The different saturation states are well identifiable on the photographies and the temperature variations seems to follow the moisture progression in the sample. Note that the phenomenon is also visible on other cases of boundary conditions, even if it is more difficult to notice the saturation variation on the photographies.

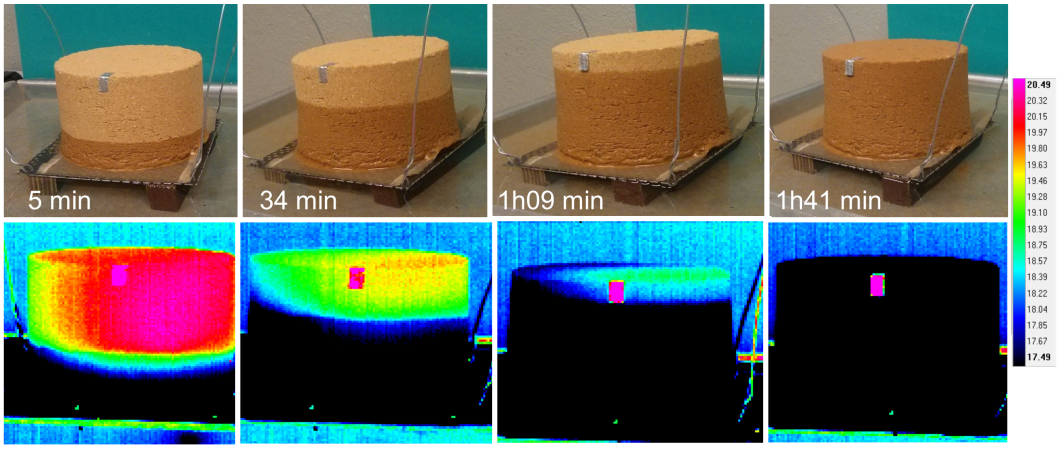

Figure 6.5: Thermographic measurements and photography of moisture ingress for sample a.1.

It is now reasonable to question the impact of the colour change of the sample with the increase of moisture content, on the emissivity of the material, and thus if the temperature front observable with the thermographic camera do represents a temperature change. Two temperatures were deduced from the energy radiated measured by the camera, one for an emissivity of 0.95 and the other of 0.85. The absolute difference between these two temperatures, divided by two, is displayed in dot lines in Figure 6.6a. The other curve represents the standard deviation of temperature measurements on the three samples of case a (a.1, a.2 and a.3). What can be noticed is that both uncertainties are of the same order of magnitude, and that the assumption on the emissivity of the material doesn't have a greater impact on the results than the experimental errors. The same approach is followed in Figure 6.6b but between 0.95 and 1, being the emissivity of the black surface. The same conclusions can also be drawn.

The surface temperature measurements now considered as reliable, the different boundary conditions can be compared. The surface temperature was measured every minute and some of them are used to illustrate the difference of heat propagation in the sample over time for the three types of boundary conditions (see Figure 6.7).

Three different evolutions of temperature are clearly noticeable, even if the rising of the front reveals a similar process. Indeed, the moisture ingress led to several stages of temperature variations. In the initial state, the surface temperature of the sample is 20°C, and the water 16°C. A first stage can be observed with the upper part of the sample remaining at its initial temperature, whereas a straight line is drawn between the water at 16°C and the front of moisture at 20°C. This stage lasts until the front of moisture reaches the top of the sample, and the latter reaches saturation. The second stage is a decreasing of surface temperature in the whole height, until it reaches equilibrium at 16°C. Theses stages are easier to distinguish in the "All open" case as the surface temperature variations are more important for not being covered.

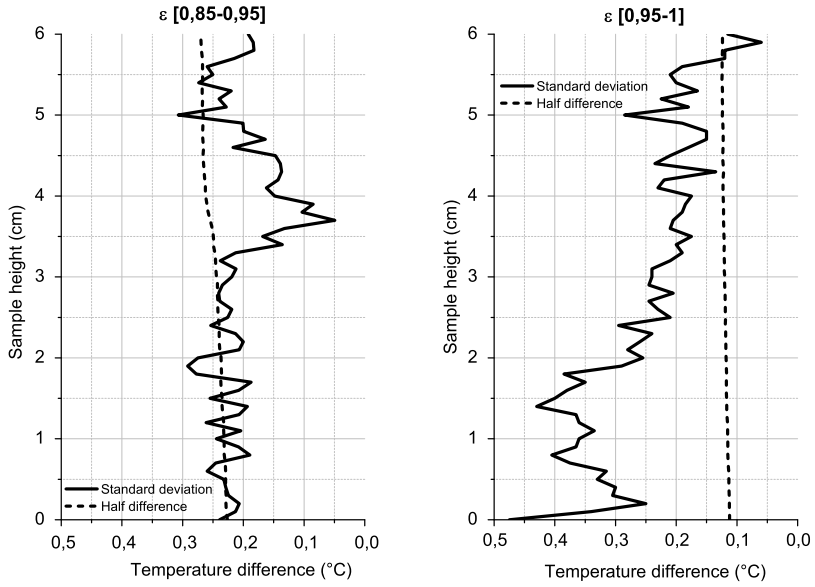

Figure 6.6: Quantification of the impact of emissivity uncertainty, for the "earth" and "black" surfaces.

On the contrary, the last stage hasn't been clearly reached for the case "All closed", even after 3h50 of immersion. The data being treated after the experimentation, this stage has unfortunately not been recorded.

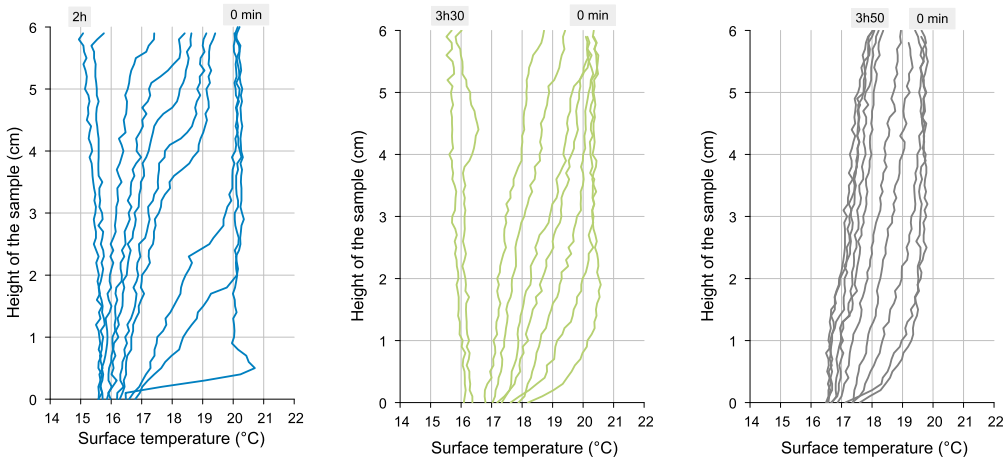

Figure 6.7: Surface temperature of the samples for the three boundary conditions during all moisture ingress process.

The results are also displayed with a focus on the temperature profiles after 10 min, 40 min and 2 hours, and more precisely on the temperature differences at those

times, in comparison with the initial state (see Figure 6.8). This enables a better comprehension of the evaporation/condensation phenomena. Standard deviation between the three samples in each case is also added.

As expected, the stages dealt with in the previous paragraph can also be observed with this representation. Positive temperature differences illustrate surface condensation whereas negative is an evaporation phenomenon. In the "all open case", during the first stage previously mentioned, condensation can be observed above the moisture front, whereas evaporation occurs below the moisture front. The evaporation process is easily understandable as the material is saturated, liquid water tends to leave the sample transforming into water vapour, thank to convection near the surface. Once the moisture front has reached the top of the sample, only evaporation occurs until the end. Regarding the other cases, the condensation at the early times seems to be of the same order of magnitude, whereas the surface evaporation is less important than for the case "all open", as the lateral surfaces were covered. The evaporation seems also to be lower in the case "all closed" than for "top open".

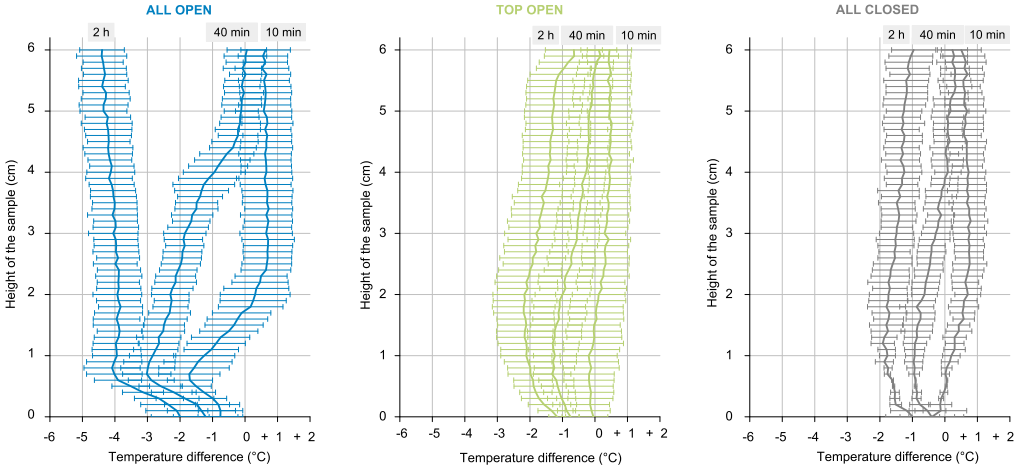

Figure 6.8: Surface temperature of the samples for the three boundary conditions - temperature difference with the initial state.

2.3 Absorbed water and surface temperature variations

The main objective of this section is to connect the differences between the three boundary conditions in terms of moisture ingress, with their respective surface temperature variation and the corresponding quantity of water vapour evaporated/created by condensation. The calculation described isn't exhaustive but enable a first evaluation of the link between these two phenomena.

2.3.1 Comparison of "all closed" and "top open" boundary conditions

These two types of boundary conditions were tested on samples from the same batch (batch 2). The moisture ingress of two samples among these categories (samples b.6 and c.7) are recalled in Figure 6.9, as well as the difference between them (named "calculated diff.").

In order to assess the quantity of water evaporated through the upper surface of the sample when open, the classical thermal balance equation is used (see Part III, Chap; 1 for more details on the formulation):

$$\rho_X C_p \frac{\Delta T_X}{\Delta t} = \lambda \nabla T_X - \dot{m}_X L \tag{6.3}$$

with :
$\Delta t = t - t_0$
$\Delta T_X = T_X(t) - T_X(t_0)$

The difference of mass of vapour evaporated through the upper surface between the two cases is calculated by subtraction of the thermal balance of each case at the same time. This assumes that the difference of saturation doesn't have any impact on the conduction of temperature, and is the same for the two boundary conditions. It also assumes that the temperature difference measured on the surface is homogeneous in a horizontal plan of the sample. The following formula is then used :

$$\dot{m_c} - \dot{m_{b2}} = \int_h \frac{\rho_{bat.2} C_p}{L \Delta t} \cdot (\Delta T_{b2} - \Delta T_c) \tag{6.4}$$

At each recorded time step, the integral along the height is calculated and reported in the previous graph in Figure 6.9 where it is designated by "measured diff.".

It can be observed that the evolution of the water quantity is the same for the two calculation methods, even if a small difference remains. Indeed, at the beginning, the water quantity deduced from the temperatures is lower than the one weighted. After about 10 minutes, the trend is reversed and the water quantity difference is more important when calculated from the surface temperature. However, given the precision of the calculation, only the order of magnitude is the matter of concern.

2.3.2 Comparison of "all open" and "top open" boundary conditions

Following the same method, the boundary conditions "all open" and "top open" are compared, through the samples a.1 and b.4. The moisture ingress of each case, as well as their difference and the deduced evaporated water vapour are gathered in Figure 6.10.

In this case, the difference of water quantity weighted is always higher than the one deduced from the surface temperatures. The same pattern is followed, i.e. the difference is always increasing, but the gap between the two methods is larger than in the comparison of the previous samples. In the case of "all open", the amount of absorbed water is larger than expected and surface evaporation can't explain alone the

differences between the two boundary conditions. Indeed, the differences in evaporating processes lead to differences in saturation and thus influence the moisture ingress. These two phenomena are coupled and this first approximation is less reliable in this case.

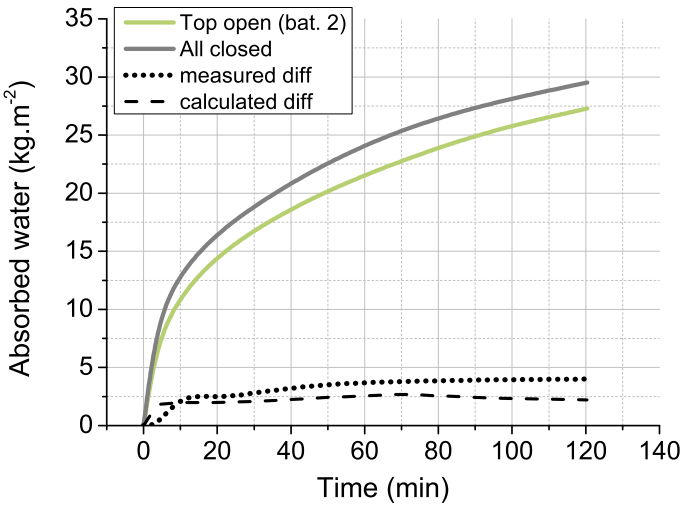

Figure 6.9: Comparison of moisture ingress between the different boundary conditions ("all closed" and "top open (bat. 2)").

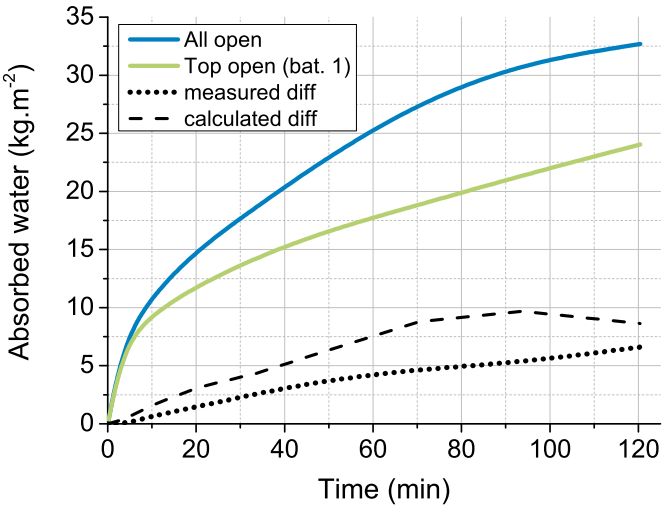

Figure 6.10: Comparison of moisture ingress between the different boundary conditions ("all open" and 'top open (bat.1)").

To sum up, thermographic camera appears to be an appropriate tool for measuring water phase change on surface due to its high sensitivity.

The surface temperature thus measured was correlated with the weight gain measured, and thus to the moisture intake in the samples.

Three different boundary conditions were investigated and the differences on the surface temperature could be measured and linked to the quantity of evaporated water thanks to an approximated calculation.

Conclusion of Part II

This part gathers the experimental evaluation of the earthen material studied, both at building and material levels. The thermal evaluation of the house enabled to highlight its good energy performance and the importance of the solar radiation. On the contrary, conclusions are more difficult to draw on the moisture buffering. However, laboratory measurements showed promising results for the moisture regulation. Finally, the hygrothermal coupling was highlighted on samples, and further investigation on the data collected on-site may also produce interesting results.

Beside experimental measurements, whether on-site or in laboratory, the development of numerical tools is an essential part of the global study, as they are what remains, once the validation and calibration carried out. The following and last part is focusing on these objectives.

Part III

Hygrothermal modelling of earthen material's behaviour

Chapter 7

Hygrothermal model set-up

Contents

As stated before, heat and moisture storage and transfers are well known phenomena, but their couplings at multiples scales still need to be investigated.

To reach this goal, some authors [66][153] did start from a microscopic scale and reach the macroscopic scale by averaging on a representative volume. This allows a better appraisal of the assumptions required. Others [89][97] [118] adopted a phenomenological approach enabling them to deal with physical problems right from the macroscopic scale. This latter even gave rise to commercially developed softwares [59][67] which can provide reliable results on a wide range of materials and climatic loads.

However, we can wonder whether these models, which are based on simplified transport and storage functions, are able to reproduce with accuracy the hygrothermal behaviour of unconventional materials like earth, when they are submitted to important hygrometry and temperature variations.

The aim of this chapter, and the up-coming, is to provide a coupled model, based on heat and mass balances, which considers separately the kinematics of each phase in interaction with each other. It aims at quantifying the influence of particular assumptions made while deriving the governing equations, and in order to examine their degree of relevance in their application to the study of the hygrothermal behaviour of earthen materials in function of their hydric characteristics.

1 Liquid water vapour equilibrium

The rammed earth is modelled as the superposition of a solid skeleton (S) and a porous network partially saturated by liquid water (L), assumed to be pure. The remaining porous network space is filled by a continuous gaseous phase (G), which is assumed to be an ideal mixture of perfect gases composed of dried air (A) and water vapour (V). The porosity ϕ is defined as the actual volume of porous network per unit of initial volume of rammed earth, while the water saturation ratio S_r, is defined as the actual volume of liquid water per unit of actual porous volume. This latter is linked to the liquid water content ($w_L = m_L/m_S$, where m_L and m_S are respectively the liquid and skeleton masses per unit of rammed earth volume), through:

$$S_r = w_L \frac{\rho_d}{\phi \rho_L} \tag{7.1}$$

with:
S_r [-] : saturation ratio
w_L [kg.kg^{-1}] : liquid mass water content
ϕ [-] : porosity
ρ_d [kg.m^{-3}] : density of the dried earthen material
ρ_L [kg.m^{-3}] : liquid water density

Note that the water content can also be defined as the total mass of water (liquid and vapour) per unit of skeleton mass ($w = (m_L + m_V)/m_S$). However, since

$m_V \ll m_L$, the difference between the two definitions remains of third order. In the following, the use of w_L is preferred because it allows a direct link between the saturation ratio and the water content.

The proportion of dry air (A) and water vapour (V) within the gaseous phase (G) is quantified by their mass concentration ρ_I, where I=A,V, defined as:

$$\rho_I = \frac{m_I}{(1 - S_r)\phi} \quad ; \quad \rho_G = \sum_{I=A,V} \rho_I \tag{7.2}$$

with:

m_I [kg.m^{-3}] : mass of I=A,V per unit of representative elementary volume of rammed earth

ρ_G [kg.m^{-3}] : density of the gaseous mixture

Finally, an exchange of matter can occur between phases L and V, due to the condensation of water vapour and the evaporation of liquid water.

A schematic representation of the porous medium is reported in Figure 7.1.

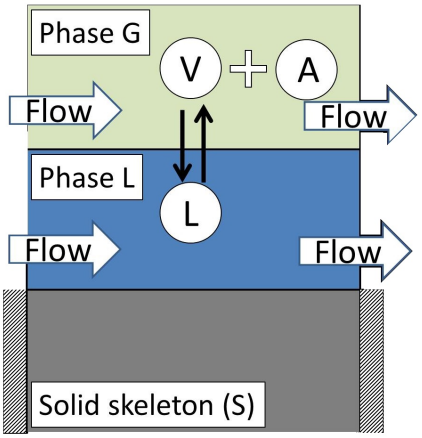

Figure 7.1: Schematic representation of the different phases considered in the model and their interactions.

A decrease (resp. increase) of water content in the porous network leads to an increase (resp. decrease) of the liquid/air interface curvature. The latter is commonly assumed to be close to the inverse of the entry radius of the pores where the evaporation (resp. condensation) process occurs. It leads to a variation of the capillary pressure (or suction) defined as:

$$p_G - p_L = \gamma_{LG} C_{LG} = f(w_L) \tag{7.3}$$

with:

γ_{LG} [N.m^{-1}] : interfacial tension between the liquid water and the air

C_{LG} [m^{-1}] : curvature of the interface

p_G [Pa] : gas pressure
p_L [Pa] : liquid water pressure
$f(w_L)$: a decreasing function of the liquid water content that depends on the porous network characteristics of the material.

According to this definition, a decrease in liquid water content leads to a decrease in liquid pressure at constant air pressure. As a consequence, the local equilibrium between in-pore confined liquid water (L) and its vapour (V) is modified, and the partial pressure of vapour within the wet air in equilibrium with the liquid water is no more equal to the saturated vapour pressure. Assuming that the total pressure of the gaseous phase p_G remains constant, this modification is expressed through the celebrated Kelvin's Law, which comes from the local equality of the specific free enthalpy of these two phases at the vicinity of their interface [41]:

$$p_G - p_L = -\frac{\rho_L RT}{M_{H_2O}} \ln \varphi \tag{7.4}$$

with :
M_{H_2O} [kg.mol^{-1}] : molar mass of water
R [J.mol^{-1}.K^{-1}] : perfect gas constant
T [K] : temperature
φ [-]: relative humidity, defined as:

$$\varphi = \frac{p_V}{p_v^{sat}} \tag{7.5}$$

with:
p_V [Pa] : partial pressure of vapour within the gaseous phase
p_V^{sat} [Pa] : saturated vapour pressure at the current temperature

Under the small perturbation assumption, this latter can be estimated by [41]:

$$p_v^{sat} = p_v^{sat}(T_{ref}) \exp\left\{\frac{M_{H_2O}}{RT}\left[\frac{L_{ref}}{T_{ref}}\Delta T + (C_{p,V} - C_{p,L}) \cdot \left(T \ln\left(\frac{T}{T_{ref}}\right) - \Delta T\right)\right]\right\} \tag{7.6}$$

with:
$\Delta T = T - T_{ref}$
L_{ref} [J.kg^{-1}] : latent heat of evaporation/condensation at T_{ref} and $p_G = p_L = 1$ bar
$C_{p,V}$ [J.kg^{-1}.K^{-1}] : vapour specific heat at constant pressure
$C_{p,L}$ [J.kg^{-1}.K^{-1}] : liquid specific heat at constant pressure

For water at $T_{ref} = 373$ K, $L_{ref} = 2.26.10^6$ J.kg^{-1} and $p_V^{sat}(T_{ref}) = 1$ bar [41].
The formulation of the equilibrium water vapour pressure used in the model was developped in [41], but many formulations are also commonly used. Another one

wide spread, more simple, is derived from the Clausius-Clapeyron equation :

$$p_v^{sat}(T) = p_v^{sat}(T_{ref}) \cdot \exp\left[\frac{M_{H_2O} L_{ref}}{R}\left(\frac{1}{T_{ref}} - \frac{1}{T}\right)\right] \tag{7.7}$$

integrated at 20°C, i.e. for T_{ref} = 293.15 K, $P_v^{sat}(T_{ref})$ = 0.23393 bar and L_{ref} = 24535 kJ.kg^{-1}, according to [75]. From the same experimental data base, the integration of the Clausius-Clapeyron equation at each temperature step leads to empirical expression of the equilibrium water vapour pressure given in [155]:

For $273.15 \leq T < 333.15K$:

$$p_v^{sat}(T) = 3.1848 \cdot 10^{13}\left(\frac{T}{273.15}\right)^{-4.8341} \exp\left(\frac{-24.6775x273.15}{T}\right) \tag{7.8}$$

For $333.15 \leq T$:

$$p_v^{sat}(T) = 1.1400 \cdot 10^{14}\left(\frac{T}{273.15}\right)^{-11.612} \exp\left(\frac{-28.7908x273.15}{T} + 2.8235\frac{T}{273.15}\right) \tag{7.9}$$

Other empirical formulations can be found in the literature (e.g. [76]) for different ranges of temperature variations. The majority of them appears with the form :

$$P_v^{sat}(T) = \exp\left(a - \frac{b}{T - c}\right) \tag{7.10}$$

where a, b, and c are parameters.

Figure 7.2 gathers and compares three of those formulations between 0°C and 100°C.

Differentiation of the Kelvin Law and the vapour pressure then leads to the two following equations:

$$dp_L = \frac{\rho_L RT}{M_{H_2O}} d\ln\varphi + \frac{\rho_L R \ln\varphi}{M_{H_2O}} dT \tag{7.11}$$

$$dp_V = p_v^{sat}(T) d\varphi + \varphi \frac{dp_v^{sat}}{dT} dT$$

The combination between eqs.(7.3) and (7.4) underlines that the water content of a material is linked, at constant temperature and at equilibrium, to the relative humidity of the surrounding air. This link is different for each tested material and was experimentally determined through sorption and desorption tests (see Part II, Chap 3).

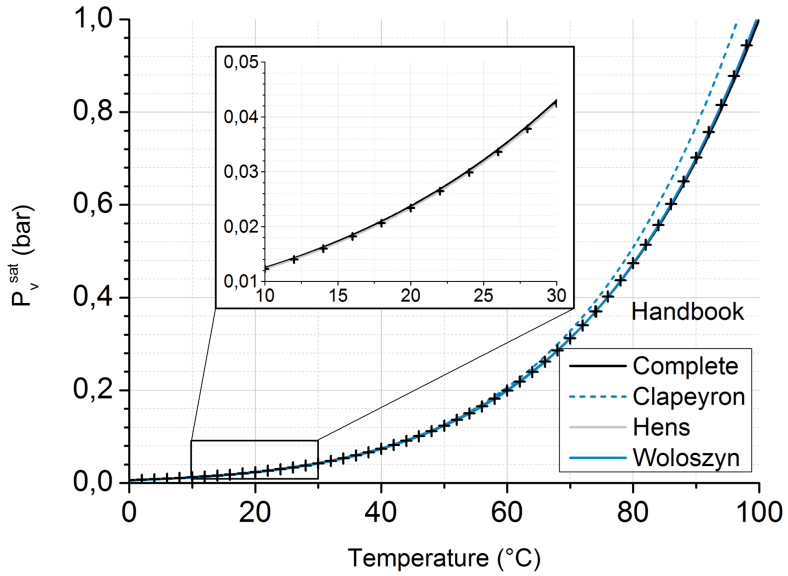

Figure 7.2: Variations of the saturation vapour pressure for temperatures between 0 and 100°C, according to different formulations.

2 Water continuity equation

2.1 Water vapour mass balance

Assuming no air flow within the porous network, the mass conservation of water vapour reads:

$$\frac{\partial m_V}{\partial t} = -\underline{\nabla} \cdot (\rho_V \phi_G (\underline{V_V} - \underline{V_G})) + \dot{m}_{\to V} \tag{7.12}$$

with:

$\dot{m}_{\to V}$ [kg.m^{-3}.s^{-1}] : rate of vapour mass production due to evaporation/condensation processes

$\underline{V_V}$ [m.s^{-1}] : relative velocity of the water vapour in the porous media

$\underline{V_G}$ [m.s^{-1}] : relative velocity of the gaseous phase in the porous media

The term $\rho_V \phi_G (\underline{V_V} - \underline{V_G})$ stands for the diffusive transport of water vapour within the gaseous phase. This latter can be evaluated through the Fick Law, here expressed in terms of vapour partial pressure [78]:

$$\phi_G (\underline{V_V} - \underline{V_G}) = -\frac{p_G}{p_V} D_e^V \underline{\nabla} \left(\frac{p_V}{p_G} \right) \tag{7.13}$$

where D_e^V is the effective diffusion coefficient.

Recalling that the water vapour follows the perfect gas relation and that total gas pressure variations are neglected, eq.(7.13) allows to express the vapour mass

conservation as:

$$\frac{\partial m_V}{\partial t} = \underline{\nabla} \cdot \left(\frac{M_{H_2O}}{RT} D_e^V \underline{\nabla}(p_V) \right) + \dot{m}_{\to V} \tag{7.14}$$

2.2 Liquid water mass balance

The conservation of the liquid water mass m_L is written as:

$$\frac{\partial m_L}{\partial t} = \rho_L \underline{\nabla} \cdot (\phi_L \underline{V_L}) - \dot{m}_{\to V} \tag{7.15}$$

where $\phi_L \underline{V_L}$ is the filtration velocity of liquid within the porous material, which is assumed to follow the generalized Darcy law (neglecting the gravity term):

$$\phi_L \underline{V_L} = -\frac{\kappa \kappa_r^L}{\eta_L} \underline{\nabla} p_L \tag{7.16}$$

with :
$\phi_L = S_r \phi$ [-] : porosity filled by the liquid phase
κ [m^2] : intrinsic permeability of the porous medium
κ_r^L [-]: relative liquid permeability
η_L [Pa.s^{-1}] : dynamic viscosity of water, equals to 10^{-3}

2.3 Equation of total mass transfer

Water in the material is present both as liquid and vapour, and these two phases can migrate through the porous medium. However, due to the equilibrium assumption expressed by eq.(7.4), these two mass transfers are linked to one another, and the global water mass balance can be assessed by a sole equation. The question that arises is the choice of the variable associated to the hydric state of the material. This latter can be the liquid pressure, the vapour pressure, the liquid water content or the relative humidity.

Actually, the scope of this model is to reproduce the behaviour of a porous wall mainly in the hygroscopic domain, where the water content of the material remains quite low. In consequence, the relative permeability of the liquid water is very small and the mass transport of water is mainly due to the gradient of vapour pressure. Then, the use of the vapour pressure or of the relative humidity is found to be the most natural option. The choice of the relative humidity is finally made as it is the physical value commonly measured by hygrothermal sensors.

Note that the model formulation was established with water pressure as driving potential for the simulations close to the saturation, where no significant difference was observed.

To carry on, as proven experimentally, the variations of water content with temperature at constant relative humidity is neglected. Using φ and T as variables, the combination of eqs.(7.1) and (7.6)-(7.11)-(7.12), accounting for $\rho_V/\rho_L \ll 1$, the balance of the overall mass of water reads:

$$m_{H_2O} = m_L + m_V = \phi S_r \rho_L + \phi(1 - S_r)\rho_V$$

$$\frac{1}{\rho_L}\left(\rho_d\frac{\partial w_L}{\partial\varphi}+\phi_G\frac{M_{H_2O}}{RT}p_v^{sat}(T)\right)\frac{\partial\varphi}{\partial t}+\frac{\phi_G\rho_V^\alpha}{\rho_L}\frac{\partial T}{\partial t}=\underline{\nabla}\cdot\left(K^\varphi\underline{\nabla}\varphi+K^T\underline{\nabla}T\right) \quad (7.17)$$

with:

$$\rho_V^\alpha=\varphi p_V^{sat}(T)\frac{M_{H_2O}}{RT}\left(\frac{1}{p_v^{sat}(T)}\frac{dp_v^{sat}(T)}{dT}-\frac{1}{T}\right) \quad (7.18)$$

$$K^T=K_1^T+K_2^T=\frac{\kappa\kappa_r^L}{\eta_L}\frac{\rho_L R}{M_{H_2O}}\ln\varphi+D_e^V\frac{\varphi M_{H_2O}}{\rho_L RT}\frac{dp_v^{sat}(T)}{dT} \quad (7.19)$$

$$K^\varphi=\frac{\kappa\kappa_r^L}{\eta_L}\frac{\rho_L RT}{M_{H_2O}\varphi}+D_e^V\frac{M_{H_2O}}{\rho_L RT}p_v^{sat}(T) \quad (7.20)$$

The main differences between eq.(7.17) and the water mass balance equation classically used in hygrothermal models [89] come from the expression of the source term due to temperature variations $((\phi_G\rho_V^\alpha)/\rho_L\partial T/\partial t-\underline{\nabla}\cdot K^T\underline{\nabla}T)$. Indeed, it is commonly assumed that the variation of liquid pressure with temperature at constant hygrometry is negligible, so that the liquid flow becomes exclusively driven by moisture gradient. Under this assumption, the term $\kappa\kappa_r^L/\eta_L\rho_L R/M_{H_2O}\ln\varphi$ vanishes and K^T is reduced to $D_e^V(\varphi M_(H_2O)/(\rho_L RT)(dp_V^{sat}(T))/dT$.

According to many authors [89], under practical conditions the influence of this assumption is disregarded, but caution should be taken when strong temperature variations occur in the material. The influence of this assumption will be discussed more in detail later in this work.

3 Equation of heat transfer

3.1 Thermal balance

The entropy balance of the wall leads to the thermal equation in its classical form for porous media with in-pore water phase change [54]. The proof is detailed in Appendix C. Here the enthalpy variation due to sorption/desorption mechanisms is assumed to be the same order of magnitude than the enthalpy variation due to evaporation/condensation:

$$\rho C_p\frac{\partial T}{\partial t}=\underline{\nabla}\cdot(\lambda\underline{\nabla}T)-\dot{m}_{\to V}L(T,\varphi) \quad (7.21)$$

where L is the integral specific enthalpy of evaporation per mass unit, and defined by:

$$L=h_V-h_L=T(s_V-s_L) \quad (7.22)$$

with:
h_V [J.kg^{-1}] : specific enthalpy of the water vapour
h_L [J.kg^{-1}] : specific enthalpy of the liquid water
s_V [J.kg^{-1}.K^{-1}] : specific entropy of the water vapour

s_L [J.kg^{-1}.K^{-1}] : specific entropy of the liquid water

where λ is the thermal conductivity and ρC_p the average heat capacity at constant pressure given by:

$$\rho C_p = (1-\phi)\rho_S C_S + \phi(S_r \rho_L C_L + (1-S_r)(\rho_A C_A + \rho_V C_V)) \tag{7.23}$$

The latent heat L is associated to the liquid/vapour phase change taking place at conditions different from the reference state. It varies with respect to temperature, liquid pressure and vapour pressure [85]. Using eq.(7.4) (i.e. the Kelvin's law), it can be expressed as follows as a function of temperature and equilibrium relative humidity. A more detailed explanation of this formulation is provided is Appendix C.

$$L(T,\varphi) = L_{ref} + (C_{p,V} - C_{p,L})(T - T_{ref}) - \frac{RT}{M_{H_2O}} \ln \varphi \tag{7.24}$$

Let's underline here that the relative humidity reported in eq.(7.24), is the relative humidity at equilibrium between the in-pore water and its vapour, which satisfies the Kelvin's law. The last term of eq.(7.24), leads to an increase of L when the equilibrium relative humidity decreases. It allows considering the effect on the enthalpy of evaporation of the linear reduction of p_V and of the strong reduction of p_L (according to eq.(7.4)) when the equilibrium relative humidity is reduced (and reciprocally for condensation when the relative humidity increases).

This term is almost always neglected. However, as it is illustrated in Figure 7.3, the variations of L with T and φ appears to be on the same order of magnitude. There is thus no apparent reason to justify such simplification and the entire expression will therefore be kept. Even if the influence of this term is likely to be negligible on the total temperature response, the matter here is to highlight the fact that it is almost as legitimate as the term $(C_{p,V} - C_{p,L})(T - T_{ref})$ usually considered.

3.2 Evaluation of the evaporation/condensation rate

To solve the system of partial differential equations (7.17)-(7.21), an additional relation on the evaporation/condensation rate is needed. Assuming that the kinetics of phase change is instantaneous, being driven by the water transport process through the porous network, it can be evaluated either by equations eq.(7.14) or eq.(7.15):

$$\dot{m}_{\to V} = \rho_L \underline{\nabla} \cdot \left[\frac{\kappa \kappa_r^L}{\eta_L} \left(\frac{\rho_L R}{M_{H_2O}} \left(\frac{T}{\varphi} \underline{\nabla} \varphi + \ln \varphi \underline{\nabla} T \right) \right) \right] - \frac{\rho_d}{\rho_L} \frac{\partial w_L}{\partial \varphi} \frac{\partial \varphi}{\partial t} \tag{7.25}$$

$$\dot{m}_{\to V} = \frac{\partial m_V}{\partial t} - \underline{\nabla} \cdot \left(D_e^V \frac{M_{H_2O}}{RT} \underline{\nabla} \left(\varphi p_v^{sat}(T) \right) \right) \tag{7.26}$$

Note that, in accordance with the overall mass conservation equation (7.17), relations (7.25) and (7.26) are theoretically equivalent. However, numerical problems can

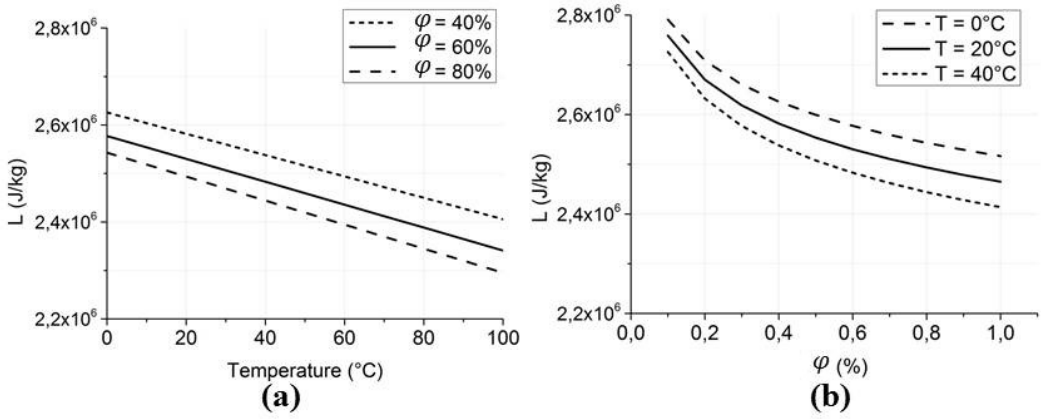

Figure 7.3: (a) Calculated and tabulated values of $L(T)$; (b) Evolution of L with the equilibrium relative humidity at different temperatures.

occur depending on which form is used, and the second option requires an evaluation of the term $\partial m_V/\partial t$ which leads to a more complex expression. In [89], this term is simply neglected and only the second term of the right side of eq.(7.26) is accounted for. It implies to consider the heat source due to phase changes as proportional to the divergence of the water vapour diffusion flow density. A further investigation is needed in order to find the best compromise between a more complicated form or a simpler one but which needs some additional assumptions. In this study, the relation (7.25) is used to estimate $\dot{m}_{\to V}$ since it does not need any simplification. In the end, the injection of eq.(7.25) in eq.(7.21) leads to the final form for the heat transfer equation:

$$\rho C_p \frac{\partial T}{\partial t} - \left(L(T,\varphi)\rho_d \frac{\partial w_L}{\partial \varphi} \right) \frac{\partial \varphi}{\partial t} = \underline{\nabla} \cdot (\lambda \underline{\nabla} T) + L(T,\varphi) \underline{\nabla} \cdot (L^T \underline{\nabla} T + L^\varphi \underline{\nabla} \varphi) \quad (7.27)$$

with:

$$L_a^T = -\rho_L^2 \frac{\kappa \kappa_r^L}{\eta_L} \frac{R}{M_{H_2O}} \ln \varphi \quad (7.28)$$

$$L_a^\varphi = -\rho_L^2 \frac{\kappa \kappa_r^L}{\eta_L} \frac{RT}{M_{H_2O} \varphi} \quad (7.29)$$

Let's note that choosing the other formulation for $\dot{m}_{\to V}$, while neglecting $\partial m_V/\partial t$ leads to the following form:

$$\rho C_p \frac{\partial T}{\partial t} = \underline{\nabla} \cdot (\lambda \underline{\nabla} T) + L(T,\varphi) \underline{\nabla} \cdot (L^T \underline{\nabla} T + L^\varphi \underline{\nabla} \varphi) \quad (7.30)$$

with:

$$L_c^T = \frac{M_{H_2O}}{RT} D_e^V \varphi \frac{dp_v^{sat}(T)}{dT} \tag{7.31}$$

$$L_c^\varphi = \frac{M_{H_2O}}{RT} D_e^V p_v^{sat}(T) \tag{7.32}$$

The influence of the use of eq.7.30 instead of eq.7.27 is studied in the following chapter.

To conclude, usually considered as a reference and implemented in the software WUFI, the formulation detailed in [89] leads to characteristic parameters. In order to ensure the right understanding of the formulation presented in this chapter, the connection between the coefficients is highlighted in this appendix.

The final formulation of the coupled equations in [89] reads :

$$\frac{\partial H}{\partial T}\frac{\partial T}{\partial t} = \underline{\nabla} \cdot (\lambda \nabla T) + h_v \underline{\nabla} \cdot (\delta p \nabla(\varphi p_{sat})) \tag{7.33}$$

$$\frac{\partial w_p}{\partial \varphi}\frac{\partial \varphi}{\partial t} = \underline{\nabla} \cdot (D_\varphi \nabla \varphi + \delta p \nabla(\varphi p_{sat})) \tag{7.34}$$

with w_p the water content in kg.m^{-3}.

Taking into account the hypothesis already mentioned in the article, and given equations 7.16 and 7.26, we finally obtain:

$$h_v = L(\varphi, T) \tag{7.35}$$

$$D_\varphi = \rho_L^2 \frac{\kappa \kappa_r^L}{\eta_L} \frac{RT}{M_{H_2O}\varphi} \tag{7.36}$$

$$\delta_p = D_e^V \frac{M_{H_2O}}{RT} \tag{7.37}$$

Chapter 8

Model validation and calibration against numerical and experimental data

Contents

The previous formulation derives from classical hygrothermal models developed for building materials. However, it took rather different forms and orientations at various steps. Therefore, a complete validation and calibration is carried out in this section. It starts with isothermal cases, to go to coupled configurations, and deals with both analytical solutions and experimental data.

1 Isothermal validation and calibration

First of all, the main task being to model the hygrothermal behaviour of the material, the ability of the model to reproduce basic configurations is investigated. The first stage of model validation focuses on mass storage and transport, as water vapour or liquid water, with no temperature variations taken into account. However, even if the responses in terms of temperature remain constant, the calculation is conducted with the two calculation variables (T and RH).

1.1 Benchmark HAMSTAD "Homogeneous wall"

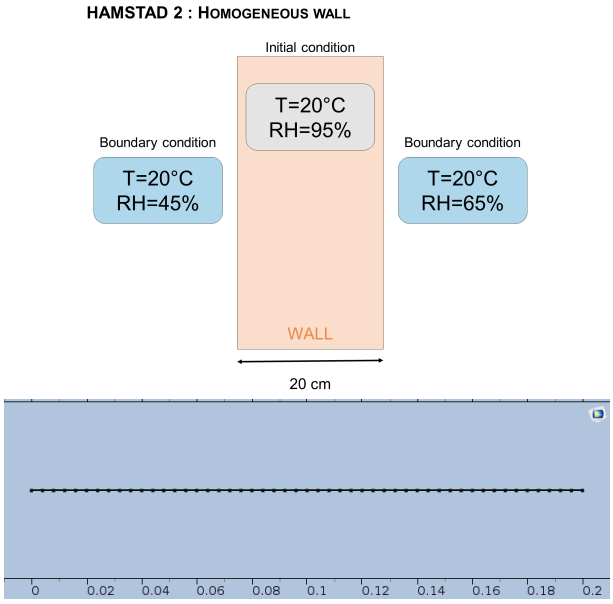

Figure 8.1: Schematic representation of the wall layout and the mesh for the benchmark HAMSTAD 2 "Homogeneous wall".

The HAMSTAD benchmark "Homogeneous wall - case with analytical solution" [70] is an analysis of a homogeneous layer under isothermal conditions in one dimension. The layer is initially in moisture equilibrium with the ambient air, having constant relative humidity. At time zero, there is a sudden change in the relative humidity of the surrounding air. One side is decreasing until 65%RH whereas the other until 45%RH. The temperature is constant and equal to 20°C.

The schematic representation of the layout as well as the mesh used for calculation, are displayed in Figure 8.1.

The simulation was made on a 1D geometry of length L=20 cm (x direction) and represented a section of the wall. The finite element mesh used is also reported in Figure 8.1 (maximum element size of 4 mm) and a time step was 360 s.

The confrontation between the analytical solution and the numerical modelling, both in terms of moisture content and temperature, can be found in Figure 8.2.

A perfect match can be observed between the analytical solution and the numerical modelling, both for the water content and the temperature.

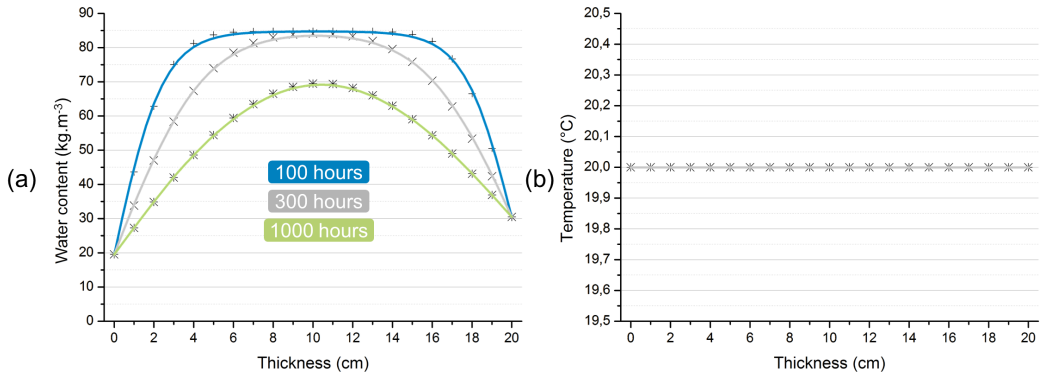

Figure 8.2: Comparison between analytical solution and numerical modelling for HAMSTAD 2 "Homogeneous wall".

1.2 Isothermal water vapour transfer

The second part of this work consists in confronting numerical modelling with experimental measurements, still in an isothermal configuration.

1.2.1 Experimental data used for validation

The water vapour resistance coefficient experiment, conducted on the earth of St Antoine, is used in this section to be compared with numerical modelling. The experimental data can be found in [28], and are recalled in Part II, Chap. 3.

The measurements were carried out according to the dry cup method after EN ISO 12572:2001. Cylindric samples were placed between two atmospheres, one in contact with silica gel. Two relative humidity were tested : 43.2% and 75.5%. The relative humidity of the air surrounding the silica gel was measured with a dew point mirror and resulted in 3%RH. The whole sets were placed in a temperature controlled box, at 20°C.

1.2.2 Model set up

This modelling will also enable a more precise calibration of the water vapour diffusive coefficient, until now evaluated in the following form:

$$D_e^V = D_V^0 \cdot \frac{w_{sat} - w_L}{w_{sat}} \tag{8.1}$$

with:
D_V^0 [$m^2.s^{-1}$] : effective diffusion coefficient
w_{sat} [$kg.m^{-3}$] : saturated water content

Note that in this formula, the liquid water content is in $kg.m^{-3}$.

Given that the lateral faces of the cylindrical sample are sealed, the vapour diffusion occurs in one direction. The simulation was made on a 1D geometry of length L=6 cm (x direction) and represented the height of the sample. The finite element mesh used is reported in Figure 8.3. The maximum element size was 2.22 mm and the time step was 1000 s for a calculation time of 46 days.

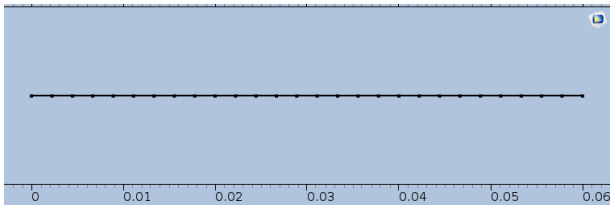

Figure 8.3: Mesh of the 1D geometry for the modelling of the water vapour resistance measurement.

In both faces, boundary conditions are defined by Neumann fluxes, and take the general form:

$$g_\varphi(t, \varphi) = \beta p_v^{sat}(T) \cdot (\varphi(t) - \varphi_{BC}) \tag{8.2}$$

with:
β [$kg.m^{-2}.s^{-1}.Pa^{-1}$] : moisture transfer coefficient
p_v^{sat} [Pa] : equilibrium vapour pressure
φ [-] : relative humidity
φ_{BC} : relative humidity set by the boundary condition

More precisely, for the case 3-43.2%, the upper boundary condition is equal to:

$$g_{\varphi,up}(t, \varphi) = \beta p_v^{sat}(T) \cdot (\varphi(t) - 0.432) \tag{8.3}$$

And, given that the relative humidity resulting from the silica gel is around 3%, the lower boundary condition is equal to:

$$g_{\varphi,down}(t, \varphi) = \beta p_v^{sat}(T) \cdot (\varphi(t) - 0.03) \tag{8.4}$$

The moisture transfer coefficient is here due to the air thickness between the lower surface of the sample and the top of the amount of silica gel, named e, and taken equal to 5 cm. The following formulation is then used:

$$\beta_{air} = \frac{\delta_a}{e} \tag{8.5}$$

with:

δ_a [kg.m^{-1}.s^{-1}.Pa^{-1}] : vapour diffusion coefficient in the air, equal to 2.10^{-10} kg.m^{-1}.s^{-1}.Pa^{-1}.

The previous boundary conditions were set for the 3%-43.2% case, and the other case is modified in consequence.

The temperature is constant and equals to 20°C.

The relative liquid permeability is set to 0. Indeed, the water vapour diffusion coefficient measurement takes place in an environment where liquid transport is neglected. It is the assumption made when calculating the vapour diffusion resistance coefficient from the experimental weightings.

1.2.3 Calculation results

The calculation program COMSOL gives access to the relative humidity (and thus the water content) in the sample at any time. This enable to collect, first, the total amount of water in the sample for each time step and, second, the outgoing flux through the lower surface, corresponding to the amount of humidity transmitted to the silica gel.

To be more specific, the evolution of the total mass can be calculated, through:

$$\frac{\Delta m(t)}{S} = \frac{\Delta m_{sample}(t)}{S} + \frac{\Delta m_{silicagel}(t)}{S} \tag{8.6}$$

$$\frac{\Delta m(t)}{S} = \int_0^h w_L(x,t)\,\mathrm{d}x + \int_0^T \varphi_{down}(t)\,\mathrm{d}t \tag{8.7}$$

with :

S [m^2] : exchange surface of the sample

h [m] : height of the sample

w_L [kg.m^{-3}] : water content

Different values of the effective diffusion coefficient were tested and the more accurate was chosen thanks to the least squares method. Each configuration was tested separately and the matching diffusion coefficient compared.

The Figure 8.4a displays the experimental data as well as the closest numerical curve for the configuration 3%-43.2%. The numerical results were found with D_V^0 equal to 4.10^{-6} m^2.s^{-1}.

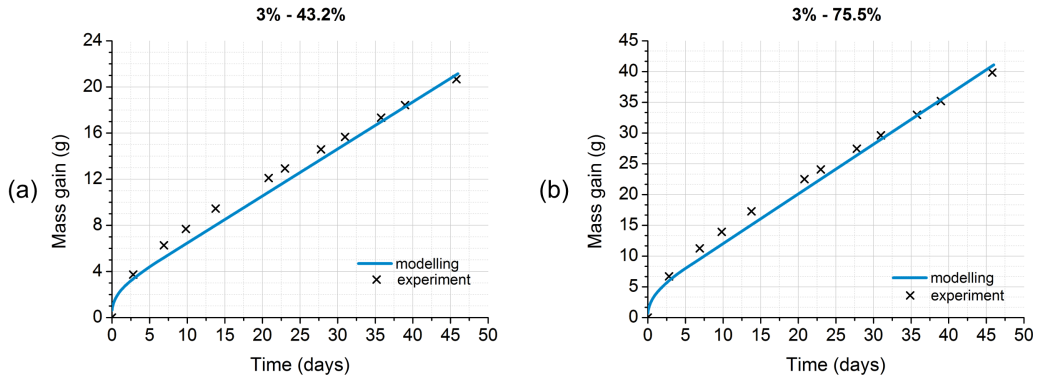

Figure 8.4: Comparison between experimental data and numerical modelling for water vapour resistance coefficient measurements.

Following the same procedure, Figure 8.3b displays the experimental and numerical data for the configuration 3%-75.5%, for D_V^0 equal to 4,5.10^{-6} $m^2.s^{-1}$.

The effective diffusion coefficients fitted numerically for the two configurations are almost equal, which ensures the accuracy of the process, and the ability of the model to reproduce experimental data.

To ensure the validity of the assumption $\kappa\kappa_r^L = 0$ in the modelling, the maximum water content of the sample for the case "3-75%" is numerically evaluated. At the end of the measurement time (about 46 days), the water content reached 19 $kg.m^{-3}$, i.e. about 5% of the total saturation. Based on the formulation of the total liquid permeability, providing the evolution against water content, the latter doesn't change much during the experiment and is equal to about 10^{-21} m^2. However, modelling with $\kappa\kappa_r^L = 10^{-21}$ provides the same results in terms of mass gain against the time. The assumption is therefore valid in this case. Note that the test was made on the "3-75%" case as it is the "moister".

1.3 Fit of the liquid permeability on water uptake experiments

Based on the experimental data detailed in the experimental part (first campaign of liquid water coefficient measurement), the numerical simulation is assessing the liquid permeability, which is an input parameter of the model.

For the record, the water fills the pores of the material through its different states: liquid and vapor. The overall mass conservation of water (in both liquid and vapor) within a representative elementary volume of the material, and considering an isothermal case, can be written in the following form (see for example [129] for detailed derivation):

$$\frac{\partial w_L}{\partial \varphi}\frac{\partial \varphi}{\partial t} = \nabla \cdot (\delta_p \nabla p_v + D_L \nabla p_L) \tag{8.8}$$

with:

∇ : nabla symbol
p_v [Pa]: partial pressure of vapour
p_L [Pa]: pressure of liquid water
δ_p [kg.m^{-1}.s^{-1}.Pa^{-1}] : vapour transport coefficient

The relation (8.8) underlines that two kinds of water transport occurs within the material. The first one, denoted by the term $\nabla \cdot (\delta_p \nabla p_v)$ corresponds to the flow of water vapour, while the second one, $\nabla \cdot (D_L \nabla p_l)$ is the transport of liquid water. Both vapour and liquid transport coefficients vary with water content. In particular, D_L can be expressed in the form:

$$D_L = \rho_L \frac{\kappa \kappa_r^L}{\eta_L} \tag{8.9}$$

with:
ρ_L [kg.m^3]: water density
κ [m^2] : intrinsic permeability
κ_r^l [-] : relative permeability for the liquid
η_l [Pa.s] : water viscosity

The intrinsic permeability κ, is a geometric parameter of the porous network, and does not depend on the nature of the fluid(s) that fill(s) the material. The relative permeability for the liquid κ_r^L is a non-dimensional function of the saturation that varies from 0 when the material is dried to 1 when it is saturated.

If the material is close to the dried state, the remaining liquid water is adsorbed on the pore surface. The term κ_r^L/η_L is close to zero and the migration of water mainly occurs by diffusion of vapour. On the opposite, when a large amount of liquid water is flowing through the material, the liquid transport is prevailing upon the water vapour diffusion. In such case, the transport of water in the material is dependent on its liquid permeability, which remains essential to assess precisely. Several authors have pointed out the practical troubles to measure the liquid water permeability of unsaturated soils, even if some experimental set up have been designed to overcome these difficulties [40][44][61][112][161]. Still, they remain quite sophisticated and not widespread. Therefore, many formulations to evaluate the liquid water transport properties have been developed, based on different measurements. In [26], the Hazen formula, provides an evaluation of the intrinsic permeability κ from the particle size distribution ; in [24], the multiscale network approach derives D_L from the water vapor permeability ; in [89], the capillary transport coefficient (similar to D_L) is approximated from the water absorption coefficient and the free water saturation.

The liquid transport depends on the product of the intrinsic permeability κ and the relative liquid permeability κ_r^L. Following the approach developed in [129], for this first set of simulations, it has been assumed that the liquid permeability varies linearly with the water content:

$$\kappa \kappa_r^L = \kappa \frac{w_L - w_{res}}{w_{sat}} = \kappa^* \cdot (w_L - w_{res}) \tag{8.10}$$

with:
w_{sat} [kg.m^{-3}] : water content at saturation
κ^* [m^5.kg^{-1}] : slope of the linear formulation

Note that in this formula, the liquid water content is in kg.m^{-3}.

This formulation will be evaluated through the comparison with experimental data, and other formulations from the literature.

1.3.1 Numerical simulation to assess the liquid water permeability

The main input material parameters are recalled in Table 8.1. The porosity is measured with the air porosimeter described in [27], and the vapour diffusivity is estimated from wet cup measurements [5]. Even if more investigation would be necessary to properly assess this parameter (at least two conditions: wet and dry cup, and several thickness to correct the skin resistance), a rough estimation is sufficient in this study, since its impact on the results remains of second order.

Parameters	**Notation**	**Value**
Porosity [-]	ϕ	0.55
Effective diffusion coefficient [m^2.s^{-1}]	D_e^V	1.50e-8
Specific heat capacity at const. pres. [J.kg^{-1}.K^{-1}]	$C_{p,S}$	648
Thermal conductivity [W.m^{-1}.K^{-1}]	$\lambda(w = 0\%)$	0.6
	$\lambda(w = 17\%)$	2.1
	$\lambda(w = 19\%)$	2.4

Table 8.1: Input material parameters used for the simulations.

The boundary condition on the top is set according to measurements of temperature and relative humidity made during the tests (second order flux – Neumann - conditions with standard transfer coefficients). A first order boundary condition - Dirichlet - is set on the bottom side with RH=100%. No flux is considered on the lateral faces as they are covered with foil. Therefore, equations are solved using 1D geometry whose dimension corresponds to the height of the samples described in the first parts.

The samples were initially oven dried at 50°C and weighted twice a day, until their mass variation between two measurements drops below 1%. Even if the samples were considered as dry, a small amount of water was still present in their pores. This residual water content can be evaluated with a drying at 105°C (but which changes the structure), and was estimated to 0.2% in mass, which, using the isotherm sorption curve, corresponds to a relative humidity of about 15%. The initial relative humidity of the sample was then set to 15%.

The model developed in [129] uses two driving potentials: temperature and relative humidity. The relation between relative humidity and water content is defined by the sorption curve described by a Van Genuchten formulation, and defined as follow:

$$w_L = \frac{w_{sat}}{\left(1 + \left(-\alpha \frac{\rho_L RT}{M_{H_2O} g} ln\varphi\right)^{(1/(1-m))}\right)^m} \tag{8.11}$$

with:
g [m^2.s^{-1}] : gravitational acceleration
α, m : Van Genuchten parameters

The parameters are determined from the previously measured sorption isotherm using the least squares method, and are: m = 0.43 and $\alpha = 0.02$. The confrontation is illustrated in Figure 8.5.

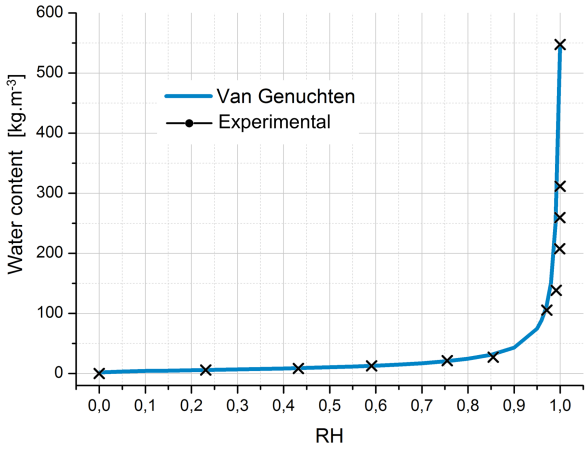

Figure 8.5: Comparison between sorption isotherms: experimental and Van Genuchten.

The simulation was made on a 1D geometry of length L=6 cm (x direction) and represented the height of the sample. The finite element mesh used is reported in Figure 8.6. The maximum element size was 0.645 mm and the time step was 1 s.

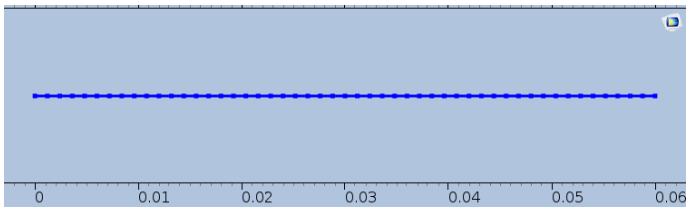

Figure 8.6: Mesh for the 1D modelling of the water absorption experiment.

The total moisture content of the sample was computed by integrating mass contents of each individual layer during the post-process treatment. It was repeated at each time-step, enabling a proper comparison between simulation and experiment.

The reliability of the linear formulation eq.9.6 and of the method has first been evaluated through the "in-situ-like" samples (i.e. with a density and a lime concentration as it was used for the house). This method leads to a good agreement between experimental data and the numerical simulation, as shown in Figure 8.7, for a permeability of $\kappa\kappa_r^L = 4.10^{-17}\frac{w_L}{w_{sat}}$ m^2.

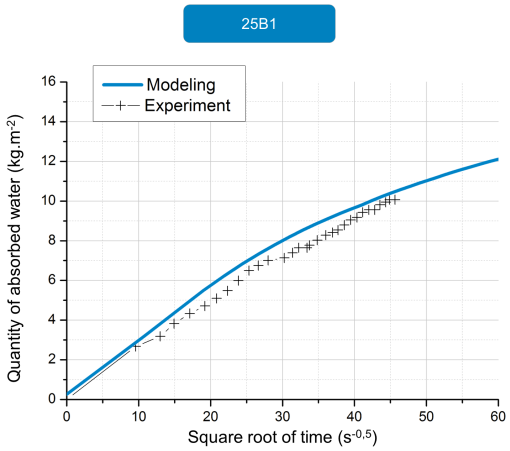

Figure 8.7: Confrontation between experimental and numerical data to fit the liquid permeability; example of the sample 25B1.

1.3.2 Discussion and comparison with existing models

It can be interesting to compare the modelling of the previous experiment with different formulations of the permeability (total, intrinsic or relative) found in the literature.

Two formulations have been elected:

- The first is proposed in [89] and draw a link between the A-value previously measured and the capillary transport coefficient for the suction process. The link between this coefficient and the liquid permeability of the proposed model is exposed in appendix C of [129]. This relationship provides the total liquid permeability.

- The second was formulated by Hazen and used in [26] ; it presents a relationship between the particle size distribution (and more precisely the diameter of particle below 10%) and the intrinsic permeability.

Note that, the well-known Van Genuchten formula for liquid relative permeability has also been investigated, using the same parameters as those set for the sorption

isotherm. However, to fit with experimental data, it required an intrinsic permeability above 10^{-14} m^2 which seems far too high for the tested material. In consequence, this formulation, developed in the field of soil physics, does not seem to be adapted for rammed earth, and it was not considered in the following of this study.

Reference	**Formula**	**Hypothesis**
Kunzel [89]	$D_w = 3.8 \left(\frac{A}{w_f}\right)^2 \cdot 1000^{\frac{w_L}{w_f}-1}$	$A = 0.20$ $w_f = 173.8$ kg.m^{-3}
Hazen [26]	$\kappa = 10^{-3} \cdot d_{10}^2$	$d_{10} = 10^{-7}$ m
Linear	$\kappa\kappa_r^L = \kappa\frac{w_L - w_{res}}{w_{sat}} = k \cdot w_L$	$w_{sat} = 547$ kg.m$^-$−3

Table 8.2: Theoretical evaluations of the liquid permeability.

It should be noticed that for the "Hazen case", the linear formulation of the relative permeability is kept. The comparison is displayed in Figure 8.8. It clearly appears that the linear formation, developed in accordance with the whole model, enable a better modelling of the tested experiment.

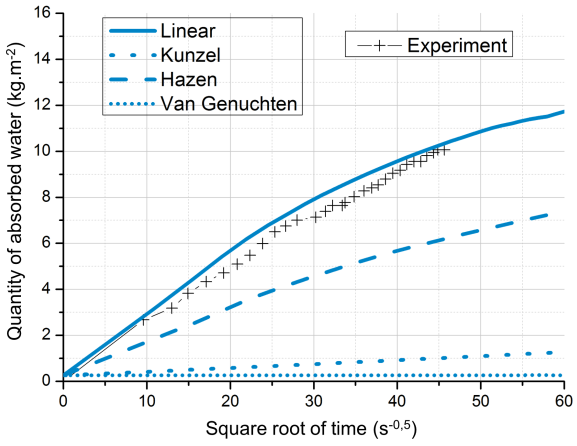

Figure 8.8: Comparison of different formulations for the liquid permeability to fit the experimental data.

The above mentioned linear formulation is then kept for the rest of the study.

1.3.3 Numerical modelling of the other experimental cases

The total permeability is here again set so that the A-value fits the experimental values. Indeed, a parametric sweep is carried out numerically by COMSOL and the more suitable permeability is chosen thanks to the least squares method. Three

examples of the comparison between experimental and numerical data are given in Figure 8.9.

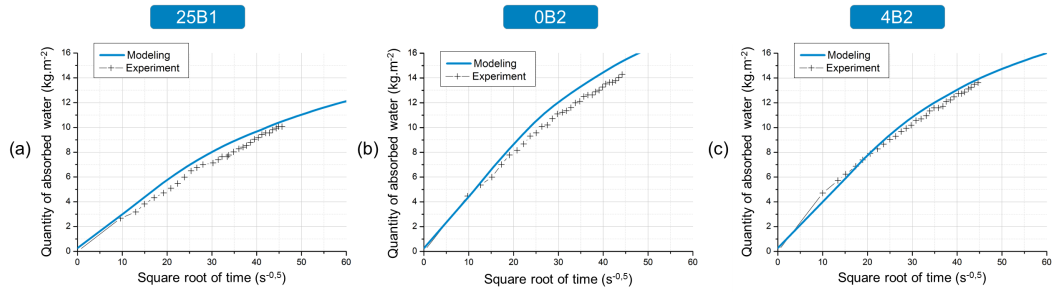

Figure 8.9: Confrontation between experimental and numerical data for three samples.

The low discrepancy between the experimental data and the modelling demonstrates the ability of the model to reproduce the behaviour of the material, even in high moisture ranges.

The Figure 8.10a displays the relationship between the liquid permeability and the A-value whereas the Figure 8.10b displays the liquid permeability against the density.

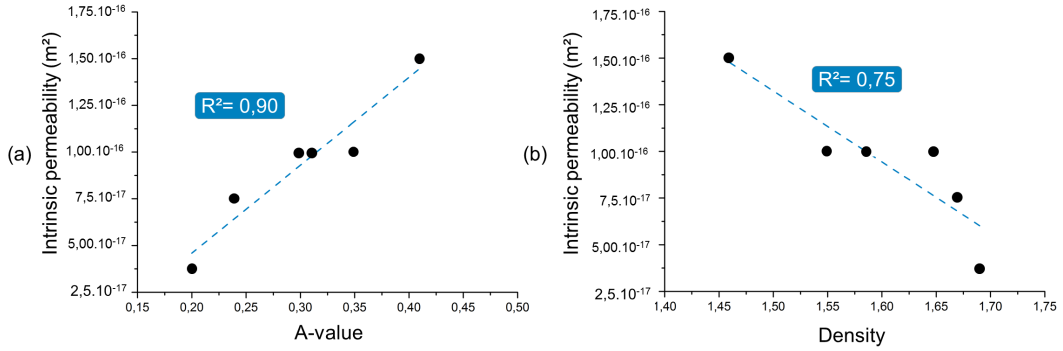

Figure 8.10: Evolution of the intrinsic permeability with the A-value and the density.

The intrinsic permeability decreases as the A-value decreases and the density increases. These relationships are expectable, given the evolution of the A-value with the density highlighted experimentally in the previous part. However, whereas there was a factor 2 between the lowest and the highest A-value in the studied density range, the variation interval of intrinsic permeability is wider. Indeed, it varies from $7.5.10^{-20}$ to 3.10^{-19} $m^5.kg^{-1}$, i.e. a factor of 4.

There are then two ways to deal with these relationships. First, they could be kept "as is" and be a tool to evaluate the liquid permeability from both sample density and A-value. However, this could lead to a misevaluation of the soil liquid parameter

as they are valid for a certain type of soil, with a certain shape of samples, etc. Care should then be taken not to misinterpreted these results. On the contrary, the other point of view is to take these observations as an evidence of the reliability of the method and set the procedure as follows: measurement of water uptake with regular processes and use the collected data to fit numerically the liquid permeability. This calculation is easier than direct experimental measurement, less time consuming and reliable enough. It enables to precisely evaluate difficult-to-measure soil parameters such as the liquid permeability.

2 Hygrothermal coupled validation and calibration

The isothermal cases having been handled with success in the previous section, fully coupled hygrothermal cases are dealt with in this section. First, thanks to analytical solution from a benchmark, and, second, in comparison with experimental data presented in the previous part of this work.

2.1 Benchmark EN 15026

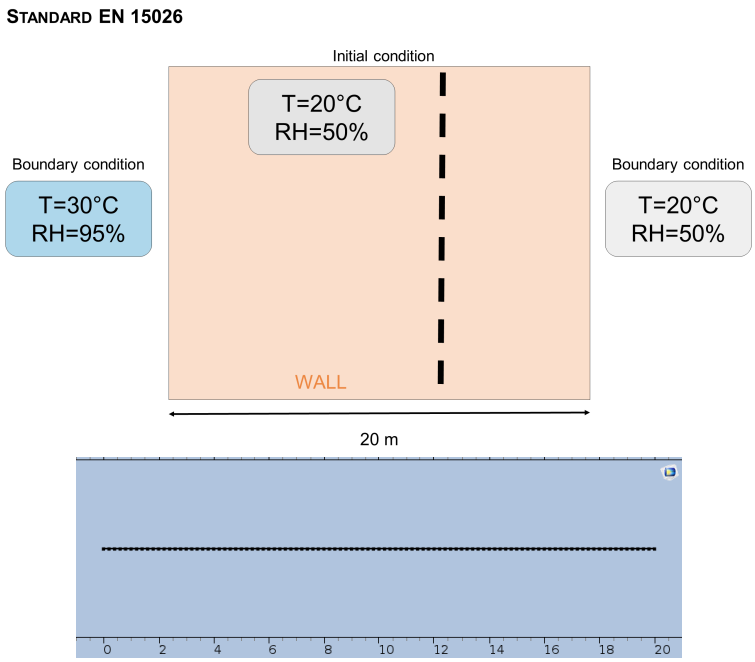

Figure 8.11: Schematic representation and mesh of the layout for the benchmark EN 15026.

The benchmark from the European regulation EN 15026 [77] deals with the influence of a step change in temperature and relative humidity. The material is a semi-infinite wall, modelled in 1D. The length having to be a finite number for the

calculation, it was taken equal to 20 m. The simulation results have to fall within the confidence intervals (+/-2.5%) of the analytical solution.

The simulation was made on a 1D geometry of length L=20 m (x direction) which represented a section of the wall. The finite element mesh used is also reported in Figure 8.1 with the schematic representation of the layout. The maximum element size was 5 mm and the time step was 0.01 d.

The results, together with the confidence intervals, are in Figure 8.12.

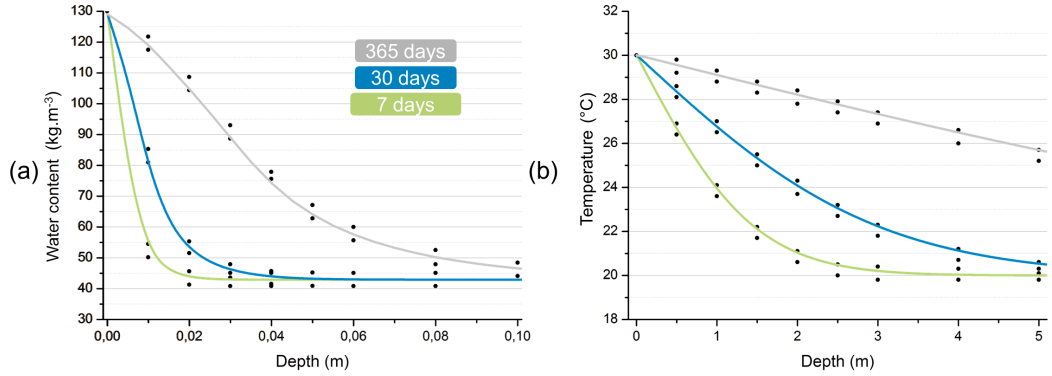

Figure 8.12: Numerical modelling and confidence intervals for EN 15026.

Regarding the moisture content, only the first 10 cm of the wall are analysed. The numerical results fit in the confidence intervals. Regarding the temperature, the first 5 m are studied and the same statement can be made regarding the accuracy of the modelling.

2.2 Rammed earth wallets

The second step is a comparison of the modelling with numerical data provided by the monitoring of rammed earth wallets, under rather simple loading paths.

2.2.1 Experimental data used for model verification

The model predictions are compared to experimental data for a rammed earth wall of dimensions 1 x 1.5 x 0.3 m^3. This wall is monitored with a water content (Campbell CS616, sensor accuracy of +/-2.5 %) and temperature sensors (Campbell CS215, sensor accuracy of +/-1.5%), positioned at the central horizontal plane at mid-height (0.5 m high). The experimental design is sketched in Figure 8.13, and is explained more in details in [29]. The wall is placed in a double climatic chamber. Temperature and relative humidity are controlled in one chamber, and their variations are monitored. The set of experimental conditions tested correspond to daily temperature variations between 15 and 20°C within a 50% relative humidity atmosphere (given that the wall is initially saturated).

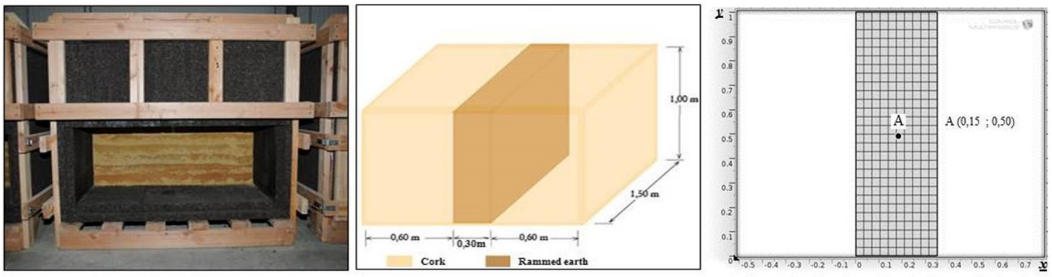

Figure 8.13: (a) Photography and schematic representation of the model wall; (b) Geometry and spatial discretization of the 30 cm wall.

The material parameters used for the simulations are measured on rammed earth blocks made by the same mason who built the wall, using the same pneumatic rammer and the same manufacturing water content of 19%.

The resulting data and the methods used for the measurements are reported in Table 8.3 and some additional details are provided in the following paragraphs.

Parameters	**Values**	**Experimental method**
ρ_d	1730 [kg.m^{-3}]	Hydrostatic weighting
ϕ	0.35	$\phi = 1 - \rho_d/2650$ according to [103]
D_e^V	2.7.10^{-6} [m^2.s^{-1}]	Dry cup method after EN ISO 12572:2001
A	0.39 [kg.m^{-2}.s$^{-0.5}$]	According to EN 1015-18
w_f	259 [kg.m^{-3}]	According to the A-value measured following [84]
$\kappa\kappa_r^l$	$10^{-18} \cdot w$ [m^2]	Deduced from the A-value, according to [84]
$C_{p,S}$	648 [J.kg^{-1}.K^{-1}]	Differential Scanning Calorimetry (DSC)
$\lambda(w = 0\%)$	0.6 [W.m^{-1}.K^{-1}]	Hot wire apparatus on CEB
$\lambda(w = 17\%)$	2.1 [W.m^{-1}.K^{-1}]	
$\lambda(w = 19\%)$	2.4 [W.m^{-1}.K^{-1}]	

Table 8.3: Input parameters used for the simulations.

The thermal conductivity was measured on compressed earth blocks (CEB) of 30 x 14 x 10 cm^3 just after their manufacture (when its water content was equal to 19%), and after a drying period of 48 hours, which results in a water content equal to 17%. To ensure the homogeneity of water content within the samples, they were wrapped in a sealed plastic film at least 48 hours at constant temperature before each measurement of thermal conductivity.

The liquid apparent permeability (i.e. $\kappa\kappa_r^l$) was deduced from the measurement of the A-value (liquid absorption coefficient) as described in [84]. This formula provides

a quite complex variation of the permeability with the water content, which is linearised in the present study for simplification purpose.

2.2.2 Results and model validation against experimental data

The simulations are made with COMSOL on a 2D prismatic geometry of length L=0.3 m (x direction) and height H=1 m (y direction). It represents a lateral cross section of the tested wall. The finite element mesh used is reported in Figure 8.13 (element size of 0.037 m) and the time step used is 1 s.

Boundary conditions of the simulations are set in accordance with measurements made on both sides of the insulated box. Thus, a null thermal and moisture flows are imposed at the y=0 and y=H boundaries.

As suggested by [89], realistic values for the transfer coefficients for water vapour (β) and for heat (α_{th}) are resp. 25.10^{-9} kg.m^{-2}.s^{-1}.Pa^{-1} and 8 W.m^{-2}.K^{-1}. These values will therefore be considered for the following studies.

The water content when just manufactured was around 19%. However, the testing period began after almost one year and a half of drying. At that stage, the water content in the middle of the wall was around to 1,6% in mass, which approximately corresponds to 71% of relative humidity according to its desorption curve. Under this condition, the gaseous phase is connected throughout the wall thickness and vapour transport can occur within the porous network, which is the condition to initiate hygrothermal couplings.

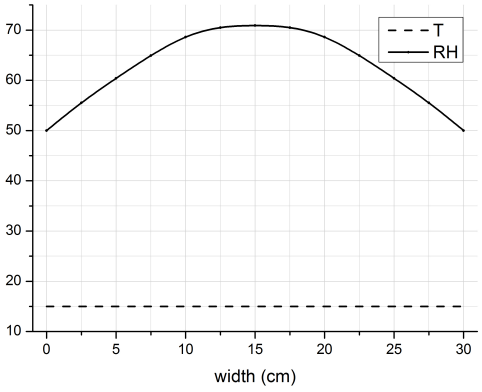

Figure 8.14: Temperature and relative humidity profiles in the wall after the precalculation.

However, this drying period was not sufficient to reach the dynamic equilibrium between the wall and the outside conditions. To take into account this effect, the initial field of temperature and humidity are extracted from the results of a presimulation. This latter is realized with the same kind of boundary conditions, i.e. Neumann type, but assuming that T_a and φ remain constant and equal to respectively

16°C and 50%, and that the initial temperature and humidity within the wall are homogeneous and respectively equal to 20°C and 99%. This pre-calculation stops when the hygrometry at the center of the wall becomes equal to 71%. The temperature and relative humidity profiles can be seen in Figure 8.14.

As a drying phenomenon is considered, the desorption isotherm was used to establish the link between the water content and relative humidity.

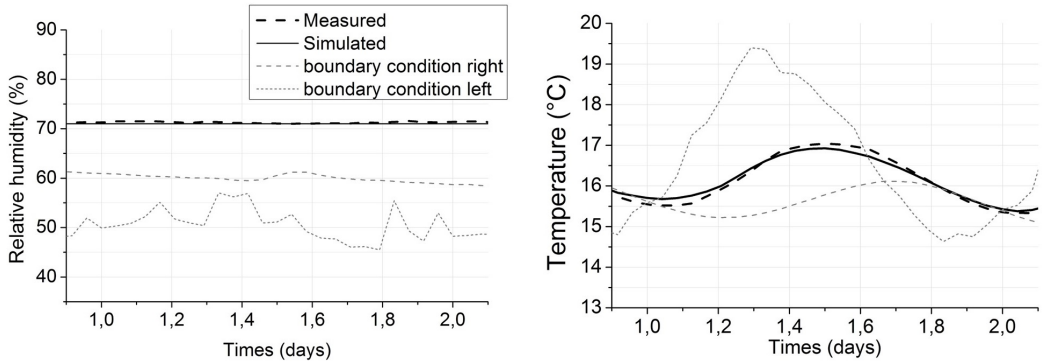

Figure 8.15: Comparison between measured and simulated distributions in the middle of the wall (point A) with boundary conditions on the right (BC_r) and left (BC_l) sides, for two days.

Results are reported in Figure 8.15, counting measured and simulated data as well as boundary conditions on right and left sides. In terms of temperature, the comparison between measured and simulated distributions in the middle of the wall shows good results. However, as for relative humidity, given the saturated state of the material, the boundary conditions have a few effects on the middle of the wall during the testing time. In addition a small time-laps in temperature is observed between the calculation and the measurements. This may be due to the rough estimation of the thermal capacity of the material. Nevertheless, the simulation and the sensor's data are close.

2.3 Modelling of temperature variations during water up-take experiment

This section rests upon the experimental set up described in the previous part, dealing with the thermographic measurements on samples subjected to moisture ingress. The aim of this study is to model the behaviour of the samples, both in terms of water content, as it has been done previously in 1D, and in terms of temperature.

Following the same procedure as detailed in the previous section, the liquid permeability will be fitted, for each batch, for one boundary condition and the good accuracy of the modelling for the other boundary conditions will be checked.

2.3.1 Model and hypothesis

The simulation was made on a 3D geometry whose dimensions correspond to the samples described in the first parts. The finite element mesh used is reported in Figure 8.16. In order to enhance the chance of convergence in the lower boundary condition, the mesh was refined on the bottom. The maximum element size was 8 mm and the time step was 360 s.

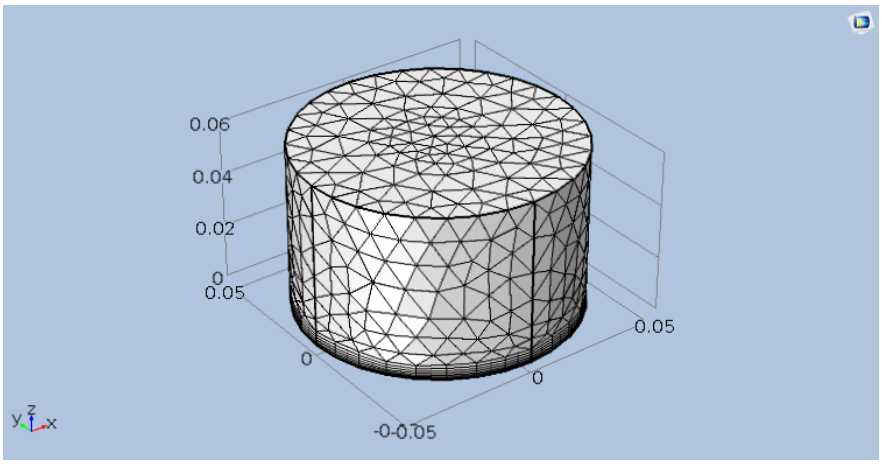

Figure 8.16: Mesh of the 3D modelling of the water absorption measurements.

Depending on the boundary condition cases, the numerical boundary conditions were set with the same formulations as for the previous section. The same is applied for other assumptions and input parameters.

2.3.2 Modelling the water uptake

The case c "all closed" was first simulated and the liquid permeability was calibrated. A parametric sweep was realized for the κ^* coefficient between 10^{-22} and 10^{-17} and the least squares method led to the following coefficient: $\kappa^* = 2.10^{-19}$ m^2. Figure 8.17a displays the comparison between numerical and experimental data.

The same liquid permeability coefficient was kept to simulate the case b "top open" with sample from the same batch (batch 2) and a good correlation was found, as can be seen in Figure 8.17b.

As expected, the same coefficient didn't suit samples from the batch 1, which have a slightly different density. The same procedure was applied with the parametric sweep and the least squares method, and the corresponding coefficient is: $\kappa^* = 1.10^{-19}$ m^2. It can easily be noticed that, as the difference in density is small, the difference in κ^* is also small. The comparison between experimental and numerical data is realized in Figure 8.17c.

Finally, keeping the same coefficient for the case a "all open", whose samples are part of the batch 1, the following correspondence is found in Figure 8.17d. Unfortu-

nately in this case, no matter the value of the liquid permeability, the best fit isn't as good as for the other cases. In the early part of the experiment, the numerical results match the experimental data, whereas a split is observable from around 50 $s^{-1/2}$ to the end. A possible explanation can be the volume dilatation of the sample, that enabled it to store a larger amount of water, even if no significant variations were observable to the naked eye. Indeed, in this case, the samples weren't confined by any device.

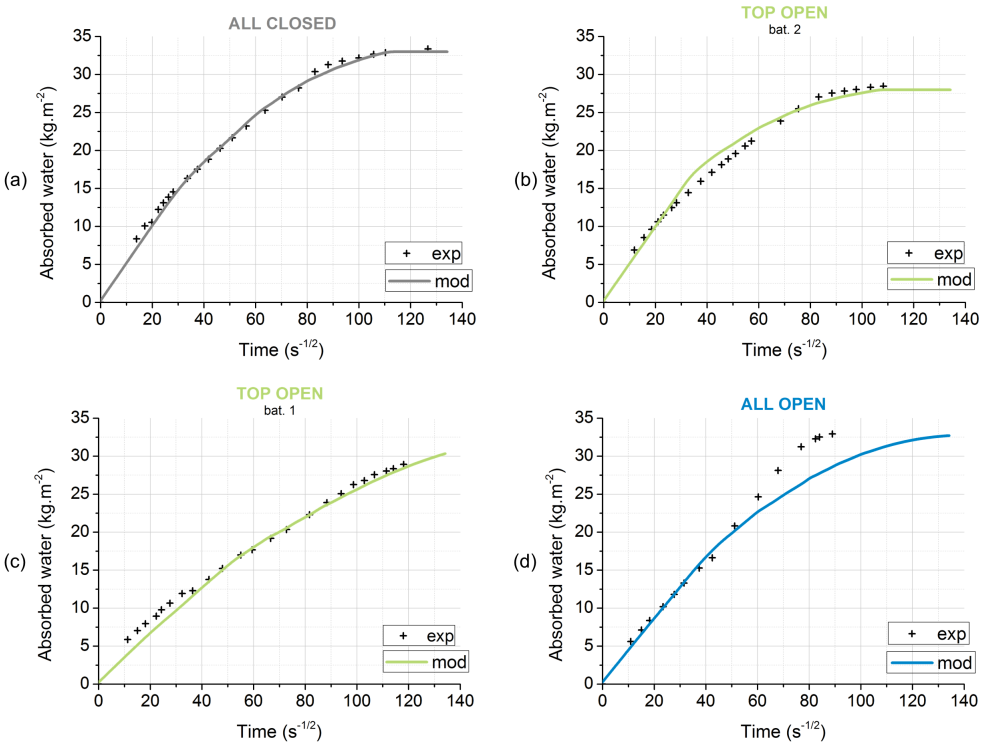

Figure 8.17: Confrontation between experimental and numerical data for three samples (resp.c.7, b.6, b.5 and a.1).

2.3.3 Modelling the temperature evolution

The modelling in COMSOL enables to export data along a vertical line, which corresponds to the vertical repartition in the height of the sample. The surface temperature is thus used to make a comparison with the surface temperature measurements detailed in a previous chapter.

The case to be studied is the case "a" "all open", where the surface temperature variations were the more important. Figure 8.18 gathers both sets of data, and displays the temperature along the sample at different times.

The main observation is the good accuracy of the modelling regarding initial and final temperature repartition. The global temperature evolution is comparable and

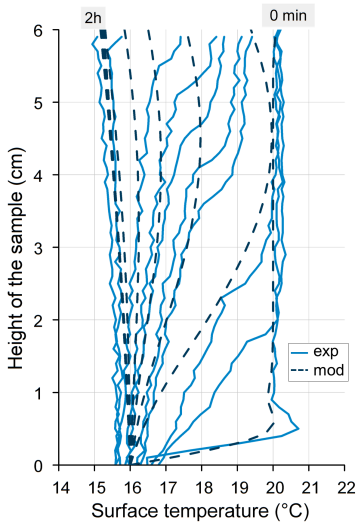

Figure 8.18: Confrontation between experimental and numerical data for the case "a" "all open" (sample a.1).

the different steps can also be distinguished. However, the modelled temperature seems to evolves much quicker than the one measured. It can be assumed that it is related to the absorption speed which was difficult to reproduce numerically.

Note that the apparent reliability of the modelling enables to carry out further instigation on the temperature evolution in the sample. One main hypothesis of the experimental exploitation of the results was to consider as homogeneous the temperature repartition in the horizontal slice. And the model is able to confirm this assumption, displaying no difference along the radius. The relative humidity, and thus the water content, also don't show any variation.

3 Conclusion

These different computation cases enabled to ensure the accurate response of the model to various configurations, with an increasing complexity, from isothermal to coupled configurations and from dry to saturated samples. It globally resulted in a good concordance between the model and numerical or experimental data.

The validation was linked to another important aspect of the numerical modelling, which is the good calibration of the coefficients. These studies enabled to evaluate the influence of some input parameters and their suitable approximation. It reveals the importance of a good measurement of the sorption isotherm for RH above 95%, for which suction measurement with filter papers seems to be appropriate. Then, the linear formulation of the liquid permeability with the water content appears to be sufficient to model the moisture ingress.

Chapter 9

Model application to numerical studies

Contents

The comparison between model predictions and experimental data gave some confidence on the ability of the model to simulate accurately the hygrothermal behaviour of rammed earth walls.

In this section, the model is first used to numerically quantify the impact of the simplifying assumptions pointed out during the equations development.

1 Evaluation of the impact of simplifying assumptions

To underline the main assets of the coupled model developed in this thesis and thus to identify the singularity of the hygrothermal behaviour of rammed earth, more complicated solicitations were simulated.

1.1 Identification of the studied hypothesis

To do so, two numerical experiments, respectively referenced as LP1 and LP2 are considered. These loading paths are applied to a wallet with the same geometry but with a width of 50 cm, and the same in-come parameters, as the one used for the experimental validation of the previous chapter. In this cases, the sorption curve (see Figure 5.8) was used.

The loading path LP1 considers daily relative humidity sinusoidal cycles between 70% and 50% at a constant temperature of 30°C within the insulated box. The loading path LP2 considers daily temperature cycles between 0°C and 20°C at a constant relative humidity of 60%. Both of the testing periods are set as 100 hours so that the stabilization time in the wall can be observed. A stationary behaviour is studied. Note that the same boundary conditions are applied on both sides of the wall and that the initial conditions were similar to the boundary conditions in the whole wall, considered as homogeneous.

Those two loading paths are summarized in Table 9.1.

		LP1	LP2
Boundary conditions	RH	Daily cycles 70-50%	60%
	T	30°C	Daily cycles 0-20°C
Initial conditions	RH	70%	60%
	T	30°C	0°C

Table 9.1: Loading paths LP1 and LP2.

For each test conditions, 4 simulations are considered. Each corresponding systems are gathered in Appendix B. The first one (referenced as "a") is based on the system of eqs.(7.17)-(7.27) "as it stands". The second one (referenced as "b") considers, like many authors, that the liquid flow is exclusively driven by a relative humidity gradient. The hypothesis 1, on which is based the case "b", can be written in the form:

Case "b" (Hypothesis 1):

$$|K_1^T| \ll |K_2^T| \tag{9.1}$$

with :
$K^T = K_1^T + K_2^T$
$K_1^T = \frac{\kappa \kappa_r^L}{\eta_L} \frac{\rho_L R}{M_{H_2O}} ln\varphi$
$K_2^T = D_e^V \frac{\varphi M_{H_2O}}{\rho_L RT} \frac{dp_v^{sat}(T)}{dT}$

As previously discussed in the model development, the expression of the source term in relative humidity due to temperature variations is thus simplified.

In the third simulation (referenced as "c"), the rate of evaporation/condensation is estimated from eq.(25) under the assumption of negligible variation of vapour mass. The hypothesis 2, on which is based the case "c", can be written in the form:

Case "c" (Hypothesis 2):

$$|MV| \ll |DD| \tag{9.2}$$

with:
$MV = \frac{\partial m_V}{\partial t}$
$DD = \underline{\nabla} \cdot \left(D_e^V \frac{M_{H_2O}}{RT} \underline{\nabla}(\varphi p_v^{sat}(T)) \right)$

Note that for cases "a" and "b", hypothesis are considered independently from one another, i.e. when studying hypothesis 2 (case "b"), the first hypothesis is not made.

At last, in the fourth simulation (referenced as "d"), both of the previous assumption are made.

Case "d" (Hypothesis 1 & 2):

$$|K_1^T| \ll |K_2^T| \& |MV| \ll |DD| \tag{9.3}$$

Results of LP1 and LP2 for the four kinds of simulations in temperature and relative humidity are respectively reported in Figure 9.1 and Figure 9.2. Each graph is composed by four curves, corresponding to the four following cases: the complete model (case "a"), model which considers the hypothesis 1 (case "b"), the model which considers the hypothesis 2 (case "c"), and the model which considers hypotheses 1 and 2 (case "d").

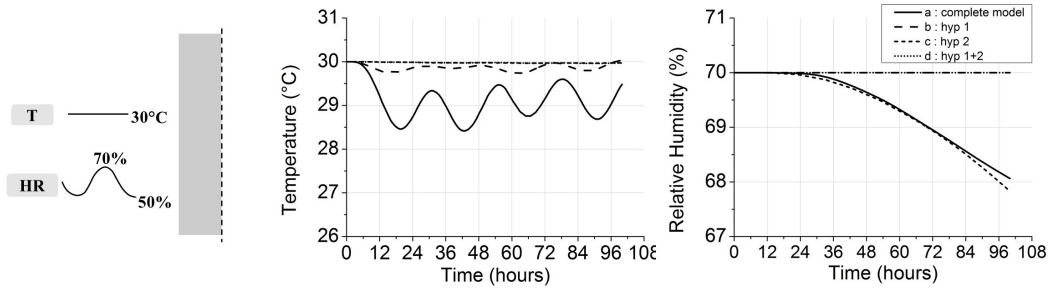

Figure 9.1: Simulations results of LP1 for the different formulations.

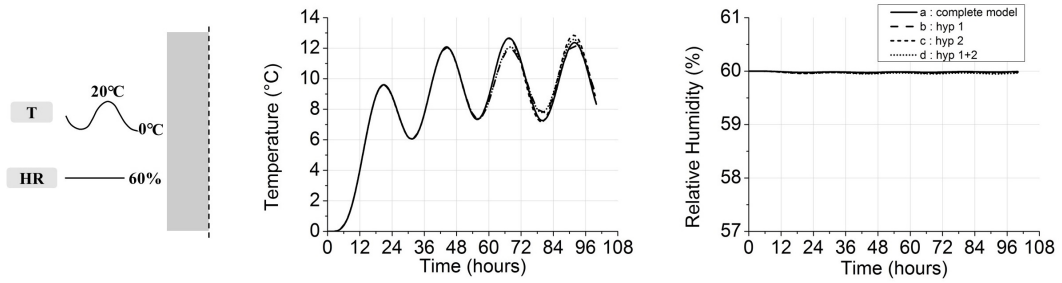

Figure 9.2: Simulations results of LP2 for the different formulations.

1.2 Effect of the temperature source term on the "relative humidity" equation (hyp. 1)

The effects of the temperature source term on the "relative humidity" equation can be estimated from the comparison between the simulations "a" and "b".

Regardless of the loading path considered (either LP1, (Figure 9.1) or LP2 (Figure 9.2)), the simplification of the source term on the relative humidity equation induced noticeable differences, and especially tends to underestimate the hygrothermal coupling.

Indeed, when LP1 is followed (i.e. hydric cycles), the results reported in Figure 9.1 show that the hygrothermal effect on temperature due to variation in relative humidity is reduced by about 1.3°C (amplitude of 1.5°C instead of 0.2°C between the complete modelling ("a") and the one which considers the hypothesis 1 ("b"). The time shift is also impacted as the difference between the two models reaches 0.6 hours (time shift of 7.9 hours for "a" and 7.3 hours for "b"). On the other side, a difference up to 2% is noticeable in terms of relative humidity variations in the middle of the wall.

No significant modifications are observable when the loading path LP2 is considered (Figure 9.2, curves "a" and "b"). This result is not surprising since the variations in relative humidity is slight, and thus the hygrothermal coupling remains limited when this loading path is followed.

These results underlines that the impact of thermal gradient on the liquid water

transports at constant relative humidity in rammed earth material can be significant. To illustrate this point, the impact of this assumption on the coefficient K^T is reported in Figure 9.3. Effects are negligible only for high relative humidity and quite high temperatures. However, considering the lifetime solicitations of earth walls, low, and even sub-zero temperatures and/or relative humidity lower that 60% are not unusual. Let's however underline that, even if strong differences are observed on the coefficient K^T, a significant modification of the hygrothermal behaviour will occur only if there is a sufficient amount of water within the porous network. Consequently, the necessity to take into account the impact of thermal gradient on liquid pressure at constant humidity is certainly due to the ability of earth materials to keep a non-negligible amount of water, even when the relative humidity decreases below 60%. This remark is then not in contradiction with the literature [78].

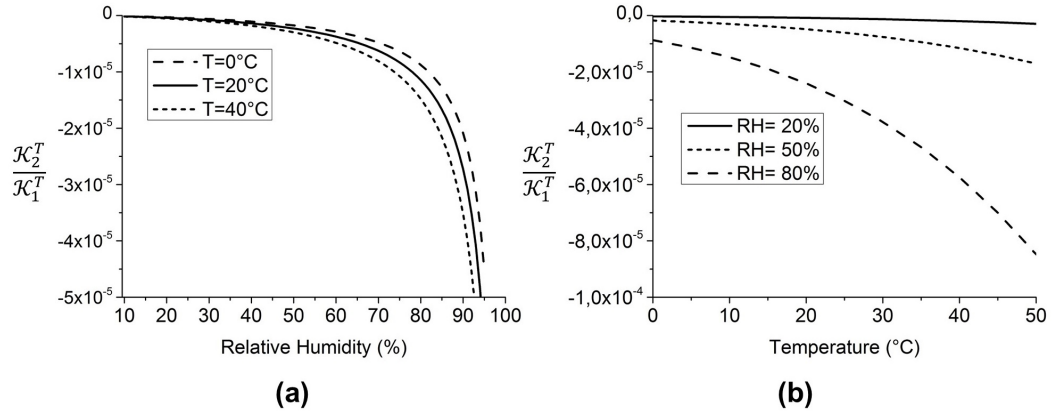

Figure 9.3: (a) Ratio of the two terms in K^T against RH for different T ; (b) Ratio of the two terms in K^T against T for different RH.

1.3 Effect of vapour mass variations (hyp. 2)

In the same way, the effect of the vapour mass variations on the hygrothermal coupling is scanned from the analysis of the simulations "a" and "c".

Results from the LP1's conditions are different between the complete simulations ("a") and the ones which consider the hypothesis 2 ("c"). Indeed, a large difference between the two formulations in terms of amplitude can be noticed (1.5°C for "a" and 0°C for "c") while the time shift is not perceptible (7.9 hours for "a" and constant for "c").

On the contrary, not many differences between simulations "a" and "c" arise when the loading path LP2 is considered (i.e. constant imposed RH with temperature cycles). After the transient period, the amplitude in the middle of the wall differs from about 0.7°C (12.7°C for simulation "a" and 12°C for simulation "c" in Figure 9.2), while time shift between the solicitations and the response in the middle of the wall is not changed (8 hours for both in Figure 9.2).

Actually, for the record, the simplification of the simulation "c" relies on the assumption that the mass flow of vapour (i.e. $\underline{\nabla} \cdot (D_e^V M_{(H_2O)}/RT \underline{\nabla}(\varphi^s at(T)))$ in eq.(7.26) is strongly higher than the overall variation of vapour mass (i.e. $(\partial m_V)/\partial t$ in eq.(7.26), which is due to temperature, vapour pressure and saturation variations. In other terms, the vapour mass income/consumption due to evaporation/condensation processes within a Representative Elementary Volume of the material is instantaneously counterbalanced by the flow of vapour with the adjacent volumes, so that the overall mass of vapour remains constant. This assumption seems quite natural when the flow of water within the porous network of the material is mostly a due to vapour diffusion process (which is the case for most of hygroscopic materials). However, when a significant mass transport of liquid water arises, and/or when strong and fast temperature variations occur, the variation of vapour mass is no longer directly linked to the flow of vapour. Consequently, in function of the external solicitation and of the whole hydric state of the material, the vapour mass variation rate within the pores volumes may become no more negligible towards the flow rate of vapour mass. Under this condition, in accordance with eq.(7.26), the hypothesis 2 can induce a bias on the estimation of the evaporation/condensation mass rate $\dot{m}_{\rightarrow V}$, and thus on the source term of the thermal equation.

1.4 Effect of both hypothesis

To enable to draw a global conclusion on the differences between the complete model and the simplifying assumptions, a last case was investigated for simulations, considering that both hypothesis 1 and 2 are made (case "d" in Figure 9.1 and Figure 9.2). Globally, the same effects can be noticed. In terms of temperature, for the loading path LP1, differences in amplitude are even additive, which leads to even larger differences with the reference simulation "a". For the loading path LP2, this case "d" is similar to the case "c", which is based on the hypothesis 2. It is not surprising since the use of the hypothesis 1 was found to have nearly no impact when this loading path is considered.

To conclude on the numerical investigations carried out here, for both cases, extending the simulation duration (to around 1000 hours), a stabilization of the wall is observable and no difference is remarkable between the different cases. However, on site, no solicitation is applied on such a long period and this scenario is considered unrealistic.

1.5 Effects of these hypothesis on moisture and thermal flux

The present investigation mainly focuses on material and wall scales. However, this study is part of a larger objective aiming at predicting global exchanges between indoor and outdoor climates through envelops. The link between these two approaches (i.e. material and buildings) can be made through the analysis of the changes induced by the previous hypothesis in terms of moisture and thermal flux at the wall surfaces.

To be clear on the compared quantities, the formulas used are written below, respectively for thermal flux (noted $g_{th} = \underline{g}_{th} \cdot \underline{n}$, in W.m^{-2}) and water vapour flux ($g_\varphi = (\underline{g}_L + \underline{g}_V) \cdot \underline{n}$, in kg.m^{-2}.s^{-1}) at the wall surfaces:

$$g_{th} = \alpha(T_a - T_S) \tag{9.4}$$

$$g_\varphi = \beta \left[p_v^{sat}(T_a)\varphi_a - p_v^{sat}(T_S)\varphi_S \right] \tag{9.5}$$

In order to evaluate the differences between the models in another point of view, Table 9.2 gathers the maximal heat and moisture fluxes during the cycles calculated with the different models.

	LP1		**LP2**	
	g_{th}^{max} $W.m^{-2}$	g_φ^{max} $kg.m^{-2}.s^{-1}$	g_{th}^{max} $W.m^{-2}$	g_φ^{max} $kg.m^{-2}.s^{-1}$
complete model (a)	12.4	- $1.35.10^{-5}$	62.7	- $3.5.10^{-8}$
Hyp. 1 (b)	3.4	- $1.70.10^{-5}$	62.7	- $6.6.10^{-8}$
Hyp. 2 (c)	0.02	- $1.59.10^{-5}$	64.3	- $3.4.10^{-8}$
Hyp. 1 + 2 (d)	0.14	- $1.85.10^{-5}$	64.3	- $3.4.10^{-8}$

Table 9.2: Heat and water vapour flux for the different formulations and for loading paths LP1 and LP2.

In the case of the hydric cycles (LP1), the absorbed thermal flow at the wall surface is strongly lowered no matter which assumption is considered (relative reduction of 72% for the simulation "b" and around 99% for the simulations "c" and "d"). Such high differences are not surprising: indeed, this case has isothermal boundary conditions; therefore heat flux is exclusively due to mass flux. Impact of hypothesis on mass flow can directly be seen on heat fluxes. Indeed, the moisture absorption of the wall increases by 26% when the hypothesis 1 is considered, by 18% when the hypothesis 2 is considered and by 37% when both hypotheses are considered.

In addition, it is worth noticing that the order of magnitude of the incomings thermal and moisture flows at the wall surface estimated by the complete model are not negligible (respectively equal to 12.4 W.m^{-2} and 1.35. 10^{-5} kg.m^{-2}.s^{-1}). According to this result, if a quite important surface of earth walls is present in a building, it will inevitably impact its thermal and air quality performances.

In the case of LP2, no significant differences are observed between the model "a" and the others, except for the moisture absorption which is increased by 88% if the hypothesis 1 is used. However, the values remain fairly low for this loading path in all the simulations.

Those results are in accordance with the differences observed in terms of temperature and relative humidity in Figure 9.1 and Figure 9.2.

1.6 Influence of these hypothesis depending on the income parameters

As it is previously underlined, the hypothesis 1 and 2 are quite common, and, most of the time, they lead to accurate results. The differences observed in this paper are due to the particular transport characteristics of rammed earth material (quite high water content and water permeability in the hygroscopic saturation domain). In order to be more specific on that point, an analysis is performed on the liquid water permeability, which is the transport parameter for which the uncertainty is the most important. Indeed, a direct measurement of the relative permeability in the hygroscopic domain is particularly difficult to realize.

The test is made considering the loading path LP1 as it is the one who leads to the strongest differences between the simulations "a" (reference) and the simulation "d" (accounting for hypothesis 1 and 2).

A linear variation of the liquid permeability with water content is considered in the simulation.

$$\kappa\kappa_r^L = \kappa^* \cdot w_L \tag{9.6}$$

with:
κ [m^2] : intrinsic permeability of the porous medium
κ_r^L [-] : relative liquid permeability
κ^* [$m^5.kg^{-1}$] : slope of the linear formulation
w_L [$kg.m^{-3}$] : water content

Since a linear variation of liquid water permeability with water content is considered in the simulation, the parametric study is made on the slope of this latter, i. e. $\kappa*$.

Note that a different form is used in this case, in comparison with the modelling of liquid water absorption, and the reason is the change of saturation domain. Indeed, even if the relation is assumed to be linear, the slope changes between the hygroscopic and capillary domains.

The results are presented in Figure 9.4. To enable a better understanding, the variation of the liquid permeability with the relative humidity, depending on the slope, are drawn in Figure 9.4a. The models were compared according to the amplitude of the temperature variations at the middle of the wall induced by the hygrothermal coupling.

The comparison between case "a" (complete model) and case "b" (hypothesis 1) is quite intuitive as the permeability is in factor of the additional term. When the permeability is low, the difference between the two formulations tends to zero; as the permeability increases, the gap increases, and can reach 5°C of difference.

It is not surprising that varying the liquid permeability doesn't seem to have any effect when considering the other hypothesis as the hygrothermal coupling are strongly reduced in these cases.

In order to provide an additional illustration of the impact of these hypotheses, the order of magnitude of the ratios K_2^T/K_1^T (test of hypothesis 1) and DD/MV

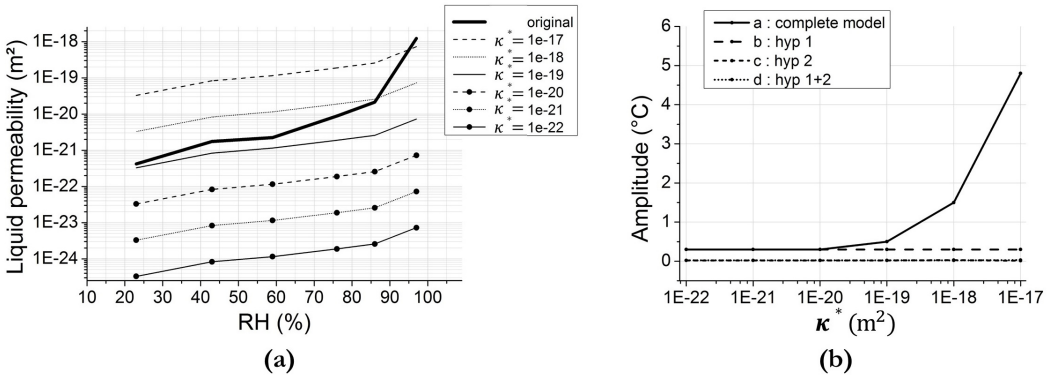

Figure 9.4: (a) Variation of the liquid permeability with the relative humidity, depending on the slope of the linear variation with water content; (b) Influence of the liquid permeability (taken at 50%RH) on the hygrothermal coupling effects (amplitude (a)) depending on the hypothesis when following LP1.

(test of hypothesis 2) is calculated for each loading path.

The results are illustrated in Figure 9.5, which represents, for each hypothesis and each loading path, the variation of the ratios with the diffusion coefficient, for different liquid permeabilities. When the ratio is lower than 10, the hypothesis is considered as not acceptable. This case is noted as "not valid" in the graphs. However, these simulations show that, when the ratio is lower than 50, noticeable differences are observed between the complete model and the models with the assumptions. This case is noted as "critical" is the graphs. It can be observed that, except for a low liquid permeability or a relatively low liquid permeability with high diffusion coefficient, the situation is critical, and both hypotheses 1 and 2 should not be assumed.

The model is used to assess the accuracy and impacts of the simplifying assumptions commonly made by the hygrothermal models for buildings materials. It follows that, due the singularities of the materials considered (from very low water content to near saturation, high porosity, large variation of water content during its life-time, ...), it is necessary to take into account the impact of thermal gradient on water flow and the variation of in-pore vapour mass. However, the sensibility analysis realized on the liquid water permeability underlines that these simplifying assumptions can be made for material with a lower water permeability, which is the case for most hygroscopic materials.

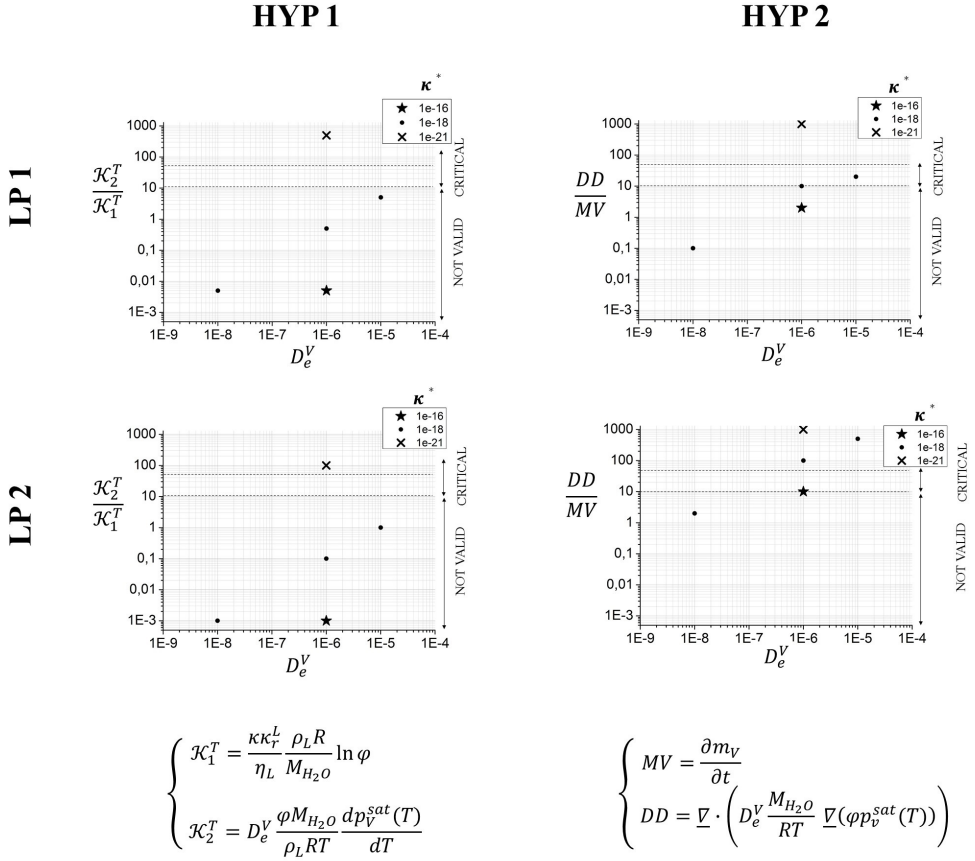

Figure 9.5: Variation of the ratio between the coefficient kept and the one neglected for different values of liquid permeabilities and coefficient diffusion, for both loading paths and hypothesis.

Part IV

General conclusion

The different parts of my PhD can be summarized recalling the main objectives of the founding project described in introduction.

First, the rammed earth behaviour is experimentally evaluated at different levels.

The thermal performances of the material were evaluated through data collected on an occupied house, both in the wall and at various spots in the building. The study reveals the great thermal capacity of the wall, which enables a large heat storage to be released with an important phase change. This capacity enables to take a great advantage of the solar radiation, and underlines the importance of a good architecture.

The moisture regulation of the house is also highlighted but the buffering capacity of the material isn't fully observable at building level, as, for instance, the sensors are located too deep in the wall and can not witness the behaviour of the surface on the first centimetres. However, a laboratory characterization, thanks to common parameters and dynamic tests, points out the good buffering capacity of the material. On the other hand, a parallel investigation is carried out to clarify the conditions of liquid absorption in the material, as the majority of pathological cases of earthen constructions are related to rising damps.

Finally, the coupling occurring between heat and moisture in the material is measured on samples thanks to a thermographic camera.

The other part of my work deals with the numerical modelling of the rammed earth's behaviour.

The coupled model is developed while taking care of the common assumptions made in the software WUFI [89] in order to question their suitability for earthen materials. It is then validated thanks to a comparison with analytical solutions from benchmarks. The in-come parameters, especially the vapour transfer coefficient and the liquid permeability, are calibrated using the previous experimental data. From simple to complex solicitations are tested, on different ranges of saturation of the material.

The coupled model is able to reproduce the majority of the experimental behaviours, provided a correct characterization of the material.

Several aspects of the work presented in this thesis drive to further investigations.

The study of the saturated material is essential given the importance of damages related to rising damps. The thermographic camera tested on samples can appear as a convenient tool to evaluate the position of the moisture front in a construction, and provide an on-site and non destructive technique to identify the risk of collapse. However, for now, it assumes no coating. On the other hand, the saturated state of the material is also observed in the early ages of the construction and the gravimetric influence on the water content repartition in the wall can constitute another field of investigation.

In terms of numerical modelling, the limits of pure thermal calculation at building scale could be noticed in the body of the manuscript, and required specific environmental conditions to be rightly used. The crossed measurements (relative humidity/temperature/water content) in the walls provide data to analyse the coupling effects on-site, and present an opportunity to face the experiment with the coupled model inside the wall. The broadening of this work would be to link the modelling with the data of the indoor and outdoor environments.

To finish with, the latest version of COMSOL Multiphysics offers the possibility to create an interface in which the model is implemented but not visible. It thus enable non-specialists to use it without having to deal with complex equations, allowing other partners of the project to fully take advantage of the research's results.

Appendix

Appendix A

Relative humidity and vapour pressure variations for internal and external environments

The flux at the internal surface of the wall is characteristic of the water vapour exchange between the wall and the indoor environment. The following appendix focus on how the walls deals with the water vapour flux, how it is changed between outdoor and indoor areas.

Figure A.1 displays the RH variations between indoor and outdoor climates for one week of each season.

First of all, note that the "indoor" relative humidity is higher than the one displayed in Figure 5.2, and the reason is that the data used is from the sensor very close to the wall. The water vapour evaporation increases the local relative humidity.

The reduction of moisture variations between external and internal climates appears to be very important for all the seasons, and the difference of amplitude even reaches a decrease of 30%RH. In order to provide a better quantification, the standard deviation of each distribution was calculated, and the scattering was representative of the amplitude of the external and internal distributions. The values, gathered in Table A.1, are very illustrative, as the standard deviation is always higher for the outside distribution, and even for the winter period where only few amplitude variations were measured.

The table and graphs also reveal the more important internal fluctuation of the relative humidity over the week in spring, even if it remains below the external variations. It can be explained by the natural ventilation of the house: the two climates tends to become similar.

Finally, for the winter's week, the very high outside relative humidity doesn't seem to affect the internal relative humidity. This reveals a rather good insulation of the house regarding the water vapour.

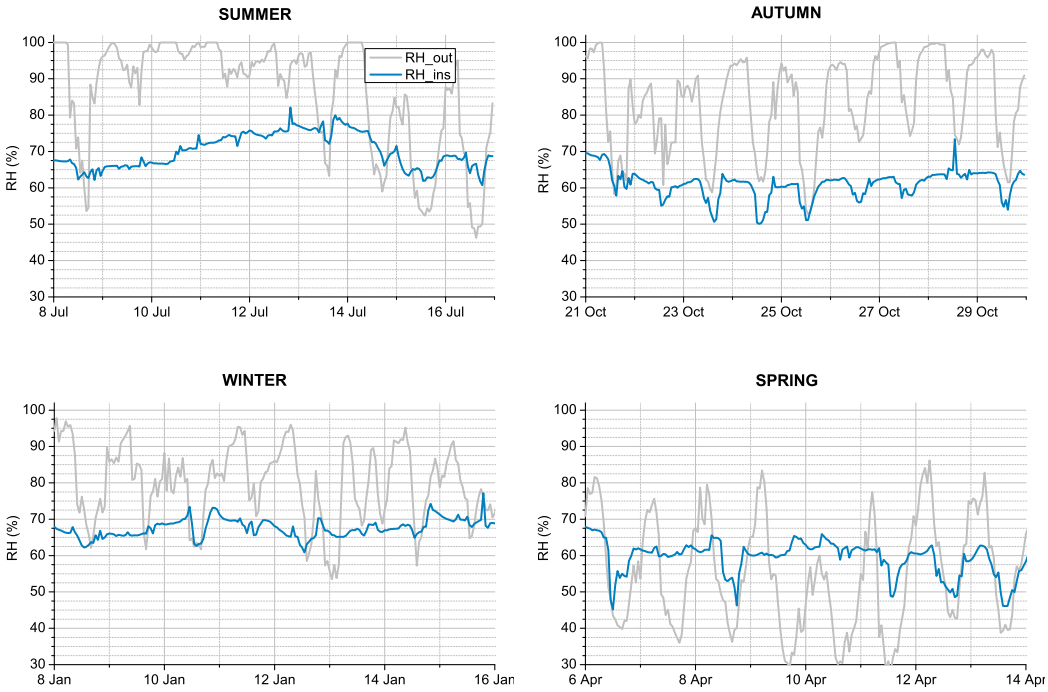

Figure A.1: Inside and outside relative humidity variations during one week, for each season.

	φ_{out}	φ_{ins}
Summer	17	7
Autumn	15	6
Winter	13	4
Spring	18	6

Table A.1: Standard deviations of the "φ_{out}" and "φ_{ins}" distribution for the selected weeks of the different seasons.

In order to have a better insight of the flux, Figure A.2 displays the vapour pressure variations for internal and external climates during the same periods.

As usual, it can be noticed that external vapour pressure is lower than the internal one. In summer, both vapour pressures become close to each other : it can be assumed that it is due to the natural ventilation of the house. The differences between the two vapour pressure is globally more important in cold seasons despite the heating device. Finally, the internal vapour pressure is rather homogeneous throughout the year, despite the seasonal variations of both external temperature and relative humidity.

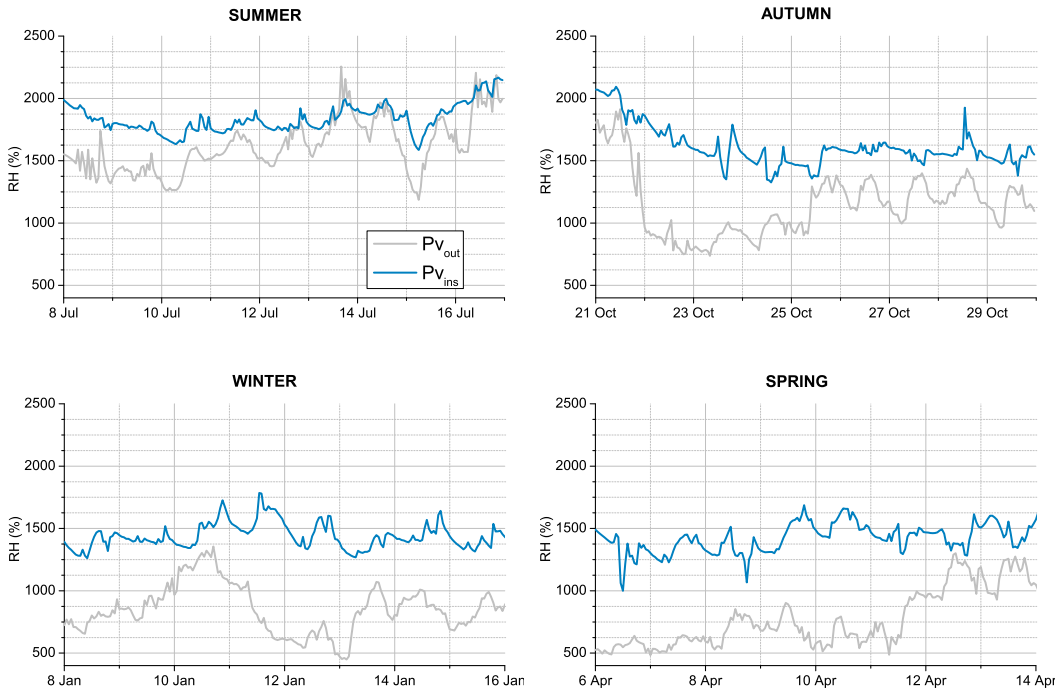

Figure A.2: Inside and outside vapour pressure variations during one week, for each season.

Appendix B

Suction measurement with filter papers

The point to be focused on in this part is to know more accurately the behaviour of the material in the range of relative humidity above 95%. Knowing the relation between the capillary pressure and the relative humidity (Kelvin Law), at constant temperature, there is a direct link between the sorption isotherm and the corresponding retention curve. Points of the sorption isotherm in the high relative humidity can be obtained measuring the capillary pressure in low pressure (below 5 MPa at 20°C), which appears to be easier.

1 Literature review

Measuring the capillary pressure or suction in soils can be done using different methods, more or less accurate for different types of soils and pressure ranges. The document [44] provides a good overview of the common methods:

- The most spread technique, the *tensiometric measurement* consists in measuring the negative pressure of liquid water using a thin saturated porous stone. The range of practical application is for pressures between 0 and 80 kPa.
- In *psychrometric measurements*, the relative humidity is measured close to the interstitial water of the non-saturated soil, from which is deduced the suction thanks to the Kelvin law. The relative humidity is calculated through the dew point temperature of the considered atmosphere. It is a quite sophisticated method and remains unusual. The pressures thus determined don't exceed 7 MPa.
- *Filter paper* method is a simple and convenient method to measure suction as it only requires a 1/10 000e weighting scale. It consists in using a filter paper

whose retention curve was determined before, putting it in a sample and wait for equilibrium between the filter paper and the soil. After extraction, knowing the water content of the paper, and its retention curve, it leads to the suction of the soil. Depending on which type of filter paper is used, several calibration curve can be found in the literature [20][21][14][110].

This last method was chosen and the practical protocol is described in the standard [14].

2 Experimental procedure

The experimental investigation is divided into two parts: the calibration of the filter paper and the suction measurement in the studied soil.

2.1 Calibration of the filter paper

Since many different calibration curves for the paper Whatman n°42 can be found, depending on the environment and other parameters, the calibration of the same filter paper was realized in the laboratory.

Three filter papers Whatman n°42 (S1,S2, and S3) were placed in Petri dishes and stored in a climatic chamber at 20°C and varying relative humidity. To ensure a more precise measurement of the atmosphere relative humidity and temperature, a T/RH sensor was placed near the Petri dishes (EL-USB-2, Lascar electronics, Salisbury, UK). The effective relative humidity were 51%, 55%, 60%, 65%, 70%, 75%, 80%, 86%, 90%, 97% with +/-2%, according to the sensor accuracy in that range. The filter papers were weighted dry and wet, after 3 days in the chamber at a given relative humidity to make sure the equilibrium was reached, for each relative humidity. This provides the water content of the paper filter for the different relative humidity. At 20°C, using the Kelvin law, the capillary pressure can be deduced from the relative humidity, thus leading to the retention curve of the filter paper.

2.2 Suction measurement

The suction was chosen to be measured on cylindrical samples whose diameter was 15.2 cm, and twice 1 cm thick. They were manufactured with the studied soils at different mass water content (4%, 8%, 12%, 15% and 18%) with four samples each. Three filter papers, dried before, were put in-between the two layers during manufacture, the one in the center having a diameter about 5 mm below the two others to prevent it from soil contamination. An illustration of the samples can be found in Figure B.1.

The sample was then sealed with plastic film and stored in a regulated room for 7 days. The samples were weighted before and after the equilibrium period to ensure the correct sealing. After that period, the samples were destroyed with care to extract the central filter paper and retrieve its mass. The dry mass being measured

previously, for each water content of the soil, the corresponding mass water content of the filter paper is obtained. Thanks to the calibration curve established before, the retention curve and then the sorption isotherm of the soil can be deduced.

Figure B.1: Suction measurement on earthen cylindrical samples.

3 Results and discussion

3.1 Calibration of the filter paper

The mass water content of the three samples (S1, S2, S3) was determined for different relative humidity, at constant temperature, which gives access to the capillary pressure (or suction) thanks to the Kelvin law. The water content for the three samples studied and the average curve are presented in Figure B.2. A good repeatability of the measure can be observed. What's more, the calibration of the filter paper was made only in the range of effective water content of the studied soil, i.e. between 3 MPa and 90 MPa. The exponential regression of the average curve (with a R^2 equal to 0.96) was then used as a calibration function in the second part.

3.2 Suction measurement

The direct correspondence between the water content of the soil and the water content of the filter paper is given in Figure B.2. During the extraction, several filter papers were damaged, which explains why there are only 2 points for 8% of mass water content of the soil and 3 points for 15%. Nevertheless, this didn't prevent the results exploitation. For each water content of the soil, the mean value was calculated and used to get the suction of the soil using the calibration curve.

At last, the retention curve of the soil could be determined, as well as the sorption isotherm at 20°C, both gathered in Figure B.3. The initial measurements ("saline solution") of the sorption isotherm were also added.

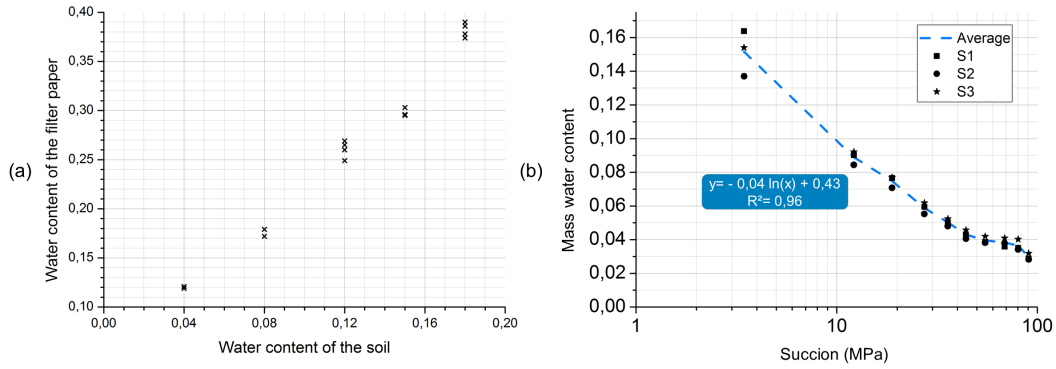

Figure B.2: (a) Water content of the filter paper against water content of the soil ; (b) Calibration curve of the filter paper Whatman n°42.

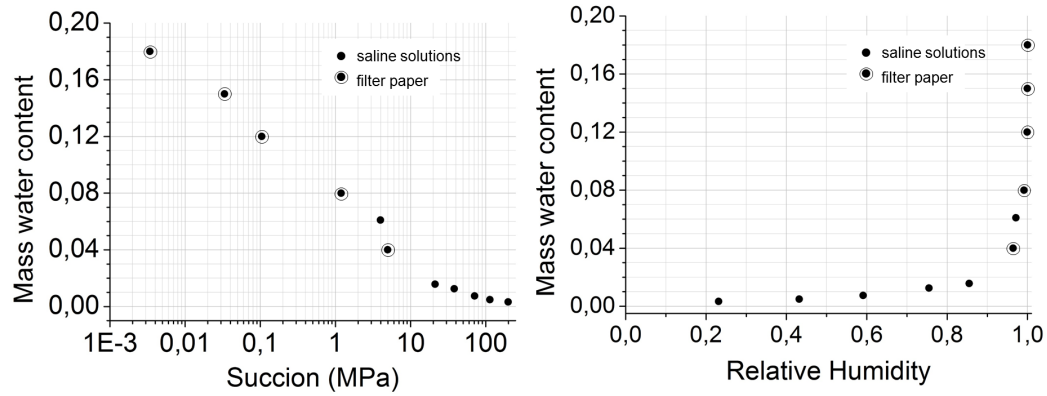

Figure B.3: Final retention curve and sorption isotherm at 20°C.

A good correlation can be observed between the "saline solution" data and the one measured with the filter paper. It then appears that these two methods complement one another to describe the behaviour of the soil in both hygroscopic and capillary domains.

Appendix C

Details on equations development

In this appendix, details are provided regarding the developpement of the equations upon different points.

1 Moisture dependant expression of latent heat

1.1 First method

Let's consider for this part the pure phase I. Its specific free enthalpy reads [85]:

$$dG_I = \phi_I dp_I - S_I dT + \mu_I dn_I \tag{C.1}$$

with:
μ_I [J.mol^{-1}] : chemical potential of I
S_I [J.K^{-1}] : entropy of I per unit of porous media
n_I [mol] : mole quantity of I per unit of porous media

Moreover, the following equations of states can be derived from the well-known Gibbs-Duhem relation:

$$\frac{1}{\rho_I} = \frac{\partial g_I}{\partial p_I} \quad ; \quad s_I = -\frac{\partial g_I}{\partial T} \tag{C.2}$$

Assuming the liquid water is a pure phase, equations (C.1) and (C.2) can be applied. Linking the free enthalpy to the chemical potential through the Euler relation, under the small perturbations assumption, and keeping only the first order terms, the integration of the equations of states leads to:

$$g_L = g_L^0 - s_L^0(T - T_0) - C_{p,L}\left(T \ln\left(\frac{T}{T_0}\right) - (T - T_0)\right) + \frac{\Delta p_L}{\rho_L} \tag{C.3}$$

Assuming the phase G as an ideal gas mixture of perfect gas and estimating the specific free enthalpy of the water vapour from its standard specific free enthalpy,

to whom equations (C.1) and (C.2) can be applied, the specific free enthalpy of the water vapour reads:

$$g_V = g_V^0 - s_V^0(T-T_0) - C_{p,V}\left(T\ln\left(\frac{T}{T_0}\right) - (T-T_0)\right) + \frac{RT}{M_{H_2O}}\ln\left(\frac{p_V}{p_V^{sat}(T_0)}\right) \quad \text{(C.4)}$$

Through equation (C.2), specific free entropy of liquid water and water vapour can be estimated, at first order, by:

$$s_L = s_L^0 + C_{p,L}\ln\left(\frac{T}{T_0}\right) \quad \text{(C.5)}$$

$$s_V = s_V^0 + C_{p,V}\ln\left(\frac{T}{T_0}\right) - \frac{R}{M_{H_2O}}\ln\left(\frac{p_V}{p_V^{sat}(T_0)}\right) \quad \text{(C.6)}$$

Finally, the latent heat associated to the liquid/vapour phase change, defined as $L = T(s_V - s_L)$ is a function of the temperature and the equilibrium vapour pressure. Using equations (7.5) (C.3) (C.6), this expression eventually becomes:

$$\boxed{L = L_0 + (C_{p,V} - C_{p,L})(T-T_0) - \frac{RT}{M_{H_2O}}\ln\varphi} \quad \text{(C.7)}$$

1.2 Second method

Another way to derive this relation is to use the following Clausius-Clapeyron-like relation:

$$L = -\frac{R}{M_{H_2O}}\left(\frac{\partial \ln p_V}{\partial(1/T)}\right)_{p_L} = \frac{RT^2}{M_{H_2O}}\left(\frac{\partial \ln p_V}{\partial(T)}\right)_{p_L} \quad \text{(C.8)}$$

L can thus be understood as the integral enthalpy of the phase change process per unit of mass. Since $p_V = \varphi p_V^{sat}$, the use of the Kelvin's law (eq.7.4) allows to write this equation in the following form:

$$L = -\frac{RT}{M_{H_2O}}\ln(\varphi) + \frac{RT^2}{M_{H_2O}p_v^{sat}(T)}\frac{dp_V^{sat}(T)}{dT} \quad \text{(C.9)}$$

The final step consists in replacing p_V^{sat} by its expression reported in eq.7.6 . It leads to:

$$\frac{dp_V^{sat}(T)}{dT} = \frac{M_{H_2}O}{RT^2}p_v^{sat}(T)\cdot(L_0 + (C_{p,V} - C_{p,L})(T-T_0)) \quad \text{(C.10)}$$

which eventually gives:

$$\boxed{L = L_0 + (C_{p,V} - C_{p,L})(T-T_0) - \frac{RT}{M_{H_2O}}\ln\varphi} \quad \text{(C.11)}$$

2 Thermal balance equation

According to the second law of thermodynamics and assuming no source volume term of heat, the entropy balance is equal to:

$$\frac{\partial S}{\partial t} + \underline{\nabla} \cdot \left(\sum_{i=L,V,A} s_i m_i \underline{V_i} \right) = -\underline{\nabla} \cdot \left(\frac{\underline{q}}{T} \right) + \frac{D}{T} \tag{C.12}$$

with :

S [J.K^{-1}]: total entropy of the porous medium, equal to the sum of the entropy of each phase: $S = s_s + m_L s_L + m_A s_A + m_V s_V$

q [W.m^{-2}] : outgoing heat flow vector that follows the Fourier Law : $\underline{q} = -\lambda \underline{\nabla} T$

D [] : total dissipation of the system, equal to the sum of the mechanical dissipation D_M of the skeleton and the in-pore fluids, and the thermal dissipation D_{th}

The latter is equal to:

$$D_{th} = -\frac{\underline{q}}{T} \underline{\nabla} T \tag{C.13}$$

The combination of all this leads to:

$$T \frac{\partial S}{\partial t} + T \left(\sum_i s_i \underline{\nabla} \cdot \left(m_i \underline{V_i} \right) + \sum_i \left(m_i \underline{V_i} \right) \underline{\nabla} s_i \right) = -T \left(\frac{1}{T} \underline{\nabla} \cdot \underline{q} - \underline{\nabla} \left(\frac{1}{T} \right) \cdot \underline{q} + \underline{q} \frac{\nabla T}{T} + D_M \right) \tag{C.14}$$

In the following, we consider the heat source due to mechanical dissipation is negligible. Under these assumptions, accounting for the mass conservation equations and the previous equations, it becomes:

$$T \left(\frac{\partial S_S}{\partial t} + \sum_{i=L,V,A} m_i \frac{\partial s_i}{\partial t} + \dot{m}_{\to V} (s_V - s_L) + \sum_{i=L,V,A} \underline{g_i} \cdot \underline{\nabla} \underline{s_i} \right) = -\underline{\nabla} \cdot \underline{q} \tag{C.15}$$

with:

$\underline{g_i} = m_i \underline{V_i}$: the mass filtration vector of the phase i.

Assuming that the entropy of the solid skeleton is only function of temperature, it reads:

$$dS_S = (1 - \phi) \rho_d \frac{C_{p,S}}{T} dT \tag{C.16}$$

On the other side, the use of the state functions combined with the specific free enthalpy expressions leads, at first order, to:

$$ds_L = \frac{C_{p,L}}{T} dT \quad ; \quad ds_V = \frac{C_{p,V}}{T} dT - \frac{R}{M_{H_2O}} \frac{dp_V}{p_V} \quad ; \quad ds_A = \frac{C_{p,A}}{T} dT + \frac{R}{M_{H_2O}} \frac{dp_A}{p_A} \tag{C.17}$$

Given the constant total gas pressure, water vapour and dry air pressures are related through : $dP_A = -dP_V$

The use of these three last relations and of the expression of the latent heat of evaporation $L = T(s_V - s_L)$ leads to the following expression:

$$\rho C_p \frac{\partial T}{\partial t} + \left(\sum_{i=L,V,A} C_{p,i} \underline{g}_i \right) \cdot \underline{\nabla} T + \dot{m}_{\to V} L(T, \varphi) = \underline{\nabla} \cdot (\lambda \underline{\nabla} T) \tag{C.18}$$

This equation allows to clearly identifying the different terms of the heat balance. The term $\lambda \underline{\nabla} T$ stands for the heat flow, which is equal to the sum of the variation in sensitive heat $\rho C_p \frac{\partial T}{\partial t} + (\sum_{i=L,V,A} C_{p,i} \underline{g}_i) \cdot \underline{\nabla} T$ (which becomes null if the temperature is constant and homogeneous) and in latent heat $\dot{m}_{\to V} L(T, \varphi)$ (which becomes null if there is no liquid to vapour phase change). The second term of the sensitive heat variation, namely $(\sum_{i=L,V,A} C_{p,i} \underline{g}_i) \cdot \underline{\nabla} T$, is due to the heat convectively transported by the fluids (vapour and water). This term can be neglected when the Péclet number is strongly lower than 1, which is the case for heat transfer within earth material (because $\sum_{i=L,V,A} C_{p,i} \underline{g}_i l \ll \lambda$, where l is the characteristic length of the considered system).

This assumption allows then to write the thermal equation in its final form:

$$\boxed{\rho C_p \frac{\partial T}{\partial t} = \underline{\nabla} \cdot (\lambda \underline{\nabla} T) - \dot{m}_{\to V} L(T, \varphi)} \tag{C.19}$$

3 Connection between the detailed formulation and the literature

Usually considered as a reference and implemented in the software WUFI, the formulation detailed in [89] leads to characteristic parameters. In order to ensure the right understanding of the formulation presented in this paper, the connection between the coefficients is highlighted in this appendix.

The final formulation of the coupled equations in [89] reads :

$$\frac{\partial H}{\partial T} \frac{\partial T}{\partial t} = \underline{\nabla} \cdot (\lambda \nabla T) + h_v \underline{\nabla} \cdot (\delta p \nabla (\varphi p_{sat})) \tag{C.20}$$

$$\frac{\partial w_p}{\partial \varphi} \frac{\partial \varphi}{\partial t} = \underline{\nabla} \cdot (D_\varphi \nabla \varphi + \delta p \nabla (\varphi p_{sat})) \tag{C.21}$$

with w_p the water content in kg.m^{-3}.

Taking into account the hypothesis already mentioned in the article, and given equations 7.16 and 7.26, we finally obtain:

$$h_v = l(\varphi, T) \tag{C.22}$$

$$D_\varphi = \rho_L^2 \frac{\kappa \kappa_r^L}{\eta_L} \frac{RT}{M_{H_2O} \varphi} \tag{C.23}$$

$$\delta p = D_e^V \frac{M_{H_2O}}{RT} \tag{C.24}$$

4 Systems of equations corresponding to the different hypothesis

The four simulations carried out consider four different systems of equations, coming from hypothesis explained previously. To make things clearer, those four systems are gathered in the appendix.

4.1 Complete model "a"

The first one considers none of the hypotheses, and is referenced as "a".

$$\frac{1}{\rho_L}\left(\rho_d\frac{\partial w_L}{\partial w_\varphi}+\phi_G\frac{M_{H_2O}p_v^{sat}(T)}{RT}\right)\frac{\partial\varphi}{\partial t}+\frac{\phi_G\rho_v^\alpha}{\rho_L}\frac{\partial T}{\partial t}=\underline{\nabla}\cdot(K^T\underline{\nabla}T+K^\varphi\underline{\nabla}\varphi) \quad \text{(C.25)}$$

$$\rho_V^\alpha=\varphi\frac{p_V^{sat}(T)M_{H_2O}}{RT}\left(\frac{1}{p_V^{sat}(T)}\frac{dp_V^{sat}(T)}{dT}-\frac{1}{T}\right) \quad \text{(C.26)}$$

$$K_a^T=K_1^T+K_2^T=\frac{\kappa\kappa_r^L}{\eta_L}\frac{\rho_L R}{M_{H_2O}}\ln\varphi+D_e^V\frac{\varphi M_{H_2O}}{\rho_L RT}\frac{dp_V^{sat}(T)}{dT} \quad \text{(C.27)}$$

$$K_a^\varphi=\frac{\kappa\kappa_r^L}{\eta_L}\frac{\rho_L R}{M_{H_2O}\varphi}+D_e^V\frac{M_{H_2O}}{\rho_L RT}p_v^{sat}(T) \quad \text{(C.28)}$$

$$\rho C_p\frac{\partial T}{\partial t}-\left(L(\varphi,T)\rho_d\frac{\partial w_L}{\partial\varphi}\right)\frac{\partial\varphi}{\partial t}=\underline{\nabla}\cdot(\lambda\underline{\nabla}T)+L(\varphi,T)\underline{\nabla}\cdot(L^T\underline{\nabla}T+L^\varphi\underline{\nabla}\varphi) \quad \text{(C.29)}$$

$$L_a^T=-\rho_L^2\frac{\kappa\kappa_r^L}{\eta_L}\frac{R}{M_{H_2O}}\ln\varphi \quad \text{(C.30)}$$

$$L_a^\varphi=-\rho_L^2\frac{\kappa\kappa_r^L}{\eta_L}\frac{RT}{M_{H_2O}\varphi} \quad \text{(C.31)}$$

4.2 Model with hypothesis 1

The second one considers only the hypothesis 1 related to the flow of liquid water, and is referenced as "b".

$$\frac{1}{\rho_L}\left(\rho_d\frac{\partial w_L}{\partial w_\varphi}+\phi_G\frac{M_{H_2O}p_v^{sat}(T)}{RT}\right)\frac{\partial\varphi}{\partial t}+\frac{\phi_G\rho_v^\alpha}{\rho_L}\frac{\partial T}{\partial t}=\underline{\nabla}\cdot(K^T\underline{\nabla}T+K^\varphi\underline{\nabla}\varphi) \quad \text{(C.32)}$$

$$\rho_V^\alpha=\varphi\frac{p_V^{sat}(T)M_{H_2O}}{RT}\left(\frac{1}{p_V^{sat}(T)}\frac{dp_V^{sat}(T)}{dT}-\frac{1}{T}\right) \quad \text{(C.33)}$$

$$K_b^T=K_2^T=D_e^V\frac{\varphi M_{H_2O}}{\rho_L RT}\frac{dp_V^{sat}(T)}{dT} \quad \text{(C.34)}$$

$$K_a^\varphi=\frac{\kappa\kappa_r^L}{\eta_L}\frac{\rho_L R}{M_{H_2O}\varphi}+D_e^V\frac{M_{H_2O}}{\rho_L RT}p_v^{sat}(T) \quad \text{(C.35)}$$

$$\rho C_p \frac{\partial T}{\partial t} - \left(L(\varphi, T) \rho_d \frac{\partial w_L}{\partial \varphi} \right) \frac{\partial \varphi}{\partial t} = \underline{\nabla} \cdot (\lambda \underline{\nabla} T) + L(\varphi, T) \underline{\nabla} \cdot (L^T \underline{\nabla} T + L^\varphi \underline{\nabla} \varphi) \quad \text{(C.36)}$$

$$L_a^T = -\rho_L^2 \frac{\kappa \kappa_r^L}{\eta_L} \frac{R}{M_{H_2O}} \ln \varphi \quad \text{(C.37)}$$

$$L_a^\varphi = -\rho_L^2 \frac{\kappa \kappa_r^L}{\eta_L} \frac{RT}{M_{H_2O} \varphi} \quad \text{(C.38)}$$

4.3 Model with hypothesis 2

The third one considers only the hypothesis 2 related to the expression of the evaporation / condensation rate, and is referenced as "c".

$$\frac{1}{\rho_L} \left(\rho_d \frac{\partial w_L}{\partial w_\varphi} + \phi_G \frac{M_{H_2O} p_v^{sat}(T)}{RT} \right) \frac{\partial \varphi}{\partial t} + \frac{\phi_G \rho_v^\alpha}{\rho_L} \frac{\partial T}{\partial t} = \underline{\nabla} \cdot (K^T \underline{\nabla} T + K^\varphi \underline{\nabla} \varphi) \quad \text{(C.39)}$$

$$\rho_V^\alpha = \varphi \frac{p_V^{sat}(T) M_{H_2O}}{RT} \left(\frac{1}{p_V^{sat}(T)} \frac{dp_V^{sat}(T)}{dT} - \frac{1}{T} \right) \quad \text{(C.40)}$$

$$K_a^T = K_1^T + K_2^T = \frac{\kappa \kappa_r^L}{\eta_L} \frac{\rho_L R}{M_{H_2O}} \ln \varphi + D_e^V \frac{\varphi M_{H_2O}}{\rho_L RT} \frac{dp_V^{sat}(T)}{dT} \quad \text{(C.41)}$$

$$K_a^\varphi = \frac{\kappa \kappa_r^L}{\eta_L} \frac{\rho_L R}{M_{H_2O} \varphi} + D_e^V \frac{M_{H_2O}}{\rho_L RT} p_v^{sat}(T) \quad \text{(C.42)}$$

$$\rho C_p \frac{\partial T}{\partial t} = \underline{\nabla} \cdot (\lambda \underline{\nabla} T) + L(\varphi, T) \underline{\nabla} \cdot (L^T \underline{\nabla} T + L^\varphi \underline{\nabla} \varphi) \quad \text{(C.43)}$$

$$L_c^T = \frac{M_{H_2O}}{RT} D_e^V \varphi \frac{dp_V^{sat}(T)}{dT} \quad \text{(C.44)}$$

$$L_c^\varphi = \frac{M_{H_2O}}{RT} D_e^V p_v^{sat}(T) \quad \text{(C.45)}$$

Appendix D

Implementation in COMSOL Multiphysics

COMSOL Multiphysics®is a finite element simulation software for multiple physic and engineering applications. The interface environment is designed for cross-disciplinary fields of study. Numerous modules are available, categorized according to applications areas such as electrical, mechanical, chemical, ... interfaces in order to facilitate the coupling of different physics on the same modelling.

This software appeared to be an ideal tool to implement the developed model, given its easy-to-use interface with no compromise on the transparency on the calculation.

The implementation of the model is described in this appendix.

1 PDE module

The system of partial differential equations is solved using COMSOL Multiphysics, via the PDE (Partial Differential Equations) interface, and more precisely the coefficients form. This enables to provide the coefficients in order to solve the following equation:

$$e_a \frac{\partial^2 u}{\partial t^2} + d_a \frac{\partial u}{\partial t} + \nabla \cdot (-c\nabla u - \alpha u + \gamma) + \beta \cdot \nabla u + au = f \tag{D.1}$$

The system of equations was then rearranged as follows:

$$\begin{bmatrix} d_a11 & d_a12 \\ d_a21 & d_a22 \end{bmatrix} \cdot \begin{bmatrix} \frac{\partial \varphi}{\partial t} \\ \frac{\partial T}{\partial t} \end{bmatrix} + \underline{\nabla} \cdot \left(- \begin{bmatrix} c11 & c12 \\ c21 & c22 \end{bmatrix} \underline{\nabla} \begin{bmatrix} \varphi \\ T \end{bmatrix} \right) = 0 \tag{D.2}$$

with the corresponding values for the different coefficients (regarding the complete

model):

$$d_a11 = \rho_d \frac{\partial w_L}{\partial \varphi} + \phi_G \frac{M_{H_2O}}{RT} p_v^{sat}(T) \tag{D.3}$$

$$d_a12 = \varphi \phi_G p_v^{sat}(T) \frac{M_{H_2O}}{RT} \left(\frac{1}{p_v^{sat}(T)} \frac{dp_v^{sat}(T)}{dT} - \frac{1}{T} \right) \tag{D.4}$$

$$d_a21 = -L(\varphi, T) \rho_d \frac{\partial w_L}{\partial \varphi} \tag{D.5}$$

$$d_a22 = \rho C_p = (1-\phi)\rho_S C_S + \phi(S_r \rho_L C_L + (1-S_r)(\rho_A C_A + \rho_V C_V)) \tag{D.6}$$

$$c11 = \rho_L^2 \frac{\kappa \kappa_r^L}{\eta_L} \frac{RT}{M_{H_2O}\varphi} + D_e^V \frac{M_{H_2O}}{RT} p_v^{sat}(T) \tag{D.7}$$

$$c12 = \rho_L^2 \frac{\kappa \kappa_r^L}{\eta_L} \frac{R}{M_{H_2O}} \ln \varphi + + D_e^V \frac{M_{H_2O}}{RT} \varphi \frac{dp_v^{sat}(T)}{dT} \tag{D.8}$$

$$c21 = -L(\varphi, T) \rho_L^2 \frac{\kappa \kappa_r^L}{\eta_L} \frac{RT}{M_{H_2O}\varphi} \tag{D.9}$$

$$c22 = \lambda(w_L) - L(\varphi, T) \rho_L^2 \frac{\kappa \kappa_r^L}{\eta_L} \frac{R}{M_{H_2O}} \ln \varphi \tag{D.10}$$

2 Boundary conditions

Boundary conditions of the simulations are set in accordance with measurements. Thermal and moisture exchanges on the surfaces, of normal outward vector $\underline{n}$, verify the following equation:

$$\begin{bmatrix} (\underline{g_L} + \underline{g_V}) \cdot \underline{n} \\ (\underline{g_T} - L\underline{g_L}) \cdot \underline{n} \end{bmatrix} = \begin{bmatrix} -\rho_L (K^T \underline{\nabla} T + K^\varphi \underline{\nabla} \varphi) \cdot \underline{n} \\ (-\lambda \underline{\nabla} T + L(L^T \underline{\nabla} T + L^\varphi \underline{\nabla} \varphi)) \cdot \underline{n} \end{bmatrix} \tag{D.11}$$

$$= \begin{bmatrix} \beta(p_v^{sat}(T_a)\varphi_a - p_v^{sat}(T_S)\varphi_S) \\ \alpha(T_a - T_S) \end{bmatrix} \tag{D.12}$$

With:
$\underline{n}$: outgoing vector at the considered boundary
$\underline{g_L}$: liquid water flow vector
$\underline{g_V}$: water vapour flow vector
$\underline{g_T}$: heat flow vector
φ_a and T_a : relative humidity and temperature of the ambient air
φ_S and T_S : surface relative humidity and temperature
α [W.m^{-2}.K^{-1}] : heat transfer coefficient

Note that this boundary condition assumes not flow of liquid water through the considered surfaces. That is to say, all the water which flows to the external surfaces is assumed to exist in vapour form. The latent effect of this phase change is taken into account by the term $-L\underline{g_L} \cdot \underline{n}$ in the boundary condition of the thermal equation.

3 Mesh and time step

The system of equations is solved using a different mesh and time step for each case. They are determined as follows :

- the calculation is successively run with a decreasing size of mesh element and time step
- when the difference between two calculations is no more observable, the mesh and time step are kept
- the selected values are then the maximum size mesh element and time step providing the correct results, while keeping the calculation resources as minimal

Bibliography

[1] Karin Adalberth. Energy use in four multi-family houses during their life cycle. *International Journal of Low Energy and Sustainable Buildings*, 1:1–20, 1999.

[2] E A Adam and P J Jones. Thermophysical Properties of Stabilised Soil Building Blocks. *Building and Environment*, 30(2):245–253, 1995.

[3] ADEME. Déchets Edition 2015. Technical report, 2015.

[4] ADEME. Se chauffer au bois. Technical report, 2015.

[5] AFNOR. NF EN ISO 12572.pdf. Technical report.

[6] AFNOR. NF EN 1015-18 : Méthodes d'essai des mortiers pour maçonnerie - Partie 18 : détermination du coefficient d'absorption d'eau par capillarité du mortier durci, 2003.

[7] F. Alamdari and G.P. Hammond. Improved Data Correlations for Buoyancy-Driven Convection in Rooms. *Building Services Engineering Reserch and Technology*, 3(4):106–112, 1983.

[8] Dorothée Alex. Petit guide des Architectures en pisé à Lyon. Technical report, ENSAL, Lyon, 2011.

[9] D Allinson and M R Hall. Hygrothermal analysis of a stabilised rammed earth test building in the UK. *Energy and Buildings*, 42:845–852, 2010.

[10] Anthony Arundel, Elia Sterling, and Judith Biggin. Indirect health effect of relative humidity in indoor environments. *Environmental Health Perspectives*, 65:351, 1986.

[11] H Asan. Numerical computation of time lags and decrement factors for different building materials. *Building and Environment*, 41:615–620, 2006.

[12] ASHRAE Task Group. *Procedure for determining heating and cooling loads for computerising energy calculation.* ASHRAE Publications, New-York, algorithms edition, 1975.

[13] Niccolo Aste, Adriana Angelotti, and Michela Buzzetti. The influence of the external walls thermal inertia on the energy performance of well insulated buildings. *Energy and Buildings*, 41:1181–1187, 2009.

[14] ASTM. Standard Test Method for Measurement of Soil Potential (Suction) Using Filter Paper. volume 11, pages 1–6. 1995.

[15] David Baggs. Thermal mass and its role in Building Comfort and Energy Efficiency. *EcoSpecifier Technical Guides*, 2013.

[16] Bauklimatik Dresden TU. Delphin.

[17] Ian Beausoleil-Morrison. Modeling mixed convection heat transfer at internal building surface. In *Building Simulation 1*, pages 313–320, 1999.

[18] J Beckert. *Wirkung von Verunreinigungen der Raumluft auf den Menschen.* Düsseldorf, Germany, beckert & edition, 1986.

[19] MS Bhandari and NK Bansal. Solar heat gain factor and heat loss coefficients for passive heating concepts. *Solar Energy*, 53(2):199–208, 1994.

[20] K V Bicalho, A Gomes Correia, S Ferreira, J-m Fleureau, and F A M Marinho. Filter paper method of soil suction measurement. In *XIII Panamerican Conference on Soil Mechanics and Geotechnical Engineering*, 2007.

[21] Katia V Bicalho, Kamila F Cupertino, and Adelmo I Bertolde. Evaluation of suction-water content calibrations of filter paper. In *14th Panamerican Conference on Soil Mechanics and Geotechnical Engineering*, 2011.

[22] Benjamin Broustey. Construire en paille, 2016.

[23] Q B Bui. *Stabilité des structures en pisé : durabilité, caractéristiques mécaniques - Thèse de doctorat, Institut National des Sciences appliquées, Lyon.* PhD thesis, 2008.

[24] Jan Carmeliet, Filip Descamps, and Geert Houvenaghel. A mutliscale network model for simulating moisture transfer properties of porous media. *Transport in Porous Media*, 35:67–88, 1999.

[25] Jan Carmeliet, Martin H D De Wit, and Hans Janssen. Hysteresis and moisture buffering of wood. In *Symposium of Building Physics in the Nordic Countries*, number 3, pages 55–62, 2005.

[26] Maurice Cassan. *Les essais de perméabilité sur site dans la reconnaissance des sols.* 2005.

[27] P A Chabriac, E Gourdon, P Gle, A Fabbri, and H Lenormand. Agricultural by-products for building insulation : Acoustical characterization and modeling to predict micro-structural parameters. *Construction and Building Materials*, 112:158–167, 2016.

[28] Pierre-Antoine Chabriac. *Mesure du comportement hygrothermique du pisé.* PhD thesis, ENTPE, Université de Lyon, France, 2014.

[29] Pierre-Antoine Chabriac, Antonin Fabbri, J C Morel, Jean-Paul Laurent, and Joachim Blanc-Gonnet. A procedure to measure the in-situ Hygrothermal Behavior of Earth Walls. *Materials*, 7:3002–3020, 2014.

[30] Florian Champiré, Antonin Fabbri, Jean-claude Morel, Henry Wong, and Fionn Mcgregor. Impact of relative humidity on the mechanical behavior of compacted earth as a building material. *Construction and Building Materials*, 110:70–78, 2016.

[31] Florian Champiré, Lucile Soudani, Antonin Fabbri, Jean-Claude Morel, Monika Woloszyn, Henry Wong, Anne-Cécile Grillet, and Stéphane Cointet. Le pisé , un atout pour la transition énergétique dans le bâtiment. In *Forum franco-suisse sur la transition énergétique dans le bâtiment*, page 1, Lyon, France, 2014. Université de Lausanne.

[32] CIBSE. *Heat transfer - Guide C.* Chartered Institution of Building Services Engineers, London, 2002.

[33] JA Clarke, CM Johnstone, NJ Kelly, RC McLean, NJ Rowan, and JE Smith. A technique for the prediction of the conditions leading to mould growth in buildings. *Building and Environment*, 34(4):515–521, 1999.

[34] Joe Clarke. Moisture flow modelling within the ESP-r integrated building performance simulation system. *Journal of Building Performance Simulation*, 6(5):385–399, 2013.

[35] Codyba. Cahier des algorithmes. Technical report, Centre de thermique de l'INSA de Lyon (CETHIL), Lyon, 1992.

[36] Collectif FFB. *Règles professionnelles pour la mise en oeuvre des enduits sur supports composés de terre crue.* Recherche et développement métier, 2012.

[37] F Collet. *Caractérisation hydrique et thermique de matériaux de génie civil à faibles impacts environnementaux - Thèse de doctorat, Institut National des Sciences Appliquées, Rennes.* PhD thesis, 2004.

[38] Florence Collet, Laurent Serres, Jacques Miriel, and Marjorie Bart. Study of thermal behaviour of clay wall facing south. *Building and Environment*, 41(3):307–315, 2006.

[39] B Contet. Caractérisation du comportement hygrothermique du pisé - Mémoire de Travail de Fin d'Etudes, Ecole Nationale des Travaux Publics de l'Etat, Vaulx-en-Velin. Technical report, 2012.

[40] AT Corey. The interrelation between gas and oil relative permeabilities. *Producers Monthly 19*, 19:38–41, 1954.

[41] Olivier Coussy. *Poromechanics*. John Wiley & Sons Ltd, West Sussex, England, 2004.

[42] H. Guillaud CRATerre, H.Houben. *Traité de construction en Terre*. Parenthèse edition, 2006.

[43] CSIRO. Mud walls give poor insulation. Technical report, 2000.

[44] Yu-Jun Cui and Pierre Delage. L'eau dans les sols non saturés. *Techniques de l'ingérieur - Construction*, 1(C301):0–20, 2000.

[45] A. Delsante. A comparison of accurate predictions with measured data from a mud brick house. In *IBPSA Australasia 2006 Conference*, pages 96–103, Adelaide, 2006.

[46] Hannelore Derluyn, Dominique Derome, Jan Carmeliet, Eric Stora, and Rémi Barbarulo. Hysteretic moisture behavior of concrete: Modeling and analysis. *Cement and Concrete Research*, 42(10):1379–1388, 2012.

[47] Hannelore Derluyn, Hans Janssen, J Diepens, Dominique Derome, and Jan Carmeliet. Hygroscopic behavior of paper and books. *Journal of Building physics*, 31(9):9–34, 2007.

[48] Armand Desbat. Rue des Farges : la terre gallo-romaine à Lyon. *Pignon sur rue*, 30:12.

[49] M.K. Dixit, JL Fernandez-Solis, S. Lavy, and C.H. Culp. Identification of parameters for embodied energy measurement: A literature review. *Energy and Buildings*, (42):1238–1247, 2010.

[50] Gerson Dos Santos and Nathan Mendes. Simultaneous heat and moisture transfer in soils combined with building simulation. *Energy and Buildings*, 38(4):303–314, 2006.

[51] Thierry Duforestel. *Des transferts couplés de masse et de chaleur à la conception bioclimatique : recherches sur l'efficacité énergétique des bâtiments*. PhD thesis, Université Claude Bernard Lyon 1, 2015.

[52] Marcelo G Emmel, Marc O Abadie, and Nathan Mendes. New external convective heat transfer coefficient correlations for isolated low-rise buildings. *Energy and Buildings*, 39:335–342, 2007.

[53] ENTPE. SATELLIGHT station : IDMP, Vaulx-en-Velin, France.

[54] Antonin Fabbri, Olivier Coussy, Teddy Fen-chong, and PJM Monteiro. Are deicing salt necessary to promote scaling in concrete ? *Journal of Engineering Mechanics*, 134:589–598, 2008.

[55] Lei Fang, Geo Clausen, and Povl Ole Fanger. Impact of temperatre and humidity on chemical and sensory emissions from building materials. *Indoor air*, 9(3):193–201, 1999.

[56] Chi Feng, Hans Janssen, Ya Feng, and Qinglin Meng. Hygric properties of porous building materials : Analysis of measurement repeatability and reproducibility. *Building and Environment*, 85:160–172, 2015.

[57] José L Fernandez, Miguel A Porta-Gandara, and Norberto Chargoy. Rapid onsite evaluation of thermal comfort through heat capacity in buildings. *Energy and Buildings*, 37:1205–1211, 2005.

[58] A Figueiredo, H Varum, A Costa, D Silveira, and C Oliveira. Seismic retrofitting solution of an adobe masonry wall. *Materials and Structures*, 46(1):203–219, 2013.

[59] Fraunhofer. IBP / WUFI.

[60] Martin Freney. *Earthship Architecture : Post occupancy evaluation , thermal performance & life cycle assessment.* PhD thesis, The University of Adelaide, 2014.

[61] WR Gardner. Some steady state solutions of the unsaturated moisture flow equation with application to evaporation from a water table. *Soil Science*, 85:228–232, 1958.

[62] V Geros, M Santamouris, A Tsangrasoulis, and G Guarracino. Experimental evaluation of night ventilation phenomena. *Energy and Buildings*, 29(2):141–154, 1999.

[63] Francesco Goia, Marco Perino, and Valentina Serra. Improving thermal comfort conditions by means of PCM glazing systems. *Energy and Buildings*, 60:442–452, 2013.

[64] Idalia Gomes, Teresa Diaz Gonçalves, and Paulina Faria. Hygric Behavior of Earth Materials and the Effects of their Stabilization with Cement or Lime: Study on Repair Mortars for Historical Rammed Earth Structures. *Journal of Materials in Civil Engineering*, 28(7), 2016.

[65] Steven Goodhew and Richard Griffiths. Sustainable earth walls to meet the building regulations. *Energy & Buildings*, 37(5):451–459, 2005.

[66] WG Gray. General conservation equations for multi-phase systems. *Advances in Water Resources*, 6:130–140, 1983.

[67] John Grünewald. *Diffusiver und Konvektiver Stoff-und Energietransport in kapillarporösen Baustoffen.* PhD thesis, Technische Universität Dresden, Germany, 1997.

[68] RJ Gummerson, Christopher Hall, and WD Hoff. Water Movement in Porous Building Materia . ls–II . Hydraulic Suction and Sorptlvlty of Brick and Other Masonry Materials. *Building and Environment*, 15(2):101–108, 1980.

[69] Carl-Eric Hagentoft. HAMSTAD, WP2: Modeling. Technical report, Chalmers University of Techonology, Chalmers, Sweden, 2002.

[70] Carl-Eric Hagentoft, Angela Kalagasidis, Bijan Adl-Zarrabi, Staf Roels, Jan Carmeliet, and Hugo Hens. Assessment method of numerical prediction models for combined heat, air, and moisture transfer in building components: benchmarks for one-dimensional cases. *Journal of Thermal Envelope and Building Science*, 27(4):327–352, 2004.

[71] M Hall and D Allinson. Assessing the effects of soil grading on the moisture content-dependent thermal conductivity of stabilised rammed earth materials. *Applied Thermal Engineering*, 29:740–747, 2009.

[72] M R Hall and D Allinson. Analysis of the hygrothermal functional properties of stabilised rammed earth materials. *Building and Environment*, 44(9):1935–1942, 2009.

[73] Matthew Hall and Youcef Djerbib. Moisture ingress in rammed earth: Part 1—the effect of soil particle-size distribution on the rate of capillary suction. *Construction and Building Materials*, 18(4):269–280, May 2004.

[74] Stéphane Hameury. Moisture buffering capacity of heavy timber structures directly exposed to an indoor climate: a numerical study. *Building and Environment*, 40(10):1400–1412, 2005.

[75] William Haynes. *Handbook of chemistry and physics*. 60th edition, 2014.

[76] Hugo Hens. *Bulding Physics - Heat, Air and Moisture Fundamentals and Engineering - Methods with Examples and Exercices*. Ernst & Sohn, Berlin, 2nd editio edition, 2007.

[77] International Organization for Standardization. EN 15026 - Hygrothermal Performance of Building Components and Building elements - Assessment of Moisture Transfer by Numerical Simulation. Technical report, 2007.

[78] Hans Janssen. Thermal diffusion of water vapour in porous materials: Fact or fiction? *International Journal of Heat and Mass Transfer*, 54:1548–1562, March 2011.

[79] Xing Jin, Xiaosong Zhang, Yiran Cao, and Geng Wang. Thermal performance evaluation of the wall using heat flux time lag and decrement factor. *Energy and Buildings*, 47(2012):369–374.

[80] Annabelle Joulin, Zohir Younsi, Laurent Zalewski, Stéphane Lassue, Daniel R Rousse, and Jean-paul Cavrot. Experimental and numerical investigation of a phase change material : Thermal-energy storage and release. *Applied Energy*, 88(7):2454–2462, 2011.

[81] B Khadka and M Shakya. Comparative compressive strength of stabilized and un-stabilized rammed earth. *Materials and Structures*, 49(9):3945–3955, 2016.

[82] Abdul-jabbar N Khalifa. Natural convective heat transfer coefficient - a review I . Isolated vertical and horizontal surfaces. *Energy Conversion and Management*, 42:491–504, 2001.

[83] Abdul-jabbar N Khalifa. Natural convective heat transfer coefficient - a review II . Surfaces in two-and three-dimensional enclosures. *Energy Conversion and Management*, 42:505–517, 2001.

[84] K Kiessl. *Capillary and vaporous moisture transport in multi-layered building components.* PhD thesis, Universität-Gesamthochschule Essen, 1983.

[85] D Kondepudi and I Prigogine. *Modern Thermodynamics : From the Heat Engines to Dissipative Structures.* John Wiley & Sons Ltd, New-York, 1998.

[86] Dimitrios Kraniotis and Kristine Nore. Thermography measurements and latent heat documentation of Norwegian spruce (Picea abies) exposed to dynamic indoor climate. *Journal of wood science*, 2015.

[87] G Kruithof. R-rating not the full story. *Owner Builder Magazine, first edition*, 2000.

[88] Martin Krus and Andreas Holm. Simple methods to approximate the liquid transport coefficients describing the absorption and drying. In *5th symposium 'Building Physics in the Nordic Countries - Göteborg*, pages 241–248, 1999.

[89] H M Künzel. Simultaneous heat and moisture transport in building components one - and two-dimensional calculation using simple parameters - Report on PhD thesis, Fraunhofer Institute of Building Physics. Technical report, Fraunhofer Institute of Building Physics, 1995.

[90] J Kurnitski, T Kalamees, J Palonen, L Eskola, and O Seppänen. Potential effects of permeable and hygroscopic lightweight structures on thermal comfort and perceived IAQ in a cold climate. *Indoor air*, 17(1):37–49, 2007.

[91] Matthieu Labat, Monika Woloszyn, Géraldine Garnier, and Jean-Jacques Roux. Dynamic coupling between vapour and heat transfer in wall assemblies : Analysis of measurements achieved under real climate. *Building and Environment*, 87:129–141, 2015.

[92] Silvana Flores Larsen, Graciela Lesino, and Article History. Thermal behavior of building walls in summer : Comparison of available analytical methods and experimental results for a case study. *Building Simulation*, (2009):3–18, 2002.

[93] Jean-Paul Laurent. *Contribution à la caractérisation thermique des milieux poreux granulaires.pdf*. PhD thesis, INSA, 1986.

[94] D Lelievre and Thibaut Colinart. Hygrothermal behavior of bio-based building materials including hysteresis effects: Experimental and numerical analyses. *Energy and Buildings*, 84:617–627, 2014.

[95] Xiang Qian Li, Youming Chen, JD Spitler, and D Fisher. Applicability of calculation methods for conduction transfer function of building constructions. *International Journal of Thermal Sciences*, 48(7):1441–1451, 2009.

[96] D L Loveday and A H Taki. Convective heat transfer coefficients at a plane surface on a full-scale building facade. *International Journal of Heat and Mass Transfer*, 39(8):1729–1742, 1996.

[97] A.V. Luikov. Systems of differential equations of heat and mass transfer in capillary-porous bodies. *International Journal of Heat and Mass Transfer*, 18(Pergamon Press):1–14, 1975.

[98] Ardeshir Mahdavi and Satish Kumar. Implications of indoor climate control for comfort, energy, and environment. *Energy & Buildings*, 24(3):167–177, 1996.

[99] Vasilios Maniatidis and Peter Walker. *A Review of Rammed Earth Construction*. Number May. 2003.

[100] Silvia Martin, Fernando Mazarron, and Ignacio Canas. Study of thermal environment inside rural houses of Navapalos (Spain): The advantages of reuse buildings of high thermal inertia. *Construction and Building Materials*, 24(5):666–676, 2010.

[101] Fountains of Bryn Mawr. Cob wall mud construction, 2007.

[102] W.H. McAdams. *Heat transmission*. McGraw-Hill, New-York, 3rd edition, 1954.

[103] Fionn Mcgregor, Andrew Heath, and Andy Shea. The moisture buffering capacity of unfired clay masonry. *Building and Environment*, 82:599–607, 2014.

[104] Nathan Mendes, RCLF Oliveira, and GH Santos. Energy efficiency and thermal comfort analysis using the powerdomus hygrothermal simulation tool. In *9th Building Simulation Conference - IBPSA'05*, pages 9–16, 2005.

[105] Nathan Mendes and PC Philippi. A method for predicting heat and moisture transfer through multilayered walls based on temperature and moisture content gradients. *International Journal of Heat and Mass Transfer*, 48(1):37–51, 2005.

[106] Paulo Mendonça. Non-structural adobe walls in housing buildings : environmental performance. In *International Symposium on Earthen Structure, Bangalore, India*, pages 167–174, 2007.

[107] Gernot Minke. *Building with earth.* Birkhäuser, 2006.

[108] J C Morel, A Mesbah, M Oggero, and P Walker. Building houses with local materials : means to drastically reduce the environmental impact of construction. *Building and Environment*, 36:1119–1126, 2001.

[109] Neal Mortensen. The naturally air conditioned house - Sharing Sustainable Solutions. *AIRAH Journal*, 48:11, 1994.

[110] H. Nowamooz and C. Chazallon. Finite element modelling of a rammed earth wall. *Construction and Building Materials*, 25(4):2112–2121, April 2011.

[111] W Nusselt and W Jürges. Die Kuhlung einer ebenen Wand durch einen Luftstrom. *Gesundheits Ingenieur*, 52(45):641–642, 1922.

[112] Florian Osselin, Antonin Fabbri, Teddy Fen-chong, Jean-michel Pereira, Arnault Lassin, and Patrick Dangla. Experimental investigation of the influence of supercritical state on the relative permeability of Vosges sandstone. *Comptes Rendus Mecanique*, 343(9):495–502, 2015.

[113] Yacine Aït Oumeziane, Marjorie Bart, Sophie Moissette, and Chrisophe Lanos. Hysteretic behaviour and moisture buffering of hemp concrete. *Transport in Porous Media*, 103(3):515–533, 2014.

[114] J A Palyvos. A survey of wind convection coefficient correlations for building envelope energy systems ' modeling. *Applied Thermal Engineering*, 28:801–808, 2008.

[115] M. Luisa Parra-Saldivar and William Batty. Thermal behaviour of adobe constructions. *Building and Environment*, 41(12):1892–1904, December 2006.

[116] PassivAct. Qualité thermique comparées des matériaux, 2012.

[117] Alessandra Patera, Hannelore Derluyn, Dominique Derome, and Jan Carmeliet. Influence of sorption hysteresis on moisture transport in wood. *Wood science and Technology*, 50(2):259–283, 2016.

[118] J.R. Philip and D.A De Vries. Moisture movement in porous materials under temperature gradients. *Transactions, American Geophysical Union*, 38:222–232, 1957.

[119] PUCPR University - Laboratorio de Sistemas Termicos. PowerDomus software.

[120] Mariarosa Raimondo, Michele Dondi, Davide Gardini, Guia Guarini, and Francesca Mazzanti. Predicting the initial rate of water absorption in clay bricks. *Construction and Building Materials*, 23(7):2623–2630, July 2009.

[121] Carsten Rode, Ruut Peuhkuri, Berit Time, Kaisa Svennberg, and Tuomo Ojanen. Moisture Buffer Value of Building Materials. Technical report, 2005.

[122] Staf Roels. How reliable are standard cup tests for the determination of the vapour permeability of building materials? In Energy Efficiency Edition and New Approaches, editors, *Proceedings of the 4th International Building Physics conference*, pages 1001–1006, Istanbul, Turkey, 2009.

[123] Staf Roels, Harold Brocken, Robert Cerny, Zbysek Pavlik, Christopher Hall, Leo Pel, and Rudolf Plagge. Interlaboratory Comparison of Hygric Properties of Porous Building Materials. *Journal of Thermal Envelope and Building Science*, 27(4):307–325, 2004.

[124] Staf Roels, Jan Carmeliet, and Hugo Hens. HAMSTAD, WP1: Final report Moisture Transfer Properties and Materials Characterization. Technical report, KU Leuven, Belgium, Leuven, 2003.

[125] Staf Roels, Prabal Talukdar, Chris James, and Carey J Simonson. Reliability of material data measurements for hygroscopic buffering. *International Journal of Heat and Mass Transfer*, 53(23-24):5355–5363, 2010.

[126] Saint Gobain. Introduction à la thermique du bâtiment. 2012.

[127] Valentina Serra, Fabio Zanghirella, and Marco Perino. Experimental evaluation of a climate façade: Energy efficiency and thermal comfort performance. *Energy and Buildings*, 42(1):50–62, 2010.

[128] Jibao Shen, Stéphane Lassue, Laurent Zalewski, and Dezhong Huang. Numerical study on thermal behavior of classical or composite Trombe solar walls. *Energy and Buildings*, 39:962–974, 2007.

[129] Lucile Soudani, Antonin Fabbri, Jean-Claude Morel, Monika Woloszyn, Pierre-Antoine Chabriac, and Anne-Cécile Grillet. Assessment of the validity of some common assumptions in hygrothermal modeling of earth based materials. *Energy and Buildings*, (116):498–511, 2016.

[130] Lucile Soudani, Antonin Fabbri, Monika Woloszyn, Pierre-Antoine Chabriac, Jean-Claude Morel, and Anne-Cécile Grillet. On the relevance of neglecting the mass vapor variation for modeling the hygrothermal behavior of rammed earth. In *ICREC 2015*, number 2, Perth, Australia, 2015.

[131] Lucile Soudani, Antonin Fabbri, Monika Woloszyn, Anne-Cécile Grillet, and Jean-Claude Morel. Water uptake experiment on rammed earth samples to fit the liquid permeability – variation with density and lime concentration. *Materials and Structures*, submitted, 2016.

[132] Lucile Soudani, Monika Woloszyn, Antonin Fabbri, Jean-Claude Morel, and Anne-Cécile Grillet. Energy evaluation of rammed earth walls using long term in-situ measurements. *Solar Energy*, submitted, 2016.

[133] International Standard. ISO 15148 - Hygrothermal performance of building materials and products - Determination of water absorption coefficient by partial immersion, 2002.

[134] Marijke Steeman, Arnold Janssens, Hendrik-Jan Steeman, M Van Belleghem, and M De Paepe. On coupling 1D non-isothermal heat and mass transfer in porous materials with a multizone building energy simulation model. *Building and Environment*, 45(4):865–877, 2010.

[135] Emma Stephan. *Méthode d'aide à la décision multicritère des stratégies de réhabilitation des bâtiments anciens en pierre calcaire - Application au patrimoine en tuffeau.* PhD thesis, ENTPE, Université de Lyon, 2014.

[136] Chuan Sun, Shuiming Shu, Guozhong Ding, Xiaoqing Zhang, and Xinghua Hu. Investigation of time lags and decrement factors for different building outside temperatures. *Energy and Buildings*, 61(2013):1–7.

[137] Jonathon Taylor, Philip Biddulph, and Michael Davies. Using building simulation to model the drying of flooded building archetypes. *Journal of Building Performance Simulation*, 6(2):119–140, 2013.

[138] P. Taylor, RJ Fuller, and M.B. Luther. Energy use and thermal comfort in a rammed earth office building. *Energy and Buildings Buildings*, 40(5):793–800, 2008.

[139] P. Taylor and M.B. Luther. Evaluating rammed earth walls: a case study. *Solar Energy*, 76(1-3):79–84, January 2004.

[140] J.L. Therkeld. *Thermal environmental engineering.* Engelwood Cliffs, Prentice-Hall, 1970.

[141] Catarina Thormark. A low energy building in a life cycle — its embodied energy , energy need for operation and recycling potential. *Building and Environment*, 37:429–435, 2002.

[142] Berit Time and S Uvslokk. Intercomparison on measurement of water vapour permeance - Nordtest-project agreement 1529-01. Technical report, Norges byggforskningsinstitutt, Oslo, 2003.

[143] Felix Trombe. Maisons solaires. *Techniques de l'ingérieur*, 3:375–382, 1974.

[144] Vineet Veer Tyagi and D Ã Buddhi. PCM thermal storage in buildings : A state of art. *Renewable & Sustainable Energy Reviews*, 11(2007):1146–1166, 2005.

[145] Koray Ulgen. Experimental and theoretical investigation of effects of wall's thermophysical properties on time lag and decrement factor. *Energy and Buildings*, 34:273–278, 2002.

[146] UNESCO. Site historique de Lyon, 1998.

[147] University of Strathclyde - Energy Systems Research Unit. ESP-r software.

[148] U.S. Department of Energy - Building technologies Office. Energy Plus sofware, 2014.

[149] U.S. Department of Energy - Office of Energy Efficiency and Renewable Energy. Software listing, 2014.

[150] B. V. Venkatarama Reddy and S.R. Hubli. Properties of lime stabilised steam-cured blocks for masonry. *Materials and Structures*, 35(5):293–300, 2002.

[151] Pernelle Vodinh and Justine Toulouse. Etude du comportement thermique d'une maison en pisé. Technical report, LOCIE, Université de Savoie, 2015.

[152] Peter Walker. Review and experimental comparison of erosion test for earth blocks. In *Terra 2000, 8th International Conference on the study and conservation of earthen architecture organised*, pages 177–181, Torquay, England, 2000. English Heritage.

[153] Stephen Whitaker. *Simultaneous Heat, Mass, and Momentum Transfer in Porous Media: A Theory of Drying*, volume 13. 1977.

[154] Alex Wilson. Thermal mass and r-value : Making sense of a confusing issue. *Environmental Building News*, 7(4), 1998.

[155] Monika Woloszyn. *Modélisation hygro-thermo-aeraulique des bâtiments multizones*. PhD thesis, CETHIL, INSA de Lyon, 1999.

[156] Monika Woloszyn, Targo Kalamees, Marc Olivier Abadie, Marijke Steeman, and Angela Kalagasidis. The effect of combining a relative-humidity-sensitive ventilation system with the moisture-buffering capacity of materials on indoor climate and energy efficiency of buildings. *Building and Environment*, 44(3):515–524, 2009.

[157] Monika Woloszyn and Carsten Rode. Tools for performance simulation of heat, air and moisture conditions of whole buildings. *Building Simulation*, 1(1):5–24, 2008.

[158] Laurent Zalewski, Annabelle Joulin, Stéphane Lassue, Yvan Dutil, and Daniel Rousse. Experimental study of small-scale solar wall integrating phase change material. *Solar Energy*, 86:208–219, 2012.

[159] Xiaobo Zhang, Wolfgang Zilig, Hartwig Künzel, Christoph Mitterer, and Xu Zhang. Combined effects of sorption hysteresis and its temperature dependency on wood materials and building enclosures – Part I: Measurements for model validation. *Building and Environment*, 106:143–154, 2016.

[160] Yinping Zhang, Guobing Zhou, Kunping Lin, Qunli Zhang, and Hongfa Di. Application of latent heat thermal energy storage in buildings : State-of-the-art and outlook. *Building and Environment*, 42:2197–2209, 2007.

[161] W Zillig, Hans Janssen, Jan Carmeliet, and Dominique Derome. Liquid water transport in wood : Towards a mesoscopic approach. In Rao & Desmarais (eds) Fazio, Ge, editor, *Research in Building Physics Engineering*, pages 107–114, London, 2006. Taylor & Francis Group.

[162] Z Zrikem and E Bilgen. Theoretical study of a composite Trombe-Michel wall solar collector system. *Solar Energy*, 39(5):409–419, 1987.

FOLIO ADMINISTRATIF

THESE SOUTENUE DEVANT L'ECOLE NATIONALE DES TRAVAUX PUBLICS DE L'ETAT

NOM : SOUDANI **DATE de SOUTENANCE** : 9 décembre 2016

Prénoms : Lucile, Caroline, Laurence

TITRE : Modelling and experimental validation of the hygrothermal performances of earth as a building material

NATURE : Doctorat **Numéro d'ordre** : 2016LYSET011

Ecole doctorale : MEGA (Mécanique, Energétique, Génie Civil, Acoustique)

Spécialité : Génie Civil

Cote B.I.U. - / et bis CLASSE :

RESUME :

La thèse s'inscrit dans un projet de recherche national (ANR Primaterre) qui a pour but d'étudier les performances (mécaniques et thermiques) réelles des matériaux de construction premiers à faible énergie grise que sont la terre crue et la limousinerie.

Le travail de thèse se concentre sur les aspects thermiques et hygrothermiques de la terre crue, c'est-à-dire le couplage entre les transferts de masse d'eau (liquide et vapeur) et de chaleur au sein du matériau. Dans une première partie, une analyse des performances thermiques et hydriques d'une habitation comportant des murs en pisé (terre crue compactée) instrumentés a été réalisée. Cette étude a été complétée par la mesure, en laboratoire, des propriétés thermiques et hydriques du matériau. Le lien entre les paramètres matériaux mesurés et les performances (hygro)-thermiques a été appréhendé à la lumière d'un modèle numérique couplé, adapté aux caractéristiques particulières du matériau. Cette étude a mis en évidence que, de par leur aptitude à stocker puis restituer l'énergie solaire, leur capacité de stockage hydrique et la complexité des transports et changements de phases de l'eau se produisant en leur sein, les murs en terre crue présentent de nombreuses particularités qu'il convient de prendre en compte pour une bonne prédiction de leur impact sur les performances d'une habitation.

MOTS-CLES : matériau terre, hygrothermie, mesures in-situ, modélisation du couplage, apports solaires, remontées capillaires

Laboratoire (s) de recherche :
- Laboratoire Génie Civil et Bâtiment (LBCG) - Laboratoire de Tribologie et Dynamique des Systèmes (LTDS) – UMR 513 CNRS, ENTPE, Université de Lyon
- Laboratoire Optimisation de la Conception et Ingénierie de l'Environnement (LOCIE), UMR 5271 CNRS, Université Savoie Mont-Blanc

Directeur de thèse:
- Antonin Fabbri
- Monika Woloszyn

Président de jury : Prof. Stéphane Lassue

Composition du jury :
Prof. Stéphane Lassue, rapporteur, Université d'Artois
Prof. Nathan Mendes, rapporteur, PUCPR, Curitiba, Brésil
Dr Thibaut Colinart, examinateur, Université Bretagne Sud
Prof. Jean-Claude Morel, examinateur, Coventry University
Dr. Anne-Cécile Grillet, examinatrice, Université Savoie Mont-Blanc
Dr. Antonin Fabbri, directeur, ENTPE
Prof. Monika Woloszyn, directrice, Université Savoie Mont-Blanc